Laboratoire Temps-Fréquence (LTF)

Studies on miniature and compact Ramsey double-resonance Rubidium atomic clocks using hot vapors and cold atoms

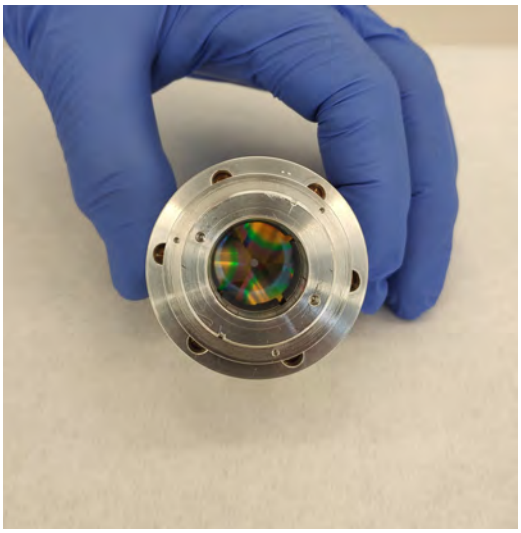

Thèse présentée à la

FACULTÉ DES SCIENCES DE L'UNIVERSITÉ DE NEUCHÂTEL

pour l'obtention du grade de

DOCTEUR ÈS SCIENCES

par

Etienne Batori
MSc en Physique de l'Ecole Polytechnique Fédérale de Lausanne (EPFL)

Thèse acceptée le 13 juin 2023 sur proposition du jury:

Prof. Dr. Gaetano MILETI, Université de Neuchâtel, CH, Directeur de thèse
Prof. Dr. Erling RIIS, University of Strathclyde, UK, Rapporteur
Prof. Dr. Thejesh N. BANDI, University of Alabama, USA, Rapporteur
Dr. Christoph AFFOLDERBACH, Université de Neuchâtel, CH, Examinateur

Neuchâtel, 12 juillet 2023

unine
Université de Neuchâtel
Faculté des sciences

Rue Emile-Argand 11
CH-2000 Neuchâtel
doctorat.sciences@unine.ch

IMPRIMATUR POUR THESE DE DOCTORAT

La Faculté des sciences de l'Université de Neuchâtel autorise l'impression de la présente thèse soutenue par

Monsieur Etienne BATORI

Titre :

"Studies on miniature and compact Ramsey double-resonance Rubidium atomic clocks using hot vapors and cold atoms"

sur le rapport des membres du jury composé comme suit :

- Prof. Gaetano Mileti, directeur de thèse, Université de Neuchâtel, Suisse
- Dr Christophe Affolderbach, Université de Neuchâtel, Suisse
- Prof. Erling Riis, University of Strathclyde, Glasgow, UK
- Prof. Thejesh N. Bandi, University of Alabama, USA

Neuchâtel, le 24 juillet 2023

Le Doyen, Prof. R. Bshary

Abstract

This thesis presents results on two microwave, double-resonance, Rubidium 87 atomic clocks. These studies are motivated by the need for compact and miniature clocks with improved performances or improved Size, Weight and Power (SWaP).

A first clock study, covered in chapter 3, focuses on the μPOP clock, the first demonstration of Double Resonance (DR) Ramsey operation in a micro-manufactured hot-vapor cell clock. With a short-term stability of $\sigma_y(\tau) \leq 2 \times 10^{-11}\tau^{-1/2}$ and long-term stability of 1.5×10^{-12} at one day, the μPOP clock features state-of-the-art stability for microwave miniature cell clocks.

As demonstrated in [1], the μPOP clock short-term stability has been optimized to mitigate the Dick effect and laser Relative Intensity Noise (RIN) contributions, with the latter being the biggest contributor to the short-term stability. The long-term instability budget shows that the intensity and frequency light shifts contributions are one and two order of magnitudes lower than the measured stability with a contribution of the order of 10^{-13} and 10^{-14} at one day, respectively. This confirms the interest of the Pulsed Optically Pumped (POP) approach compared to the Continuous Wave (CW) scheme and sets the potential performances of the μPOP clock. Other long-term contributors to the instabilities have been evaluated. In the upper limit, the contribution of the cell-temperature shift to the instability is estimated to be two orders of magnitude below the measured stability, confirming the benefit of the N_2 and Ar buffer gas-mixture approach for a close to zero cell-temperature sensitivity coefficient. The last two effects, the microwave-power and the position shifts are the greatest contributor to the mid and long-term stability with the latter being the limiting long-term phenomenon whose contribution must be carefully evaluated using the Groslambert covariance.

The μPOP studies conclude with the description of a fast and reliable method for measuring the relaxation rates in Ramsey DR vapor-cell clocks. At the nominal cell temperature, namely ≈ 100°C, the population and coherence relaxations rates are measured to be at the order of 5 kHz and 4 kHz, respectively. Their values have been measured down to 60°C with both at the order of 1 kHz. Finally, a theoretical model using only parameters taken from the literature has been derived to describe the measured relaxation rates values with agreement within 20%.

Chapter 4 focuses on the simulation and realization of a microwave cavity for a DR cold-atom clock using a Grating Magneto-Optical Trap (GMOT). The final cavity shows a low quality factor of $Q \approx 360$ which is in the interest of reducing the cavity-pulling shift. The TE_{011}-like cavity mode is separated by at least 500 MHz from the neighbouring modes as predicted by the simulations. The same simulations allowed to effectively predict the cavity's resonance frequency with a small error of

60 MHz which can easily be compensated by the cavity frequency tuning mechanism. The expected simulated excellent properties of the resonance mode in term of microwave field uniformity and homogeneity are confirmed by measurement of the field field orientation factor of 97% and low Rabi oscillation damping, respectively.

Chapter 5 focuses on the integration of the microwave cavity in a clock setup designed by Erling Riis group from the university of Strathclyde. The clock described in this chapter is the first realization of a DR Ramsey Rb cold-atom clock using a GMOT for cooling and trapping which reduces the clock footprint. In practise, $\approx 10^6$ atoms at ≈ 10 μK are loaded thanks to the grating. Ramsey fringes were successfully obtained with Ramsey times up to 20 ms, limited by the clock geometric design. The clock implements state-selection that allows for increased Signal-to-Noise Ratio (SNR) and better short-term stability of $\approx 1.5 \times 10^{-11}\tau^{-1/2}$. This stability is well-explained by SNR of the fringes. Long-term stability is dominated by the 2^{nd}-order Zeeman shift contribution as the clock is not magnetically shielded.

The two studies presented in this thesis, namely the μPOP and cold-atom clocks, pave the way towards more miniature and compact frequency standards, respectively. Further improvements of the former would yield a intensity light shift limited clock with $\approx 10^{-13}$ stability at one day. Further version of the latter clock using the cavity as standalone vacuum system would allow for reduced SWaP cold-atom frequency standards.

Keywords: Atomic frequency standard, Rubidium, double-resonance, Ramsey scheme, microfabricated vapor-cell, cold-atom, additive-manufacturing.

Résumé

Cette thèse présente deux nouvelles horloges atomiques au Rubidium 87 à double résonance. Le chapitre 3 se concentre sur l'horloge μPOP, la première démonstration d'une horloge double résonance en mode Ramsey dans une cellule à vapeur micro-fabriquée. La stabilité court-terme de $\sigma_y(\tau) \leq 2 \times 10^{-11}\tau^{-1/2}$ et la stabilité long-terme the 1.5×10^{-12} à la journée en font l'état de l'art dans la catégorie des horloges micro-onde double résonance dans les cellules micro-fabriquées.

Comme démontré dans [1], la stabilié court-terme a été optimisée pour minimiser les contributions de l'effet Dick et de la contribution du bruit d'intensité relatif du laser, avec ce dernier limitant majoritairement les performances de l'horloge à court-terme. le budget long-terme montre que les effets de light-shift en intensité et en fréquence sont respectivement un et deux ordres de grandeurs en-dessous de la stabilité mesurée de l'horloge à la journée ce qui confirme la validité de l'approche POP pour limiter ces deux effets. Dans la limite supérieure, la contribution du décalage de fréquence dû à la température de la cellule est deux ordres de grandeurs au-dessous de la stabilité mesurée grâce au mélange de gaz tampons N_2 et Ar. Les deux derniers effets évalués, les shifts de puissance micro-onde et de position, permettent d'expliquer les limites de performances de l'horloges à moyen et long-terme. Le shift de position est le facteur limitant au long-terme et est évalué avec soin grâce à la variance de Groslambert.

Les études du μPOP se concluent par la démonstration d'une méthode fiable et rapide pour mesurer les taux de relaxation dans les horloges à cellules double résonance en mode Ramsey. Les valeurs des taux de relaxation de population et de cohérence sont d'environ 5 kHz et 4 kHz respectivement à la température nominale de $\approx 100°$C. A $60°$C, les deux taux tombent à 1 kHz. Ces valeurs sont globalement bien expliquées par le modèle présenté entièrement basé sur des coefficients physiques de la litérature. Dans ces conditions la différence entre le modèle et l'expérience est d'au maximum 20%.

Le chapitre 4 démontre la réalisation d'une cavité micro-onde pour une horloge à atomes froids refroidis et prégés à l'aide d'un GMOT. Le facteur de qualité est $Q \approx 360$ ce qui à l'avantage de réduire de shift du cavity-pulling. Le mode de type TE_{011} est séparé d'au moins 500 MHz de ses voisins, comme prédit par les simulations. Ces dernières ont également permis de simuler la fréquence du mode d'intérêt à 60 MHz près qui sont aisément compensés par la gamme d'accordage de la cavité. Les excellentes propriétés du champ magnétique prédites par les simulations en terme d'uniformité et d'homogénéité sont confirmées par la mesure du facteur d'orientation de champ de 97% et l'amortissement faible des oscillations de Rabi, respectivement.

Le chapitre 5 décrit les résultats obtenus lors de l'intégration de la cavité micro-onde susmention-

nées dans une manipulation d'horloge à atomes froids ayant eu lieu à l'université de Strathclyde dans le groupe d'Erling Riis. Cette horloge est la première démonstration d'une horloge à atomes froids de Rb à double résonance utilisant un GMOT pour le refroidissement et le piégeage des atomes. Cette approche permet de réduire considérablement la taille de l'horloge. En pratique, environ 10^6 atomes à 10 μK sont piégés grâce à celui-ci. Les franges de Ramsey sont obtenues avec un temps de Ramsey allant jusqu'à 20 ms limité par la géométrie du setup. Le cycle de l'horloge implémente également une phase de sélection d'état quatique permettant d'augmenter le signal-sur-bruit de l'horloge. La stabilité finale à court-terme est d'environ $1.5 \times 10^{-11}\tau^{-1/2}$ et est en adéquation avec la limite estimée à partir du signal-sur-bruit venant des franges de Ramsey. La stabilité long-terme de l'horloge est limitée par le shift de Zeeman 2$^{\text{ème}}$ ordre dû à l'absence de blindage magnétique du setup.

Mots-clés: Référence de fréquence atomique, Rubidium, double résonance, schéma Ramsey, cellule à vapeur microfabriquée, atomes froids, impression 3d.

Il faut être toujours ivre, tout est là ; c'est l'unique question. Pour ne pas sentir l'horrible fardeau du temps qui brise vos épaules et vous penche vers la terre, il faut vous enivrer sans trêve.

Mais de quoi ? De vin, de poésie, ou de vertu à votre guise, mais enivrez-vous !

Et si quelquefois, sur les marches d'un palais, sur l'herbe verte d'un fossé, vous vous réveillez, l'ivresse déjà diminuée ou disparue, demandez au vent, à la vague, à l'étoile, à l'oiseau, à l'horloge; à tout ce qui fuit, à tout ce qui gémit, à tout ce qui roule, à tout ce qui chante, à tout ce qui parle, demandez quelle heure il est. Et le vent, la vague, l'étoile, l'oiseau, l'horloge, vous répondront, il est l'heure de s'enivrer ; pour ne pas être les esclaves martyrisés du temps, enivrez-vous, enivrez-vous sans cesse ! De vin, de poésie ou de vertu, à votre guise.

— Charles Baudelaire, à qui j'aurais aimé dire qu'on peut aussi oublier le temps qui passe en l'étudiant.

Je dédie cette thèse à mes parents qui m'ont toujours honoré de leur confiance, de leur amour et soutenu dans mes choix[a].

[a] Le lecteur décidera s'ils ont eu raison.

Acknowledgements

When I started writing my thesis, I decided to leave what I thought would be the *simple stuff* for the end of my months-long writing effort: abstract (or *résumé*), resume, title page and... acknowledgements.

Little did I know that thinking back at the last 4 years of my life would revive strong memories intimately linked to incredible people. The insouciant task of writing acknowledgements became the root of one fear: failing to give credit to all people that helped me during this challenge. Let the hasty reader be reassured: reading this section is absolutely not mandatory to understand what follows next.

I cannot thank enough Gaetano Mileti, who first gave me the opportunity to start a PhD in his group. I would lie if I said that knowing about his love for rowing did not help me to be convinced that his group would be the right place for me to work in with a balanced lifestyle. In a more serious tone, I enjoyed our talks and meetings, whether they would be work or life-related. I hope that some of your talent for communication, showcasing and resources management will follow me in my professional career.

Next, I want to thank all my colleagues, especially those who dared to enter the D8 office for coffee.

Thank you Christoph, for supervising me for four years. Your impressive and infinite well of knowledge helped me more than once. I enjoyed all our discussions, whether they would be about normal or Schrödinger cats.

Thank you Florian for helping me many times for technical stuff and basically teaching me how to couple light into optical fibres. Thank for being always in a good mood and your developed sense of humour.

I thank all the other PhD students and post-docs who came in Gaetano's group: Nil, who helped me starting my experiments in the lab, Vladimir who showed me how to simulate microwave cavities, William, thanks to whom I have been aware of the opportunity of doing a PhD in Neuchâtel and with whom I have had great scientific discussions. Thank you Matthieu for your challenging physics questions and sharingmany sport adventures with me.

I would like to thank the people from Thomas Südmeyer group, other PhD students and post-docs with whom I was always happy to share adventures with whether they would consists of a

simple after-work beer, a ski-touring weekend or sharing a sea-food platter in little Italy: thank you Renaud, Nayara, François, Norbert, Michael, Alexandre, Jakub, Kenichi, Julian, Nathan and Marin.

I would like to thank all the technical staff whose help was crucial: thank you Patrick for your help and your acuteness. Thank you Dominique and Daniel for your discussions and help about the D17. Thank you Cyril, your help was invaluable during these four years.

I would like to thank the Scottish team with whom I spent 2 months doing different physics. Thank you Pr. Riis and James for giving me this great opportunity. Special thanks to Alan, who had to accept to work with me everyday for two months which is not a typical thing to do in the lab. Thank you Ben, Rachel, Rachel, Allan and Oliver. Thank you Sean for having me trying Irn-Bru and climbing the Cobbler.

Thank you Pr. Bandi and Pr. Riis for accepting to be part of my thesis jury.

During my PhD, I had the opportunity to work as UFFC student representative for frequency control. I would like to thank the AdCom Committee who gave me this great opportunity to participate in the organization of international conferences.

Lastly, I would like to thank my parents, Frederic and Francine, sister**s**, Valentine and Sophie and close friends, who helped me keep balance during this challenging adventure. Thank you Simon, Vincent, Robin, Yohan and Dimitri; I hope you all know why you deeply matter to me.

Etienne

Author's contributions

Articles in peer-reviewed journals

E. Batori, A. Bregazzi, B. Lewis, P. F. Griffin, E. Riis, G. Mileti, and C. Affolderbach, *An additive-manufactured microwave cavity for a compact cold-atom clock*, J. Appl. Phys. 133, (2023), 10.1063/5.0151207.

E. Batori, C. Affolderbach, M. Pellaton, F. Gruet, M. Violetti, Y. Su, A.K. Skrivervik, and G. Mileti, *μPOP Clock: A Microcell Atomic Clock Based on a Double-Resonance Ramsey Scheme*, Phys. Rev. Appl. 18, 054039 (2022), 10.1103/PhysRevApplied.18.054039.

E. Batori, N. Almat, C. Affolderbach, and G. Mileti, *GNSS-grade space atomic frequency standards: Current status and ongoing developments*, Adv. Sp. Res. (2020), 10.1016/j.asr.2020.09.012.

International conferences with proceedings

A. Bregazzi, **E. Batori**, B. Lewis, C. Affolderbach, G. Mileti, E. Riis, and P. Griffin, *A compact cold-atom double-resonance clock*, in Quantum Sensing, Imaging, Precis. Metrol., edited by S.M. Shahriar and J. Scheuer (SPIE, 2023), p. 18.

E. Batori, C. Affolderbach, M. Pellaton, F. Gruet, Y. Su, M. Violetti, A. K. Skrivervik and G. Mileti, *LEMAC: Design and studies towards miniature Rb atomic clocks in continuous wave and Ramsey-mode*, 8th International Colloquiumon Scientific and Fundamental Aspects of GNSS, 2022

E. Batori, C. Affolderbach, F. Gruet, M. Pellaton, Y. Su, M. Violetti, A. K. Skrivervik and G. Mileti, *Long-Term Instability of a Pulsed Optically Pumped Micro-cell Rubidium Frequency Standard*, Joint Conference of the European Frequency and Time Forum and IEEE International Frequency Control Symposium (EFTF/IFCS), 2022

E. Batori, C. Affolderbach, M. Pellaton, F. Gruet, G. Mileti, Y. Su, M. Violetti, and A.K. Skrivervik, *Ramsey Spectroscopy in a Micro-Fabricated Rb Vapor Cell for Miniature Atomic Clocks*, in 2021 Jt. Conf. Eur. Freq. Time Forum IEEE Int. Freq. Control Symp. (IEEE, 2021), pp. 1–2.

E. Batori, N. Almat, C. Affolderbach, F. Gruet, and G. Mileti, *High-Performance Pulsed Laser-Pumped Rb Clock for GNSS*, in 2020 Eur. Navig. Conf. (IEEE, 2020), pp. 1–10.

Posters

E. Batori, C. Affolderbach, F. Gruet, M. Pellaton, G. Mileti, Y. Su, M. Violetti, and A.K. Skrivervik, *Experimental Determination of Relaxation Rates in a Ramsey-mode Rubidium Cell Atomic Clock*, in 2022 Jt. Conf. Eur. Freq. Time Forum IEEE Int. Freq. Control Symp. (IEEE, 2022), pp. 1–2.

M. Pellaton, C. Affolderbach, **E. Batori**, G. Mileti, Y. Su, M. Violetti, and A.K. Skrivervik, *LEMAC: LTF-EPFL Miniature Atomic Clock : current status*, in 2022 Jt. Conf. Eur. Freq. Time Forum IEEE Int. Freq. Control Symp. (IEEE, 2022), pp. 1–2.

E. Batori, C. Affolderbach, V. Dolgovskiy, M. Pellaton, B. Lewis, P. F. Griffin, E. Riis, G. Mileti, *Additive Manufactured Microwave Cavity for a Compact Rb cold-Atom Clock*, Joint Conference of the European Frequency and Time Forum and IEEE International Frequency Control Symposium (EFTF/IFCS), 2021

Talks without proceedings

E. Batori, C. Affolderbach, F. Gruet, Y. Su, M. Violetti, A.K. Skrivervik, and G. Mileti, *Miniature Atomic Clock Using Pulsed Double Resonance on a Micro-fabricated Rubidium Vapor Cell*, Precise Time and Time Interval Systems and Applications Meeting, 2022 (oral presentation)

Arxiv

E. Batori, A. Bregazzi, B. Lewis, P. Griffin, E. Riis, G. Mileti, and C. Affolderbach, *An additive-manufactured microwave cavity for a compact cold-atom clock*, To Be Publ. (2023), http://arxiv.org/abs/2305.02898.

A. Bregazzi, **E. Batori**, B. Lewis, C. Affolderbach, G. Mileti, E. Riis, and P. Griffin, *A cold-atom Ramsey clock with a low volume physics package*, To Be Publ. (2023), http://arxiv.org/abs/2305.02944.

Contents

List of Figures

List of Tables

List of acronyms

ACT Auto Cavity Tuning

AFS Atomic Frequency Standard

AOM Acusto-Optic Modulator

APPS Automatic Precise Positioning Service

CPT Coherent population Trapping

Cs Cesium

CSAC Chip Scale Atomic Clock

CW Continuous Wave

DFB Distributed-Feedback Laser

DR Double Resonance

DSAC Deep-Space Atomic Clock

DUT Device Under Test

ECDL Extended Cavity Diode Laser

EOM Electro-Optic Modulators

EQOP Experimental Quantum Optics and Photonics Group

ESA Europen Space Agency

FFT Fast Fourier Transform

FOF Field Orientation Factor

FOM Figure Of Merit

FWHM Full Width at Half Maximum

GMOT Grating Magneto-Optical Trap

GNSS Global Navigation Satellite System

GPS Global Positioning System

H Hydrogen

INMAQS International Network for Micro-fabricated Atomic Quantum Sensors

JPL Jet Propulsion Lab

LGR Loop Gap Resonator

LO Local Oscillator

LTE Long-Term Evolution

LTF Laboratoire Temps-Fréquence

MASER Microwave Amplification by Stimulating Emission of Radiation

MAD Median Absolute Deviation

NTC Negative Temperature Coefficient Thermistor

OCXO Oven Controlled Crystal Oscillator

PHM Passive Hydrogen Maser

PID Proportional–Integral–Derivative controller

PML Perfectly Matched Layers

POP Pulsed Optically Pumped

RAFS Rubidium Atomic Frequency Standard

RIN Relative Intensity Noise

Rb Rubidium

SAFS Space Atomic Frequency Standard

SNR Signal-to-Noise Ratio

SWaP Size, Weight and Power

TA tappered amplifier

TAI Temps Atomique International

UppMac Ultra-compact physics package for miniature cold-atom clock

UppMac-2G UppMac 2nd Generation

UTC Universal Time Coordinated

VCSEL Vertical-Cavity Surface-Emitting Laser

Thesis outline

This thesis presents results on microwave, double-resonance, Rubidium 87 atomic clocks. The format of the document is called an *"article thesis"* in accordance with the rules of the University of Neuchâtel. This format allows the candidate to directly display published peer-reviewed articles, in preparation articles or proceedings authored by the candidate. The document must also contain an introduction and a summary chapter, which is the role of chapter 6 which summaries all results and proposes future possible steps.

Aside from the conclusion, each chapter presents a peer-review article, an article in preparation or a proceeding. When relevant, supplementary material complements the paper content. This supplementary material either consists of relevant additional details on the paper itself or further studies that were not published.

Chapter 1

Introduction

1.1 Clocks and frequency standards

1.1.1 General considerations

In light of today's physics – which is still best described by the century-old theory of quantum mechanics – the history of the measurement of time and time intervals starts with the greatest challenge: an impossibility. Indeed, according to the laws of the said theory, there is no so-called *time operator* [2]. In other words, it is not possible to build an experiment that tells time. Despite this fundamental wall, countless scientists worked for centuries to develop better and better clocks, which always made me think of them – or us – as some sort of modern version of Camus' Sisyphus[1].

Apart from a few cases such as the sundial, the hourglass and the clepsydra, all ancient and modern clocks share a similar design: a **frequency standard** and a **counter** which are put together. The ensemble is then called a **clock** [3]. This rigorous definition is openly abused by people working in the time and frequency community where frequency standards are first obviously more researched than counters and second because they have other use cases than clocks. For these reasons people researching frequency standards often refer to them as clocks. This conceptual shortcut applies in this thesis.

Frequency standards come in two fashions: **active** and **passive**. The former consists of a self-oscillating resonator whose frequency is captured and usually amplified. In order to allow the oscillator to vibrate, energy is required. Before atomic frequency standards, active oscillators were the most popular: all mechanical clocks such as Swiss cuckoos, tower clocks, wrist watches or the marine chronometer lie in this category. In the same manner, the quartz requires energy to oscillate. When an opera singer hits a diapason on a lectern to tune his or her voice, he or she uses an active frequency standard.

In the case of passive frequency standards (see Figure 1.1), an oscillator – whose frequency must be

[1] In his essay on Sisyphus, Albert Camus states that the punished king has no choice but to accept his absurd fate, which eventually makes him happy: *"The struggle itself [...] is enough to fill a man's heart. One must imagine Sisyphus happy"*.

stabilized – drives a resonator with a well-known resonance frequency. When the frequency of the first oscillator approaches the one of the resonator, maximum absorption of the probing excitation occurs, signifying that the oscillator is on tune [3]. Returning to our musical example, an opera singer might use a diapason in a passive manner by singing at it until it vibrates the most, meaning that the voice is tuned to the diapason.

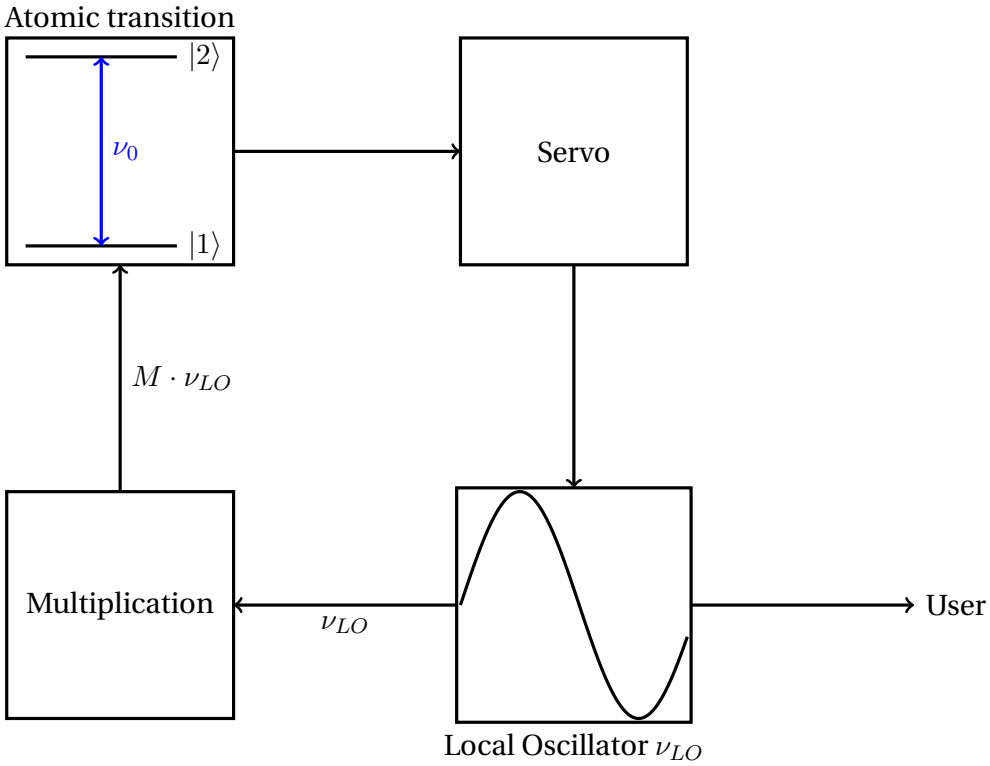

Figure 1.1: Passive atomic frequency standard schematics.

In fact, all the metrological issues encountered by the scientists in their quest for the perfect frequency standard can be understood through the diapason analogy. Being made out of metal, the diapason's frequency can be affected by the slow fluctuations of the temperature in the concert hall or the variations of the humidity in the singer airflow. In the passive model, the frequency could even be affected by the singer's voice intensity. As a last example, as being subject to mechanical stress, the natural frequency of the diapason could age. This phenomenon, known as frequency ageing – or drift – happens to be particularly relevant for vapor-cell frequency standards as the one described in chapter 3.

1.1.2 Atomic frequency standards

Atoms are extremely good resonators for at least two reasons: unlike diapasons, watches and quartz, they[2] do not age and are extremely insensitive to fluctuations of external parameters. Furthermore, atoms of the same species are[2] identical, anywhere, anytime, making them particularly suitable for a general definition physical unit of time, the second. The first statement is coincidently challenged by today's research thanks to the most stable optical clocks [4]. It is important to point out that although microwave atomic frequency standards show excellent long-term stability (i.e. $\tau > 10^3$ s), they also feature poor short-term stability ($\tau < 10$ s) compared to the best commercial Oven Controlled Crystal Oscillator (OCXO)s [5]. Atomic Frequency Standard (AFS)s are hence best candidates for applications requiring excellent long-term stability.

The relevant atoms frequencies for making clocks are those defined by the energy difference between two energy levels E_1 and E_2. The frequency ν of the transition is given by Planck's law, namely:

$$\nu = \frac{E_2 - E_1}{h}, \quad E_2 > E_1 \tag{1.1}$$

with h the Planck's constant. In general, special care is made to choose two quantum states $|1\rangle$ and $|2\rangle$ with low sensitivity to the first order to magnetic fields and other external parameters [5]. Before the optical frequency standards era, as described in [6], the best candidates were the alkali atoms thanks to their simple electronic structure although other technologies like the ammonia maser were investigated [7]. In addition, their clock frequencies (see eq. (1.1)) lay in the microwave domain, which are much easier to work with compared to optical frequencies. Historically, among all the three classical [5], [8], [9] microwave frequency standards were developed: the Hydrogen (H) Microwave Amplification by Stimulating Emission of Radiation (MASER), the Cesium (Cs) beam tube and the RAFS. The first demonstration of an atomic clock – a Cs beam – was made by Essen and Parry [10] in 1955. Only 12 years later, the definition of the SI second was redefined and still holds today. The SI second is hence fixed through the following definition [11]:

> *the unperturbed ground state hyperfine transition frequency of the cesium 133 atom $\Delta\nu_{Cs}$ is 9 192 631 770 Hz.*

Although only Cs frequency standards have the potential to be qualified as primary frequency standards, other clocks were developed based on other atomic species. For instance, this thesis presents work on two proof-of-concept Rubidium (Rb) frequency standards: the first one [1] – named μPOP –, is the first realization of a Ramsey-type clock in a miniature vapor-cell. The second [12], [13] is the first realization of a compact cold-atom Rb clock using a Ramsey DR scheme and a GMOT for cooling and trapping.

1.1.3 SWaP - Or why there is no single good frequency standard

Empirically, there exists a correlation between the performances of a clock and its SWaP [14]. In other words, the bigger, heavier and the more energy-consuming a clock, the potentially better its

[2] To the best of humankind knowledge.

performances. Although it is true to say that a quartz wristwatch – loosing about ± 70 ms a day [15] – is not suitable as GNSS reference, it is also true that an optical atomic clock cannot be worn on a day-to-day basis to catch trains. Clocks are hence always a compromise of SWaP and performances tailored for a specific application.

In terms of performances, it is customary to refer to clocks loosing less than 1 μs (10^{-11} relative stability) a day as telecomgrade. For instance, Long-Term Evolution (LTE) networks – often referred to as 4G – need 1.5 μs stability a day, which is the typical time needed for maintenance in case of the loss of GNSS signal [16], [17]. However, future telecom applications like the future 5G network might need ≈ 400 ns (10^{-12}) stability a day [18]. Those clocks are traditionally GNSS-disciplined [17]. Telecom grade clocks also can improve positioning in GNSS-denied environment [19].

Clocks with a time error up to 1 ns a day (or 10^{-14} fractional stability) are often denoted as GNSS-grade and are described in detail in [6]. One nanosecond stability allows for a theoretically ground instantaneous accuracy of 30 cm [20]. Clocks with similar or slightly better performances such as Active H MASER, Cs beam tubes and cold-atom frequency standards [21]–[23] are generally used as valuable lab frequency references, to synchronize large interferometry experiments [24], to test general relativity [25], [26], in astrophysics experiments [27] or as backbone to national time scales necessary for the economy [28].

Clocks with better long-term performances can be denoted as *science*-grade as they are mostly used in today's research. For instance, a clock with 10^{-16} fractional stability allows to detect an altitude variation of 1 m on earth surface due to gravitational red-shift [29]. The best microwave clocks lay in this category with Cs and Rb fountains [30], [31]. Their performances are outperformed by current optical standards that use either single $^{27}Al^{+}$[32], [33], $^{40}Ca^{+}$[34], [35], $^{88}Sr^{+}$[36], [37] and $^{171}Yb^{+}$[38], [39] ions or ^{87}Sr and ^{88}Sr [40], [41] and ^{171}Yb[42], [43] neutral atoms lattices. These standards are relevant for fundamental science experiments and Temps Atomique International (TAI) building. Discussions on the redefinition of the SI definition of the second based on one or many [44] optical transitions is one of the most metrological hot topics with, at the time of writing, no consensus on the new definition.

Size-wise, denominations of clocks smaller than lab experiments usually include (in decreasing order or SWaP), transportable [45]–[47], portable [48], [49], compact [22], [50] and chip-scale [51]–[53]. Efforts to increase performances of clocks in these categories are usually rewarded with new applications and markets. For instance, transportable optical clocks could allow earth geoid mapping [54].

1.2 Microwave frequency standards

1.2.1 The Rubidium Atomic Frequency Standard (RAFS)

History of microwave frequency standards is partially covered in [6]. Similarly, context on miniature-cell clocks and cold-atom frequency standards are given in [1] and [12], [13], respectively. Given the

content of this thesis, it is however appropriate to give a proper introduction on the RAFS.

History of the RAFS before the laser optical pumping era is well described by Riley [17]. He traces the origin of the first RAFS to Arditi [55]. Interestingly, Rb was not the first atomic species to be considered for vapor-cell frequency standards. It was however preferred because of the mixture of the 85 and 87 isotopes present in nature which allows for simplified lamp optical pumping by means of light filtering [5]. ^{87}Rb is usually preferred before ^{85}Rb because it features a higher resonance frequency which is associated with better relative stability. The advantage of the RAFS compared to the Cs beam and the H MASER is the low SWaP allowed by the vapor-cell as well as longer lifetime. Indeed, in the two other classical frequency standards, Cs and H atoms are consumables. It probably explains why the RAFS is likely the one being the most produced so far being widely used in telecom [17] and GNSS applications [6]. Lamp-based RAFSs are still produced and developed to this day – mainly in GNSS applications – because they feature a mature and well-known technology. To this day, only a few laser-pumped frequency standards were launched into orbit [6] due to the lack of trust in the laser technology for the typical 15 years of operations of a typical GNSS satellite.

All frequency standards have been positively impacted by the development of lasers. In particular, 780 nm GaAlAs diode lasers developed in the beginning of the 1980s for the compact disc technology [56] with wavelength close to the ^{87}Rb D_2 line [57] allowed researchers to develop the first laser-pumped ^{87}Rb frequency standards using affordable and robust technology [58]. Laser-pumped CW-DR show typical short-term performances $\approx 10^{-13}\tau^{-1/2}$ which is one order of magnitude better than lamp-pumped AFS [59]. Long-term performances of Rb CW-DR AFS ultimately remain limited by the light-shift effect which motivated the reconsideration of the Ramsey or POP type Rb frequency standards [60]. This approach was successful [61], [62] and is still studied [63]–[68], notably for GNSS applications [69]. They however remain limited by the same effect [64] probably due to light leakage through the AOM during the Ramsey part of the cycle. These developments for high-performances Rb AFS motivated the studies shown in chapter 3 for improving the performances of miniature-cell frequency standards with ultimately state-of-the-art performances.

1.3 Compact cold-atom frequency standards

Performances of vapor-cell standards remain ultimately limited by the need of a least one buffer gas whose shift is responsible for frequency drift and higher sensitivity to external parameters. Furthermore, this shift prevents vapor-cell standards to be accurate. Laser technologies and the development of laser cooling and trapping allowed the realization of the Cs fountains clocks used for international timekeeping and metrology. Recent efforts towards compact cold-atom AFS using the same principle are now undergoing with the first products available [21], [23]. This context has led us to develop and realize the cold-atom clock shown on chapters 4 and 5 with the first realization of a DR grating mot Ramsey-type atomic clock for the next generation of compact frequency standards.

The history of compact DR cold atoms frequency standards simultaneously starts in the 2010s in France with Horace [22] and in Brazil [70]. As shown on Table 1.1, it is interesting to note that both standards used Cs whereas most recent attempts and products use Rb. The reasons to prefer Rb over

Cs — which motivated the change of atomic species when Horace was transferred to the MuQuans company — are the 30 times lower collision shift in ^{87}Rb cold atoms compared to ^{133}Cs[71] and more easily available laser technologies [72].

Table 1.1 summarizes the Rb DR cold-atom research and products found in the literature. Different microwave resonators designs are used: waveguide, spherical, cylindrical and LGR. Available data suggest that most setups use isotropic cooling except for [73], [74] and this work. Manufacturers obviously rather communicate on SWaP and less on technology features (e.g., cavity type) whereas research paper focus more and concepts and less on SWaP.

Short-term stability ($\tau^{-1/2}$ fit) range from 1.5×10^{-11} (this work) to 3.2×10^{-13} [23] which is comparable to high-performance vapor-cell POP Rb standards. Most cold-atom clocks exhibit a $\tau^{-1/2}$ behaviour up to 10^5 s and more thanks to the absence of frequency aging found in vapor-cell standards. As comparison, Cesium fountain clocks show typical $8 \cdot 10^{-14}\tau^{-1/2}$ [75].

References	Type	Atom	Cavity	Cooling	N_A	T [μK]	$\sigma_y(1\mathbf{s})$	$\sigma_y(10^5\mathbf{s})$	Drift [day^{-1}]	SWaP [L·kg·W]
Horace [22]	Research	Cs	Spherical	Isotropic	2×10^6	5	2.9×10^{-13}			
Muller 2011 [70]	Research	Cs	Cylindrical	Isotropic	10^8	10	5.0×10^{-13}			
MuClock [72], [76]	Product	Rb	Spherical	Isotropic	10^7	~ 100	3.2×10^{-13}	1.0×10^{-15}		$682 \times 135 \times 200$
SDI cRb [21], [48], [77]	Product	Rb		Isotropic			8.0×10^{-13}	3.0×10^{-15}	$\leq 1 \times 10^{-17}$	$39.8 \times 30.5 \times 100$
AOSENSE [78]	Product	Rb					2.0×10^{-12}	$^{\dagger}4.1 \times 10^{-15}$		NA $\times$ NA $\times$ 40
ISCAC [79]	Research	Rb	Spherical	Isotropic	1.2×10^7		5.4×10^{-13}	2.9×10^{-15}		
TACC [74], [80]	Research	Rb	Waveguide	Mirror [81]	3×10^6	20	5.8×10^{-13}			
Lee 2021 [82]	Research	Rb	LGR	Isotropic	5×10^7	2.5	$^{\dagger}2.3 \times 10^{-12}$		1×10^{-16}	
Givon 2022 [73]	Research	Rb	LGR	Pyramidal						
This work [83], [84]	Research	Rb	LGR	Grating	$> 3.6 \times 10^6$	10	1.5×10^{-11}			

Table 1.1: Informations on research or product compact cold atom clocks. The $\sigma_y(1\mathrm{s})$ corresponds to the $\tau^{-1/2}$ component of the Alan deviation. Blank cell means unavailable data. †: Extrapolated data. $\sim$: Order of magnitude. NA: Data not available.

1.4 GNSS-grade frequency standards

Available online at www.sciencedirect.com

ScienceDirect

Advances in Space Research 68 (2021) 4723–4733

ADVANCES IN SPACE RESEARCH (a COSPAR publication)

www.elsevier.com/locate/asr

GNSS-grade space atomic frequency standards: Current status and ongoing developments

Etienne Batori *, Nil Almat, Christoph Affolderbach, Gaetano Mileti *

Laboratoire Temps – Fréquence (LTF), Institut de Physique, Université de Neuchâtel, 2000 Neuchâtel, Switzerland

Received 8 April 2020; received in revised form 4 September 2020; accepted 5 September 2020
Available online 18 September 2020

Abstract

We present an overview on the current state of Global Navigation Satellite Systems (GNSS)-grade or better space atomic frequency standards' (SAFS) technologies and discuss their applications. We estimate that a total of more than 1000 such standards were sent to space so far, the vast majority consisting of rubidium-cell frequency standards, Cs atomic beam frequency standards, and passive hydrogen masers. Finally, we review a variety of ongoing developments in view of future new generations of GNSS-grade SAFSs.

Keywords: Space atomic frequency standards; GNSS; RAFS; Hydrogen maser; Cesium beam

1. Introduction

Since the first demonstration of an atomic frequency standard (AFS) (Essen and Parry, 1955) and the following redefinition of the SI second in 1967, AFSs have found a multitude of applications (Maleki and Prestage, 2005), both on ground as well as in space.

Primary frequency standards directly interrogate the unperturbed Cesium (Cs) 133 ground state hyperfine transition whose frequency of 9.192631770 GHz corresponds to the definition of the second in the SI system and should have undergone an accuracy evaluation (Riehle, 2003). Laser-cooled Cs fountain primary frequency standards - as operated in national metrology institutes - represent a tiny proportion of the total number of AFSs (Wynands and Weyers, 2005). They are the successors of the early primary Cs hot beam frequency standards (Bauch, 2003). Note that a small number of certain non-Cs frequency standards realizing the secondary representation of the second (Riehle et al., 2018) are considered being traceable to the primary Cs AFS, such as rubidium (Rb) fountains (Gill, 2005; Peil et al., 2017). These AFS are mainly employed in metrology and timekeeping applications on ground by national metrology institutes and in fundamental or industrial metrology applications.

Other AFSs either interrogate a different frequency reference or a Cs reference without full accuracy evaluation of its frequency bias. Examples are AFSs based on other alkali atoms microwave transitions, trapped-ion microwave transitions (Gill et al., 2003), optical clocks (Ludlow et al., 2015), Cs vapor-cell and commercial Cs hot beams (Microsemi, 2020). For many space and ground (Akiyama et al., 2019) applications, such AFSs with good long-term frequency stability are sufficient and accuracy of the frequency output is generally not required.

Most industrial and space-oriented developments focused on the "classical three" (Vanier and Tomescu, 2015) atomic frequency standards: the thermal Cs beam, the hydrogen (H) maser (H-maser) (passive or active) and the Rb atomic frequency standard (RAFS). It is therefore no surprise that so far almost all space AFS (SAFS) ever sent into orbit or deep space are of one of these kinds.

* Corresponding authors.
E-mail addresses: etienne.batori@unine.ch (E. Batori), gaetano.mileti@unine.ch (G. Mileti).

https://doi.org/10.1016/j.asr.2020.09.012
0273-1177/

SAFSs' and ground AFSs' qualifications differ. First, the former generally need to be smaller, lighter and consume less energy than the latter. Second, aside from being compatible with the absence of (or controlled) atmosphere, SAFSs must be launch-resilient, radiation hard with respect to ionizing radiation in space and reliable for the whole mission's duration. In addition, Global Navigation Satellite Systems (GNSS) grade SAFSs are generally required to achieve high stability performance on the level of 10^{-14} over one day (Droz et al., 2009).

To our knowledge, the most recent review on GNSS-grade SAFS was presented 14 years ago by (Mallette et al., 2006). Updated reviews on the development status of different GNSS were published in 2010 and 2012 by the same authors (Mallette et al., 2012, 2010), however without detailed data on the number of GNSS-grade SAFS flown. In (Mallette et al., 2006) it was estimated that at least 452 GNSS-grade SAFS had been sent to orbit or deep space compared to 300 in 1996 (Bhaskar et al., 1996).

In this publication, we aim to give an updated overview on the numbers and types of GNSS-grade or better SAFS sent to space so far or under on-going development. Section 2 will give an overview of the currently existing established SAFSs technologies. In Section 3 we describe the main applications of SAFSs with an emphasis on GNSS. Section 4 will estimate the number of GNSS-grade or better SAFSs sent into orbit and deep space so far. Section 5 will review some recent or on-going developments relevant for next generations of SAFSs.

2. Current SAFS technologies

2.1. The RAFS

The RAFS was the first frequency standard to be tested in a suborbital flight in 1961 (Bhaskar et al., 1996). It is also the first SAFS placed in orbit in the NTS-1 satellite in the early days of the Global Positioning System (GPS) in 1974 (McCaskill and Buisson, 1975). RAFS is also the first and only SAFS having been sent into deep space for the Cassini-Huygens mission in 1977. The two RAFS units sent were necessary to achieve sufficiently stable communication between the receiver and transmitter during the Doppler wind experiment descent time (Bird et al., 1997).

The RAFS (Camparo, 2007) physics package consist of ^{87}Rb-filled glass cell placed in a microwave cavity tuned near the 6.834 GHz Rb ground-state hyperfine transition frequency. The F = 2 ground state level is populated by a discharge lamp's radiation after passing through a ^{85}Rb filtering cell. A control loop tunes the microwave frequency such that the light transmission signal through the Rb cell detected by a photodiode is minimized. This configuration is known as the separated filter technique (SFT) (Mei et al., 2016), as opposed to the integrated filter technique (IFT) (Rochat et al., 1994). In both cases, the atoms are interrogated in a continuous-wave double-resonance scheme (CW-DR) where the optical and microwave radiations are applied simultaneously to the atoms.

Still today, a primary interest in RAFS comes from its low volume, low cost and low power consumption compared to the Cs beam and H-maser standards. Its simple design is also particularly suited for miniaturization (Vanier and Tomescu, 2015). Furthermore, atoms in RAFS do not consume themselves rapidly, unlike Cs and H atoms in Cs beams and H-masers, which in principle is advantageous for the instrument lifetime.

The performance limitations of RAFS are to be separated between short (1 s to 10^4 s) and long-term stabilities. The short-term stability is generally limited by the quality factor (Q_l) of the atomic resonance signal and its signal-to-noise ratio (SNR). The long-term stability limits arise from frequency biases that can vary in time in response to external or operational parameters acting on the AFS. An early example is the satellite's temperature oscillations (McCaskill and Buisson, 1975). One of today's "most problematic" shifts is the light shift making the atomic reference frequency vary in response to variations in the frequency or intensity of the pump light source (Formichella et al., 2017).

Today's space RAFSs' basic design and operation mode remain largely unaltered. Furthermore, recent and future developments for the Chinese GNSS (BeiDou) (Mei et al., 2016) and the Indian Regional Navigation Satellite System (IRNSS) (Bandi et al., 2019) still feature this mature technology.

2.2. The cesium beam frequency standard

Soon after the redefinition of the second in 1967, four Cs beam atomic standards flew on commercial airplane flights around the earth in the so-called "Hafele-Keating experiment" to demonstrate the theory of relativity effects on clocks flying around the world in opposite directions (Hafele and Keating, 1972). A few years later, the first two Cs beam frequency standards were sent into orbit in 1977 in the NTS-2 satellite (Bhaskar et al., 1996). Since then, dozens of them have been regularly sent to space in the Russian Global Navigation Satellite System (GLONASS) and GPS satellites (Mallette et al., 2006).

In the physics package of a Cs beam AFS, a thermal beam of ^{133}Cs atoms is generated by an oven. Magnetic state deflectors select the atoms in the $|F = 4, m_F = 0>$ atomic ground state. The beam passes in a so-called Ramsey cavity whose two arms will excite the atoms twice with the microwave transition, according to Ramsey's method of separated oscillating fields (Ramsey, 1990). A second magnetic state selector called the analyzer selects the $|F = 3, m_F = 0>$ states and atoms are detected using a hot wire. The microwave frequency is tuned such that the signal, called Ramsey fringes, is maximized (Vanier and Tomescu, 2015). This interrogation scheme is called a Ramsey scheme and was proposed by (Arditi and Carver, 1964) following (Ramsey, 1956) to improve the transition's

quality factor and hence reduce the short-term instabilities' level.

Interest in Cs frequency standards come from the wide availability of Cs on earth as well as its low melting point (Vanier and Audoin, 2005). Compared to their cell-type counterparts (RAFS or H-maser), they show small long-term frequency drifts and can thus reach excellent long-term stability (Microsemi, 2020). These advantages come however at the price of a relatively complex vacuum chamber to be maintained for the atomic beam.

The short-term stability is limited by the detection shot noise. For the Cs frequency standards featuring magnetic selectors the mainly time-varying frequency biases affecting the long-term stability are "the magnetic field and its homogeneity, the second-order Doppler effect, and the cavity phase shifts" (Vanier and Tomescu, 2015).

2.3. The hydrogen maser

The first (Bhaskar et al., 1996) H-maser (active) was sent into space in 1976 for less than 2 h in the framework of the "Gravity Probe A experiment" (Vessot et al., 1980). In 1996, the H-maser technology was seen as "uniquely suited for testing the fundamental physics laws" (Bhaskar et al., 1996). The European GNSS (GALILEO) GIOVE-B technology validation satellite including the first orbiting H-maser (passive) changed this perspective (Waller et al., 2009). Since then, as it is presented in Section 3.1 and figure Fig. 2, many GALILEO and BeiDou satellites including passive H-masers were sent into orbit. Vremya-CH is building a passive space-grade H-maser that is very likely to be seen in GLONASS in the future (Belyaev et al., 2019). Vremya-CH also built the first continuously orbiting active H-masers sent within the Radioastron satellite launched in 2011 (Belyaev et al., 2019; Utkin et al., 2012).

The active H-maser is different from that of the two other classic AFS types in the sense that no microwave probing power is needed to interrogate the 1420.405 MHz ground state hyperfine microwave frequency. Molecular hydrogen from a reservoir is dissociated to hydrogen atoms and formed to an atomic beam. By means of a magnetic state selector only higher energy atoms with $F = 1$, $m_F = 0,1$ are streamed into a bulb placed inside a microwave cavity with sufficiently high quality factor so that self-sustained oscillations due to stimulated emission occur. This detected signal is used to stabilize the frequency of a crystal oscillator (Vanier and Tomescu, 2015). Constraints such as high quality factor or cavity mode homogeneity makes this particular device more difficult to build than the passive H-maser. In that case, the H atoms are used as an amplifier of a microwave input frequency.

In its active form, the H-maser is one of the most stable SAFS. However, due to constraints regarding the cavity quality factor resulting in a voluminous, heavy and high power device, its usage has been restricted to ground and fundamental space applications. The passive form is however more prone to miniaturization with a compromise on the frequency's stability (Vanier and Tomescu, 2015).

2.4. $^{199}Hg^{+}$ trapped-ion for DSAC

The Jet Propulsion Laboratory (JPL) mercury trapped-ion ($^{199}Hg^{+}$) (Burt et al., 2016; Tjoelker et al., 2016) is one of the few non-classical frequency standards sent into space. Mercury is not only a new atom in space but also is not an alkali atom. The AFS was launched in June 2019 (Georgescu, 2019). There are currently no publications on the operation or performance of this SAFS.

In a mercury trapped-ion AFS, a $^{202}Hg^{+}$ discharge lamp is used to prepare and interrogate the ion cloud placed in a first part of an ion trap, which traditionally consist of either combined static electric and magnetic fields (Penning trap) or combined dc and rf electric fields (Paul trap) (Dehmelt, 1990). In order to avoid light shift, the 40.5 GHz hyperfine frequency microwave interaction takes place in a light free area. Thanks to the combination of different electrodes, the ions are shuttled between the two respective regions. These operations consist of up to 50% cycle time resulting to an equivalent cycle dead time (Tjoelker et al., 2016; Vanier and Tomescu, 2015).

Short-term stability is also governed by SNR and transition line quality factor (Tjoelker et al., 2016). The electromagnetic trap technology is less sensitive to external perturbation sources such as wall collisions, magnetic sensitivity and temperature sensitivity resulting in better long-term stability (Seubert et al., 2013).

3. SAFS applications

Applications of high-performance SAFS can be roughly divided into two main categories: In first place, Global Navigation Satellite Systems (GNSS) regroup by far the highest number of SAFS sent into space. As the second category, other and often science-motivated space missions account for a far lesser number of SAFS, but show a richer variety of SAFS in use. In the following, we discuss these two main application categories.

3.1. GNSS

GNSS applications were one of the primary motivations to develop space-borne frequency standards (Bhaskar et al., 1996). First, SAFSs need less frequent time and frequency ground corrections than quartz. Second, according to (Bhaskar et al., 1997) and (Bloch et al., 2002), SAFSs are insensitive to space radiations compared to quartz.

As we will see in Section 4, the vast majority of SAFSs were sent into orbit within the GNSS framework. The reasons for this high number of SAFS are multiple: In the first place, each GNSS system requires an elevated number of satellites to operate. For example, the GALILEO system requires 27 working plus three backup satellites (Droz et al., 2009), with similar requirements for other systems.

In addition, for redundancy several SAFSs are typically flown on each satellite. For example, the BeiDou-2 and BeiDou-3 satellites contain four SAFSs each (Wu et al., 2018). Furthermore, there is an increasing number of different GNSS systems operating or under development, reflecting the wish of several local powers on different continents to use their own systems. Finally, the limited lifetime of each GNSS satellite requires their continuous replacement. Note that in the early days of GNSS, satellites' lifetime were as short as one year (Mallette et al., 2006) whereas GALILEO's current requirements are 12 years lifetime per satellite (Droz et al., 2009).

Past and current lines of development on SAFS on one hand concern the constant search for SAFSs with reduced cost, volume, mass, and power consumption, in order to achieve more cost-effective GNSS satellites and launches. On the other hand, new applications and improvements in positioning accuracy being directly linked to the GNSS satellites' navigation message stability, i.e. a compromise between the SAFSs mid-term stability and the recalibration frequency from the ground segment, are calling for improved clock performances.

In order to illustrate the evolution of the GNSS-grade SAFSs stability from the beginning of GNSS to today, a set of flown SAFSs' Allan deviations are presented Fig. 1.

GNSS also accidentally contributed to fundamental physics within the **G**alileo gravitational **R**edshift test with **E**ccentric s**AT**ellites (GREAT) experiment. Here, two satellites that initially had been sent into non-nominal elliptical orbits due to launch problems, finally were exploited to improve the experimental validation of gravitational redshift of Gravity Probe A's (Vessot et al., 1980) by a factor 5.6 (Delva et al., 2019).

The following subsections describe the state of the different GNSSs as of today. For a complete history starting from the beginning of the GNSS era to 2012, the reader is referred to (Mallette et al., 2006) and (Mallette et al., 2012). A detailed description of the different GNSS systems can be found in (Teunissen and Montenbruck, 2017).

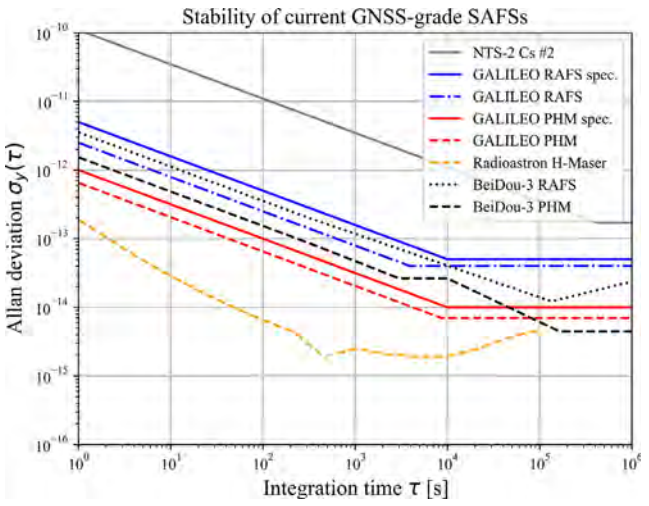

Fig. 1. Allan deviations of different current space clocks. NTS-2 Cs#2 (McCaskill et al., 1978), GALILEO RAFS and PHM specifications and data (Droz et al., 2006; Micalizio et al., 2012), Radioastron (Utkin et al., 2012), BeiDou-3 RAFS and PHM (Guo et al., 2020).

3.1.1. BeiDou

As of July 2020, 55 BeiDou-2 and BeiDou-3 block satellites were launched, completing the BeiDou constellation (BeiDou Navigation Satellite System, 2020). The satellites contain four RAFS for BeiDou-2 or 2 RAFS plus 2 H-masers for BeiDou-3 (Wu et al., 2018; Xu et al., 2019). The H-masers have been built in China (Wu et al., 2018). The RAFS were built by SpectraTime and in China (Huang et al., 2019; Xu et al., 2019).

3.1.2. GALILEO

Apart from the GIOVE-A and GIOVE-B satellites, 26 regular GALILEO satellites were launched so far (European GNSS Agency, 2020). Each of them contains two RAFSs and two passive H-masers.

3.1.3. GLONASS

Between 10 December 2003 and 16 March 2020, we counted 50 reported GLONASS-M satellites (including 6 failed launches) carrying 3 Cs beam clocks each (Betz, 2015). This generation of satellites is not under production anymore and the last GLONASS-M satellite is expected to be launched in 2020. Two GLONASS-K1 satellites – the successor of GLONASS-M – were launched in 2011 and 2014 and contain two Cs beams and two RAFSs each (Betz, 2015; ISS-Reshetnev, 2020).

3.1.4. GPS

A total of 12 IIF satellites were launched, each containing one Cs beam clock and two RAFS (Los Angeles Air Force Base, 2012a). The first three block III satellites containing three RAFSs each (Los Angeles Air Force Base, 2012b) were sent into orbit in 2018, 2019 and 2020.

3.1.5. IRNSS

The IRNSS space segment consists of 9 (including one unsuccessful launch) satellites launched between 2013 and 2018 (Department of Space Indian Space Research Organisation, n.d.). The IRNSS-1A satellite contains three RAFS fabricated by SpectraTime (Thoelert et al., 2014).

3.1.6. QZSS

The Japanese local navigation system quasi-zenith satellite system (QZSS) space segment consists of four satellites launched between 2010 and 2017 (Quasi-Zenith Satellite System, 2020). The QZS-1 satellite has two RAFS on board (Nakamura et al., 2011).

3.2. Other applications

Other applications of SAFSs (Maleki and Prestage, 2005) concern fields such as fundamental physics, astrome-

try, time-keeping, deep-space navigation and telecommunications. Although the number of SAFSs used in such applications is not comparable to that of the ones used for GNSS, they can feature more advanced and more stable, yet also heavier, bigger, and more expensive types of clocks.

In the preceding sections, we already mentioned past missions that featured key SAFSs such as the Gravity probe A experiment and the Cassini-Huygens mission. In the following, we discuss a selection of present and future space missions benefiting from AFSs.

3.2.1. Radioastron

The Russian Radioastron radio telescope program began in the 1990s. Its early development included the development of the active hydrogen maser and RAFS manufacture in the Observatoire of Neuchâtel, based on previous RAFS development under ESA programme. Due to lack of budget, the program stopped and only two RAFS were finally built (Couplet et al., 1995; Droz et al., 2009; Rochat et al., 1994). Both technologies were transferred to SpectraTime who is now manufacturing space-grade RAFS, passive H-maser and the active H-maser included in the Atomic Clock Ensemble in Space (ACES) mission (Droz et al., 2009).

Within the Radioastron program, the Spektr-R satellite carrying a 10-m radio telescope was sent into orbit in 2011 flying the two RAFS and the first two active H-masers ever sent into orbit built by Vremya-CH (Kardashev et al., 2013). The mission was officially abandoned in May 2019 due to loss of contact in January 2019 (Astro Space Center, 2019).

3.2.2. GAIA

The European Space Agency (ESA) astrometric satellite is placed in one of the Sun-Earth-Moon Lagrange points. The purpose of the mission is to measure kinematic, dynamic and chemical properties of the Milky Way for a nominal five-year lifetime. It contains one RAFS whose stability of "a few ns for 6 h" (Prusti et al., 2016) is used to accurately attribute time tags to the images. The mission duration was extended in 2018 (European Space Agency, 2018).

3.2.3. ACES

The future ACES ESA mission will, among others, measure the physical constants' time dependency (Laurent et al., 2007). The payload contains two clocks: a laser-cooled Cs beam clock named PHARAO that was developed by SYRTE, LKB, and the French space agency CNES, and a space active H-maser (SHM) developed by SpectraTime (Droz et al., 2009).

PHARAO will make use of the low-gravity condition once installed on the international space station (ISS). The clock will also allow performing improved time transfer and clock comparison on intercontinental scale (Heß et al., 2011).

3.2.4. AEHF

The advance extremely high frequency (AEHF) system is the military strategic and tactical relay satellite (MILSTAR)'s follow-on mission serving for secure military telecommunication. Since the publication of the previous review by Mallette et al. (Mallette et al., 2006), the 6 satellites were sent into orbit and the constellation was completed 26 March 2020 (Lockheed Martin, 2020).

The satellites contain three Frequency Electronics Inc. (FEI) space RAFSs (FEI, 2013) fulfilling the stability requirements of such secure telecommunication applications (Bhaskar et al., 1997).

3.2.5. Deep space applications

The presence of a SAFS on board a spacecraft allows quicker, more accurate and more efficient positioning by means of the one-way technique instead of the two-way technique (Ely and Seubert, 2015). The National Aeronautics and Space Administration (NASA) JPL project Deep Space Atomic Clock (DSAC) mission aims to determine what frequency standard would fit this mission best (Ely and Seubert, 2015). An apparently good and already far-developed clock candidate for such DSAC applications is the JPL mercury trapped-ion currently in test, see Section 2.4.

4. Estimated number of SAFSs launched so far

Estimation of the accumulated GNSS-grade or better AFSs sent in space can be found in Fig. 2. We drew the separation between GNSS-grade SAFSs and others for two reasons. First, the comprehensible lack of data regarding non GNSS-grade SAFSs flown by private companies compared to publicly available pieces of information regarding GNSSs. Second, the continuum of AFSs technologies below the GNSS-grade threshold. Indeed, the use of a par-

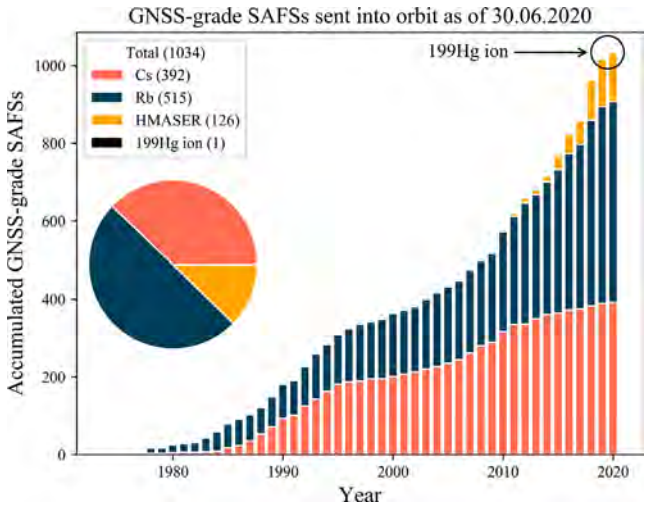

Fig. 2. Estimated number of GNSS-grade or better SAFSs sent in space as of 26 March 2020. The last database entry is the GPS-III third satellite launched 30 June 2020 (SMC Public Affairs, 2020).

ticular SAFS strongly depends on the application's specific requirements. One end of the AFS spectrum are the ground Cs fountains clocks where the principal issue is intrinsic accuracy at the price of huge volume, weight and power consumption (Sullivan et al., 2001). One other end of the spectrum are chip-scale space atomic clocks detailed in Section 5.

We estimate that at least 1034 SAFSs have been sent into orbit or deep space, the main contributor by numbers being GNSS applications. We did not count sub-orbital flights like the Gravity Probe A experiment but took into account failed and wrong orbit launches because they reflect interest in particular technologies.

It has been difficult to find pieces of information regarding some systems and we had to make reasonable assumptions. For instance, the MILSTAR satellites are said to have three or four RAFS (Mallette et al., 2006). In that particular case, we accounted three RAFS per satellite to make sure not to overestimate the real number of SAFSs sent into space.

For all years up to 1996 and 2006 we estimated at least 325 and 448 SAFSs accumulated in space compared to the 300 and 452 estimated by (Bhaskar et al., 1996) and (Mallette et al., 2006), respectively. The most sent type of SAFS (a bit less than 50%) is the RAFS followed by Cs-beam clocks, H-maser (passive and active) and finally trapped ion clock (only one reported). As of today, we estimate that the number of GNSS-grade SAFSs has more than doubled over the last 13 years. This is partially due to the rebuilding of the GLONASS constellation and the presence of two new GNSS systems, GALILEO and BeiDou. The former constellation is still being completed with new satellites whereas the latter has been completed end of June 2020 (BeiDou Navigation Satellite System, 2020).

From Fig. 2, we note a tendency to replace the Cs beam standards by passive H-masers. Therefore, the proportion of each SAFS technology has significantly changed since the 2010s.

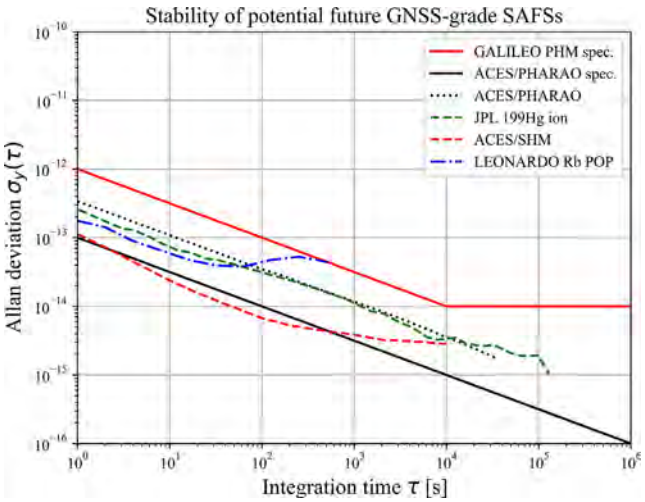

Fig. 3. Allan deviations of GNSS-grade SAFSs ongoing developments, all measured on ground. The GALILEO PHM specification is repeated as means of comparison with Fig. 1. PHARAO specifications (Sharing Earth Observation Resources, 2020), ACES/PHARAO and ACES/SHM (Laurent et al., 2015), JPL 199Hg ion (Tjoelker et al., 2016), LEONARDO Rb POP (detailed in Section 5), drift removed (Arpesi et al., 2019).

5. Ongoing developments

In this section, we review the ongoing developments that show promising candidates for space applications such as GNSS or telecommunication. The stability performances of potential future GNSS-grade SAFSs are shown in Fig. 3.

5.1. CW-DR laser-pumped rubidium vapor cell clocks

The CW-DR laser-pumped Rb clock is very similar to the RAFS' design (Camparo, 2007). In particular, the vapor cell and the microwave cavity do not change. The discharge lamp and the filter cell are however replaced by a laser whose frequency is stabilized on one of the Rb transitions (Affolderbach et al., 2006; Vanier and Mandache, 2007). The operation mode of the clock is however the same as the lamp RAFS. The laser's narrower optical spectrum implies higher optical pumping efficiency and higher signal to noise ratio compared to the lamp RAFS resulting in an improved clock frequency stability by one order of magnitude compared to the current GNSS RAFS (Bandi et al., 2011; Gharavipour et al., 2016; Vanier and Tomescu, 2015).

The clock frequency instability is governed by the same phenomena as in the lamp RAFS (Vanier and Tomescu, 2015). In the long-term, it is also sensitive to external and operational parameters' oscillations in time (Bandi et al., 2014). Both lamp and laser-pumped vapor cell clocks exhibit frequency aging and hence stability degradation in the 10^4 s region and longer time scales, the origins of which are still not well understood but are likely to be caused by the light shift (Camparo, 2007, 2005; Formichella et al., 2017).

5.2. POP rubidium vapor-cell clocks

The physics package of the Pulsed Optically Pumped (POP) Rb clock is similar to the CW-DR laser-pumped Rb clock. Nevertheless, in the POP clock the optical and microwave interactions are separated in time (Dong et al., 2016; Kang et al., 2015; Micalizio et al., 2012). The pulsed interrogation scheme consists in applying the Ramsey's separated fields method to an atomic vapor confined in a glass cell. Following an intense optical pumping pulse, two microwave pulses separated in time are applied to the vapor cell. Finally, the clock signal is detected either via the transmission of a weak detection light or the atomic decay microwave signal is captured by the microwave cavity. The main technical difference of the POP clock compared to the CW-DR clocks is the necessity of optical and microwave

switches to realize the pulsed light for pumping (and detection) and microwave interrogation (Micalizio et al., 2010).

Both short- and long-term stabilities benefit from the use of laser and POP scheme. In the first case, Ramsey fringes result in an improved quality factor of the resonance signal compared to the CW-DR signal and better SNR. On long-term timescales, the absence of light during the two microwave pulses significantly reduces the instability contribution due to the AC Stark shift effect (also known as the light shift effect). A recent budget of long-term instabilities in such clocks however showed that residual light-induced effects still remain one of the main contributors to long term clock instability (Almat et al., 2018).

The closest industrial realization of a Rb POP clock for space applications is the LEONARDO and INRIM clock currently under development (Arpesi et al., 2019; Micalizio et al., 2019).

5.3. CPT clocks

The Coherent Population Trapping (CPT) phenomenon application is not limited to the field of AFS only (Vanier and Tomescu, 2015). In CPT clocks, the atoms are confined in a glass cell and only a bichromatic laser light is used to prepare and interrogate the atoms. The choice of atom, physics package and interrogation scheme is particularly wide and range from the continuous so-called Λ interrogation scheme of the Cs and ^{87}Rb atoms to the more exotic CPT ^{87}Rb maser and the Cs CPT-POP clock (Abdel Hafiz et al., 2018). All these implementations and associated models are described in the review by Vanier (Vanier, 2005).

The main advantage of the clocks based on the CPT approach is the absence of a microwave cavity, which makes this technique suitable for miniaturization down to chip-scale size for low power consuming clocks (Kitching, 2018; Knappe, 2007; Vanier, 2005). The interrogation is realized using two laser lights whose frequency difference coincides with the atomic transition frequency. The required multi-frequency light field can be produced by direct frequency modulation of the laser emission. Therefore, the CPT clocks require relatively more complicated optical system than the laser-pumped DR clocks described in Section 5.1.

Many miniature and Chip Scale Atomic Clock (CSAC) industrial developments such as Microsemi CPT Cs (Cash et al., 2018) and Rb (Deng et al., 2008) CSACs, AccuBeat NAC1 Rb CPT clock (Stern et al., 2016) and Symmetricom Cs MAC (Lutwak et al., 2004) target applications where small volume, low mass and low power consumption are needed and a moderate stability performance is sufficient. Typical one day time- and Allan deviations are ≤ 100 μs and 10^{-11}, respectively (Kitching, 2018). The cell's size reduction implies greater relaxation rate due to the environment and therefore degraded stability compared to the more high-performing clocks discussed above (Kitching, 2018). Although these clocks are not suitable as GNSS standards, Space CSACs were already launched in low orbit satellites (Cash et al., 2018).

5.4. Optically-pumped Cs beam clocks

The optically-pumped Cs beam clocks employ essentially the same interrogation principle as their magnetic ancestors (Audoin and Vanier, 1989). However, in place of using magnets for atomic state selection they employ laser light to optically pump the atoms before entering the Ramsey cavity and to optically detect the clock signal at the end of it. The short-term stability (Vanier and Tomescu, 2015) is better than that of the magnetically-selected Cs beam clocks, and they are now becoming available as commercial products. The simplest design consists of using the emission of one laser source divided in two parts for state preparation by optical pumping and detection.

Development of space-grade optically-pumped Cs beam clocks have been reported for GPS (Lutwak et al., 2001), GALILEO (Lecomte et al., 2007) as well as for industrial applications (Schmeissner et al., 2016).

5.5. Cold atom clocks

In Cs fountain clocks, the primary frequency standards used for international timekeeping, the laser-cooled atoms travel vertically on a fountain-like trajectory. Thanks to the low speed of the laser-cooled atoms, very long Ramsey times and thus narrow Ramsey signal fringes and ultimate clock stability at the level of $10^{-13}\ \tau^{-1/2}$ or better are obtained. The first and only demonstration as of today of such SAFS in orbit is the Chinese Rb cold atom clock (CAC) (Liu et al., 2018) whose space presence is a first step towards laser-based SAFS. We already mentioned the upcoming laser-cooled Cs beam clock PHARAO in Section 3.2.3.

In view of realizing much more compact cold-atom clocks for both ground and space GNSS segments, laser-cooled atomic samples based on vapor-cell technology are envisaged. An example for this was the HORACE cold Cs clock aiming for both ground-based and in microgravity applications, in which the atoms were cooled and interrogated inside a vapor-cell-like glass container (Esnault et al., 2011). The technology was transferred to the Muquans company and a first compact cold atom clock named Rubiclock was developed based on Rb atoms. Even though the design is similar, the change from Cs to Rb was motivated by the potentially lower collision shifts (Pelle et al., 2018) and the easier realization of the required laser systems based on high-reliability telecom components. This technology is now a commercially available product aiming for ground applications (MuQuans, 2019). Another commercially available cold Rb clock is cRb-clock developed by SpectraDynamics (Ascarrunz et al., 2018). We further note the alternative approach of creating the optical molasses by means of a grating magneto-optical trap

(gMOT) shows promising results in view of its application in atomic clocks and reducing the clock's size (Elvin et al., 2019).

5.6. Other types of potential SAFS and optical lattice clocks

We have reviewed in the previous sections the most promising advances reported towards high-performance SAFS. There are many other developments ongoing on advanced technology for ground AFS or other that may also be of interest for space applications in the future whose detailed discussion is beyond the scope of this work, such as nuclear frequency standards (NFS) (Thirolf et al., 2019).

In particular, several approaches to trapped-ion clock candidates, such as Ytterbium (Mulholland et al., 2019), are under development, using different atomic species (Burt et al., 2010; Delehaye and Lacroûte, 2018; Vanier and Tomescu, 2015). Nevertheless, we should lastly mention the most stable and most accurate (Vanier and Tomescu, 2015) ground clocks so far are the optical lattice clocks (Ludlow et al., 2015). ESA foresees sending such a clock to space before "the end of the decade" (Schiller et al., 2017).

6. Conclusion

Today's GNSS constellations rely on well-established classical technologies such as the lamp-pumped Rb vapor-cell clocks, the passive H-maser and the Cs thermal-beam AFSs. The new GNSS constellations such as GALILEO and BeiDou have sent a dozen of passive H-masers in orbit, making this type of clock not only dedicated to scientific missions anymore.

Three milestones are to be noted. First, we have estimated that by mid-2020, more than 1000 SAFS have been sent in space so far. Second, the presence in orbit of the JPL mercury trapped ion clock that, as a new type of SAFS, brings the number of flying clock technologies to a total of four. Third, the in-orbit demonstration of the Chinese laser-pumped cold atom clock.

Furthermore, efforts to improve the metrological properties of the three classical SAFS technologies are still ongoing. New technologies making use of lasers are about to leave the Earth into space for scientific missions. As history has shown, it is probably only a matter of time before they are also widely used in GNSS applications and others.

Declaration of Competing Interest

The authors declare that they have no known competing financial interests or personal relationships that could have appeared to influence the work reported in this paper.

Acknowledgments

This work was supported by the University of Neuchâtel, the Swiss Space Center (UppMAC project 0720_MR_001_SSC01_00), the European Space Agency ESA (ESTEC contracts 4000129974 and 4000131046), and by the European Union's Horizon 2020 Research and Innovation Program through Quantum Technology Flagship (project macQsimal, grant 820393).

The authors thank Dr. Hartmut Schweda and Dr. Songbai Kang for helpful exchanges.

References

Abdel Hafiz, M., Coget, G., Petersen, M., et al., 2018. Symmetric autobalanced Ramsey interrogation for high-performance coherent-population-trapping vapor-cell atomic clock 244102. Appl. Phys. Lett. 112. https://doi.org/10.1063/1.5030009.

Affolderbach, C., Droz, F., Mileti, G., 2006. Experimental demonstration of a compact and high-performance laser-pumped Rubidium gas cell atomic frequency standard. IEEE Trans. Instrum. Meas. 55, 429–435. https://doi.org/10.1109/TIM.2006.870331.

Akiyama, K., Alberdi, A., Alef, W., et al., 2019. First M87 event horizon telescope results. IV. Imaging the central supermassive black hole. Astrophys. J. Lett. 875, L4. https://doi.org/10.3847/2041-8213/ab0e85.

Almat, N., Pellaton, M., Moreno, W., et al., 2018. Rb vapor-cell clock demonstration with a frequency-doubled telecom laser. Appl. Opt. 57, 4707. https://doi.org/10.1364/ao.57.004707.

Arditi, M., Carver, T.R., 1964. Atomic clock using microwave pulse-coherent techniques. IEEE Trans. Instrum. Meas. IM–13, 146–152. https://doi.org/10.1109/TIM.1964.4313389.

Arpesi, P., Belfi, J., Gioia, M., et al., 2019. Rubidium Pulsed Optically Pumped Clock for Space Industry. IFCS/EFTF 2019 - Jt. Conf. IEEE Int. Freq. Control Symp. Eur. Freq. Time Forum, Proc. 2, 1–3. https://doi.org/10.1109/FCS.2019.8856140

Ascarrunz, F.G., Dudin, Y.O., Delgado Aramburo, M.C., et al., 2018. A Portable Cold 87Rb Atomic Clock with Frequency Instability at One Day in the 3 x 10−15 Range. IFCS 2018 - IEEE Int. Freq. Control Symp. 1–3. https://doi.org/10.1109/FCS.2018.8597585

Astro Space Center, 2019. RadioAstron Newsletter Number 36 [WWW Document] accessed 31.03.20 http://www.asc.rssi.ru/radioastron/news/news_en.pdf, .

Audoin, C., Vanier, J., 1989. The Quantum Physics of Atomic Frequency Standards, Volume 1, Bristol, England: loP Publishing Ltd. https://doi.org/10.1201/9781420050851.fmatt

Bandi, T., Affolderbach, C., Calosso, C.E., et al., 2011. High-performance laser-pumped rubidium frequency standard for satellite navigation. Electron. Lett. 47, 698–699. https://doi.org/10.1049/el.2011.0389.

Bandi, T., Affolderbach, C., Stefanucci, C., et al., 2014. Compact high-performance continuous-wave double-resonance rubidium standard with $1.4 \times 10^{-13}\ \tau^{-1/2}$ stability. IEEE Trans. Ultrason. Ferroelectr. Freq. Control 61, 1769–1778. https://doi.org/10.1109/TUFFC.2013.005955.

Bandi, T., Kaintura, J., Saiyed, A.R., et al., 2019. Indian Rubidium Atomic Frequency Standard (IRAFS) development for satellite navigation, in: 2019 URSI Asia-Pacific Radio Science Conference, AP-RASC 2019. Institute of Electrical and Electronics Engineers Inc. https://doi.org/10.23919/URSIAP-RASC.2019.8738208

Bauch, A., 2003. Caesium atomic clocks: function, performance and applications. Meas. Sci. Technol. 14, 1159–1173. https://doi.org/10.1088/0957-0233/14/8/301.

BeiDou Navigation Satellite System, 2020. The BDS-3 Constellation Deployment Is Fully Completed Six Months Ahead of Schedule UNOOSA Sends a Congratulation Letter [WWW Document] accessed

08.07.20 http://en.beidou.gov.cn/WHATSNEWS/202006/t20200623_20692.html, .

Belyaev, A.A., Demidov, N.A., Medvedev, S.Y., et al., 2019. Russian hydrogen masers for ground and space applications. 2019 URSI Asia-Pacific Radio Sci. Conf. AP-RASC 2019 1. https://doi.org/10.23919/URSIAP-RASC.2019.8738340

Betz, J.W., 2015. Engineering satellite-based navigation and timing: global navigation satellite systems, signals, and receivers. John Wiley & Sons, Hoboken NJ, USA.

Bhaskar, N.D., Matt, A.D., Russo, N., et al., 1997. On-orbit performance of Milstar rubidium and quartz frequency standards. In: Proceedings of the Annual IEEE International Frequency Control Symposium. IEEE, pp. 329–337. https://doi.org/10.1109/freq.1997.638566.

Bhaskar, N.D., White, J., Mallette, L.A., et al., 1996. Historical review of atomic frequency standards used in space systems. Proc. Annu. IEEE Int. Freq. Control Symp. 24–31. https://doi.org/10.1109/freq.1996.559816.

Bird, M.K., Heyl, M., Allison, M., et al., 1997. The Huygens doppler wind experiment. Huygens Sci. Payload Mission. Proc. an ESA Conf. 1177, 139–162.

Bloch, M., Mancini, O., McClelland, T., 2002. Performance of rubidium and quartz clocks in space. In: Proceedings of the Annual IEEE International Frequency Control Symposium, pp. 505–509. https://doi.org/10.1109/freq.2002.1075936.

Burt, E.A., Taghavi-Larigani, S., Tjoelker, R.L., 2010. A new trapped ion atomic clock based on 201Hg+. IEEE Trans. Ultrason. Ferroelectr. Freq. Control, 629–635. https://doi.org/10.1109/TUFFC.2010.1458.

Burt, E.A., Yi, L., Tucker, B., et al., 2016. JPL ultrastable trapped ion atomic frequency standards. IEEE Trans. Ultrason. Ferroelectr. Freq. Control 63, 1013–1021. https://doi.org/10.1109/TUFFC.2016.2572701.

Camparo, J., 2005. Does the light shift drive frequency aging in the rubidium atomic clock? IEEE Trans. Ultrason. Ferroelectr. Freq. Control 52, 1075–1078. https://doi.org/10.1109/TUFFC.2005.1503993.

Camparo, J., 2007. The rubidium atomic clock and basic research. Phys. Today 60, 33–39. https://doi.org/10.1063/1.2812121.

Cash, P., Krzewick, W., MacHado, P., et al., 2018. Microsemi Chip Scale Atomic Clock (CSAC) technical status, applications, and future plans. In: 2018 European Frequency and Time Forum, EFTF 2018. Institute of Electrical and Electronics Engineers Inc., pp. 65–71. https://doi.org/10.1109/EFTF.2018.8408999

Couplet, C., Rochat, P., Mileti, G., et al., 1995. Miniaturized rubidium clocks for space and industrial applications. In: Proceedings of the Annual IEEE International Frequency Control Symposium. IEEE, pp. 53–59. https://doi.org/10.1109/freq.1995.483882.

Dehmelt, H., 1990. Experiments with an isolated subatomic particle at rest (Nobel Lecture). Angew. Chemie Int. Ed. English 29, 734–738.

Delehaye, M., Lacroûte, C., 2018. Single-ion, transportable optical atomic clocks. J. Mod. Opt. 65, 622–639. https://doi.org/10.1080/09500340.2018.1441917.

Delva, P., Puchades, N., Schönemann, E., et al., 2019. A new test of gravitational redshift using Galileo satellites: The GREAT experiment. Comptes Rendus Phys. 20, 176–182. https://doi.org/10.1016/j.crhy.2019.04.002.

Deng, J., Vlitas, P., Taylor, D., et al., 2008. A commercial CPT rubidium clock. EFTF 2008 - 22nd Eur. Freq. Time Forum 99.

Department of Space Indian Space Research Organisation, n.d. List of Navigation Satellites [WWW Document]. URL https://www.isro.gov.in/spacecraft/list-of-navigation-satellites (accessed 30.03.20).

Dong, G., Deng, J., Lin, J., et al., 2016. The progress of pulsed optically pumped rubidium clock at SIOM. 2016 Prog. Electromagn. Res. Symp. PIERS 2016 - Proc. i, 3716–3719. https://doi.org/10.1109/PIERS.2016.7735410.

Droz, F., Mosset, P., Barmaverain, G., et al., 2006. The on-board Galileo clocks: Rubidium standard and passive hydrogen maser - Current status and performance. Proc. 20th Eur. Freq. Time Forum, EFTF 2006, 420–426.

Droz, F., Mosset, P., Wang, Q., et al., 2009. Space passive hydrogen maser - Performances and lifetime data. 2009 IEEE Int. Freq. Control Symp. Jt. with 22nd Eur. Freq. Time Forum, 393–398. https://doi.org/10.1109/FREQ.2009.5168208.

Elvin, R., Hoth, G.W., Wright, M., et al., 2019. Cold-atom clock based on a diffractive optic. Opt. Express 27, 38359. https://doi.org/10.1364/oe.378632.

Ely, T.A., Seubert, J., 2015. One-way radiometric navigation with the Deep Space Atomic Clock. Proc. AAS/AIAA Sp. Flight Mech. Meet, pp. 1–18

Esnault, F.X., Rossetto, N., Holleville, D., et al., 2011. HORACE: A compact cold atom clock for Galileo. Adv. Sp. Res. 47, 854–858. https://doi.org/10.1016/j.asr.2010.12.012.

Essen, L., Parry, J.V.L., 1955. An atomic standard of frequency and time interval: A cæsium resonator. Nature 176, 280–282. https://doi.org/10.1038/176280a0.

European GNSS Agency, 2020. Constellation Information [WWW Document] accessed 30.03.20 https://www.gsc-europa.eu/system-service-status/constellation-information, .

European Space Agency, 2018. Extended life for ESA's science missions [WWW Document] accessed 04.04.20 https://sci.esa.int/web/director-desk/-/60943-extended-life-for-esas-science-missions#1, .

FEI, 2013. FEI' s Next-Generation Rubidium Atomic Frequency Standard For Space Applications. New York, USA. Available online at https://freqelec.com/wp-content/uploads/2019/03/4-RAFS-Brochure.pdf (accessed 30.03.20)

Formichella, V., Camparo, J., Tavella, P., 2017. Influence of the ac-Stark shift on GPS atomic clock timekeeping 043506. Appl. Phys. Lett. 110. https://doi.org/10.1063/1.4975071.

Georgescu, I., 2019. A space chronometer. Nat. Rev. Phys. 1, 421–421. https://doi.org/10.1038/s42254-019-0084-9

Gharavipour, M., Affolderbach, C., Kang, S., et al., 2016. High performance vapour-cell frequency standards. J. Phys. Conf. Ser. 723. https://doi.org/10.1088/1742-6596/723/1/012006012006.

Gill, P., 2005. Optical frequency standards. Metrologia 42, S125–S137. https://doi.org/10.1088/0026-1394/42/3/S13.

Gill, P., Barwood, G.P., Klein, H.A., et al., 2003. Trapped ion optical frequency standards. Meas. Sci. Technol. 14, 1174. https://doi.org/10.1088/0957-0233/14/8/302.

Guo, M., Fan, Y., Fan, X., et al., 2020. Performance analysis of BDGIM. In: China Satellite Navigation Conference. Springer, pp. 101–113. https://doi.org/10.1007/978-981-15-3715-8_10.

Hafele, J.C., Keating, R.E., 1972. Around-the-world atomic clocks: Predicted relativistic time gains. Science (80-.) 177, 166–168. https://doi.org/10.1126/science.177.4044.166.

Heß, M.P., Stringhetti, L., Hummelsberger, B., et al., 2011. The ACES mission: System development and test status. Acta Astronaut. 69, 929–938. https://doi.org/10.1016/j.actaastro.2011.07.002.

Huang, G., Cui, B., Zhang, Q., et al., 2019. Switching and performance variations of on-orbit BDS satellite clocks. Adv. Sp. Res. 63, 1681–1696. https://doi.org/10.1016/j.asr.2018.10.047.

ISS-Reshetnev, 2020. News [WWW Document]. URL http://www.iss-reshetnev.com/media/news/ (accessed 30.03.20).

Kang, S., Gharavipour, M., Affolderbach, C., et al., 2015. Demonstration of a high-performance pulsed optically pumped Rb clock based on a compact magnetron-type microwave cavity. J. Appl. Phys. 117, 19–23. https://doi.org/10.1063/1.4914493.

Kardashev, N.S., Khartov, V.V., Abramov, V.V., et al., 2013. "Radio-Astron"-A telescope with a size of 300 000 km: Main parameters and first observational results. Astron. Reports 57, 153–194. https://doi.org/10.1134/S1063772913030025.

Kitching, J., 2018. Chip-scale atomic devices. Appl. Phys. Rev. 5, 31302. https://doi.org/10.1063/1.5026238.

Knappe, S.A., 2007. MEMS atomic clocks. In: Gianchandani, Y.B., Tabata, O., Zappe, H. (Eds.), Comprehensive Microsystems. Elsevier, Amsterdam, NL, pp. 571–612.

Laurent, P., Abgrall, M., Clairon, A., et al., 2007. The space program PHARAO/ACES, in: Time and Frequency Metrology. International Society for Optics and Photonics, p. 667308.

Laurent, P., Massonnet, D., Cacciapuoti, L., et al., 2015. The ACES/PHARAO space mission. Comptes Rendus Phys. 16, 540–552. https://doi.org/10.1016/j.crhy.2015.05.002.

Lecomte, S., Haldimann, M., Ruffieux, R., et al., 2007. Performance demonstration of a compact, single optical frequency cesium beam clock for space applications. Proc. IEEE Int. Freq. Control Symp. Expo. 1127–1131. https://doi.org/10.1109/FREQ.2007.4319254

Liu, L., Lü, D.S., Chen, W.B., et al., 2018. In-orbit operation of an atomic clock based on laser-cooled 87Rb atoms. Nat. Commun. 9, 2760. https://doi.org/10.1038/s41467-018-05219-z.

Lockheed Martin, 2020. Protected Globally: AEHF-6 Satellite Actively Communicating With U.S. Space Force [WWW Document]. URL https://news.lockheedmartin.com/AEHF6_satellite_successfully_launched?_ga=2.65465959.810220687.1593614164-2042781626.1583256981 (accessed 01.07.20).

Los Angeles Air Force Base, 2012a. GPS IIF [WWW Document] accessed 30.03.20 https://www.losangeles.af.mil/About-Us/Fact-Sheets/Article/343724/gps-iif/, .

Los Angeles Air Force Base, 2012b. GPS III [WWW Document] accessed 30.03.20 https://www.losangeles.af.mil/About-Us/Fact-Sheets/Article/343728/gps-iii, .

Ludlow, A.D., Boyd, M.M., Ye, J., et al., 2015. Optical atomic clocks. Rev. Mod. Phys. 87, 637–701. https://doi.org/10.1103/RevModPhys.87.637.

Lutwak, R., Deng, J., Riley, W., et al., 2004. The chip-scale atomic clock – low-power physics package. In: Proceedings of the 36th Precise Time and Time Interval (PTTI) Systems and Applications Meeting, p. 33.

Lutwak, R., Emmons, D., Garvey, R.M., et al., 2001. Optically Pumped Cesium-Beam Frequency Standard for Gps-Iii. 33rd Annu. Precise Time Time Interval Meet. 19–32.

Maleki, L., Prestage, J., 2005. Applications of clocks and frequency standards: from the routine to tests of fundamental models. Metrologia 42, S145. https://doi.org/10.1088/0026-1394/42/3/S15.

Mallette, L.A., Rochat, P., White, J., 2006. Historical review of atomic frequency standards used in space systems - 10 year update, in: 38th Annual Precise Time and Time Interval (PTTI) Systems and Applications Meeting 2006. pp. 69–80.

Mallette, L.A., White, J., Rochat, P., 2010. Space qualified frequency sources (clocks) for current and future GNSS applications. Rec. - IEEE PLANS, Position Locat. Navig. Symp., 903–908 https://doi.org/10.1109/PLANS.2010.5507225.

Mallette, L.A., Rochat, P., White, J., et al., 2012. Space Qualified Frequency Sources (Clocks) for GNSS Applications : 2012 Update, in: Joint Navigation Conference 2012. Available online at https://www.researchgate.net/publication/311667882 (accessed 30.04.20)

McCaskill, T.B., Buisson, J.A., 1975. NTS-1 (TIMATION III) Quartz- and Rubidium-Oscillator Frequency-Stability Results, in: Proceedings of the 29th Annual Symposium on Frequency Control. NAVAL RESEARCH LAB WASHINGTON DC, pp. 425–435.

McCaskill, T.B., White, J., Stebbins, S., et al., 1978. NTS-2 cesium frequency stability results. Proc. 32nd Annu Symp. Freq. Control 1978, 560–566. https://doi.org/10.1109/freq.1978.200290.

Mei, G., Zhong, D., An, S., et al., 2016. Main features of space rubidium atomic frequency standard for BeiDou satellites. 2016 Eur. Freq. Time Forum, EFTF 2016 0–3. https://doi.org/10.1109/EFTF.2016.7477803

Micalizio, S., Calosso, C.E., Godone, A., et al., 2012. Metrological characterization of the pulsed Rb clock with optical detection. Metrologia 49, 425–436. https://doi.org/10.1088/0026-1394/49/4/425.

Micalizio, S., Calosso, C.E., Levi, F., et al., 2019. Preliminary characterization of a rb pulsed optically pumped clock for space applications. 2019 IEEE Int. Work. Metrol. AeroSpace, Metroaerosp. 2019 - Proc. 682–686. https://doi.org/10.1109/MetroAeroSpace.2019.8869595

Micalizio, S., Godone, A., Levi, F., et al., 2010. Pulsed optically pumped Rb clock with optical detection: first results. European Frequency and Time Forum. IEEE, pp. 1–8.

Microsemi, 2020. 5071A - Cesium Clock Primary Frequency Standard [WWW Document]. URL https://www.microsemi.com/product-directory/cesium-frequency-references/4115-5071a-cesium-primary-frequency-standard (accessed 06.04.20).

Mulholland, S., Klein, H.A., Barwood, G.P., et al., 2019. Laser-cooled ytterbium-ion microwave frequency standard. Appl. Phys. B 125, 198. https://doi.org/10.1007/s00340-019-7309-6.

MuQuans, 2019. MuClock: A high-performance frequency standard based on cold atoms [WWW Document]. URL https://www.muquans.com/wp-content/uploads/2019/03/muquans_muclock.pdf (accessed 30.04.20).

Nakamura, M., Takahashi, Y., Amagai, J., et al., 2011. Time management system of the QZSS and time comparison experiments, in: 29th AIAA International Communications Satellite Systems Conference (ICSSC-2011). p. 8067.

Peil, S., Swanson, T.B., Hanssen, J., et al., 2017. Microwave-clock timescale with instability on order of 10^{-17}. Metrologia 54, 247.

Pelle, B., Szmuk, R., Desruelle, B., et al., 2018. Cold-Atom-Based Commercial Microwave Clock at the 10−15 Level. IFCS 2018 - IEEE Int. Freq. Control Symp. 1–5. https://doi.org/10.1109/FCS.2018.8597468

Prusti, T., De Bruijne, J.H.J., Brown, A.G.A., et al., 2016. The gaia mission. Astron. Astrophys. 595, A1. https://doi.org/10.1051/0004-6361/201629272.

Quasi-Zenith Satellite System, 2020. List of Positionning Satellites [WWW Document] accessed 30.03.20 https://qzss.go.jp/en/technical/satellites/index.html#QZSS, .

Ramsey, N.F., 1956. Thermodynamics and statistical mechanics at negative absolute temperatures. Phys. Rev. 103, 20.

Ramsey, N.F., 1990. Experiments with separated oscillatory fields and hydrogen masers. Science (80-.) 248, 1612–1619.

Riehle, F., 2003. Frequency Standards: Basics and Applications. Wiley-VCH, Weinheim, DE. https://doi.org/10.1002/3527605991.

Riehle, F., Gill, P., Arias, F., et al., 2018. The CIPM list of recommended frequency standard values: guidelines and procedures. Metrologia 55, 188. https://doi.org/10.1088/1681-7575/aaa302.

Rochat, P., Schweda, H., Mileti, G., et al., 1994. Developments of rubidium frequency standards at Neuchatel observatory. In: Proceedings of IEEE 48th Annual Symposium on Frequency Control. IEEE, pp. 716–723.

Schiller, S., Lemonde, P., Tino, G.M., et al., 2017. The space optical clocks project. In: Kadowaki, N. (Ed.), International Conference on Space Optics — ICSO 2010, 47. SPIE. https://doi.org/10.1117/12.2309166

Schmeissner, R., Douahi, A., Barberau, I., et al., 2016. Towards an engineering model of optical space Cs clock. 2016 Eur. Freq. Time Forum, EFTF 2016 3–6. https://doi.org/10.1109/EFTF.2016.7477843

Seubert, J., Ely, T., Prestage, J., et al., 2013. The deep space atomic clock: Ushering in a new paradigm for radio navigation and science. Adv. Astronaut. Sci. 148, 1851–1865.

Sharing Earth Observation Resources, 2020. ISS Utilization: ACE (Atomic Clock Ensemble in Space) [WWW Document] accessed 30.03.20 https://earth.esa.int/web/eoportal/satellite-missions/i/iss-aces, .

SMC Public Affairs, 2020. SMC and its partners successfully launch third GPS III satellite [WWW Document] accessed 06.07.20 https://www.losangeles.af.mil/News/Article-Display/Article/2243339/smc-and-its-partners-successfully-launch-third-gps-iii-satellite/, .

Stern, A., Levy, B., Levy, C., et al., 2016. The NAC-a miniature CPT Rubidium clock. In: 2016 European Frequency and Time Forum (EFTF). IEEE, pp. 1–4.

Sullivan, D.B., Bergquist, J.C., Bollinger, J.J., et al., 2001. Primary atomic frequency standards at NIST. J. Res. Natl. Inst. Stand. Technol. 106, 47.

Teunissen, P., Montenbruck, O. (Eds.), 2017. Springer Handbook of Global Navigation Satellite Systems. Springer International Publishing, Cham, CH. https://doi.org/10.1007/978-3-319-42928-1

Thirolf, P.G., Seiferle, B., von der Wense, L., 2019. The 229-thorium isomer: doorway to the road from the atomic clock to the nuclear clock. J. Phys. B At. Mol. Opt. Phys. 52, 203001.

Thoelert, S., Montenbruck, O., Meurer, M., 2014. IRNSS-1A: signal and clock characterization of the Indian regional navigation system. GPS Solut. 18, 147–152.

Tjoelker, R.L., Prestage, J.D., Burt, E.A., et al., 2016. Mercury ion clock for a NASA technology demonstration mission. IEEE Trans. Ultrason. Ferroelectr. Freq. Control 63, 1034–1043. https://doi.org/10.1109/TUFFC.2016.2543738.

Utkin, A., Belyaev, A., Pavlenko, Y., et al., 2012. On-Board active hydrogen maser for RADIOASTRON mission (design and experimental results) Parameters of the Orbit. 6th Int. Symp. "METROLOGY TIME SPACE". Available online at http://www.vremya-ch.com/english/materials/files/utkin.pdf (accessed 30.04.20)

Vanier, J., 2005. Atomic clocks based on coherent population trapping: A review. Appl. Phys. B Lasers Opt. https://doi.org/10.1007/s00340-005-1905-3

Vanier, J., Audoin, C., 2005. The classical caesium beam frequency standard: fifty years later. Metrologia 42, S31. https://doi.org/10.1088/0026-1394/42/3/S05.

Vanier, J., Mandache, C., 2007. The passive optically pumped Rb frequency standard: The laser approach. Appl. Phys. B Lasers Opt. 87, 565–593. https://doi.org/10.1007/s00340-007-2643-5.

Vanier, J., Tomescu, C., 2015. The Quantum Physics of Atomic Frequency Standards: Recent Developments. CRC Press, Boca Raton FL, USA.

Vessot, R.F.C., Levine, M.W., Mattison, E.M., et al., 1980. Test of relativistic gravitation with a space-borne hydrogen maser. Phys. Rev. Lett. 45, 2081–2084. https://doi.org/10.1103/PhysRevLett.45.2081.

Waller, P., Gonzalez, F., Binda, S., et al., 2009. Update on the in-orbit performances of GIOVE clocks. In: 2009 IEEE International Frequency Control Symposium Joint with the 22nd European Frequency and Time Forum, pp. 388–392. https://doi.org/10.1109/FREQ.2009.5168207.

Wu, Z., Zhou, S., Hu, X., et al., 2018. Performance of the BDS3 experimental satellite passive hydrogen maser. GPS Solut. 22. https://doi.org/10.1007/s10291-018-0706-1.

Wynands, R., Weyers, S., 2005. Atomic fountain clocks. Metrologia 42, S64. https://doi.org/10.1088/0026-1394/42/3/S08.

Xu, X., Wang, X., Liu, J., et al., 2019. Characteristics of BD3 global service satellites: POD, open service signal and atomic clock performance. Remote Sens. 11, 1–17. https://doi.org/10.3390/rs11131559.

1.4.1 Complements on "GNSS-grade space atomic frequency standards: Current status and ongoing developments" [6]

Results on the performances of the DSAC in space have been published [85]. Figure 1 from [6] is consequently updated and presented in Figure 1.2 with performances comparable to the BeiDou-3 PHM. Another noteworthy effort towards a new generation of laser-pumped RAFS is the LaliPOP [86], an hybrid, switchable mode, lamp and laser pumped RAFS developed to build trust in the laser technology for space applications.

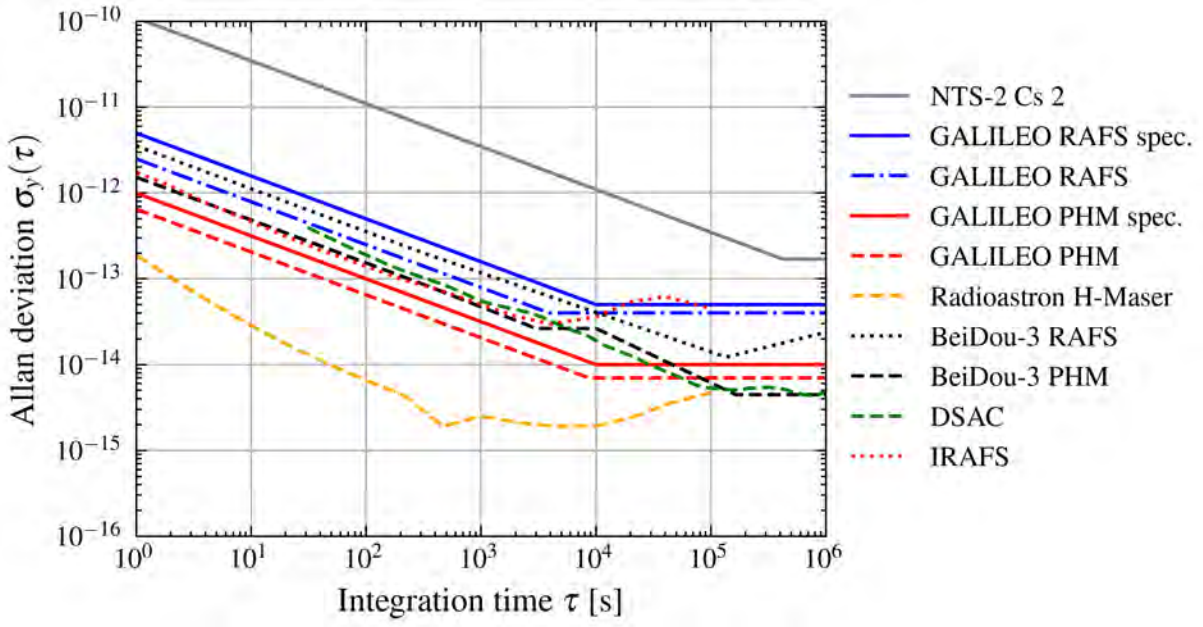

Figure 1.2: Performances of current GNSS-grade frequency standards: NTS-2 Cs 2 [87], GALILEO RAFS and PHM [62], [88], Radioastron [27], BeiDou-3 RAFS and PHM [89], DSAC [85].

Since our last estimation of the number of Space Atomic Frequency Standard (SAFS) sent into orbit, launches of the new generation of GPS III have continued with three more launches. QZSS-1R replaced QZSS-1 with an additional frequency standard anticipating the new design of QZSS second generation [90]. To the best of my knowledge, no information was given on the type of the third frequency standard. Without speculating too much, it is very likely that this is not a third RAFS following other constellations logic to feature hybrid composition of standards. The GLONASS constellation was also complemented with three K1 and one M satellites. Finally, the NavIC constellation was completed with the first NVS satellite, NVS-01, to replace IRNSS-1G. The satellite features the first indian RAFS (IRAFS) [91]. The number of on-board frequency standards was not disclosed. Figure 2 from [6] is updated and presented on figure 1.3.

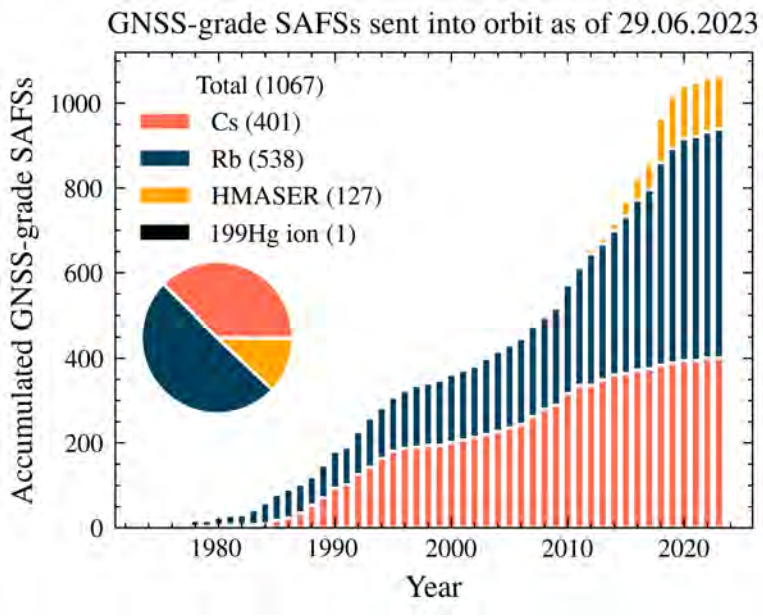

Figure 1.3: Estimated number of GNSS-grade space atomic frequency standards sent to space as of 29.06.2023. The number of RAFS in the NVS-01 satellite was assumed to be 3 following the payloads of the former satellites.

Chapter 2

The theory of laser-pumped Ramsey Rb frequency standards

This chapter provides necessary theoretical information on Rb frequency standards. In particular, details on the measurement of the frequency stability of the pulsed laser head presented that were published in the overview proceeding included at the end of this chapter [92].

2.1 The theory of Rubidium frequency standards

2.1.1 ^{87}Rb energy levels

2.1.1.1 Energy levels in a static magnetic field

In the presence of a magnetic field, the Hamiltonian of the ^{87}Rb valence electron is given by:

$$\hat{H} = \hat{H}_0 + \hat{H}_B \tag{2.1}$$

with [5] $\hat{H}_0$ the natural Hamiltonian including the kinetic energy, the Coulomb interaction of the electron with the nucleus and the electrons in the other subshells, the relativistic correction coupling the nucleus spin $I = \frac{3}{2}$ and the electron angular momentum $\hat{L}$ responsible breaking the degeneracy of the fine structure and the electron-nucleus interaction, or hyperfine coupling, which lifts the hyperfine structure degeneracy. Given that $\hat{H}_0$ depends on the nucleus spin $\hat{\boldsymbol{I}}$, the valence electron spin $\hat{\boldsymbol{S}}$ and angular moment $\hat{\boldsymbol{L}}$, it is convenient to work with the equivalent angular moment [5]:

$$\hat{\boldsymbol{F}} = \underbrace{\hat{\boldsymbol{L}} + \hat{\boldsymbol{S}}}_{\hat{\boldsymbol{J}}} + \hat{\boldsymbol{I}} \tag{2.2}$$

such that every eigenvector of $\hat{H}$ can be expressed in the basis:

$$|n, L, J, F, m_F\rangle \tag{2.3}$$

with $n = 1, 2, 3...$ the principal quantum number, $L = 0, 1, ..., n-1$ with corresponding letters $s, p, d, f, ...$, $J = -|L+S|, -|L+S|+1, ..., L+S$ and $F = -|J+I|, -|J+I|+1, ..., |J+I|$ with $I = \frac{3}{2}$ for ^{87}Rb and $m_F = -F, -F+1, ..., F$. The energy levels of the ^{87}Rb atom are given in Figure 2.1. The ^{87}Rb electron structure is $(1s^2, 2s^2, 2p^6, 3s^2, 3p^6, 4s^2, 3d^{10}, 4p^6, 5s^1)$ with, in absence of magnetic field, the ground state:

$$|5S_{1/2}, F = 1\rangle \,. \tag{2.4}$$

In principle, the values of energy levels of state given by eq. (2.3) can be calculated to a good precision by quantum mechanics. If one adds quantum electrodynamics corrections, the energy levels can be determined to a few significant digits only [5]. Consequently, experimental determination of the ^{87}Rb energy levels is necessary.

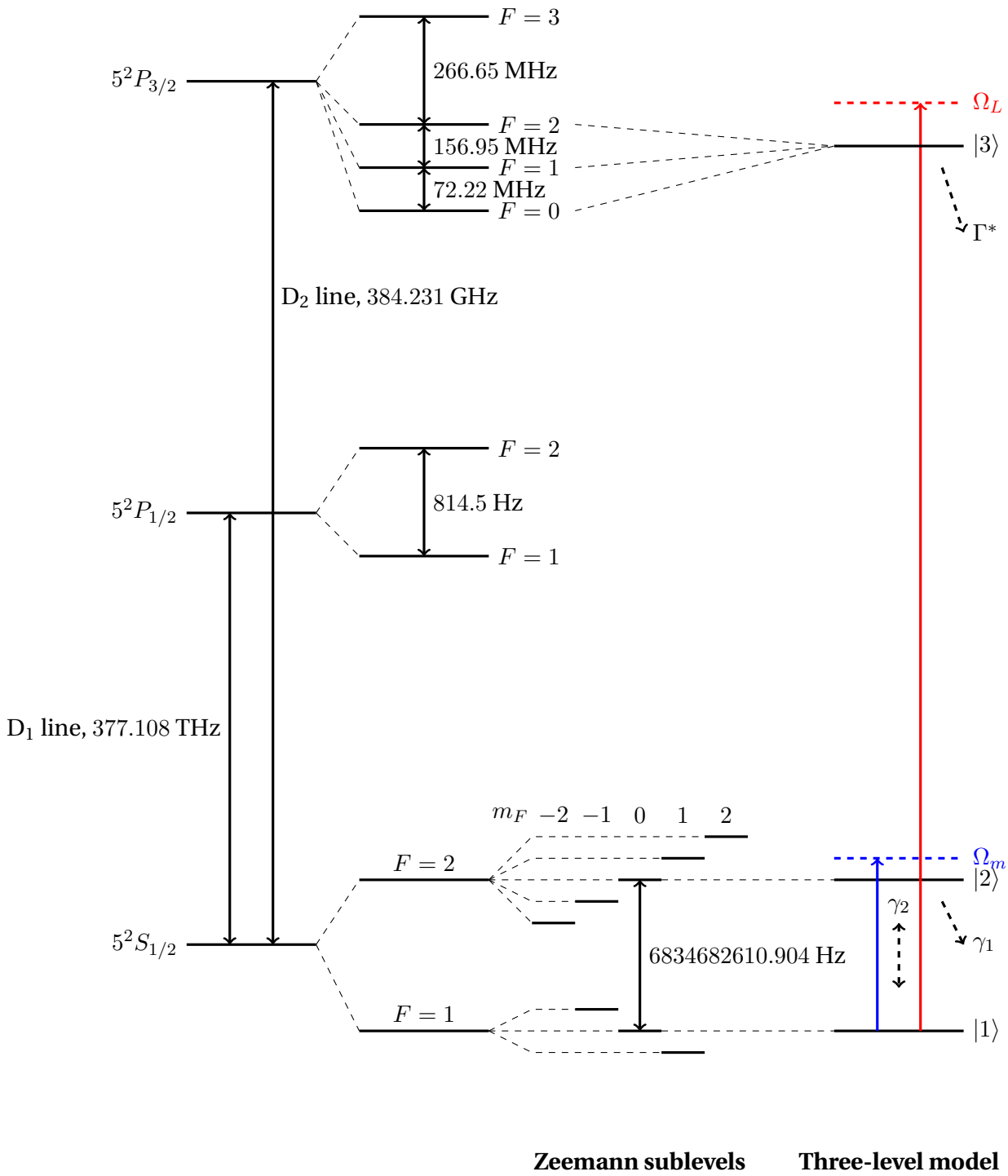

Figure 2.1: Energy levels of ^{87}Rb [57].

The magnetic interaction Hamiltonian $\hat{H}_B$ is given by [57]:

$$\hat{H}_B = -\hat{\boldsymbol{\mu}} \cdot \boldsymbol{B} = -\mu_B(\hat{\boldsymbol{L}} + g_J\hat{\boldsymbol{J}} - g_I\hat{\boldsymbol{I}}) \tag{2.5}$$

with μ_B the Bohr magnetron and g_J, g_I Landé g-factors [57]. In the case of a static magnetic field oriented along axis, namely $\hat{\boldsymbol{B}} = B_z\hat{z}$, eq. (2.5) reads:

$$\hat{H}_B = \mu_B(\hat{L}_z + g_J\hat{J}_z - g_I\hat{I}_z)B_z. \tag{2.6}$$

The change of energy difference of the clock transition, namely between the states $|5^2S_{1/2}, F = 1, m_F\rangle$ and $|5^2S_{1/2}, F = 2, m'_F\rangle$, is given by the Breit-Rabi formula [57], namely:

$$\Delta E = E_{HFS} + (m_F + m'_F)\frac{g_J\mu_B}{4}B_z + \frac{(g_J\mu_B)^2}{2E_{HFS}}B_z^2 \tag{2.7}$$

with E_{HFS} the unperturbed clock energy difference [57]. For ^{87}Rb, the linear and quadratic sensitivity coefficients of eq. (2.7) are $(m_F + m'_F)0.7$ MHz/G and 575.14 Hz/G^2, respectively. The reduced sensitivity of the clock transition, with $m_F = m'_F = 0$, to magnetic fields to the first order is why this transition was chosen for making atomic clocks [5]. As described by eq. (2.7), the clock transition is still sensitive to the 2$^{\text{nd}}$ Zeeman shift, namely the sensitivity to the second order to static magnetic fields.

2.1.1.2 Other frequency shifts

Apart from the already mentioned Zeeman 2$^{\text{nd}}$ order frequency shift, other shifts influence the clock frequency, especially for vapor-cell standards. The list of relevant frequency shifts for the two clocks presented in the next chapters is presented below.

Buffer gas shift

Buffer gases are inherent component of vapor-cell standards. Indeed, the presence one or more buffer gases reduces the Rb atoms diffusion constant which allows to prevent wall-collision and reduce Doppler broadening [5], [93]–[95]. Neutral gases such as noble gases or Dinitrogen (N_2) are preferred because they do not chemically react with the alkali atoms. In particular, Dinitrogen is preferred as the alkali atoms de-excite via quenching processes which avoid fluorescence. In general, a mixture of buffer gases with opposite sign temperature-shift linear coefficients is is used with the purpose of exhibiting a quadratic frequency shift dependency on the cell temperature [5].

The need for buffer gases in vapor-cell frequency standards ultimately limits their performances making them more sensitive to the fluctuations of external parameters such as vapor-cell temperature shift or room pressure barometric shifts. Finally, vapor-cell frequency standards exhibit frequency ageing due to helium permeation [96], another inherent limitation of the vapor-cell

technology. A model of relaxation rates in the presence of an arbitrary buffer gases is presented in section 3.3.3.

The frequency shift of the clock transition due to collisions with one buffer-gas i is described by [95]:

$$\nu(T) = \nu_0 + P\left[\beta_i + \delta_i \cdot (T - T_0) + \gamma_i \cdot (T - T_0)^2\right] \tag{2.8}$$

with P the buffer gas pressure during the sealing, T the cell temperature and β_i,δ_i,γ_i the constant, linear and quadratic shifts coefficients proper to the considered buffer gas i. T_0 is a reference temperature close to which the shift is measured. In the presence of more than one buffer gas, the equivalent β,δ and γ are linearly weighted according to the normalized pressure of each buffer gas, namely:

$$\beta = \sum_i p_i \beta_i, \quad \sum_i p_i = 1. \tag{2.9}$$

For single buffer gas the temperature-dependent linear shift δ is usually dominant [95]. The trick of the two-buffer gases mixture is to select two buffer gases with opposite linear coefficients signs. With the right mixture, it is then possible to reach $\delta \approx 0$ which yields a parabolic $\nu(T)$ shape featuring an operation point T_{inv} with no sensitivity to fluctuations of cell the temperature.

Light-induced shifts

The AC Stark shift [97] is responsible for sensitivity of the clock frequency to the laser intensity and frequency. Indeed, in presence of light close to an optical transition, a supplementary Hamiltonian term couples the light with the electron dipole moment. In the case of light tuned near the optical transition between the Rb ground state and an excited state of frequency ν_3, the light-induced shift reads [98]:

$$\Delta\nu_{LS} = \left(\frac{\omega_R}{4\pi}\right)^2 \left(\frac{\Delta\nu_2}{\left(\frac{\Gamma^*}{4\pi}\right)^2 + \Delta\nu_2^2} - \frac{\Delta\nu_1}{\left(\frac{\Gamma^*}{4\pi}\right)^2 + \Delta\nu_1^2} \right) \tag{2.10}$$

where $\Delta\nu_i = \nu_R - \nu_{i3}$ is the optical frequency detuning between the laser frequency $\nu_R = \omega_R/2\pi$ and the transition frequency between the $|5S_{1/2}, F = i, m_F = 0\rangle$ state and the excited state $|5^2P_{3/2}\rangle$, Γ^* the excited state intrinsic decay rate and $\omega_R/(2\pi)$ the optical Rabi frequency as defined in section 2.2.2.1.

The two lightshifts coefficients α_{LS} and β_{LS} are hence defined as:

$$\alpha_{LS} := \frac{\partial\Delta\nu_{LS}/\nu_{clock}}{\partial I_L/I_L} \quad [\%^{-1}] \tag{2.11}$$

and

$$\beta_{LS} = \frac{\partial\Delta\nu_{LS}/\nu_{clock}}{\partial\nu_3} \quad [\mathrm{MHz}^{-1}]. \tag{2.12}$$

In the ideal case, the coefficients of eq. (2.11) and (2.12) should be zero in POP operation which is not the case for high-performance Rb DR POP Ramsey vapor-cell clocks [64]. This can be explained by two different phenomena: light leakage through the AOM or residual coherence between each Ramsey cycle [99]. In the case of the cold-atom experiments discussed in chapter 4 and 5, there should be no leakage during the Ramsey part of the cycle as the light is blocked thanks to mecanical shutters [100].

Position shifts

Spatial frequency and phase distribution inhomogeneities can be the cause of clock frequency shifts [101]. For instance, the Zeeman 2$^{\text{nd}}$-order shift is fundamentally not homogeneous because of Maxwell equations [102] enforcing that the divergence of the C-field is zero, namely $\nabla \cdot \vec{C} = 0$. Consequently, in the case of spatially confined atoms, which is the case of buffer gas vapor-cells and trapped cold-atoms clocks, any change in atom density distribution, resonance frequency distribution or interrogation volume will lead to a frequency shift. The position shift studied in chapter 3 is an example of the latter.

Microwave-power shift

Similarly to the position shift, fluctuations of the input microwave power change the optimal spatial distribution of atoms interacting with the microwave field [103], [104]. This effect has been studied in the framework of DR Rb vapor-cell clocks showing a strong correlation with light-shifts. In spite of the absence of light during microwave operation, this effect is still relevant for Ramsey type clocks [99], [101].

2.2 ^{87}Rb Ramsey-type clock

2.2.1 Concept

Figure 2.2 shows the principal setup of a DR Ramsey-type Rb clock. Rb atoms are placed in a microwave cavity resonant to the clock frequency. Atoms can be either placed in a vapor-cell or trapped cooled via laser interaction. In all cases a static magnetic field, named C-field in reference to the magnetic field in the C section of Cs beam tubes [5], is placed to lift the degeneracy of the ground states levels $|5S_{1/2}, F = 1, 2, m_F \neq 0\rangle$.

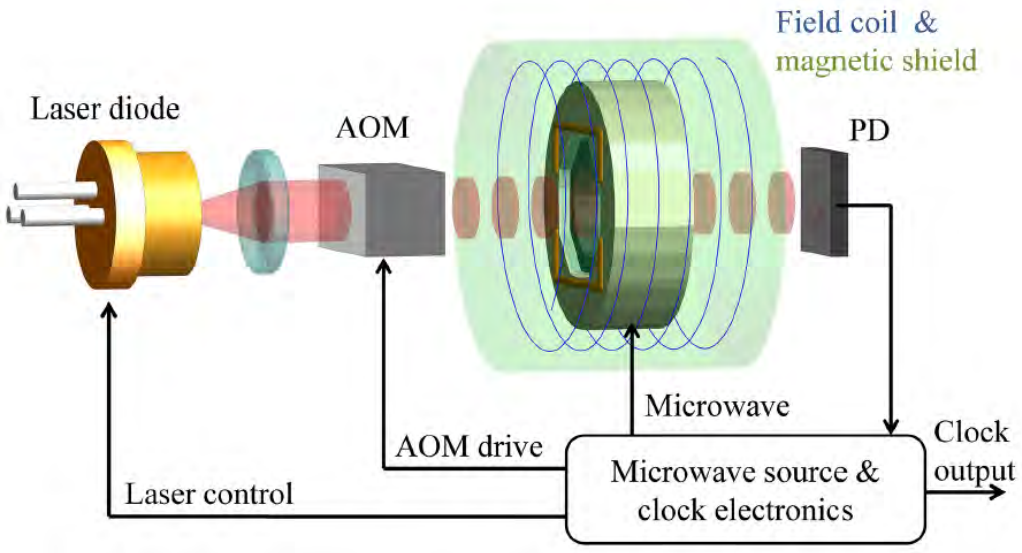

Figure 2.2: μPOP passive double resonance Ramsey clock [1].

The first part of the Ramsey cycle (see Figure 2.3) consists of preparing the atoms to one of the ground states $|5S_{1/2}, F = 1, 2, m_F = 0\rangle$. In the case of vapor-cell clocks, this is achieved with an optical pump pulse acting on one of the two $|5S_{1/2}, F = 1, 2, m_F = 0\rangle \leftrightarrow |5P_{3/2}\rangle$ transitions. In the studies of chapter 3, the laser frequency was externally stabilized on subdoppler cross-over line using our in-house laser head [105]. In the case of cold-atom clocks, atom preparation is more complex and was covered in chapter 5 and in [84].

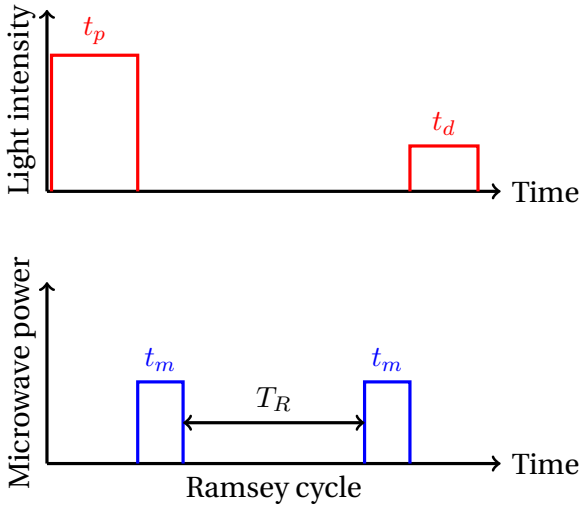

Figure 2.3: Ramsey cycle in the case of a vapor-cell clock.

The pumping step is followed by two $\pi/2$ microwave pulses separated by the Ramsey time T_R with light off. The goal of the two pulses is to transfer as many atoms from the original ground-state to the other one. Longer Ramsey times improve the quality factor Q_A as shown on eq. (2.28) while the SNR decreases which limits the Ramsey time duration [1]. Ultimately, the Ramsey time is limited by the relaxation rates, introduced in section 2.2.2 and discussed in detail in section 3.3. The shape of the signal is called Ramsey fringes and is shown on Figure 2.4.

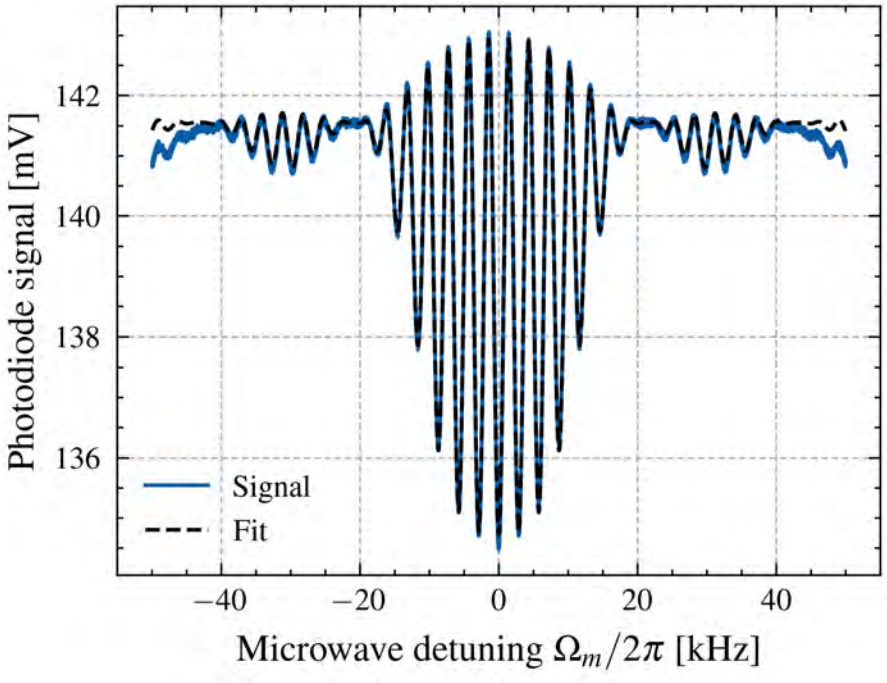

Figure 2.4: Example of Ramsey fringes acquired during the μPOP measurement campaign.

After the microwave phase, the population difference Δ defined in section 2.2.2, namely the proportion of atoms in the second ground-state, is measured. In the case of vapor-cell clocks, this step is achieved using the same optical transition that was used in the pumping phase yet with different intensity. In the case of cold atoms, as described in chapter 5, a two-step readout process is needed to account for deviation of the atom number from one atom loading to another.

2.2.2 Three-level model

2.2.2.1 Single-atom model

In this section, the three-level model for the vapor-cell Rasmey clock is presented. The model was developed by Moreno [99] following Micalizio et al. [106] and Godone et al [60] for the pulsed Rb vapor-cell standard and Godone et al. [107] for the Coherent population Trapping (CPT) maser. Is is

worth pointing out that the microwave part of the cycle yielding the Ramsey fringes shape is also usable for the cold-atom clock presented in chapter 5.

The three-level model is constituted from the two ground-states $|1\rangle = |5^2S_{1/2}, F = 1, m_F = 0\rangle$ and $|2\rangle = |5^2S_{1/2}, F = 2, m_F = 0\rangle$ and the excited states $|3\rangle = |5^2P_{3/2}, F = 1, 2, 3\rangle$ or $|3\rangle = |5^2P_{3/2}, F = 0, 1, 2\rangle$. The aggregation of the last states is motivated by the low frequency separation of the $|5^2P_{3/2}\rangle$ states compared to the optical linewidth dominated by Doppler and collision broadening making it impossible to address the states separately.

Since the atomic radius of ^{87}Rb is of the order of 303 pm [108] and the wavelength of the D_2 transition 780 nm, the dipole approximation [109] holds. In the case of a linearly polarized light-field on axis $\hat{e}_\lambda$, amplitude E_0, angular frequency ω_R and wavenumber $\vec{k}$ namely:

$$\vec{E}(\vec{r}, t) = \frac{1}{2} E_0 e^{i\omega_R t - \vec{k}\cdot\vec{r}} \hat{e}_\lambda + c.c \tag{2.13}$$

the dipole Hamiltonian reads:

$$\hat{W}_E = -e\hat{\boldsymbol{r}} \cdot \hat{\boldsymbol{E}} = -\hat{d}\frac{1}{2} E_0 e^{i\omega_R t} + c.c \tag{2.14}$$

with $\hat{d} = q\hat{\boldsymbol{r}} \cdot \hat{e}_\lambda$ the dipole moment.

The magnetic interaction can be handled similarly. In the case of an oscillating magnetic field aligned with the C-field, namely:

$$\vec{B} = \frac{1}{2} B_z(r, t) e^{i\omega_m t + i\varphi} \hat{e}_z + c.c. \tag{2.15}$$

with angular frequency ω_m and phase φ, the magnetic interaction Hamiltonian reads:

$$\hat{W}_B = -\hat{\boldsymbol{\mu}} \cdot \vec{B} = -\frac{1}{2} \hat{\mu}_z B_z(r, t) e^{i\omega_m t + i\varphi} + c.c. \tag{2.16}$$

The final Hamiltonian is hence:

$$\hat{H} = \hat{H}'_0 + \hat{W}_E + \hat{W}_B = \hbar \begin{pmatrix} \omega_1 & -b\cos(\omega_m t + \varphi) & -\omega_R \cos(\omega_R t) \\ -b\cos(\omega_m t + \varphi) & \omega_2 & 0 \\ -\omega_R \cos(\omega_R t) & 0 & \omega_3 \end{pmatrix} \tag{2.17}$$

with $\omega_{1,2,3}$ the eigen angular frequencies of the diagonal Hamiltonian $\hat{H}'_0$ encapsulating the fundamental energy levels of the ^{87}Rb structure as well as all the static frequency shifts developed in the previous section such as the Zeeman shift, the pressure shift, etc... $\omega_R = \langle 1|\hat{d}|3\rangle \frac{E_0}{\hbar}$ and $b = \langle 1|\hat{\mu}_z|2\rangle \frac{B_z}{\hbar}$ the optical and microwave Rabi frequencies. It is worth recalling the reader that eq. (2.17) holds for light tuned near to the $|1\rangle \leftrightarrow |3\rangle$ transition. An equivalent Hamiltonian in the case of $|2\rangle \leftrightarrow |3\rangle$ optical tuning can be developed [99].

In order to take into account for the relaxation processes, one must use the density matrix formalism and empirically include a relaxation matrix $\hat{\Gamma}$ in the Liouville equation, namely:

$$\frac{\partial\hat{\rho}}{\partial t} = -\frac{i}{\hbar}[\hat{H},\hat{\rho}] - \hat{\Gamma}. \tag{2.18}$$

With $\hat{\Gamma}$ a matrix including Γ^*, γ_1 and γ_2 the relaxation rate of state $|3\rangle$, the population relaxation rate and the coherence relaxation rate, respectively. It is worth mentioning that excitation terms coming from the cavity feedback are neglected which is a reasonable approximation given the low quality factor of the microwave resonators considered in this thesis and other works [110].

Equation (2.18) can be solved separately for optical pumping (i.e. $b = 0$), Ramsey phase $\omega_R = 0$ and free-evolution phase ($b = \omega_R = 0$). The solution steps include taking the rotating wave approximation for off-diagonal terms of the density matrix and making assumption that $\Gamma^* \gg \gamma_1, \gamma_2, \Omega_m$. The solution for each phase can be expressed in the Bloch sphere in the basis $\vec{R} = (2\Re(\delta_{12}), 2\Im(\delta_{12}), \Delta)$ with:

$$\Delta = \rho_{22} - \rho_{11} \quad \text{and} \quad \delta_{12} = \rho_{12}e^{-i\omega_m t}. \tag{2.19}$$

2.2.2.2 Solution for the pumping phase

In the pumping and interrogation phases, the solution of eq. (2.18) in the Bloch vector basis is [99], [107]:

$$\Delta(t) = \Delta_0 e^{-\gamma_1' t} + \frac{\Gamma_R}{\gamma_1'(1+\delta_0^2)(1-e^{-\gamma_1' t})} \tag{2.20}$$

and

$$\delta_{12}(t) = \delta_{12}^{(0)} e^{-\gamma_2' t} e^{i\Omega_m' t} \tag{2.21}$$

with $\gamma_i' = \gamma_i + \frac{\Gamma_R}{1+\delta_0^2}$, $\Omega_m' = \Omega_m + \frac{\Gamma_R\delta_0}{1+\delta_0^2}$ and $\delta_0 = \frac{2\Delta_0}{\Gamma^*}$ the regularized relaxation rates, microwave angular frequency and optical detuning, respectively.

2.2.2.3 Solution for microwave interaction

Let us write the evolution of the Bloch vector after pumping in matrix form, namely [99], [107]:

$$M_m(t_m) = \begin{pmatrix} \cos(\xi t_m) & \frac{\Omega_m}{\xi}\sin(\xi t_m) & -\frac{b}{\xi}\sin(\xi t_m) \\ -\frac{\Omega_m}{\xi}\sin(\xi t_m) & \frac{b^2+\Omega_m^2\cos(\xi t_m)}{\xi^2} & \frac{\Omega_m b}{\xi^2}(1-\cos(\xi t_m)) \\ \frac{b}{\xi}\sin(\xi t_m) & \frac{\Omega_m b}{\xi^2}(1-\cos(\xi t_m)) & \frac{b^2+\Omega_m^2\cos(\xi t_m)}{\xi^2}. \end{pmatrix} \tag{2.22}$$

With t_m the duration of the microwave pulse and $\xi^2 = b^2 + \Omega_m^2$. On resonance, $\Omega_m = 0$ and $\xi = b$ and eq. (2.22) is more simple. We define here the pulse area θ:

$$\theta = \xi t_m. \tag{2.23}$$

2.2.2.4 Solution for free evolution part

In the case of free evolution, the Liouville equation is much simpler and reads:

$$M_R(T_R) = \begin{pmatrix} e^{-\gamma_2 T_R}\cos(\Omega_m T_R) & e^{-\gamma_2 T_R}\sin(\Omega_m T_R) & 0 \\ -e^{-\gamma_2 T_R}\sin(\Omega_m T_R) & e^{-\gamma_2 T_R}\cos(\Omega_m T_R) & 0 \\ 0 & 0 & e^{-\gamma_1 T_R} \end{pmatrix} \tag{2.24}$$

which also simplifies greatly for $\Omega_m = 0$. It is worth mentioning that the $M_R(T_R)_{33}$ directly shows the dependence of the signal on the population relaxation processes. Longer Ramsey times imply population loss and hence lower SNR.

2.2.2.5 Ramsey fringes

The Ramsey part of the cycle, namely the two microwave pulses separated by the free-evolution time, can be written in term of the matrices derived above, namely, the evolution of an initial Bloch vector $\vec{R}_0$ is given by:

$$\vec{R} = M_m(t_m) M_R(T_R) M_m(t_m) \vec{R}_0. \tag{2.25}$$

Developing eq. (2.25) and solving for $\Delta(t)$ with the hypothesis that there is no residual coherence at the beginning of the process, namely $\vec{R}_0 = (0, 0, \Delta_0)$, one finds [99]:

$$\begin{aligned} &\Delta(t_m, T_R, \Omega_m) \\ &= \Delta_0 \left(e^{-\gamma_1 T_R} m_{33}^2 + e^{-\gamma_2 T_R}\cos(\Omega_m T_R)(m_{23}^2 - m_{13}^2) - e^{-\gamma_2 T_R}\sin(\Omega_m T_R)(2 m_{13} m_{23}) \right) \end{aligned} \tag{2.26}$$

with:

$$m_{ij} = (M_m(t_m))_{ij}\,, m_{13}^2 + m_{23}^2 + m_{33}^2 = 1. \tag{2.27}$$

It is important to say that we respectfully want to point out that the sign of the $\sin(\Omega_m T_R)$ term in eq. (2.26) has been corrected compared to the development shown in [99].

Equation (2.26) generally described the shape of Ramsey fringes in vapor-cell Ramsey clocks. An example of such fringes is shown on Figure 2.4.

An important result of (2.26) is that is allows to show the well-known relation linking the central

fringe Full Width at Half Maximum (FWHM) to T_R and t_m, namely [106]:

$$FWHM \approx \frac{1}{T_R + \frac{4}{\pi}t_m} \quad \Rightarrow \quad Q_A = \nu_0 \left(T_R + \frac{4}{\pi} t_m \right) \tag{2.28}$$

with Q_A the atomic quality factor.

2.2.2.6 Phase shift

Eq. (2.26) and (2.28) can be used to estimate the phase shift between two distributions. Indeed, by neglecting the microwave time dependence of the fringe FWHM, a second pulse with a phase difference $\Delta\phi$ would shift the fringe position by a value of:

$$\Delta\nu = \frac{\Delta\phi}{2\pi T_R}. \tag{2.29}$$

2.2.2.7 Ramsey fringes for cold-atom clocks

It is worth mentioning how the development presented here can be applied to the cold-atom clock presented in chapter 5. Indeed, one of the main differences between the two clocks presented in this work is the temperature of the atoms. According to Boltzmann statistics, the thermal equilibrium distribution of atoms obey the relation:

$$\rho_{11}/\rho_{22} = e^{(E_2-E_1)/(k_B T)} = \begin{cases} \approx 1 & T \sim 373\text{K} \\ \infty & T \sim 10\mu\text{K} \end{cases} \tag{2.30}$$

In other words, the temperature has a great impact on the equilibrium statistical state in absence of light or microwave interaction. The relaxation model presented in eq. (2.18) must hence be adapted to the cold-atom case replacing the population and coherence relaxation rates with rates processes pushing the system in the state $\hat{\rho}_{cold}^{(eq)} = |1\rangle\langle 1|$ rather than $\hat{\rho}_{hot}^{(eq)} = \frac{1}{2}|1\rangle\langle 1| + \frac{1}{2}|2\rangle\langle 2|$. However, since relaxation processes for cold atoms are extremely small and given the low Ramsey time values, the shape of the cold-atom Ramsey fringes can be approximated using eq. (2.26) with $\gamma_1 = \gamma_2 = 0$. For longer Ramsey times such as the one found in Cs fountains, this approximation does not hold anymore. In our studies, the shape of the envelope is flat (see. Figure 5.9), which confirms the validity of the approximation.

2.2.3 Ensemble of atoms

So far, the equations presented above apply to single-atoms and do not include any measurement process, that is the evaluation of the population difference Δ after the Ramsey cycle. The measurement process via absorption is governed by the Beer-Lambert law [111]. In the cases of thin-layer

approximation, the Beer-Lambert law reads:

$$I(\vec{r},t) = I(0,t)e^{-N_0|\vec{r}|\sigma_{i3}n_i(\vec{r}/2,t)} \tag{2.31}$$

with $I(0,t)$ and $I(\vec{r},t)$ the probe laser intensity before and after traversing the atoms, $n_i(\vec{r}/2,t)$ the density of atoms in the state $|i\rangle$, assumed homogeneous, N_0 the density of Rb atoms, assumed homogeneous and $\sigma_{i3}(\Omega_L)$ the absorption cross-section that depends on the laser angular frequency detuning Ω_L. The proportion of atoms in the first state depends on the population difference $\Delta(r,t)$. In the case of vapor-cell Ramsey standard with $|1\rangle \leftrightarrow |3\rangle$ optical pumping, one has:

$$n_1 = \frac{3}{8} - \frac{\Delta}{2} \tag{2.32}$$

which takes into account that not all atoms participate to the signal. In the case of cold-atom clocks with state selection as implemented in chapter 5, one has:

$$n_i \approx \Delta. \tag{2.33}$$

2.3 Stability of a frequency standard

2.3.1 Allan deviation

2.3.1.1 Definition

The stability of a quantity A at integration time τ is often measured in terms of the Allan deviation $\sigma_A(\tau)$, which is defined as [112]:

$$\sigma_A^2(\tau) = \frac{1}{2}\left\langle (A(t+\tau) - A(t))^2 \right\rangle_\tau \tag{2.34}$$

where the Allan deviation has the same unit as A and $\langle\cdot\rangle_\tau$ represents the statistical expected value. Other deviations for the measurement of stabilities exist such as the Hadamard deviation [113], the modified Allan deviation [114] or the Theo1 deviation [115].

In order to compare the stability of oscillators with different nominal frequencies ν_0 [Hz], one compares their relative frequencies y, which is defined as:

$$y(t) := \frac{\nu(t) - \nu_0}{\nu_0}, \tag{2.35}$$

with $\nu(t)$ [Hz] the oscillator frequency at time t.

Note that all the details for computing and analyzing the Allan deviation can be found in the "Hand-

book of frequency stability analysis" [112] or in the more recent review by Rubiola and Vernotte [116].

There exist different estimators of eq. (2.34) the most popular being the overlapping estimator [112] which greatly improves the statistical confidence interval over the natural estimator. Calculation of the error bars of overlapping estimators is more involved as the samples are not statistically independent [112]. The more recent TheoBR estimator [117] of the Allan variance which allows for estimating Allan deviations for longer τ is seldom used.

2.3.2 Allan deviation of a function of other variables

2.3.3 Correlation and Groslambert covariance

The Allan deviation follows the usual multiplication and addition rules of the standard deviation, in particular, if $y = y(A_1, A_2, ..., A_N)$, then:

$$\sigma_y^2(\tau) = \sum_{i=1}^{N} \left(\partial_{A_i} y\right)^2 \sigma_{A_i}^2(\tau) + 2 \sum_{1 \leq i < j \leq N} \left(\partial_{A_i} y \cdot \partial_{A_j} y\right) \cdot \mathrm{GCov}(A_i, A_j), \tag{2.36}$$

with GCov the Groslambert covariance defined as [118],

$$\mathrm{GCov}(A_i, A_j) = \frac{1}{2} \left\langle \left(A_i(t+\tau) - A_i(t)\right) \left(A_j(t+\tau) - A_j(t)\right) \right\rangle_\tau , \tag{2.37}$$

and

$$\partial_{A_i} y := \left. \frac{\partial y}{\partial A_i} \right|_{\langle A_i \rangle} . \tag{2.38}$$

It is worth mentioning that the second term of eq. (2.36) is often approximated as zero as it is assumed that all the parameters $\{A_i\}$ are uncorrelated from each other. This term will however be of the greatest importance when assessing the long-term instability budget of the μPOP experiment shown in chapter 3.

As eq. (2.37) can be negative, the Groslambert codeviation is defined as:

$$\mathrm{GDev}(A_i, A_j) := \mathrm{sgn}(\mathrm{GCov}(A_i, A_j)) \sqrt{\mathrm{GCov}(A_i, A_j)}. \tag{2.39}$$

Estimation of the error bars of the Groslambert covariance needs the implementation of an involved procedure only recently developed by Vernotte et al. [118], [119].

2.3.3.1 Proof of equation 2.36

Due to the usual uncorrelated nature of the parameters influencing the frequency of frequency standards, eq. (2.36) was, to the best of my knowledge, never been properly developed in the literature related to frequency standards.

Lemma 1. *If* $y = y(A_1, ..., A_N)$*, then:*

$$y(A_1, ..., A_N) \approx y(\underbrace{\langle A_1 \rangle, ..., \langle A_N \rangle}_{:=\langle \vec{A} \rangle}) + \sum_{i=1}^{N} \left. \frac{\partial y}{\partial A_i} \right|_{\langle \vec{A} \rangle} \cdot (A_i - \langle A_i \rangle) . \tag{2.40}$$

Proof. The relation can be proved by rewriting $A_i = A_i + \langle A_i \rangle - \langle A_i \rangle$ and expanding $y(A_1, ..., A_N)$ to the first order around $|A_i - \langle A_i \rangle| \ll |\langle A_i \rangle|$. Note that in the case where $\langle A_i \rangle / A_i \approx 0$, the approximation is still valid if the higher derivatives $\partial^n_{A_i} y,\ n \geq 2$ are sufficiently small. □

Lemma 2. *Proof of eq.* (2.36).

Proof.

$$\begin{aligned}
\sigma_y^2(\tau) &= \langle \frac{1}{2} \left[y\left(A_1(t+\tau), ..., A_N(t+\tau)\right) - y\left(A_1(t), ..., A_N(t)\right) \right]^2 \rangle \\
&\approx \frac{1}{2} \langle \left[\left(y(\langle \vec{A} \rangle) + \sum_{i=1}^{N} \left. \frac{\partial y}{\partial A_i} \right|_{\langle \vec{A} \rangle} \cdot (A_i(t+\tau) - \langle A_i \rangle) \right) \right. \\
&\quad \left. - \left(y(\langle \vec{A} \rangle) + \sum_{i=1}^{N} \left. \frac{\partial y}{\partial A_i} \right|_{\langle \vec{A} \rangle} \cdot (A_i(t) - \langle A_i \rangle) \right) \right]^2 \rangle \\
&= \frac{1}{2} \langle \left[\sum_{i=1}^{N} \left. \frac{\partial y}{\partial A_i} \right|_{\langle \vec{A} \rangle} \cdot (A_i(t+\tau) - A_i(t)) \right]^2 \rangle \\
&= \sum_{i=1}^{N} \left(\partial_{A_i} y\right)^2 \underbrace{\frac{1}{2} \langle (A_i(t+\tau) - A_i(t))^2 \rangle}_{\sigma^2_{A_i}} \\
&\quad + 2 \sum_{i \neq j}^{N} \left(\partial_{A_i} y\right) \left(\partial_{A_j} y\right) \underbrace{\frac{1}{2} \langle (A_i(t+\tau) - A_i(t)) \left(A_j(t+\tau) - A_j(t)\right) \rangle}_{\mathrm{GCov}\,(A_i, A_j)} .
\end{aligned} \tag{2.41}$$

Where in the second line lemma 1 was used. □

2.4 Monitoring of maser infrastructure

In the LTF facility, two masers are used to measure the performances of the less stable Rb frequency standards. The most stable standard is the iMaser 3000 [120]. Its frequency and long-term stability

are monitored thanks to a GNSS antenna and 1-way frequency comparison named common view [121]. The JPL Automatic Precise Positioning Service (APPS) allows to augment the accuracy on the position and clock estimates of a local oscillator. In our case, we use a PolaRx3e TR PRO GNSS receiver whose quartz is referenced to our maser. Indeed, the instantaneous estimation of those quantities depends on the orbit of the satellites in sight which are also estimated. It is hence possible to increase the accuracy on position and clock by using the measured positions whose accurate versions, named products [122] are delivered 10 days after the actual measurement. The mean frequency stability $\bar{y}(t)$ over the duration τ_0 is calculated by using [112]:

$$\bar{y}(t) = \frac{x(t+\tau_0) - x(t)}{\tau_0} \tag{2.42}$$

where $x(t)$ [s] is the phase of the local oscillator.

Figure 2.5 shows the relative frequency of the iMaser 3000 compared to the GNSS disciplined oscillator after final GNSS products correction from January 1st, 2018 to April 2023. Note that prior to January 2019, the maser frequency was manually tuned, which was last done on February 16th, 2018. The inaccuracy of the maser frequency increased up the 2.5×10^{-13} on December 18, 2018 before the ACT was turned on. Since then the relative deviation has returned to $\leq 2 \times 10^{-14}$.

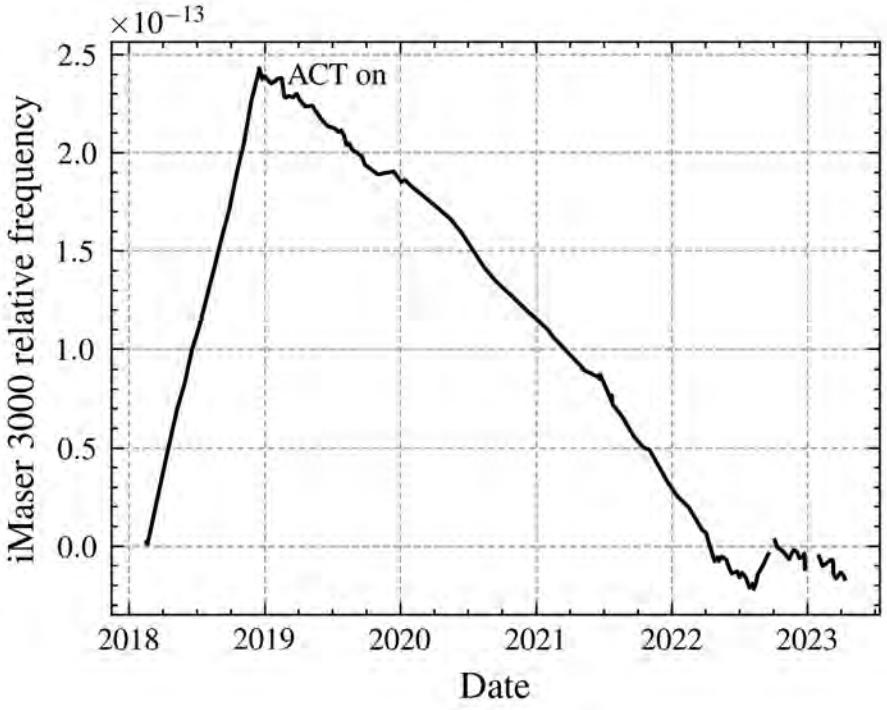

Figure 2.5: Relative frequency of the maser with respect to time. Courtesy of Dominique Schenker and Daniel Varidel.

Measurement of the maser frequency stability is shown on Figure 2.6, with ACT on and off for comparison. Note that the specification is very likely to be drift-removed. It is worth noting that the measured short-term stability is strongly degraded compared to the specification of the maser [120] with more than one order of magnitude degradation up to $\tau = 10^4$ s. Up to this integration time, the Allan deviation level is higher than that of the maser with $\sigma_y(\tau) = 4.3 \times 10^{-12}\tau^{-0.7}$ which is consistent with the stabilities of current GNSS-grade frequency standards used in satellites shown on Figure 1.2. Interestingly, the power law is in-between τ^{-1} and $\tau^{-1/2}$ behaviours which is still not explained. Since the on-board clocks are steered to the ground atomic clocks, the drift measured after $\tau = 10^5$ s are likely to be the maser. Indeed, the measurement (ACT on) is compatible with the drift of 2×10^{-16}/day advertised in the datasheet [120]. Furthermore, the plot shows the positive influence of the ACT, lowering the maser drift.

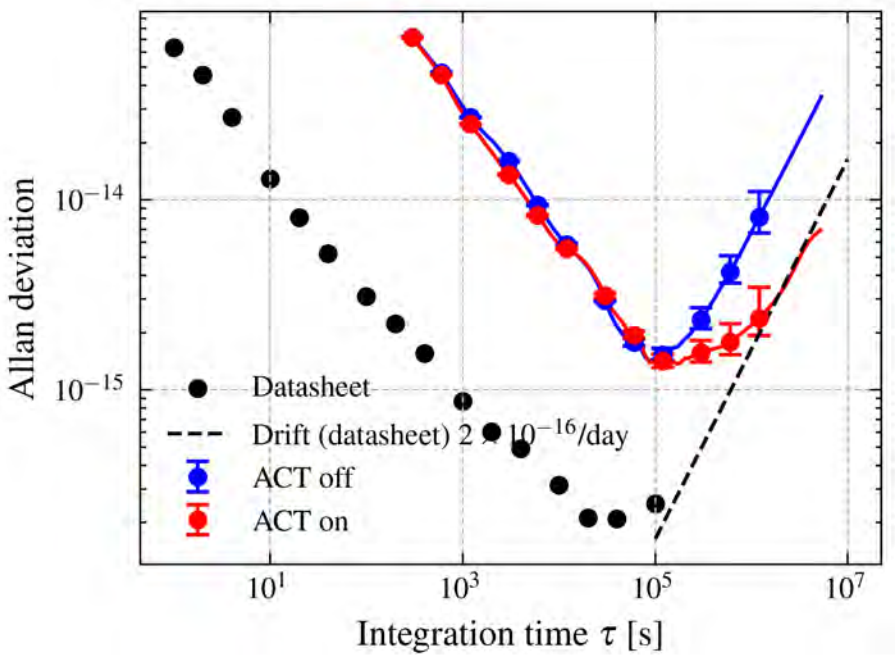

Figure 2.6: iM3000 relative frequency Allan deviation measured against the JPL time scale with ACT on and off.

The oscillations shown from $\tau = 6 \times 10^4$ s are attributed to boundary discontinuities [123].

2.5 Case study: measurement of a laser head stability in pulsed mode

We wish to conclude the chapter by illustrating how the stability of a laser head in pulsed mode can be measured. This study was necessary for correctly assessing the performances of the laser head used in the μPOP studies but also in the high-performance Rb clock studied by Moreno [99] and Almat [124].

2.5.1 Motivation

The question of measuring the frequency stability of a laser head in pulsed mode rather than in continuous mode was motivated by the following observation: each time the laser head AOM is switched on and off, the AOM undergoes a thermal cycle. Its influence on the ability to evaluate the relaxation rates of a Ramsey clock in a reasonable amount of time is discussed in chapter 3. Observation was made that when switching the AOM on, temporary supplementary cross-over peaks would appear in the sub-Doppler spectrum of the laser head. Given that in pulsed mode the AOM is switched on and off in the kHz range, it was important to evaluate whether this unwanted phenomenon could be a source of frequency stability degradation.

2.5.2 Method

The frequency of the laser head is measured by detecting the beat frequency between the Device Under Test (DUT) laser head frequency and a reference laser head operated in continuous mode. The beating signal is measured with a fast photodiode and a counter. Each time the AOM is driven, the counter is triggered, and stability is measured over a few 100 μs before the AOM is switched off again, providing hundreds of beating frequency samples per second of duration τ_C separated by a dead time T_C. The proper Allan deviation is calculated with $\tau_c = T_c$. This is illustrated on Figure 2.7.

Noise type	Power law exponent μ
Flicker and white PM	-1
White FM	$-1/2$
Flicker FM	0
Random walk FM	$1/2$
Frequency drift	1

Table 2.1: Noise types associated with the dominant power-law exponent μ [116].

Unfortunately, computing the Allan deviation using dead-time separated samples will lead to determination of a biased Allan deviation. The improper Allan deviation can be corrected for deadtime

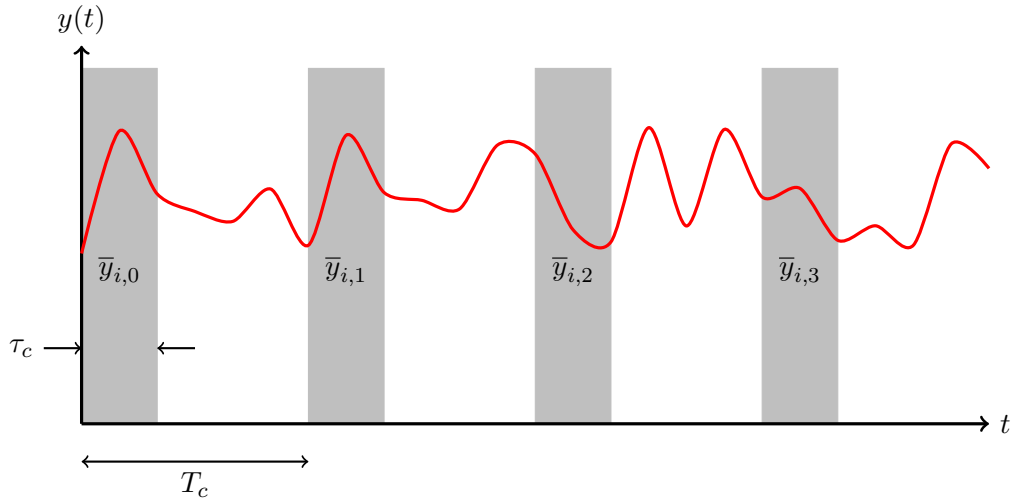

Figure 2.7: Measurement of relative frequency y with dead time. Samples of duration τ_c [s] are measured periodically with period T_c [s]. Proper Allan deviation is measured when $\tau_c = T_c$.

using bias functions defined in [112]. In particular, if:

$$\sigma_y(\tau) \propto \tau^{\mu}, \quad \mu = -2, -1, 0, 1 \tag{2.43}$$

with μ the dominant noise type (see Table 2.1), the deadtime and Allan measurement are linked by the following relation:

$$\sigma_y(M\tau_c)^2 = \frac{\sigma_y^2(2, M, MT_c, M\tau_c)}{B_2(r, \mu)B_3(2, M, r, \mu)} \tag{2.44}$$

with B_2 and B_3 two bias functions, M the number of samples used to calculate the mean frequency during the interval MT_c with effective up time $M\tau_c$ and $r = T_c/\tau_c$. $\sigma_y^2(2, M, MT_c, M\tau_c)$ is the two-sample variance calculated with the deadtime using the nominal Allan deviation estimators. In the experiment one takes 208 samples per seconds of duration $\tau_c = 400$ μs with $208 \cdot 400\mu s = 83$ ms effective integration time. Eq. (2.44) hence allows us to calculate the Allan deviation at $\tau = M\tau_c$ using the improper deviation calculated for $\tau' = MT_c$ with a correction factor depending on the two bias functions whose explicit forms can be found in [112]. Interestingly, the correction factor shown on eq. (2.44) is close to 1 in the case of higher order noise types ($\mu = 0, 1$) which means that no correction for long-term Allan deviations is required.

2.5.3 Results

In order to validate the method, we apply the procedure described above to two different signals. The first one is the one acquired by our DUT operated in Ramsey operation. The second is signal acquired by operating the same device in continuous mode but my mimicking the Ramsey operation using a switch between the photodiode and the counter. These two modes are presented on Figure 2.8.

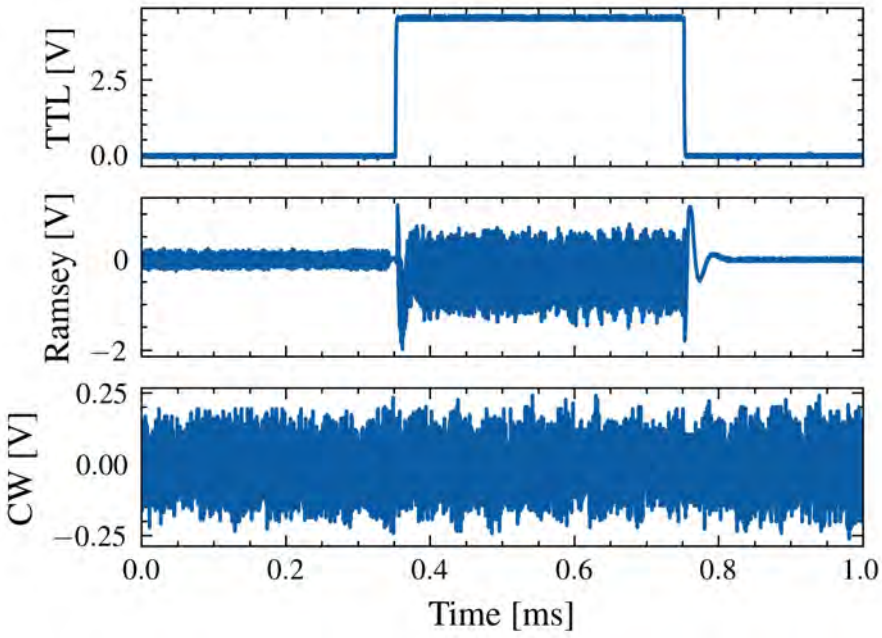

Figure 2.8: Signal shape on the photodiode in Ramsey and CW mode. In both cases the signal is gated with the TTL signal. The CW hence mimicks a Ramsey-type signal.

The Allan deviations are shown on Figure 2.9. Note that the deviations are not corrected according to eq. (2.44).

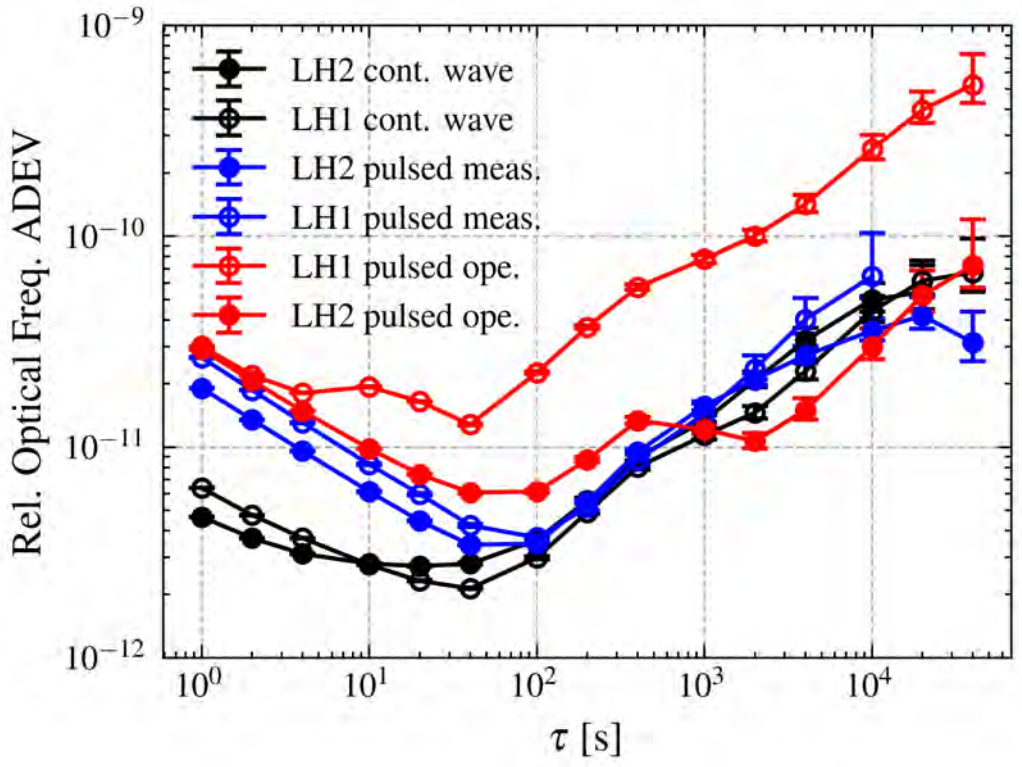

Figure 2.9: Allan deviations of two laser heads (LH1 and LH2) in continuous mode, pulsed (Ramsey) mode and pulsed measurement mode.

Two laser heads (LH1 and LH2) are considered with similar relative frequency stability in CW mode (LH1 and LH2 cont. wave). In CW mode with pulsed acquisition, the Allan deviations meet the pure CW deviations from $\tau = 100$s, confirming that the statistics only play a role in the short-term. This is explained qualitatively because a loss of samples will tend to overestimate white and brown noises which is not the case for long-term stability dominated by drift. In the long-term, it is clear that LH1 shows degraded performances compared to LH2. The reason was later attributed to the only difference between the two laser heads that respectively contain 1 and 2 optical isolators. In the first case, when the AOM enter thermal cycles in Ramsey mode, spurious back reflections enter the laser head internal vapor-cell and disturb the sub-Doppler signal used to lock the laser head frequency. This effected is cancelled when using a second optical isolator.

2.5.4 Conclusion

In this small study, it was shown that dead-time-sampled measurement tend to overestimate the Allan deviation in the short-term where an incomplete integration time will fail to average white and brown processes down. As one is usually concerned with long-term Allan deviations only, the correction can be neglected.
Finally, it was shown that the stability of our laser head is worse in pulsed compared than that of

continuous mode. This is a general statement, as demonstrated in chapter 3 when comparing the microwave power stability in continuous or pulsed mode. In general, stability of relevant quantities should always be measured in nominal operation mode, if possible.

High-Performance Pulsed Laser-Pumped Rb Clock for GNSS

Etienne Batori, Nil Almat, Christoph Affolderbach, Florian Gruet and Gaetano Mileti

University of Neuchâtel, Laboratoire Temps-Fréquence

Neuchâtel, SWITZERLAND

email: Gaetano.mileti@unine.ch

Abstract: *In this communication, we give an overview of the field of space atomic clocks and motivate the need for novel types of space atomic clocks, notably based on laser technology. We outline the development status of our pulsed laser-pumped Rb clock in view of combined state-of-the-art stability (~10^{-14} @ 1 day) and small volume (< 5L). The frequency and intensity stability of a custom made compact pulsed laser source is discussed in view of its implementation in the pulsed laser-pumped clock. Finally, we analyze spectral aging data for a DFB laser diode accumulated over several years and discuss new lines of atomic clock development.*

1. Introduction

Highly stable on-board atomic clocks form the essential backbone of Global Navigation Satellite Systems (GNSS), where fractional frequency instabilities of few 10^{-14} or better are required, for timescales ranging from few hours to one day. Such excellent stability performance can only be achieved by atomic clocks, in which the frequency of a quartz oscillator is tightly stabilized to an intrinsically stable atomic reference transition, thus improving its long-term stability by orders of magnitude. Most existing GNSS systems currently rely on lamp-pumped Rb clocks (RAFS), Cs atomic beam clocks, or passive H-maser (see section 2). However, it has been pointed out that the performance of RAFS-type atomic clocks can be significantly enhanced by the implementation of laser optical pumping, such as to meet the superior stability performance of the much bigger (≈ 15-28 liters volume) passive H-maser [1], [2] of few 10^{-15} at 1 day timescales, but from a much more compact RAFS clock outlines (≈ 3-5 liters volume) [2], [3].

Here we report on our recent studies and advances towards such compact and high-performance laser-pumped Rb clocks for GNSS applications, notably in view of a compact clock realization and the identification of physical performance limitations. In section 2, we first give a short overview of atomic clock technologies used in current GNSS applications. In section 3, we describe the development of our pulsed laser-pumped Rubidium (Rb) clock. Finally, in section 4 we give an overview of our laser spectral aging studies, analyzing data accumulated over several years.

2. Clocks for GNSS

As of today, there are 4 GNSSs, namely the American Global Positioning System (GPS), the Chinese BeiDou, the Russian GLONASS and the European GALILEO [4]. Other systems make use of GNSS-grade clocks such as GNSS augmentation systems (e.g. the Japanese Quasi-Zenith Satellite System (QZSS) and the Indian Regional Navigation Satellite System (IRNSS)) or

978-3-944976-28-0

defense satellite systems such as the American Advanced Extremely High Frequency (AEHF) system. In [5], we updated the previous [6] status on GNSS systems and emerging new clock technologies.

Clocks for GNSS need to meet stringent technical and stability requirements. The technical requirements emerge from the in-space operation of the clocks. Low mass, low volume, and low power consumption are required, as well as resilience to the space environment (e. g. radiation hardness), which can result in a reduced clock's stability compared to instruments for on-ground applications. The clock stability requirements are given by the need for sufficiently stable frequency references on long-term timescales (a few hours to one day, depending on the system's satellite updating time) to guarantee the required position's accuracy.

Typical modern GNSSs stability requirements and clock performances in terms of Allan deviation (ADEV) fall in the 10^{-13} to 10^{-12} range at one second (short term stability) and in the 10^{-14} to 10^{-13} range at one day (long term stability), as shown in Fig. 1. A typical system requirement is 10^{-14} on timescales from 10^4 seconds to one day.

Fig. 2 shows the number of GNSS-grade clocks launched into space over the past decades. Until 2009, most clocks were either lamp-pumped Rb Atomic Frequency Standards or atomic cesium beams, with a few exceptions for science experiments featuring H-masers [7]. From 2009, passive H-masers appear on GNSS satellites within the GALILEO and BeiDou constellations.

As of 30.06.2020, almost all GNSS clocks belong to the three classical technologies for atomic frequency standards for on-ground operation [5], namely the RAFS, the passive H-maser and the Cs atomic beam (with magnetic state selection). We respectively counted 514, 126 and 392 of each. To our knowledge, only two non-classical GNSS-grade clocks were sent into orbit so far, the Jet Propulsion Laboratory (JPL) mercury trapped ion ($^{199}Hg^{+}$) frequency standard [8] and the Chinese Rb Cold Atom Clock (CAC) [9]. In total, we estimated that at least 1034 GNSS-grade clocks have been sent into orbit so far, more than twice the number given in 2006

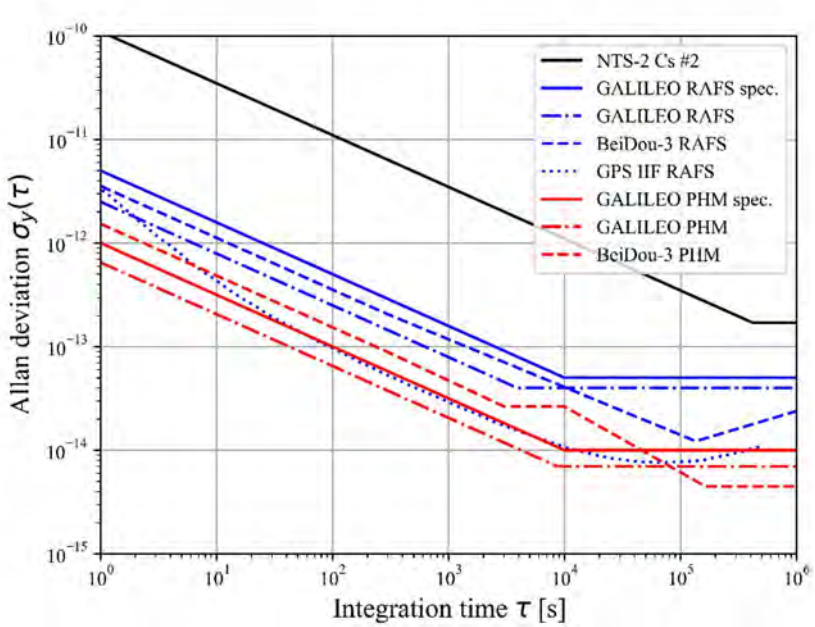

Figure 1. Typical GNSS clock stability requirements and selected clock performances, in terms of Allan deviation. GPS IIF RAFS data from [22]. For other data references see [5].

[6]. This number will increase in the future, as satellites have a limited life-span and must be replaced. Furthermore, new types of atomic clocks may be expected to be launched into space.

The pulsed laser-pumped Rb clock presented in the following section is one of these new clock candidates for future GNSS on-board clocks. In Fig. 3 we show the expected short-term and long-term stability goals for this clock, as compared to the performances of other commercial clock realizations, as a function of the instrument's size, weight, and power (SWaP). For simplicity, here SWaP is expressed as one single parameter calculated as the instrument volume · mass · power consumption (in units of liters · kg · W). The pulsed laser-pumped Rb clock can show attractive GNSS-grade performances, at very low SWaP.

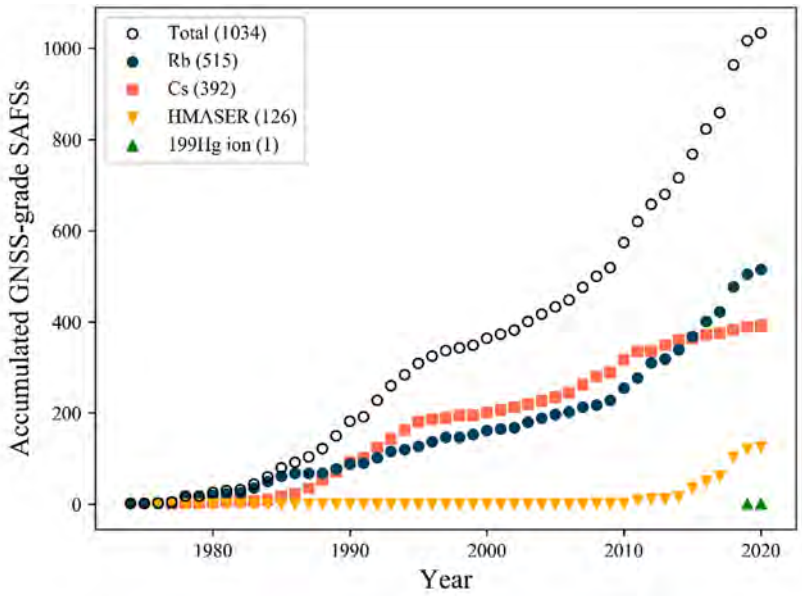

Figure 2. Estimated accumulated number of atomic clocks sent into space, by reference atomic species, as of June 30, 2020. Only clocks of GNSS-grade performance or better are considered. Figure adapted from [5].

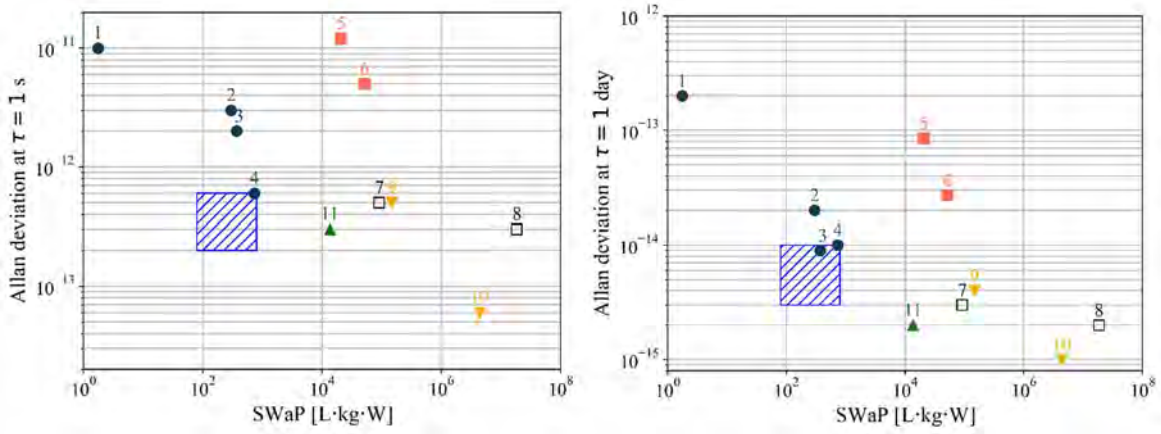

Figure 3. frequency stability of various atomic clocks against the SWaP parameter (see text). **Left**: short-term stability. **Right**: long-term stability. Blue area: performance goals for the pulsed laser-pumped Rb clock [10], see section 3. Symbols (same as in Fig. 2): Commercial and space clocks. 1 and 2: Spectratime space mini RAFS [11] and space RAFS [12], 3: Excelitas space RAFS [13], 4: FEI space RAFS [14], 5: Oscilloquartz Cs beam [15], 6: Microsemi Cs beam [16], 7: SDI cold Rb clock [17], 8: Muquans cold Rb clock [18], 9: T4Science PHM [19], 10: T4Science AHM [20]. 11 : JPL Hg ion clock [8].

3. Pulsed laser-pumped Rb clock development

It has been shown that the use of laser optical pumping in Rb clocks allows for improved clock stabilities compared to traditional lamp-pumped RAFS [3], [21]. Combined with a Ramsey interrogation scheme realized in the pulsed optical pumping (POP) approach (Fig. 4), performances similar to the H-maser can be reached, at lower volume and weight, without greatly altering the traditional lamp RAFS's design [22], [23]. Today, development efforts in this direction are active in Italy [24], our Swiss group [10], in China [25] as well as in industry [26].

Our pulsed laser-pumped Rb clock development is based on a highly compact core Physics Package (PP), based on a compact magnetron-type microwave resonator, originally developed for a continuous-wave (CW) Rb clock [27]. This microwave resonator allows obtaining a highly homogeneous microwave field across the 25 mm diameter Rb vapor cell while maintaining a cavity volume 3-5 times smaller than for a simple fundamental-mode cavity. The clock's block scheme is given in Fig. 4, detailing the main clock parts of the core PP with the microwave resonator (in black), the frequency-stabilized laser source (in red), and the microwave synthesizer and control loop for interrogating the atomic reference transition at 6.8 GHz and stabilizing the quartz oscillator (in blue). With respect to our previous CW-mode clock [27], the pulsed clock requires only little additional functionalities shown on light-blue background: an acousto-optic modulator (AOM) serving as optical switch and some synchronization electronics. The latter allows realizing the pulsed Ramsey-type interrogation sequence, such that the optical and microwave fields are applied separated in time. In this way, clock instabilities due to the light-shift effect are avoided and the clock stability is improved.

The measured clock stability is shown in Fig. 5. The current clock instability reaches $< 2 \cdot 10^{-14}$ at timescales of few hours to one day, comparable to GALILEO and BeiDou-3 passive H-maser performances. A summary of the main sources of long-term instability is given in Table 1, where the listed clock sensitivities are understood to apply to the Rb atoms in the vapor cell serving as reference (as opposed to system-level sensitivities applying to the overall clock).

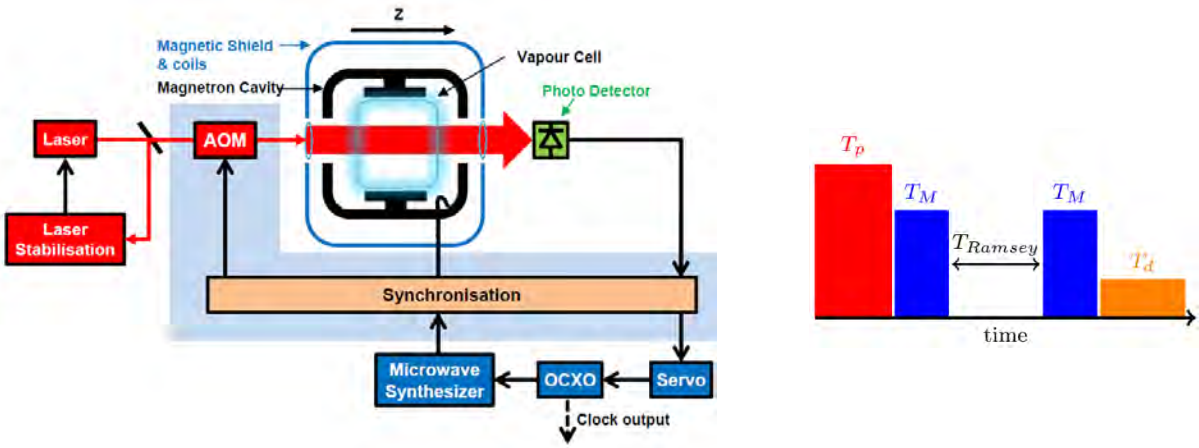

Figure 4. **Left**: Clock schematics. OCXO: oven-controlled quartz oscillator. **Right:** pulsed Ramsey interrogation sequence. *Red:* optical pumping pulse, typical duration $T_p = 0.4$ ms, *Blue:* microwave pulse, $T_M = 0.3$ ms, *Orange:* optical detection, $T_d = 0.7$ ms. *Ramsey time* $T_{Ramsey} = 3$ ms.

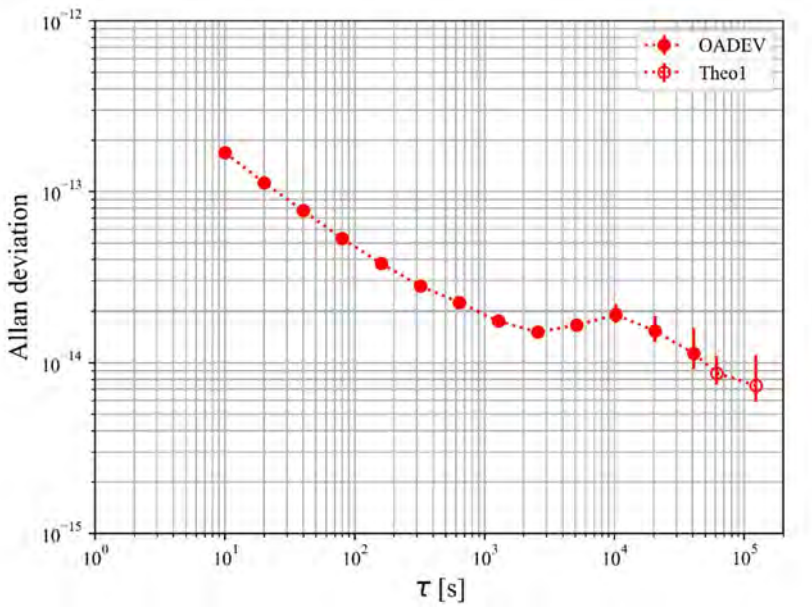

Figure 5. pulsed Rb clock stability. OADEV: overlapping Allan deviation. Theo1: theo1 variance estimation. The data are taken from [10].

In order to assess in more detail the impact of the laser source's characteristics on the long-term clock stability, we measured the stabilities of the optical pump intensity (no active intensity stabilization applied) and the laser frequency of the laser head used, when operated in pulsed mode, see Fig. 6.

First, as predicted by the formalism of [28], we note that the measurement dead times (≈ 90 %) result in an overestimation of the short-term frequency stability (timescales of 10^0 to 10^2 s), whereas they have no statistical impact on the estimation of the long-term stability. This is in particular seen in the frequency stability data of Fig. 6, by comparing the data measured in pulsed mode (black circles) to the one recorded in cw operation but pulsed measurement during the optical pumping phase only (blue circles). Similar observations hold for the optical intensity stability.

Table 1. Long-term clock instability budget for $10^4 < \tau < 10^5$ s adapted from [10]. The frequency and intensity light-shift contributions are updated using the measured laser stabilities from Fig. 6.

Physical effect	Relative sensitivity coefficient	Clock instability contribution σ_y ($10^4 < \tau < 10^5$ s)
Barometric	$6.6 \cdot 10^{-14}$ /hPa	$2.0 \cdot 10^{-15}$
Microwave-power shift	$4.0 \cdot 10^{-13}$ /μW	$6.0 \cdot 10^{-15}$
Intensity light shift	$2.3 \cdot 10^{-14}$ /%	$1.8 \cdot 10^{-14}$
Frequency light shift	$1.5 \cdot 10^{-13}$ /MHz	$4.0 \cdot 10^{-15}$
Second-order Zeeman shift	$5.8 \cdot 10^{-5}$ /T	$1.2 \cdot 10^{-15}$
Buffer-gas shift – cell temperature	$2.3 \cdot 10^{-12}$ /K	$1.2 \cdot 10^{-15}$
Total clock instability, $[\sum_i \sigma_i^2]^{1/2}$		$2.0 \cdot 10^{-14}$

Second, a degradation of the long-term optical frequency stability was found, for the laser head operating in pulsed Ramsey mode. The origin of this degradation lies in spurious optical back reflections in the laser head, that perturbed the atomic reference signal used for laser stabilization. This feature was suppressed in an optimized laser head that reestablished the superior frequency stability found in cw operation, even when operated in Ramsey mode (filled red circles).

The clock's sensitivity to variations of the optical frequency and intensity (Table 1) was assessed in [10]. Although the measurements were not simultaneous, the estimation of the clock's long-term stability according to Table 1 using our recent laser stability measurements (Fig. 6) is compatible with the actual clock's stability (Fig. 5). We note that the biggest long-term instability contribution currently arises from the optical intensity fluctuations, that can be reduced by implementing an active stabilization loop, e. g. acting on the AOM drive. Similarly, the instability contribution from the frequency light-shift can be reduced by using the optimized laser head.

Finally, the pulsed interrogation scheme presented here for high-performance clocks based on cm-scale Rb vapor cells can advantageously also be applied to other types of atomic reference samples, thus giving rise to new types of atomic clocks. On one hand, the recent demonstration of simplified and highly compact cold atom systems based on diffraction gratings opens the way for the development of a novel GNSS-grade clock type [29]. Replacing the Rb cell of our clock with such compact cold atom samples is expected to lead to further improved long-term stability and possibly absolute frequency accuracy, with beneficial impact for GNSS systems. On the other hand, the pulsed interrogation scheme can also be applied to miniature and "chip-scale" atomic clocks based on mm-scale micro-fabricated vapor cells [30]. In this way, the currently typical long-term stability performance at 10^{-11} level of miniature atomic clocks could be improved by at least one order of magnitude towards the 10^{-12} level, with new application potentials for such miniature devices.

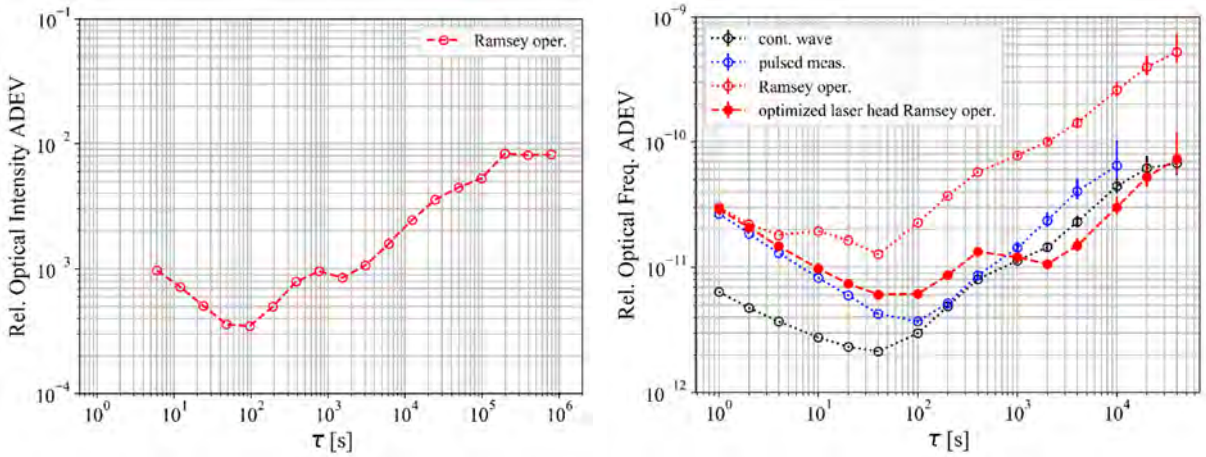

Figure 6. **Left:** optical intensity stability. The measurement is realized in pulsed operation. **Right:** optical frequency stability. *Cont. wave:* the laser head is operated in cw mode. *Pulsed meas.:* The laser head is operated in cw mode, but data are acquired with dead times equivalent to the Ramsey cycle. *Ramsey oper.:* The laser head is operated in Ramsey cycle.

4. Laser spectral aging studies

Laser diodes are known to show aging effects, and a slow degradation of their spectral properties due to device aging may impact the atomic clocks' performances. In order to establish the reliability of the final product as well as its application, it is therefore of importance to estimate the variation over time of these properties. Our study focuses on the long-term variations of the laser's injection current needed to reach the exact optical frequency of the Rb D2 transition, termed the current at resonance, and thus estimate its impact on the clock frequency drift.

The measurement setup is fully automated and consists in scanning the laser wavelength through the Rb D2 transition line, detected in a home-made evacuated Rb cell. With the laser chip's temperature held constant, analysis of the recorded spectra allows to determine the current at resonance. The laser is continuously running and a wavelength scan occurs every three hours. Another scan is also performed every three hours to measure the evolution of the threshold current.

The first data of this type was reported in [31] for a commercial distributed-feedback (DFB) diode laser, and showed an aging of the current at resonance of - 45 µA/month. In 2017 the experiment was restarted using the same DFB device, but with a slightly different laser operating point close to the Rb D2 transition wavelength. After almost three years of continuous operation, the experiment is still ongoing and the aging of the current at resonance is now of - 234 µA/month with a relatively good linearity, however slightly decreasing since the value reported in [32] of - 283 µA/month. The threshold current measurement during the same period shows an increase from 42.5 mA to 49.7 mA, with an accelerating trend, distinctly indicating an aging of the sample.

In order to keep the laser at the Rb D2 wavelength throughout a desired clock lifetime of 20 years, and according to the current and temperature tuning coefficients of the laser, the laser's temperature should be adjusted by 2.7 K leading to an optical power change of 1.8%. If we consider a clock intensity light-shift of 2.5×10^{-14}/% [10], the relative clock frequency drift arising from this process would then amount to 5.1×10^{-16}/month, which is clearly acceptable for a GNSS-grade clock.

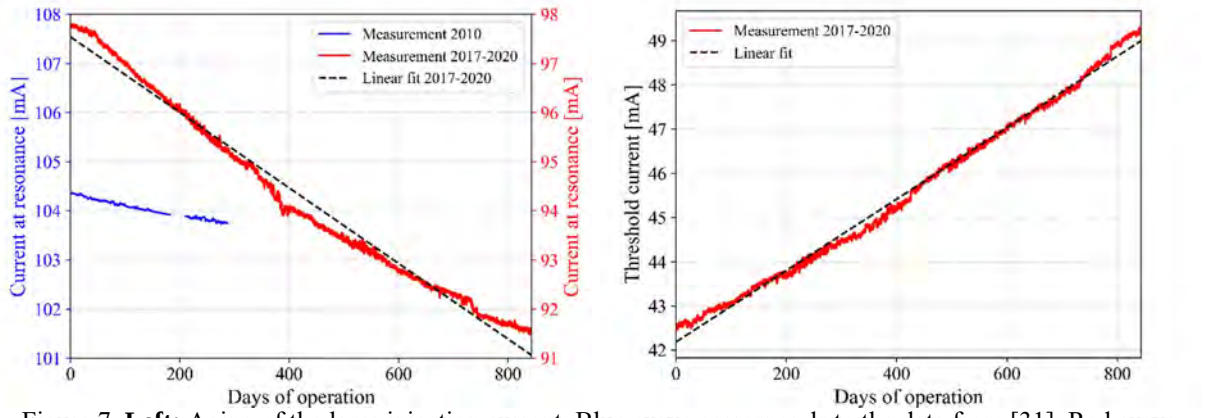

Figure 7. **Left:** Aging of the laser injection current. Blue curve corresponds to the data from [31]. Red curve corresponds to 2017-2020 measurement, with a slightly different laser operating point. **Right:** Aging of the threshold current during the period 2017-2020, for the same laser sample as left.

5. Conclusions

We reviewed the status of GNSS-grade atomic clocks sent into space since 1974 and counted a total of at least 1034 clocks, underlining the importance of this technology for all GNSS systems. Despite the growing number of clocks, we note only few changes in the core GNSS clock technologies.

The pulsed laser-pumped Rb clock is a promising candidate for future on-board GNSS clocks, addressing the challenge of high-performance clock stability with reduced weight, volume and power. Our laboratory pulsed laser-pumped Rb clock under development already shows stability performances on the same order as the GNSS passive H-masers. The clock's long-term stability reaches $< 2 \cdot 10^{-14}$ at timescales around one day, in good agreement with the instability budget that was updated for the frequency and intensity light-shift contributions, based on laser stability data measured in pulsed operation. Strategies for further improvement of the long-term clock stability were identified. We are also studying the application of the same pulsed interrogation scheme to other atomic references such as compact cold atom systems and micro-fabricated Rb cells, in view of further improved GNSS-grade or miniature atomic clocks for various applications, including GNSS, telecommunication, and others.

We finally addressed the question of long-term aging of the laser spectral properties, measuring the aging of the current at resonance for a DFB laser diode during more than 2 years. By extrapolating the data we find that an atomic clock using such lasers could operate during 20 years without noticeable incidence of the laser aging on the clock stability.

Acknowledgments

This work was supported by the University of Neuchâtel, the Swiss Space Center (UppMAC project 0720_MR_001_SSC01_00), the European Space Agency ESA (ESTEC contracts 4000129974 and 4000131046), and by the European Union's Horizon 2020 Research and Innovation Program through Quantum Technology Flagship (project macQsimal, grant 820393).

References

[1] P. Rochat *et al.*, "The onboard galileo rubidium and passive maser: status and performance," in *Proceedings of the 2005 IEEE International Frequency Control Symposium and Exposition, 2005.*, 2005, pp. 26–32, doi: 10.1109/FREQ.2005.1573898.

[2] P. Rochat, "Atomic Clocks Technologies for GALILEO & Related Applications," in *13th Annual PNT Symposium*, 2019.

[3] C. Affolderbach, F. Droz, and G. Mileti, "Experimental demonstration of a compact and high-performance laser-pumped Rubidium gas cell atomic frequency standard," *IEEE Trans. Instrum. Meas.*, vol. 55, no. 2, pp. 429–435, Apr. 2006, doi: 10.1109/TIM.2006.870331.

[4] P. Teunissen and O. Montenbruck, Eds., *Springer Handbook of Global Navigation Satellite Systems*. Cham, CH: Springer International Publishing, 2017.

[5] E. Batori, N. Almat, C. Affolderbach, and G. Mileti, "GNSS-grade Space Atomic Frequency Standards: Current Status and Ongoing Developments," *Adv. Sp. Res.*, Sep. 2020, doi: 10.1016/j.asr.2020.09.012.

[6] L. A. Mallette, P. Rochat, and J. White, "Historical review of atomic frequency standards used in space systems-10 year update," in *38th Annual Precise Time and Time Interval (PTTI) Systems and Applications Meeting*, 2006, pp. 69–80.

[7] R. F. C. Vessot *et al.*, "Test of relativistic gravitation with a space-borne hydrogen maser," *Phys. Rev. Lett.*, vol. 45, no. 26, pp. 2081–2084, Dec. 1980, doi: 10.1103/PhysRevLett.45.2081.

[8] E. A. Burt, L. Yi, B. Tucker, R. Hamell, and R. L. Tjoelker, "JPL Ultrastable Trapped Ion Atomic Frequency Standards," *IEEE Trans. Ultrason. Ferroelectr. Freq. Control*, vol. 63, no. 7, pp. 1013–1021, 2016, doi: 10.1109/TUFFC.2016.2572701.

[9] L. Liu *et al.*, "In-orbit operation of an atomic clock based on laser-cooled 87 Rb atoms," *Nat. Commun.*, vol. 9, no. 1, 2018, doi: https://doi.org/10.1038/s41467-018-05219-z.

[10] N. Almat, M. Gharavipour, W. Moreno, F. Gruet, C. Affolderbach, and G. Mileti, "Long-term stability analysis toward $<10^{-14}$ level for a highly compact POP Rb cell atomic clock," *IEEE Trans. Ultrason. Ferroelectr. Freq. Control*, vol. 67, no. 1, pp. 207–216, 2020, doi: 10.1109/TUFFC.2019.2940903.

[11] Spectratime, "iSpace+^{TM} Space-Qualified miniRAFS." [Online]. Available: https://www.spectratime.com/sites/default/files/document-files/iSpace_miniRAFS_Spec.pdf.

[12] Spectratime, "iSpace+^{TM} Space-Qualified RAFS." [Online]. Available: https://www.spectratime.com/uploads/documents/ispace/iSpace_RAFS_Spec.pdf.

[13] Excelitas, "High-Performance Space-Qualified Rubidium Atomic Frequency Standard." [Online]. Available: https://www.excelitas.com/product/space-qualified-rubidium-atomic-frequency-standard-clocks.

[14] FEI, "FEI' s Next-Generation Rubidium Atomic Frequency Standard For Space Applications," New York, USA, 2013. Accessed: Mar. 30, 2020. [Online]. Available: https://freqelec.com/wp-content/uploads/2019/03/4-RAFS-Brochure.pdf.

[15] Oscilloquartz, "OSA 3235B Cesium Clock." [Online]. Available: https://www.oscilloquartz.com/en/products-and-services/cesium-clocks/osa-3230-series.

[16] Microsemi, "5071A Primary Frequency Standard." [Online]. Available: https://www.microsemi.com/document-portal/doc_download/133269-5071a-datasheet.

[17] SpectraDynamics, "cRb-Clock." [Online]. Available: https://spectradynamics.com/product-sheets/cRb-Clock-2019.pdf.

[18] MuQuans, "MuClock: A high-performance frequency standard based on cold atoms," 2019. https://www.muquans.com/wp-content/uploads/2019/03/muquans_muclock.pdf (accessed Apr. 30, 2020).

[19] T4Science, "pHMaser 1008 Passive Hydrogen Maser Clock." [Online]. Available: https://www.t4science.com/products/phmaser-1008/.

[20] T4Science, "iMaser 3000 Smart Active Hydrogen Maser Clock." [Online]. Available: https://www.t4science.com/products/imaser3000/.

[21] G. Mileti, J. Deng, F. L. Walls, D. A. Jennings, and R. E. Drullinger, "Laser-pumped rubidium frequency standards: New analysis and progress," *IEEE J. Quantum Electron.*, vol. 34, no. 2, pp. 233–237, Feb. 1998, doi: 10.1109/3.658700.

[22] J. C. Camparo, T. U. Driskell, and A. F. S. Command, "The mercury-ion clock and the pulsed-laser rubidium clock: Near-term candidates for future GPS deployment," *Aerosp. Rep. NO. TOR-2015-03893S*, 2015.

[23] S. Micalizio *et al.*, "The pulsed optically pumped Rb frequency standard: A proposal for a space atomic clock," in *2015 IEEE Metrology for Aerospace (MetroAeroSpace)*, 2015, pp. 384–388, doi: 10.1109/MetroAeroSpace.2015.7180687.

[24] S. Micalizio, C. E. Calosso, A. Godone, and F. Levi, “Metrological characterization of the pulsed Rb clock with optical detection,” *Metrologia*, vol. 49, no. 4, pp. 425–436, 2012, doi: 10.1088/0026-1394/49/4/425.
[25] G. Dong, J. Deng, J. Lin, S. Zhang, H. Lin, and Y. Wang, “Recent improvements on the pulsed optically pumped rubidium clock at {SIOM},” *Chin. Opt. Lett.*, vol. 15, no. 4, p. 40201, 2017, doi: 10.3788/COL201715.040201.
[26] P. Arpesi *et al.*, “Rubidium Pulsed Optically Pumped Clock for Space Industry,” *IFCS/EFTF 2019 - Jt. Conf. IEEE Int. Freq. Control Symp. Eur. Freq. Time Forum, Proc.*, vol. 2, pp. 1–3, 2019, doi: 10.1109/FCS.2019.8856140.
[27] T. Bandi, C. Affolderbach, C. Stefanucci, F. Merli, A. K. Skrivervik, and G. Mileti, “Compact high-performance continuous-wave double-resonance rubidium standard with $1.4 \times 10^{-13}\ \tau^{-1/2}$ stability,” *IEEE Trans. Ultrason. Ferroelectr. Freq. Control*, vol. 61, no. 11, pp. 1769–1778, 2014, doi: 10.1109/TUFFC.2013.005955.
[28] J. A. Barnes and D. W. Allan, “Variances based on data with dead time between the measurements,” in *Proceedings of the 19th Annual Precise Time and Time Interval Systems and Applications Meeting*, 1989, pp. 227–234.
[29] R. Elvin *et al.*, “Cold-atom clock based on a diffractive optic,” *Opt. Express*, vol. 27, no. 26, p. 38359, 2019, doi: 10.1364/oe.378632.
[30] J. Kitching, “Chip-scale atomic devices,” *Appl. Phys. Rev.*, vol. 5, no. 3, p. 31302, 2018, doi: 10.1063/1.5026238.
[31] R. Matthey, C. Affolderbach, and G. Mileti, “Methods and evaluation of frequency aging in distributed-feedback laser diodes for rubidium atomic clocks,” *Opt. Lett.*, vol. 36, no. 17, pp. 3311–3313, 2011.
[32] C. Affolderbach *et al.*, “Selected Studies on High Performance Laser-Pumped Rubidium Atomic Clocks,” in *2018 IEEE International Frequency Control Symposium (IFCS)*, 2018, pp. 1–6, doi: 10.1109/FCS.2018.8597452.

Chapter 3

μPOP clock

The μPOP clock is the first demonstration of DR Ramsey-type operation in a miniature micro-fabricated vapor-cell. Indeed, the low vapor-cell volume implies important relaxation rates which potentially limit the Ramsey time to the extend where Ramsey operation is not feasible. The μPOP studies do not only show the feasibility of this approach but also demonstrate state-of-the-art performances for DR miniature-cell clocks. The feasibility, state-of-the-art performances and short-term optimization are shown in the peer-reviewed article [1] that is included on the following pages.

This chapter furthermore contains supplementary material on the μPOP demonstration as well as two relevant non-published studies. The first one is the full long-term stability budget showing limited contribution of the light shifts to the clock stability and demonstrating that the limiting factor is the position shift. Finally, a fast and reliable technique for measuring the relaxation rates, the fundamental parameters limiting the Ramsey operation, is demonstrated.The first subject has been presented at PTTI 2022 and EFTF-IFCS 2022 as presentations whereas the latter was presented in a poster session at EFTF-IFCS 2022.

μPOP Clock: A Microcell Atomic Clock Based on a Double-Resonance Ramsey Scheme

Etienne Batori,[1,*] Christoph Affolderbach,[1] Matthieu Pellaton,[1] Florian Gruet,[1] Maddalena Violetti,[2,3] Yuanyan Su,[2] Anja K. Skrivervik,[2] and Gaetano Mileti[1]

[1] *University of Neuchâtel, Institute of Physics, Laboratoire Temps-Fréquence, Avenue de Bellevaux 51, 2000 Neuchâtel, Switzerland*

[2] *École Polytechnique Fédérale de Lausanne, Microwave and Antenna Group (MAG), SCI-STI-AS, Station 11, 1015 Lausanne, Switzerland*

[3] *Fondazione Toscana Life Sciences, Via Fiorentina 1, 53100 Siena, Italy*

(Received 4 April 2022; revised 2 September 2022; accepted 26 September 2022; published 14 November 2022)

We demonstrate and study a microcell microwave atomic clock based on optical-microwave double resonance (DR) interrogation operated in a pulsed Ramsey scheme, called the μPOP clock, based on a microfabricated Rb vapor cell and a micro-loop-gap microwave resonator. For the mm-scale dimensions of this cell, the population and coherence relaxation rates of the Rb clock transition are on the order of 4–5 kHz, which puts constraints on the useful Ramsey times and overall pulse sequence in view of optimized clock performance. Our proof-of-principle demonstration of the μPOP clock shows that the pulsed DR approach is nevertheless feasible and results in a short-term clock stability of $1 \times 10^{-11}\ \tau^{-1/2}$ and reaching the $\leq 2 \times 10^{-12}$ level at timescales of 1000 s to one day. The short-term instability budget established for the μPOP clock shows that the main limitation to the short-term stability arises from the detection noise. Thanks to the pulsed Ramsey scheme, light-shift effects are strongly reduced in the μPOP clock, which opens perspectives for further improvements of long-term clock stability, in view of future generations of miniature vapor-cell clocks with enhanced performances based on the DR scheme.

DOI: 10.1103/PhysRevApplied.18.054039

I. INTRODUCTION

Since their initial laboratory demonstration roughly 20 years ago, miniature or "chip-scale atomic clocks" (CSACs) [1,2] have retained a high level of interest and research activities. Key performance specifications of such CSAC realizations are a small volume (<15 mm^3), low power consumption (<120 mW), and a frequency instability of few $10^{-10}\ \tau^{-1/2}$ and around 1×10^{-11} at one day. With this, CSACs are of high interest for applications in telecommunication networks [3], remote or distributed sensor arrays, such as for ocean bottom seismology [4], and for improved Global Navigation Satellite Systems (GNSS) receivers [5].

Such CSACs exploit the ground-state microwave reference transition in alkali atoms contained in a microfabricated vapor cell [6]. This reference can conveniently be detected using coherent population trapping spectroscopy (CPT) [7] using a vertical-cavity surface-emitting laser (VCSEL) directly modulated at the microwave transition frequency [8]. The CPT approach allows extreme miniaturization and low power consumption, but also comes with drawbacks of small signal contrasts (1% level) and is particularly sensitive to light-shift effects [9,10] that limit the long-term stability, which is one of the key specifications of interest for an atomic clock.

Pulsed CPT interrogation in the Ramsey scheme [11,12] allows for narrower linewidth and reduced light-shift effects, as studied on cm-scale hot atomic vapor cells [13–17] and laser-cooled atomic samples [18]. Recently, pulsed CPT schemes were also studied for application to microfabricated vapor cells and clocks demonstrating short-term clock stabilities around 4 to 9×10^{-11} at one second. The medium-term clock stability reached 4×10^{-12} at 10^4 s, constituting a factor of 20 improvement

*etienne.batori@unine.ch

compared to the same clock in cw operation, corresponding to similarly reduced light-shift effects [14,19].

In contrast to CPT, the "classical" optical-microwave double-resonance (DR) clock approach [20] uses direct coupling of the microwave radiation to the atomic sample, and has some distinct advantages. Notably, Ramsey-mode DR-based clocks using cm-scale vapor cells achieve signal contrasts of $C = 20$–30% or more, resulting in excellent short-term clock stabilities of few $10^{-13}\ \tau^{-1/2}$ and state-of-the-art long-term stabilities on the level of 1×10^{-14} or better at one day [21–24], with small instability contributions from light-shift effects [25,26]. It was quantified that in these Ramsey-mode DR clocks the long-term instability contribution due to light-shift effects is reduced by at least one order of magnitude or more, compared to an optimized cw DR clock [27]. It may thus be expected that applying the Ramsey DR scheme to miniature atomic clocks can overcome the present limitations in such clocks, including CPT-based CSAC, towards long-term stabilities on the level of 10^{-12} or better at timescales of one day and beyond.

Early studies on a cw DR microcell atomic clock with a short-term stability of $2 \times 10^{-11}\ \tau^{-1/2}$ were reported in Ref. [28] and demonstrated the competitiveness of this approach. However, the possible advantages of Ramsey-mode operation of a DR microcell clock have not been studied yet.

In the present work, we investigate the μPOP clock, using a Ramsey-mode DR scheme applied to a microfabricated vapor cell. This scheme allows for a strong suppression of light-shift effects compared to cw operation and bears high potential for improved long-term clock stability to the 10^{-12} level at a few hours to one day timescales, thus outperforming current CSAC long-term stability.

II. EXPERIMENTAL APPROACH

In ^{87}Rb atomic clocks, the $\nu_0 \approx 6.8347$-GHz ground-state microwave transition $5S_{1/2}, |F = 1, m_F = 0\rangle \leftrightarrow |F = 2, m_F = 0\rangle$ serves as stable atomic reference [see Fig. 1(a)]. The microwave transition is enhanced and detected using a light field, such as the 780.24-nm D2-line transition, coupling one of the ground states to an excited state [20]. In the pulsed Ramsey-mode DR scheme (also referred to as POP clock) we apply a series of distinct interrogation steps to the atomic sample held in the microcell, separated in time [see Fig. 1(b)]. First, a strong optical pump pulse (duration t_p) accumulates the atomic ground-state population into one single state. Then, two microwave $\pi/2$ pulses (duration t_m), separated by a Ramsey time T_R, drive the atomic ground-state transition. Finally, the atomic transition probability is read out with a weak optical detection pulse (duration t_d) and the signal is constituted by the absorption of the detection pulse by the atomic vapor, detected on a photodetector placed behind the cell.

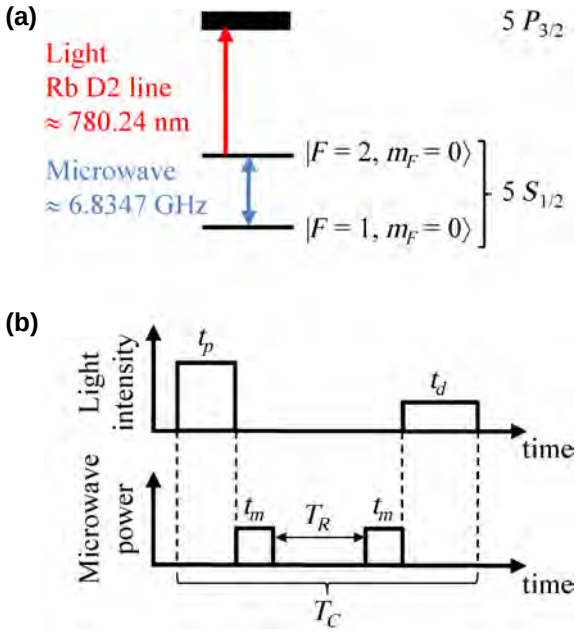

FIG. 1. (a) Rb level scheme. (b) Optical and microwave pulse sequence for the Ramsey scheme.

The experimental setup used in this study is schematically presented in Fig. 2 and described in more detail in the following sections. The microfabricated Rb cell is placed in a miniature microwave resonator, the micro-loop-gap resonator (μLGR) [29], see Sec. II A. Light pulses are generated by a custom-made stabilized laser head, see Sec. II B. The microwave signal is provided by a low-noise microwave synthesizer, piloted by a state machine that also controls the clock PI loop.

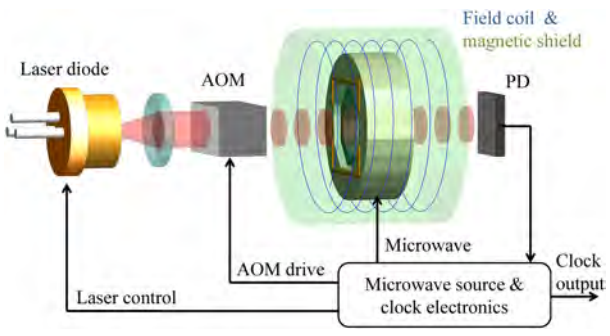

FIG. 2. Schematics of the μPOP clock setup. The microcell is held inside the μLGR resonator, the whole surrounded by field coils and a magnetic shield. 780-nm light from a laser diode is switched using an acousto-optical modulator (AOM). A photodetector (PD) detects the optical signal.

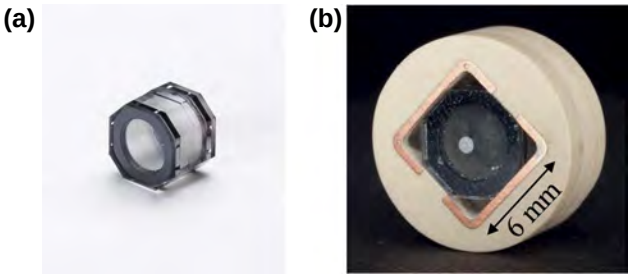

FIG. 3. Photographs of (a) the Rb microcell, and (b) the μLGR microwave resonator holding the cell. The external diameter of the white dielectric is 11 mm.

A. Microcell and atomic resonator

The microcell used [30] is fabricated from silicon and glass wafers using anodic bonding techniques and has an internal size of 4 mm diameter and 4.1 mm height [see Fig. 3(a)]. It contains Rb atomic vapor in natural isotopic mixture and an Ar-N_2 buffer-gas mixture ($P_{Ar}/P_{N2}=1.27$, 55 mbar total pressure). The cell temperature is 99 °C for a density of 2.5×10^{10} atoms/mm^3 [31]. The cell is held inside the μLGR miniature microwave resonator [29] used to apply the microwave radiation to the atomic sample. The μLGR [see Fig. 3(b)] consists of four layers of square-shaped metallic electrodes, patterned on three layers of dielectric substrates using printed-circuit-board techniques [29], which makes this type of microwave resonator suitable for miniature atomic clock realizations. The μLGR shows a small volume of <0.9 cm^3 and a high field orientation factor [32] that favors selective interrogation of the desired microwave clock transition. It has a moderate Q factor of approximately equal to 100 and a coupling of $S_{11}=-15$ dB on resonance.

B. Laser source

For this proof-of-concept study, the optical pump and detection pulses are generated by a custom-made frequency-stabilized laser head also integrating an acousto-optical modulator as the fast optical switch [33, 34]. The laser emits at 780.24 nm, resonant with the ^{87}Rb D2-line transition from $5S_{1/2}$, $F=1$ ground-state level to the $5P_{3/2}$ multiplet. Maximum output power is around 7 mW, in a 0.78 mm^2 cross-section beam ($1/e^2$ area). Typical relative intensity and relative frequency stabilities [35] are presented on Table I. A typical detection relative intensity noise (RIN) spectrum is presented on Fig. 4. The RIN is measured after the vapor cell to account for noise conversion in the atomic vapor [36].

C. Microwave source

The clock electronics unit, similar to the one described in Ref. [37], handles the pattern generation (transistor-transistor logic pulses for laser switching) and generation of the 6.834 GHz ^{87}Rb clock transition microwave frequency, by up-conversion from a 10-MHz quartz oscillator. The microwave pulses have sufficiently low phase noise (<-110 dBc/Hz from $T_C^{-1} \approx 1$ kHz) to minimize the Dick effect, see Sec. III C.

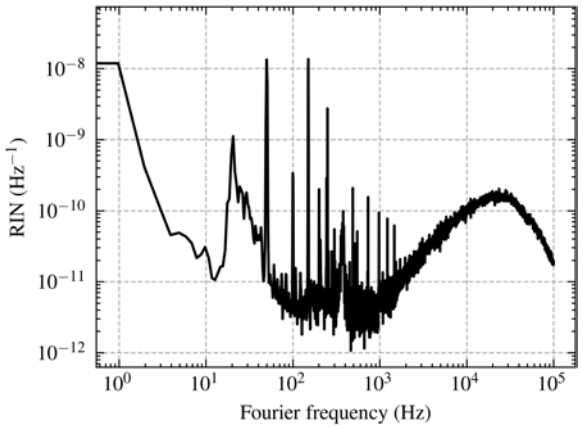

FIG. 4. Typical spectrum of detection noise in terms of RIN, measured after the vapor cell.

III. RESULTS

A. Ramsey fringes

Typical Ramsey fringes of the μPOP clock in nominal conditions are presented on Fig. 5. The chosen time steps of the sequence are $t_p = 200$ μs, $t_m = 46$ μs, $T_R = 290$ μs, and $t_d = 200$ μs, resulting in a total cycle time $T_C = 2t_m + t_d + t_p + T_R = 782$ μs. The microwave power is adjusted to $+1.3$ dBm to achieve short $\pi/2$ pulses. The contrast is 6.7% (peak-to-peak amplitude of the cental fringe divided by the central fringe maximum) and the FWHM is 1.43 kHz, in agreement with the well-known relation for the Q-factor [38]:

$$Q = \frac{\nu_0}{\mathrm{FWHM}} = 2\nu_0 \left(T_R + \frac{4}{\pi} t_m \right). \qquad (1)$$

B. Relaxation rates

The achievable fringe widths at useful signal contrast and thus the achievable short-term stability are physically limited by the population and coherence relaxation rates, γ_1 and γ_2, respectively, of the Rb ground-state transition in

TABLE I. Typical laser head intensity and frequency relative stabilities, in pulsed operation.

	1 s	10^4 s
Rel. intensity stability	2×10^{-2}	3×10^{-3}
Rel. frequency stability	3×10^{-11}	3×10^{-10}

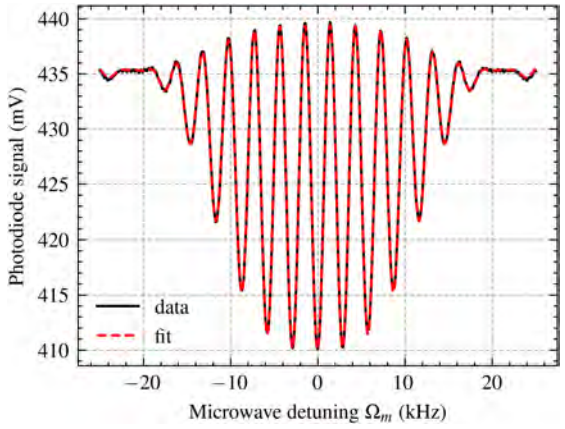

FIG. 5. Typical Ramsey fringes of the μPOP clock.

our mm-scale microcell. Indeed, the signal amplitude, contrast, and background decrease exponentially with increasing Ramsey and microwave times, T_R and t_m. In particular, for fixed t_m [39],

$$C \propto e^{-\gamma_2 T_R}, \tag{2}$$

which is used to fit γ_2 that impacts on the signal contrast and thus the obtainable clock stability. γ_1 is measured using the signal background via the Franzen method [40] and mainly impacts on the signal background and the fringe envelope [41,42]. Numerical fits to the experimental data shown in Fig. 6 yield $\gamma_1 \approx 5.3$ kHz and $\gamma_2 \approx 4.2$ kHz, corresponding to relaxation times $T_i = \gamma_i^{-1}$ of $T_1 \approx 190$ μs and $T_2 \approx 240$ μs, respectively, thus restricting the useful Ramsey times to $T_R \lesssim 250$ μs. For comparison, this is approximately 10 times shorter than the $T_R \approx 3$ ms typically used in high-performance cell clocks based on glass-blown cells of, e.g., 25 mm diameter and length showing $T_1 = 3.2$ ms and $T_2 = 4.3$ ms [43].

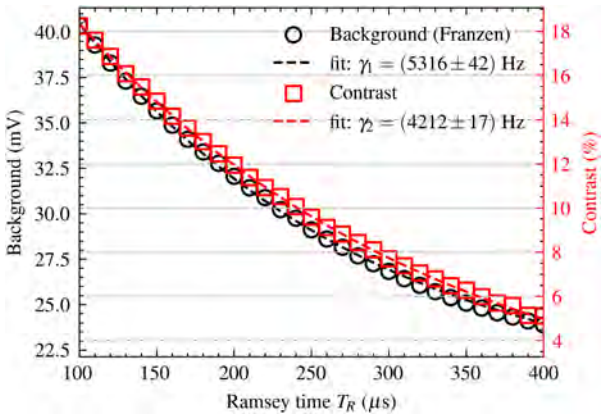

FIG. 6. Exponential dependence of fringe contrast and transmitted signal as a function of Ramsey time T_R.

C. Signal optimization

One possible and simple metric for optimization of the clock's parameters is maximizing the product of contrast and quality factor, the CQ factor [19,44]. For this purpose, Ramsey fringes are acquired for Ramsey times T_R varying from 100 to 450 µs, to measure the corresponding C and Q. The result of this CQ optimization is shown in Fig. 7 and yields an optimal T_R of 180 µs.

However, this CQ optimization consists of an approximative optimization of the SNR. Indeed, because of the pulsed operation, the sampling of the optical detection noise into the clock's short-term stability must be considered.

In the following, we analyze simultaneously the SNR and Dick-effect contributions for the μPOP clock to directly minimize its short-term stability given by

$$\sigma_y^{\text{total}}(\tau) = \sqrt{\sigma_y^{\text{SNR}}(\tau)^2 + \sigma_y^{\text{Dick}}(\tau)^2}. \tag{3}$$

The SNR contribution reads [45]

$$\sigma_y^{\text{SNR}}(\tau) = \frac{2(1-C/2)}{\pi CQ} \times \left(\sum_{\substack{k>0 \\ k\,\text{odd}}}^{\infty} \text{sinc}^2\left(\frac{k\pi t_d}{2T_C}\right) S_{\text{RIN}}\left(\frac{k}{2T_C}\right) \right)^{1/2} \tau^{-1/2} \tag{4}$$

with C the contrast, S_{RIN} the one-sided detection's RIN and Q the signal's quality factor from Eq. (1).

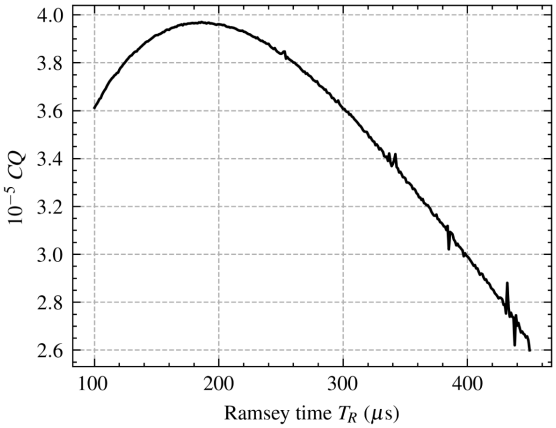

FIG. 7. CQ as a function of T_R, determined from a series of 350 Ramsey signals, yielding an optimal $T_R \approx 180$ μs.

The Dick effect contribution reads [46]

$$\sigma_y^{\mathrm{Dick}}(\tau) = \left(\sum_{k=1}^{\infty} \mathrm{sinc}^2\left(\frac{k\pi T_R}{T_C}\right) S_y^{\mathrm{LO}}\left(\frac{k}{T_C}\right)\right)^{1/2} \tau^{-1/2}, \tag{5}$$

with S_y^{LO} the local-oscillator frequency noise spectrum measured at nominal output power.

The optimization of Eq. (3) is a trade-off. Maximizing the detection and Ramsey duty cycles, respectively, $d_d = t_d/T_C$ and $d_R = T_R/T_C$ tends to minimize the infinite sums in Eqs. (4) and (5) but at the price of lower contrast and lower photodiode signal, which increases the prefactor in Eq. (4) and increases the RIN, thus degrading the clock stability. For instance, t_p and consequently T_C can be reduced in order to increase the duty cycles, as long as the contrast is not diminished. For the same reason, the microwave time t_m is set to the lowest possible value (which is limited by the maximum microwave power) for realizing $\pi/2$ pulses. Optimization of T_R is similar, with the difference that long T_R also improve the quality factor, Eq. (1) leading to a different trade-off.

Full optimization of T_R around the nominal other parameters is shown on Fig. 8. For each T_R, Eqs. (4) and (5) are computed with the other cycle's durations fixed to the optimal ones presented in Sec. III A and using the measured C and Q data from Fig. 7. From 0 to 150 µs, the Dick-effect contribution is dominant and decreases with increasing Ramsey time, whereas the SNR limit becomes dominant from 150 µs. It increases as the contrast and relevant RIN decrease with increasing T_R. The optimal Ramsey time region is wide and rather shallow and goes from 150 to 300 µs. For our study we set $T_R = 290$ μs because it experimentally shows the best short-term stability and gives an additional margin on the Dick-effect contribution. Note that in the case of μPOP, the SNR contribution as a function of T_R is most sensitive to the variation of d_d and RIN degradation, which explains why the CQ optimum at $T_R = 180$ μs seen on Fig. 7 is barely noticeable on Fig. 8. The final, optimized pulse durations are those given in Sec. III A.

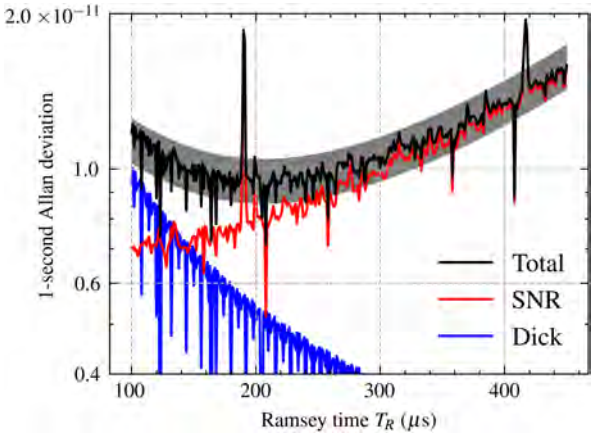

FIG. 8. Estimated SNR contribution, Dick-effect contribution and total limit to the short-term stability, as a function of T_R. The gray region represents the 10% experimental uncertainty in the estimation of the total short-term stability.

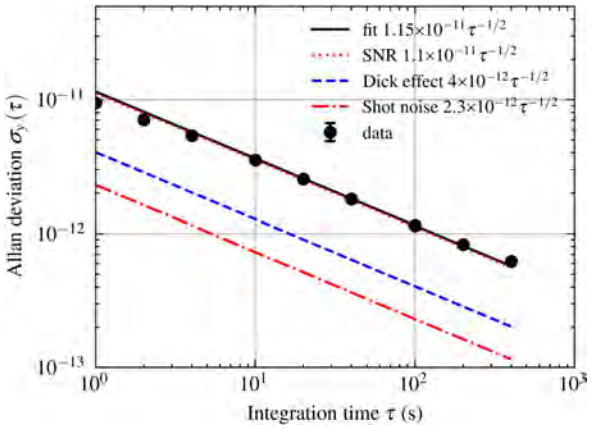

FIG. 9. Clock's short-term stability. The behavior of the stability from 1 to 5 s slightly deviates from the expected $\tau^{-1/2}$ power law because of a low integrator loop gain.

IV. CLOCK STABILITY

For clock measurements, the microwave frequency applied to the μLGR is stabilized to the center of the observed fringes (see Fig. 5) using frequency modulation by half the fringe width (approximately equal to±700 Hz) and subsequent lock-in detection to stabilize the 10-MHz frequency of the quartz oscillator. The quartz output frequency is then compared to an in-house H-maser reference [47].

A. Short-term stability

The measured short-term stability (see Fig. 9 and Table II) is $1.15 \times 10^{-11}\tau^{-1/2}$ and is dominated by the SNR contribution, with a small contribution of the Dick effect. Preliminary estimations show that the light-shift contributions are negligible contributors of the short-term stability, at least 2 orders of magnitude below the measured stability.

B. Long-term stability and performance enhancement

Figure 10 shows the long-term stability of the μPOP clock, compared to the one for cw operation of the same clock setup, as well as to other microcell and miniature microwave atomic clocks. At short timescales, the μPOP clock stability is roughly 2 times better than in cw operation and at least 5 times to 1 order of magnitude better than its competitors. For comparison, the contrast and FWHM

TABLE II. Short-term stability budget. The intensity and frequency light-shift contributions are consistent with white noise up to 50 s [35].

Contribution	$\sigma_y(\tau)$
SNR (theory)	$1.1 \times 10^{-11}\ \tau^{-1/2}$
of which shot-noise limit	$2.3 \times 10^{-12}\ \tau^{-1/2}$
Dick effect (theory)	$0.4 \times 10^{-11}\ \tau^{-1/2}$
Intensity light shift (measured)	$1.8 \times 10^{-13}\ \tau^{-1/2}$
Frequency light shift (measured)	$9.1 \times 10^{-16}\ \tau^{-1/2}$
Total (theory)	$1.2 \times 10^{-11}\ \tau^{-1/2}$
Measured	$1.15 \times 10^{-11}\ \tau^{-1/2}$

of the cw version are 15% and 10 kHz, respectively, resulting in a roughly 3 times worse *CQ* factor compared to the μPOP. From 10^3 s integration time and beyond, the performances of the μPOP clock is improved by 1 order of magnitude compared to the cw case, reaching 5×10^{-13} at 2000 s and 2×10^{-12} at 2×10^5 s. This result establishes the current state of the art for a microcell microwave atomic clock. We further note that the μPOP clock performance of 5×10^{-13} at $\tau = 2000$ s comes very close to the stability of 3×10^{-13} at these timescales reported in Ref. [48] for a microcell optical atomic clock using a much more complex optical clock architecture.

From the measured light-shift coefficients and laser characteristics [33] we estimate the long-term instability contribution from the frequency and intensity light shifts to be of the order of 2.45×10^{-14} and 2.47×10^{-13}, respectively, at least one order of magnitude below the measured stability.

The strong reduction of the light-shift effects opens perspectives for further improvements on the long-term stability of the μPOP clock, provided the other now dominating limitations can be understood and controlled. A detailed full metrological study of the long-term stability budget has been initiated and is currently on going.

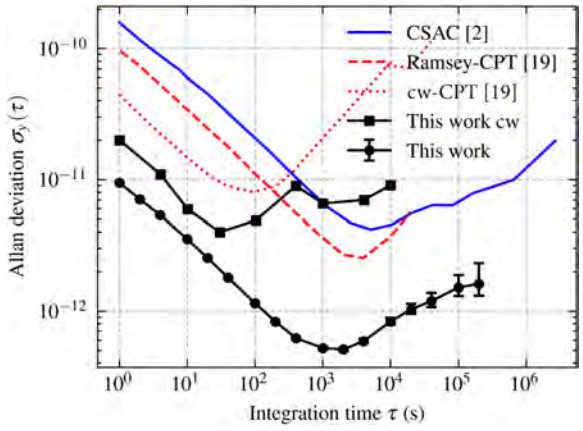

FIG. 10. Allan deviation of the μPOP clock, compared to other microcell atomic clocks.

V. CONCLUSIONS

We report a proof-of-principle study of the DR μPOP clock, in view of reducing light-shift effects for improved long-term stability of microcell microwave atomic clocks. The short-term stability is 1.15×10^{-11} at one second and in good agreement with the instability budget. The long-term stability is below 1×10^{-12} from 200 s to 10^4 s and $\leq 2 \times 10^{-12}$ at 2 days. Thanks to the POP scheme, the light-shift effect is strongly reduced and the medium- to long-term performances are consequently up to 1 order of magnitude better than in cw operation of the same physics' package and outperform other CPT-based microcell clocks. In pulsed mode, we observe an improvement of the short-term stability compared to cw mode, which is not reported for Ramsey-CPT microcell clocks [19].

The physical limitations to the short-term stability arise from the relatively high relaxation rates in the microcell that limit useful Ramsey times to $T_R \leq 400$ μs, with an optimum around 250 μs. The dependence of stability on T_R is relatively flat and wide, and operating closer to its upper end gives an additional margin for the Dick effect contribution. Our short-term stability analysis shows that this may be particularly useful in view of future implementation of a miniaturized microwave source with relaxed phase noise specifications, while degrading the overall stability by less than a factor of 2.

In the present study, we use a frequency-stabilized laser head and AOM for generating the optical pulses. In future studies, a much smaller and low-power laser source like a VCSEL could be implemented in view of a miniaturized and low-power atomic clock. Furthermore, alternative optical switching means are of interest for replacing the AOM, for instance direct current modulation of a VCSEL as studied for CPT-based clocks [49,50].

The main advantage of the μPOP approach lies in the very low light-shift effects that are among the main limitations to the long-term stability in cw miniature atomic clocks. Further studies are of interest to address a complete long-term instability budget of the μPOP clock in view of fully exploiting its improved stability potential.

ACKNOWLEDGMENTS

This work has received funding from the European Union's Horizon 2020 research and innovation programme under Grant Agreement No. 820393, macQsimal project. We also acknowledge support from the European Space Agency (ESTEC Contracts No. 4000101390 and No. 4000129974/20/NL/LW) and from University of Neuchâtel. We thank P. Scherler and M. Durrenberger for technical support. The experimental data presented in this work is accessible open access under DOI: https://b2share.eudat.eu/records/12c17379d9b443a693ec5a2e54abb8d7.

[1] S. Knappe, in *MEMS Atomic Clocks Comprehensive Microsystems*, edited by Y. B. Gianchandani, et al., Vol. 3.

[2] R. Lutwak, A. Rashed, M. Varghesea, G. Tepolt, J. LeBlanc, M. Mescher, D. K. Serkland, K. M. Geib, G. M. Peake, and S. Römisch, in *39th Annual Precise Time and Time Interval (PTTI) Meeting* (2007).

[3] S. Bregni, *Synchronization of Digital Telecommunications Networks* (John Wiley & Sons, Hoboken NJ, USA, 2002).

[4] A. T. Gardner and J. A. Collins, in *2012 Oceans* (IEEE, 2012), pp. 1–8.

[5] E. Fernández, D. Calero, and M. E. Parés, CSAC characterization and its impact on GNSS clock augmentation performance, Sensors **17**, 370 (2017).

[6] L.-A. Liew, S. Knappe, J. Moreland, H. Robinson, L. Hollberg, and J. Kitching, Microfabricated alkali atom vapor cells, Appl. Phys. Lett. **84**, 2694 (2004).

[7] E. Arimondo, in *Progress in Optics*, edited by E. Wolf (Elsevier, Amsterdam, 1996), Vol. 35, p. 257.

[8] C. Affolderbach, A. Nagel, S. Knappe, C. Jung, D. Wiedenmann, and R. Wynands, Nonlinear spectroscopy with a vertical-cavity surface-emitting laser (VCSEL), Appl. Phys. B Lasers Opt. **70**, 407 (2000).

[9] M. Abdel Hafiz, G. Coget, M. Petersen, C. E. Calosso, S. Guérandel, E. de Clercq, and R. Boudot, Symmetric autobalanced Ramsey interrogation for high-performance coherent-population-trapping vapor-cell atomic clock, Appl. Phys. Lett. **112**, 244102 (2018).

[10] M. Abdel Hafiz, R. Vicarini, N. Passilly, C. E. Calosso, V. Maurice, J. W. Pollock, A. V. Taichenachev, V. I. Yudin, J. Kitching, and R. Boudot, Protocol for Light-Shift Compensation in a Continuous-Wave Microcell Atomic Clock, Phys. Rev. Appl. **14**, 034015 (2020).

[11] N. F. Ramsey, Experiments with separated oscillatory fields and hydrogen masers, Science **248**, 1612 (1990).

[12] V. I. Yudin, A. V. Taichenachev, M. Y. Basalaev, T. Zanon-Willette, J. W. Pollock, M. Shuker, E. A. Donley, and J. Kitching, Generalized Autobalanced Ramsey Spectroscopy of Clock Transitions, Phys. Rev. Appl. **9**, 54034 (2018).

[13] O. Kozlova, J. Danet, S. Guérandel, and E. de Clercq, Limitations of long-term stability in a coherent population trapping Cs clock, IEEE Trans. Instrum. Meas. **63**, 1863 (2014).

[14] Y. Yano, W. Gao, S. Goka, and M. Kajita, Theoretical and experimental investigation of the light shift in Ramsey coherent population trapping, Phys. Rev. A **90**, 13826 (2014).

[15] P. Yun, F. Tricot, C. E. Calosso, S. Micalizio, B. François, R. Boudot, S. Guérandel, and E. de Clercq, High-Performance Coherent Population Trapping Clock with Polarization Modulation, Phys. Rev. Appl. **7**, 014018 (2017).

[16] M. Abdel Hafiz, G. Coget, M. Petersen, C. Rocher, S. Guérandel, T. Zanon-Willette, E. de Clercq, and R. Boudot, Toward a High-Stability Coherent Population Trapping Cs Vapor-Cell Atomic Clock Using Autobalanced Ramsey Spectroscopy, Phys. Rev. Appl. **9**, 064002 (2018).

[17] V. I. Yudin, M. Y. Basalaev, A. V. Taichenachev, J. W. Pollock, Z. L. Newman, M. Shuker, A. Hansen, M. T. Hummon, R. Boudot, E. A. Donley, *et al.*, General Methods for Suppressing the Light Shift in Atomic Clocks Using Power Modulation, Phys. Rev. Appl. **14**, 1 (2020).

[18] E. Blanshan, S. M. Rochester, E. A. Donley, and J. Kitching, Light shifts in a pulsed cold-atom coherent-population-trapping clock, Phys. Rev. A **91**, 41401 (2015).

[19] C. Carlé, M. Petersen, N. Passilly, M. A. Hafiz, E. De Clercq, and R. Boudot, Exploring the use of Ramsey-CPT spectroscopy for a microcell-based atomic clock, IEEE Trans. Ultrason. Ferroelectr. Freq. Control **68**, 3249 (2021).

[20] J. Camparo, The rubidium atomic clock and basic research, Phys. Today **60**, 33 (2007).

[21] N. Almat, M. Gharavipour, W. Moreno, C. Affolderbach, and G. Mileti, in *2019 Joint Conference of the IEEE International Frequency Control Symposium and European Frequency and Time Forum (EFTF/IFC)* (IEEE, 2019), Vol. 67, pp. 1–2.

[22] S. Micalizio, F. Levi, C. E. Calosso, M. Gozzelino, and A. Godone, A pulsed-laser Rb atomic frequency standard for GNSS applications, GPS Solut. **25**, 94 (2021).

[23] Q. Shen, H. Lin, J. Deng, and Y. Wang, Pulsed optically pumped atomic clock with a medium- to long-term frequency stability of 10^{-15}, Rev. Sci. Instrum. **91**, 045114 (2020).

[24] Q. Hao, W. Xue, W. Li, F. Xu, X. Wang, W. Guo, P. Yun, and S. Zhang, Microwave pulse-coherent technique-based clock with a novel magnetron-type cavity, IEEE Trans. Ultrason. Ferroelectr. Freq. Control **67**, 873 (2020).

[25] J. C. Camparo, R. P. Frueholz, and C. H. Volk, Inhomogeneous light shift in alkali-metal atoms, Phys. Rev. A **27**, 1914 (1983).

[26] F. Levi, J. Camparo, B. Francois, C. E. Calosso, S. Micalizio, and A. Godone, Precision test of the ac Stark shift in a rubidium atomic vapor, Phys. Rev. A **93**, 23433 (2016).

[27] M. Gharavipour, C. Affolderbach, S. Kang, T. Bandi, F. Gruet, M. Pellaton, and G. Mileti, High performance vapour-cell frequency standards, J. Phys. Conf. Ser. **723**, 12006 (2016).

[28] M. Pellaton, C. Affolderbach, Y. Pétremand, N. de Rooij, and G. Mileti, Study of laser-pumped double-resonance clock signals using a microfabricated cell, Phys. Scr. **2012**, 14013 (2012).

[29] M. Violetti, M. Pellaton, C. Affolderbach, F. Merli, J.-F. Zurcher, G. Mileti, and A. K. Skrivervik, The microloop-gap resonator: A novel miniaturized microwave cavity for double-resonance rubidium atomic clocks, IEEE Sens. J. **14**, 3193 (2014).

[30] Y. Pétremand, C. Affolderbach, R. Straessle, M. Pellaton, D. Briand, G. Mileti, and N. F. de Rooij, Microfabricated rubidium vapour cell with a thick glass core for small-scale atomic clock applications, J. Micromech. Microeng. **22**, 25013 (2012).

[31] C. B. Alcock, V. P. Itkin, and M. K. Horrigan, Vapor pressure equations for the metallic elements: 298–2500 K, Can. Metall. Q. **23**, 309 (1984).

[32] T. Bandi, C. Affolderbach, C. Stefanucci, F. Merli, A. K. Skrivervik, and G. Mileti, Compact high-performance continuous-wave double-resonance rubidium standard with 1.4×10^{-13} $\mathrm{Tau}^{-1/2}$ stability, IEEE Trans. Ultrason. Ferroelectr. Freq. Control **61**, 1769 (2014).

[33] F. Gruet, M. Pellaton, C. Affolderbach, T. Bandi, R. Matthey, and G. Mileti, in *Proc. ICSO* (2012).
[34] S. Kang, M. Gharavipour, F. Gruet, C. Affolderbach, and G. Mileti, in *2015 Joint Conference of the IEEE International Frequency Control Symposium the European Frequency and Time Forum* (2015), pp. 800–803.
[35] E. Batori, N. Almat, C. Affolderbach, F. Gruet, and G. Mileti, in *2020 European Navigation Conference (ENC)* (IEEE, 2020), pp. 1–10.
[36] J. C. Camparo, Conversion of laser phase noise to amplitude noise in an optically thick vapor, J. Opt. Soc. Am. B **15**, 1177 (1998).
[37] C. E. Calosso, S. Micalizio, A. Godone, E. K. Bertacco, and F. Levi, Electronics for the pulsed rubidium clock: Design and characterization, IEEE Trans. Ultrason. Ferroelectr. Freq. Control **54**, 1731 (2007).
[38] S. Micalizio, C. E. Calosso, F. Levi, and A. Godone, Ramsey-fringe shape in an alkali-metal vapor cell with buffer gas, Phys. Rev. A **88**, 33401 (2013).
[39] M. Gozzelino, S. Micalizio, C. E. Calosso, A. Godone, and F. Levi, Kr-Based buffer gas for rb vapor-cell clocks, IEEE Trans. Ultrason. Ferroelectr. Freq. Control **68**, 1442 (2021).
[40] W. Franzen, Spin relaxation of optically aligned rubidium vapor, Phys. Rev. **115**, 850 (1959).
[41] S. Micalizio, A. Godone, F. Levi, and C. Calosso, Pulsed optically pumped 87Rb vapor cell frequency standard: A multilevel approach, Phys. Rev. A **79**, 013403 (2009).
[42] W. Moreno, Université de Neuchâtel., 2019.
[43] M. Gharavipour, C. Affolderbach, F. Gruet, I. S. Radojičić, A. J. Krmpot, B. M. Jelenković, and G. Mileti, Optically-detected spin-echo method for relaxation times measurements in a Rb atomic vapor, New J. Phys. **19**, 063027 (2017).
[44] V. Shah and J. Kitching, in *Advances in Atomic, Molecular and Optical Physics*, edited by E. Arimondo (Elsevier Inc, Amsterdam, 2010), Vol. 59, p. 21.
[45] C. E. Calosso, M. Gozzelino, A. Godone, H. Lin, F. Levi, and S. Micalizio, Intensity detection noise in pulsed vapor-cell frequency standards, IEEE Trans. Ultrason. Ferroelectr. Freq. Control **67**, 1074 (2020).
[46] S. Micalizio, C. E. Calosso, A. Godone, and F. Levi, Metrological characterization of the pulsed Rb clock with optical detection, Metrologia **49**, 425 (2012).
[47] T4Science, PHMaser 1008 Passive Hydrogen Maser Clock.
[48] Z. L. Newman, V. Maurice, T. Drake, J. R. Stone, T. C. Briles, D. T. Spencer, C. Fredrick, Q. Li, D. Westly, B. R. Ilic, *et al.*, Architecture for the photonic integration of an optical atomic clock, Optica **6**, 680 (2019).
[49] Y. Yano, S. Goka, and M. Kajita, Two-step pulse observation to improve resonance contrast for coherent population trapping atomic clock, Appl. Phys. B Lasers Opt. **123** (2017).
[50] T. Ide, S. Goka, and Y. Yano, in *2015 Jt. Conf. IEEE Int. Freq. Control Symp. Eur. Freq. Time Forum, FCS 2015 - Proc.* (2015), Vol. 978, p. 167.

3.1 Supplementary material to "μPOP Clock: A Microcell Atomic Clock Based on a Double-Resonance Ramsey Scheme" [1]

3.1.1 Preliminary measurements

3.1.1.1 S_{11} spectrum

The S_{11} spectrum of the μLGR is shown on Figure 3.1. The fitting function consists of two Lorentz peaks. The mode of interest frequency is 6852.09 ± 0.13 MHz for a FWHM of 93.9 ± 7 MHz where as the neighbouring peak stands at 6947 ± 6 MHz with FWHM of 381 ± 1 MHz. At resonance, approximately one third of the energy is coupled to the neighbouring mode.

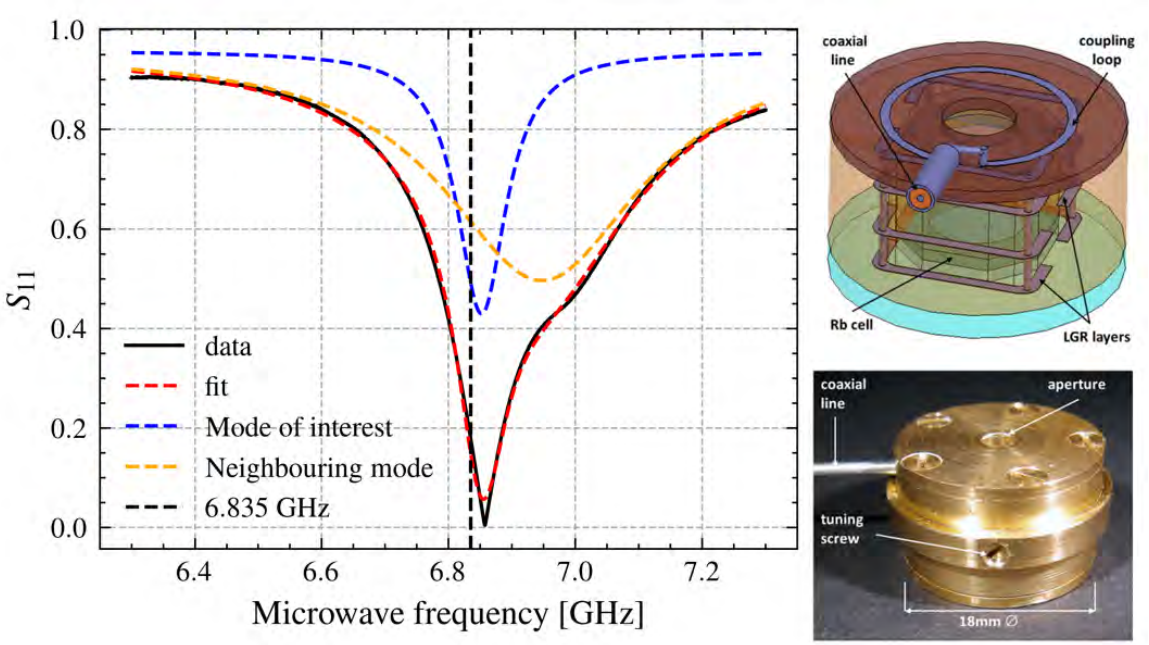

Figure 3.1: **Left:** S_{11} spectrum of the μLGR. **Right:** μLGR used in the μPOP setup [125].

3.1.2 Details on short-term stability estimation

3.1.2.1 Detection noise measurement

Measurement of the laser RIN after the vapor-cell is mandatory for best estimation of FM-AM conversions [126]. The RIN is measured in CW operation for different laser intensities, as shown on Figure 3.2. The RIN is not measured in pulsed operation as the Fast Fourier Transform (FFT) spectrum analyser is not fast enough to acquire the signal. The FM-AM conversion is approximated in CW mode which is a reasonable approximation given the accuracy with which the short-term

stability of the μPOP clock could be predicted [1]. The RIN increases as the laser intensity decreases, especially for frequencies > 30 Hz.

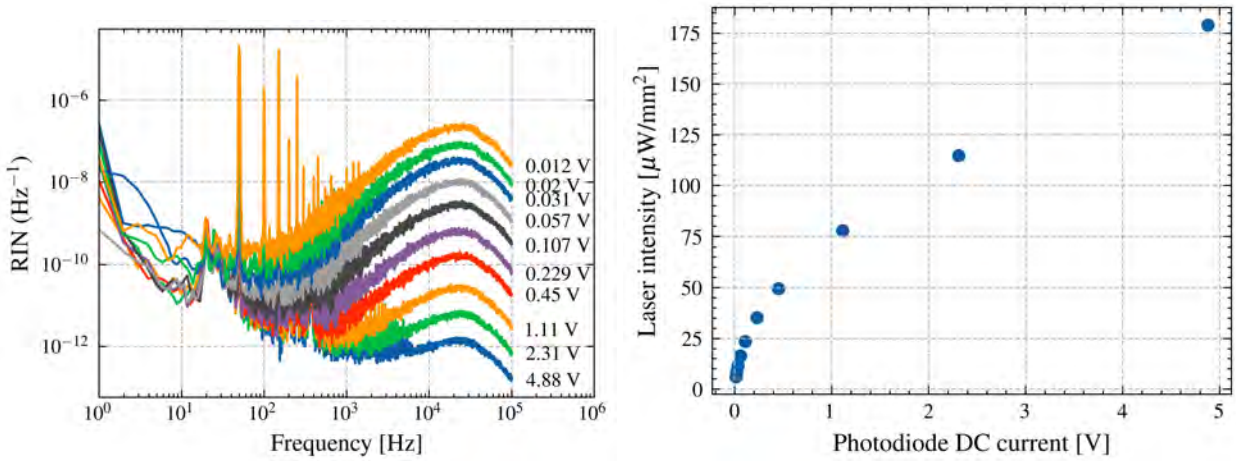

Figure 3.2: **Right:** RIN with respect to DC voltage on the photodiode. **Left:** Conversion DC current to laser intensity.

3.1.2.2 RIN contribution to the short-term stability

Different formulas have been proposed to estimate the detection noise contribution to the short-term stability of Ramsey clocks. Let us consider the one from [127] that we used in [1]:

$$\sigma_y^{cal} = \frac{2(1-C/2)}{\pi CQ}\left(\sum_{k>0,odd}^{\infty} \mathrm{sinc}^2\left(\frac{k\pi t_d}{2T_C}\right) S_{RIN}\left(\frac{k}{2T_C}\right)\right)^{1/2} \tau^{-1/2} \tag{3.1}$$

and the one from [128]

$$\sigma_y^{kang} = \frac{1}{\pi CQ}\left(\sum_{k>0}^{\infty} \mathrm{sinc}^2\left(\frac{k\pi t_d}{T_C}\right) S_{RIN}\left(\frac{k}{T_C}\right)\right)^{1/2} \tau^{-1/2}, \tag{3.2}$$

with C the contrast, Q the atomic quality factor, t_d the detection time and T_C the cycle time.

The two equations differ in two subtle points: first, eq. (3.1) sums weighted contributions of the RIN for odd multiples of the half-cycle frequency whereas eq. (3.2) sums weighted contributions of all integer multiples of the cycle frequency. Second, they don't have the same prefactor.

Each short-term estimation is conducted as follows:

1. Ramsey fringes are measured.
2. Short-term estimation using eq. (3.1) for all different RINs shown on Figure 3.2 is computed.

3. The series of point obtained at step 2 is fitted against the DC voltage on the photodiode. The function is then evaluated at the half-maximum voltage obtained from the fringes in step 1.

Example of convergence of eq. (3.1) and determination of the RIN short-term contribution are shown on Figure 3.3. Even though it is shown that frequencies above 4×10^4 Hz do not contribute much to the value of (3.1), all the frequencies provided by the FFT spectrum analyser bandwidth were considered when estimating eq. (3.1).

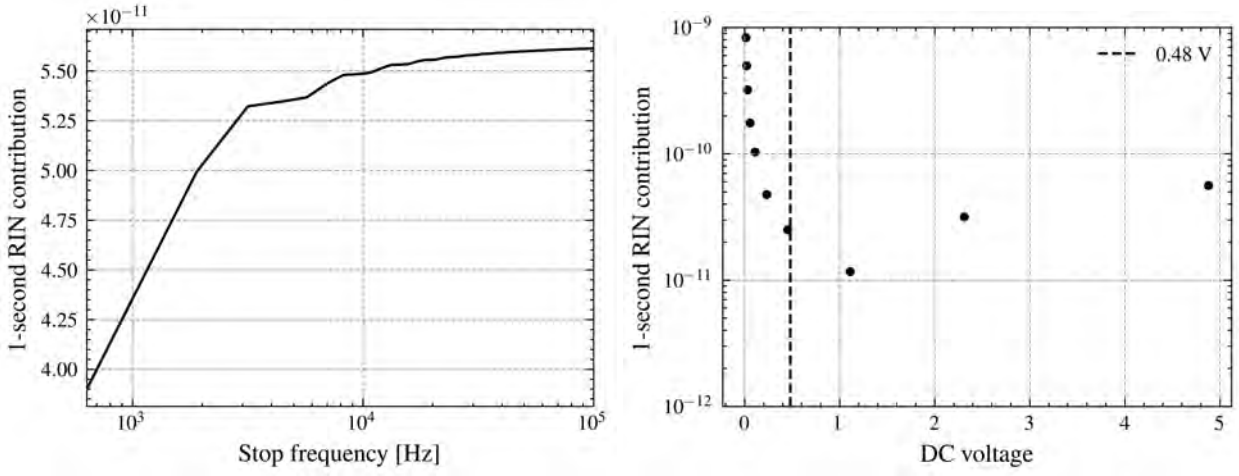

Figure 3.3: **Left:** Convergence of eq. (3.1) for the nominal μPOP parameters using the RIN acquired for $DC = 4.88$ V. **Right:** Estimation of short-term contribution σ_y^{cal} for the nominal μPOP parameters. The DC level at the clock signal half-maximum was 0.48 V.

Figure 3.4 shows a comparison of equations (3.1) and (3.2) for estimating the μPOP short-term stability for sweeping Ramsey time. As mean of comparison, the right-hand-side figure shows the difference of short-term estimation in the hypothesis of pure white noise such that:

$$S_{RIN}^{white} = \frac{1}{f_{max} - f_{min}} \int_{f_{min}}^{f_{max}} S_{RIN}(f) \mathrm{d}f \tag{3.3}$$

with f_{min} and f_{max} the min and max frequencies of Figure 3.2 to maintain similar order of magnitude compared to the left-hand-side figure. In the case of pure white noise, the two equations (3.1) and (3.2) differ much more for $T_R \leq 300$ μs compared compared to the case of the measured laser RIN.

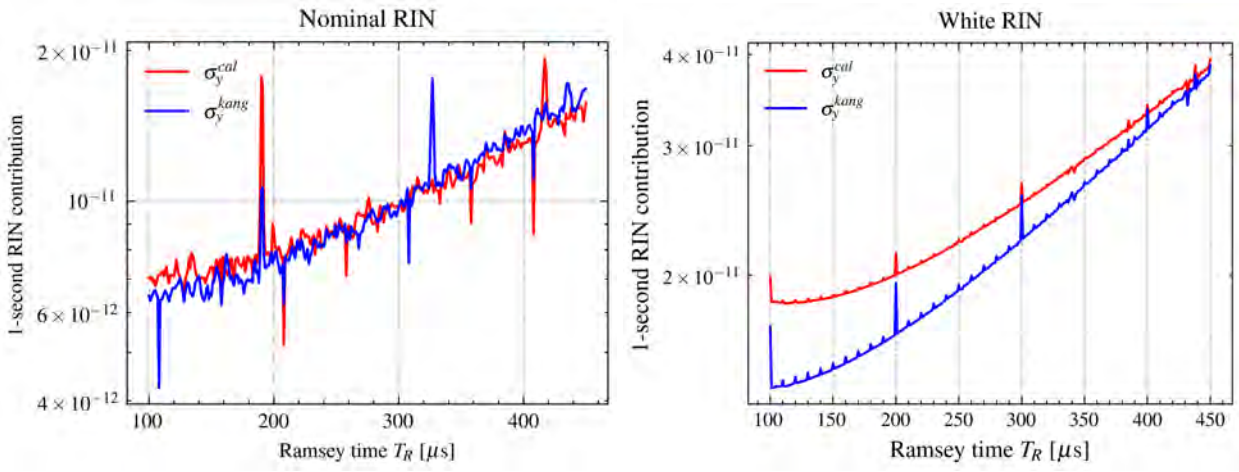

Figure 3.4: **Left:** μPOP short-term stability estimation according to equations (3.1) and (3.2). **Right:** Estimation of the μPOP short-term stability in the case of white noise only.

In the μPOP case (Figure 3.4 left) , the estimations given by the two equations do not differ much: the order of magnitude is quite the same, although they do not share the same summation indices. The RIN contribution does not decreases with the Ramsey time as it would be expected from the sole improvement of the quality factor: this, as developed more in details in [1], illustrates the conclusion that in this case the RIN aliasing plays a more important role than the Ramsey time in the optimization of the short-term stability. The main difference is the values of the contribution when the stabilities show peaks and dips. The former appear when one of the frequencies of the inner summation falls on a RIN spur while the latter are a consequence of $kt_d/T_C \approx n \in \mathrm{N}$. Since the two equations show slightly different summation indices, the predicted peaks and dips structure is different. Eq. (3.1) shows more pronounced peaks and dips when compared with eq. (3.2). Eq. (3.2) shows more peaks and dips as illustrated by the one at $T_R \approx 310\mu$s.

An interesting experiment that was not conducted would be to measure the short-term stability of the μPOP clock for different Ramsey times in a RIN-limited regime; in the case of μPOP that would mean for $T_R \geq 300$ μs. In particular, it would be interesting to know whether the supplementary peaks and dips exist to validate or invalidate one or both equations.

3.2 Long-term instability budget

3.2.1 Long-term frequency measurements

During the μPOP studies, other stability measurements with different clock parameters were taken. In particular, after the $99°$C measurement presented in the paper, a long-term measurement for cell-temperature of $96°$C was conducted in hope to improve the long-term instability budget. This temperature was motivated by the temperature shift studies presented in section 3.2.2. The frequency

time series and related Allan deviations are shown on Figure 3.5 and 3.6, respectively.

In both cases, the short-term behaviour at one second slightly deviates from the perfect $\tau^{-1/2}$ behaviour for very short τ. This is attributed to the PI-loop gains used to lock the quartz. Fortunately the deviations recover the expected white noise averaging for $\tau \in [10s, 100s]$ which is used to fit the $\tau^{-1/2}$ trend.

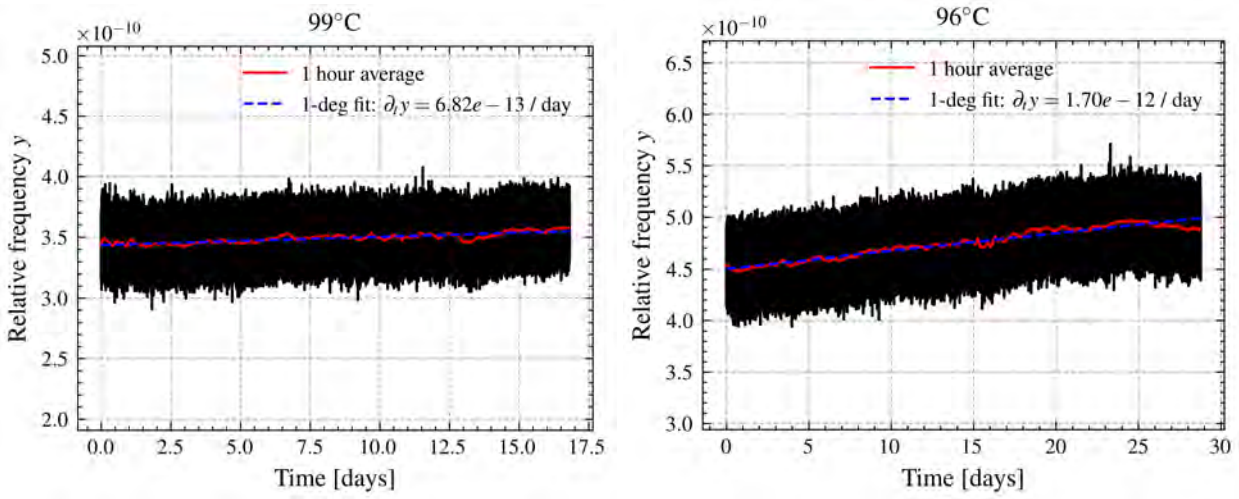

Figure 3.5: **Left:**(**Right:**) 99°C (96°C) clock relative frequency.

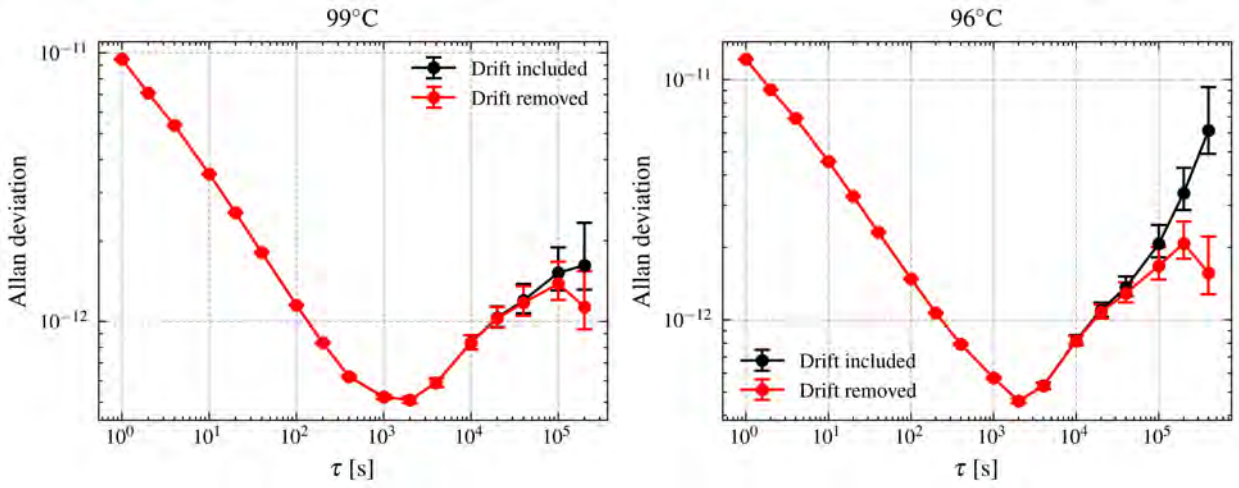

Figure 3.6: **Left:** (**Right:**) 99°C (96°C) Allan deviation.

The two runs are compared in Table 3.1. The performances of the 96°C run are slightly worse than that compared to the 99°C. The slight degradation of the short-term stability is attributed to the loss of atom density at 96°C. It is important to note that the 96°C measurement was made in the conditions optimizing the short-term stability found at 99°C and presented in [1]. In principle

the operation mode (i.e. optimal t_d, T_R, etc...) should be re-optimized. Long-term stability is not improved between the two runs, showing that the temperature shift is not the principal contributor to the instabilities.

T_{cell} =	99°C	96°C
Drift [day^{-1}]	6.82×10^{-13}	1.70×10^{-12}
$\sigma_y(1s)$ ($\tau^{-1/2}$ fit)	1.15×10^{-11}	1.45×10^{-11}
$\sigma_y(10^5 s)$	1.52×10^{-12}	2.07×10^{-12}
$\sigma_y(10^5 s)$ drift removed	1.38×10^{-12}	1.68×10^{-12}

Table 3.1: Comparison of the two long-term stability measurements.

3.2.2 Temperature shift and buffer gas content

3.2.2.1 Sensitivity coefficients

The frequency of the clock with respect to the temperature is shown on Figure 3.7. For each point, the clock frequency is measured by locking the clock and measuring the quartz frequency after changing the cell temperature and waiting for thermal equilibrium. Note that thanks to the low intensity light-shift as shown on section 3.2.4, no correction for light-shift as done in CW clocks is necessary.

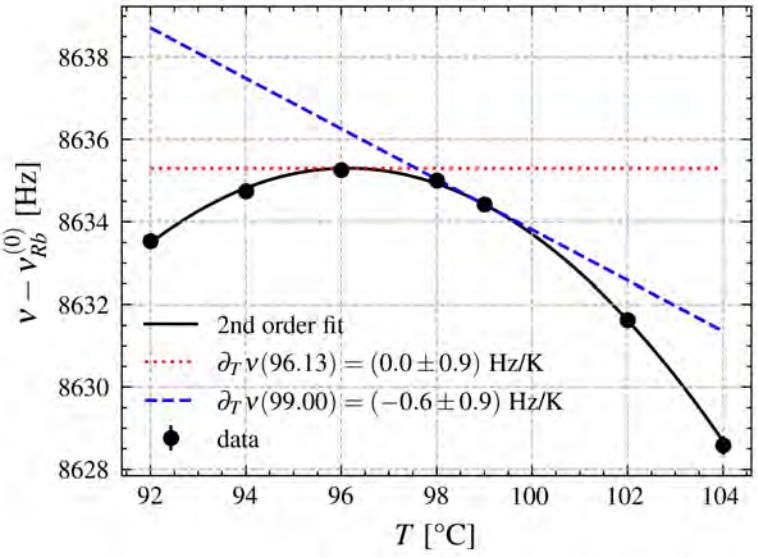

Figure 3.7: Clock frequency with respect to cell temperature.

The parabola shape is compatible with eq. (2.8). The overall 8.6 kHz shift is mostly attributed to

the buffer gas mixture. The inversion temperature given by the fit is $T_{inv} = 96.13°$C. The sensitivity coefficients are obtained by taking the derivative of the fit at the points of interest. In both cases the uncertainty is greater than the coefficient which suggests that they are compatible with zero to the level of uncertainty. In the full instability budget presented on section 3.2.7, the highest possible values will be used as sensitivity coefficient, namely 1.5 Hz/K and 0.9 Hz/K for $99°$C and $96°$C, respectively.

3.2.2.2 Buffer-gas content

The temperature-shift measurement shown on Figure 3.7 can be used to measure the buffer gas content of the vapour-cell. Indeed, using eq. (2.8), the inversion point is given by:

$$T_{inv} = T_0 + \frac{\delta}{2\gamma}. \tag{3.4}$$

In the present case, there are two buffer gases: Ar and N_2. By using eq. (3.4), one measures:

$$p_{Ar} = 56\% \quad \text{and} \quad p_{N_2} = 44\%. \tag{3.5}$$

Assuming that the total shift from the Rb clock frequency is due to the buffer gas shift and using eq. (2.8), one finds that the buffer gas pressure is $P = 55$ mbar with a sensitivity coefficient:

$$\frac{\partial}{\partial P}\nu = 160 \text{ Hz/mbar}. \tag{3.6}$$

3.2.2.3 Cell-temperature

The cell temperature is measured with a Negative Temperature Coefficient Thermistor (NTC) which is out of the temperature control Proportional–Integral–Derivative controller (PID) loop. The 96°C cell temperature stability is shown on Figure 3.8. At one day, the fluctuation is of the order of $0.2^{+0.04}_{-0.02}$ mK.

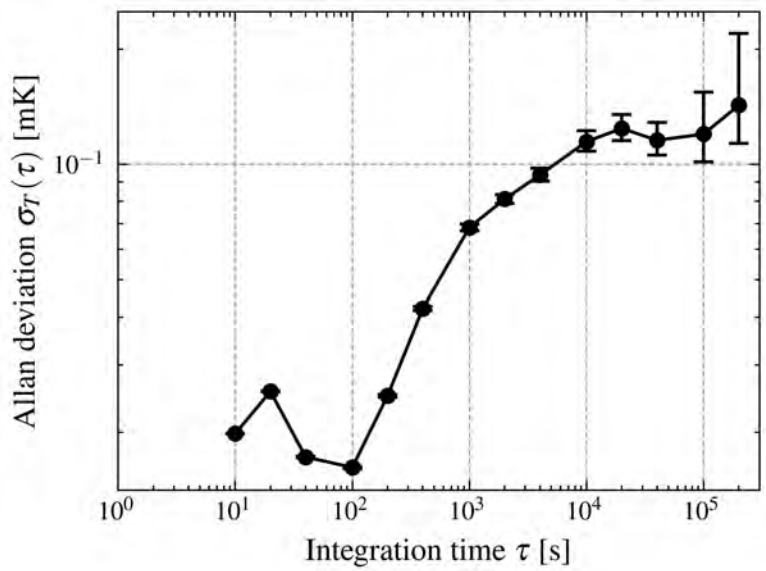

Figure 3.8: Typical cell temperature Allan deviation acquired during the $96°$C long-term measurement.

3.2.3 Frequency light-shift

3.2.3.1 Sensitivity coefficients

The measurement of the frequency light-shift coefficient β_{LS} is presented on Figure 3.10. Each point consists of a locked clock stability measurement with parallel measurement of the laser frequency. The laser frequency is tuned by changing the laser diode current, in free-running mode. It is worth reminding the reader that the laser head from [105] (LH2) was used. The frequency is measured thanks to a wavemeter with the AOM first order beam as input and applying the appropriate correction. An example of such measurement is shown on Figure 3.9.

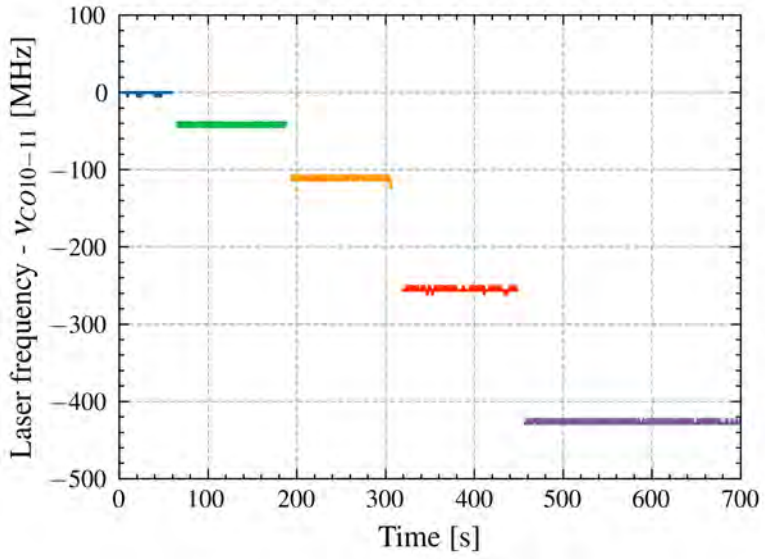

Figure 3.9: Laser head frequency with respect to time for the 99°C case.

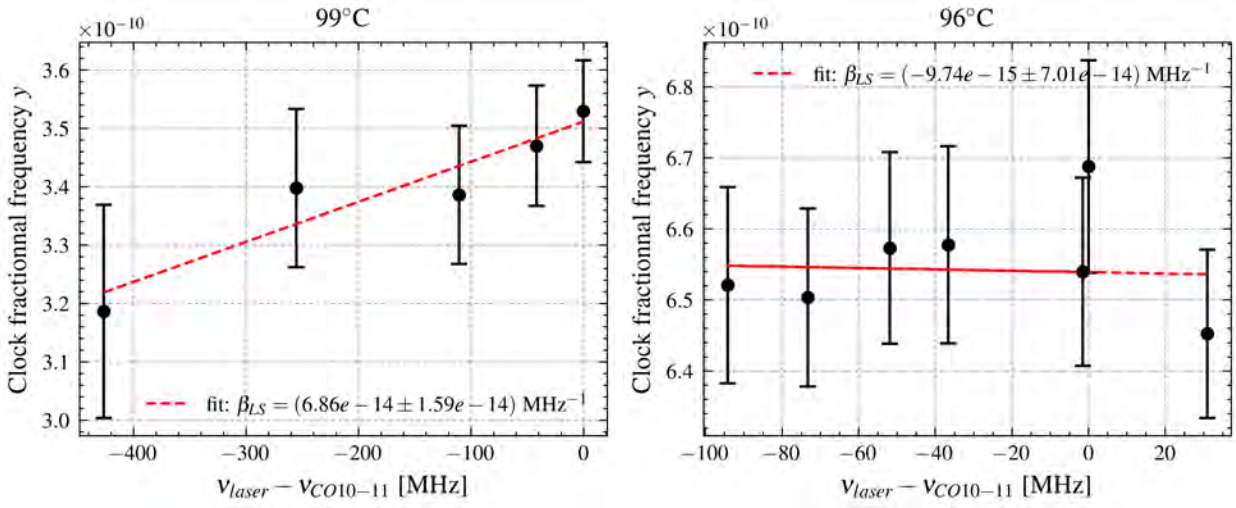

Figure 3.10: **Left:** (**Right**) Frequency light coefficient for 99°C (96°C) measurement.

In both cases, the errors on the clock relative frequency y during the measurements are quite big compared to the variation of frequency due to the change of laser frequency. This illustrates the low sensitivity of the transition frequency due to the variation of the change of light frequency thanks to the AOM blocking the light during the Ramsey part of the cycle. Indeed, the short-term stability of the clock limits the measurement of the light-shift coefficient. It is hence more than important to take account for these errors when fitting the linear lines. In both cases the sensitivity coefficients are of the order of $\beta_{LS} \approx 7 \times 10^{-14}$ MHz^{-1} which is comparable to the same coefficient obtained for the high-performance Rb vapor-cell clocks in [64].

3.2.3.2 Laser frequency stability

The laser-head frequency stability was estimated in [8] and the method described in section 2.5. The stability at 10^5 s is estimated from the fit of the Allan deviation and is shown on Figure 3.11. The fluctuation is $0.312^{+0.106}_{-0.004}$ MHz at 10^5 s which in both cases means a contribution to the instabilities at the order of $\approx 2.2 \times 10^{-14}$.

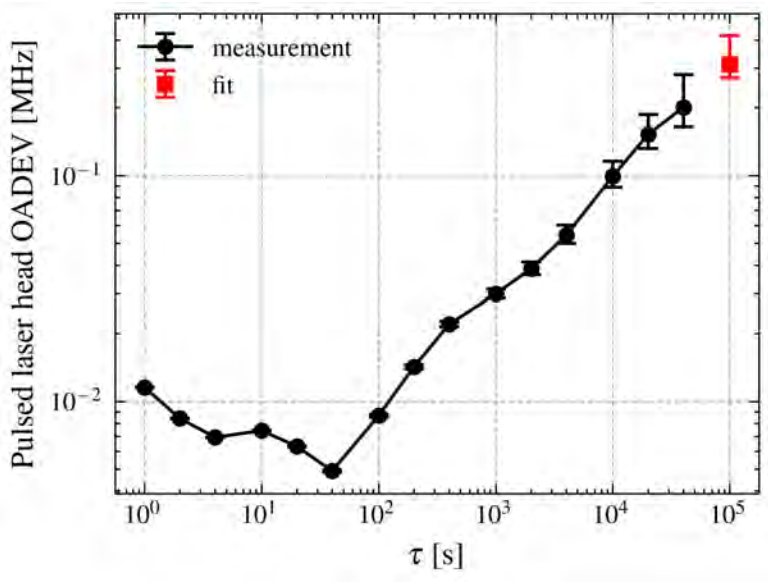

Figure 3.11: Laser head frequency stability in pulsed mode. The last point is inferred from a fit assuming linear drift from $\tau = 10^3$s.

3.2.4 Intensity light-shift

3.2.4.1 Sensitivity coefficients

Measurement of the intensity light-shift coefficient is presented on Figure 3.12. Each point is acquired by locking the quartz for different laser intensities. Once again, as developed for the frequency light-shift, the magnitude of the errors bars show little sensitivity of the clock to the change of light intensity. The intensity is varied using optical filters. In the field of Rb microwave clocks, the intensity light-shift coefficient α_{LS} is traditionally given in $[\%^{-1}]$. This standard is particularly convenient as the light intensity varies drastically between the pumping (≈ 9 mW/mm^2) and the interrogation (≈ 78 μW/mm^2) phases hence reflecting the overall behaviour during the whole cycle.

Although the curves of the clock frequency with respect to the laser intensity show lower SNR compared to the frequency lightshift ones, they remain compatible with a linear fit. As in the previous case, the highest possible sensitivity coefficients will be used while computing the stability budget.

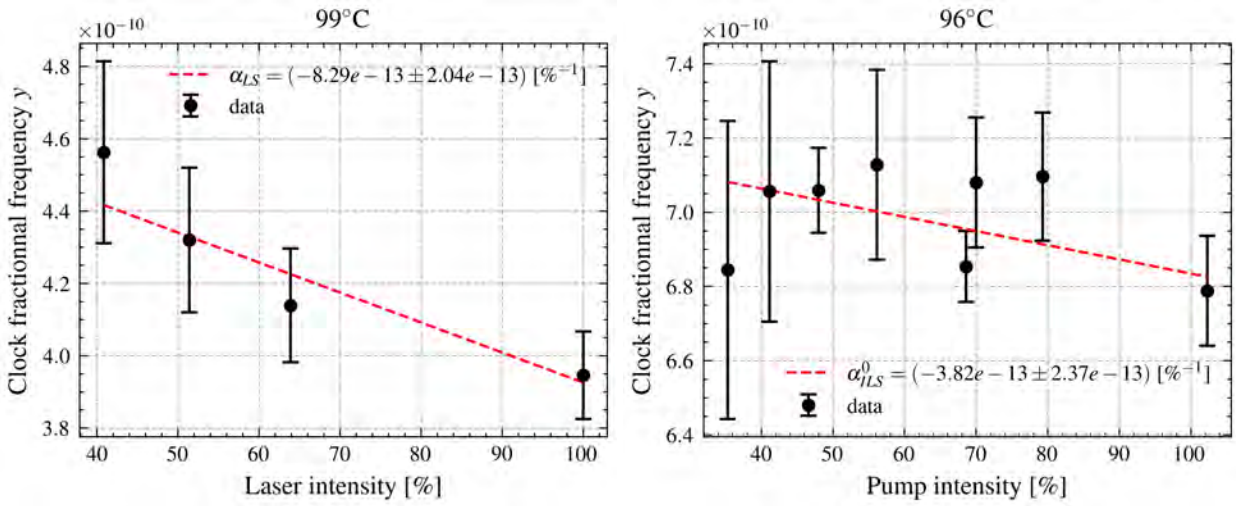

Figure 3.12: **Left:** (**Right:**) Intensity light coefficient for 99°C (96°C) measurement.

3.2.4.2 Laser intensity stability

Measurement of the laser intensity is measured in POP mode thanks to a photodiode inside the leaser head. The measurement for 96°C is presented on Figure 3.13. The stability at $\tau = 10^5$ s is $0.3^{+0.05}_{-0.03}\%$ which corresponds to a maximum contribution to clock instabilities of $\approx 3 \times 10^{-13}$.

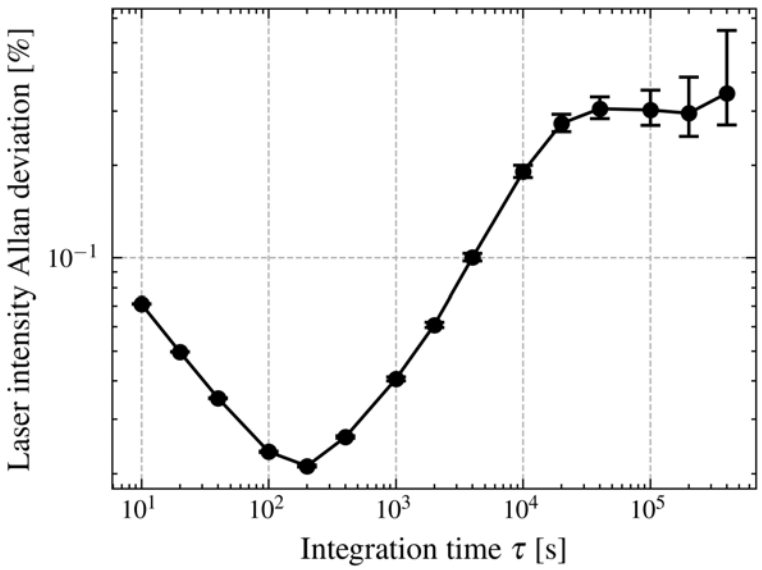

Figure 3.13: Relative laser intensity Allan deviation measured during the 96°C measurement.

3.2.5 Microwave powershift

3.2.5.1 Sensitivity coefficients

The microwave powershift coefficient is measured by locking the clock for different microwave power values. The microwave power is lowered thanks to passive variable attenuators. The dependency of the clock relative frequency with respect to the microwave power is shown on Figure 3.14. To being able to compare the microwave power stability in CW and POP modes, the coefficient is expressed in relative units. The nominal microwave power in POP mode is 1.3 dBm.

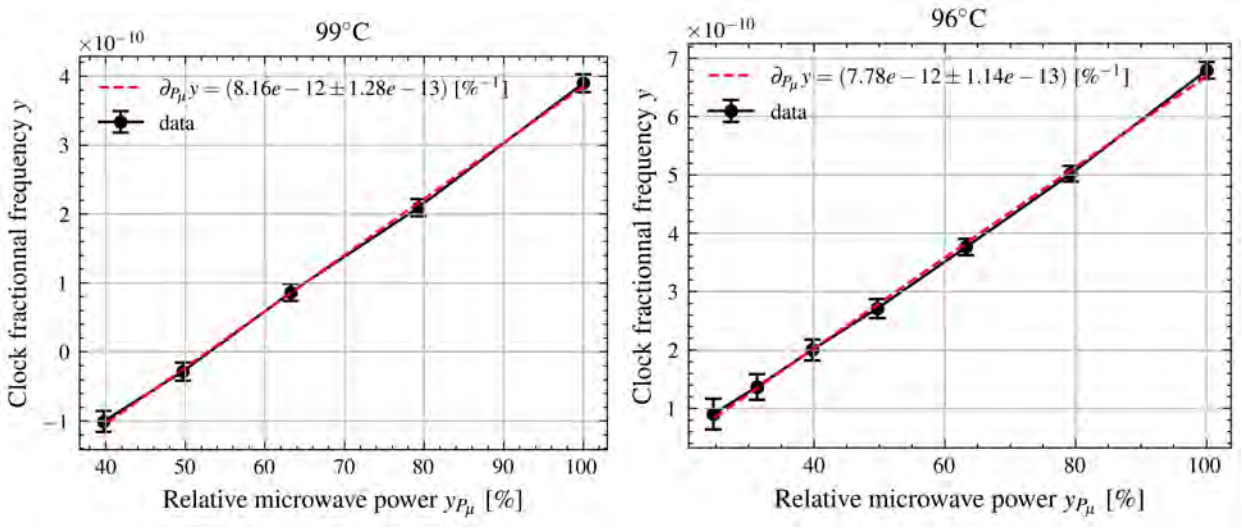

Figure 3.14: **Left:** (**Right:**) Clock fractionnal frequency with respect to microwave power for the $99°$C ($96°$C) long-term measurement. The microwave powers are normalized by the nominal microwave power: 1.3 dBm.

In both cases, the trend is clearly linear, with error bars smaller than that compared to the frequency and intensity light-shifts.

3.2.5.2 Microwave power stability

The microwave power stability is not measured during the clock operation to avoid adding one more element to the microwave chain who could potentially deteriorate the microwave power stability. Figure 3.15 shows the microwave power stability from the electronics in CW and POP modes. Note that in principle the short-term stability of the latter should be corrected for the deadtime operation as demonstrated in section 2.5 using eq. (2.44). The short-term stability in POP mode is hence hugely overestimated. The relative microwave stability at $\tau = 10^5$ s is $0.11^{+0.002}_{-0.001}$ %. In the long-term, the relative stability of the microwave power in POP mode is deteriorated from of factor of ≈ 2 compared to the CW mode. This is of great importance because this factor will allow to understand

the limitation of the clock in the mid-term.

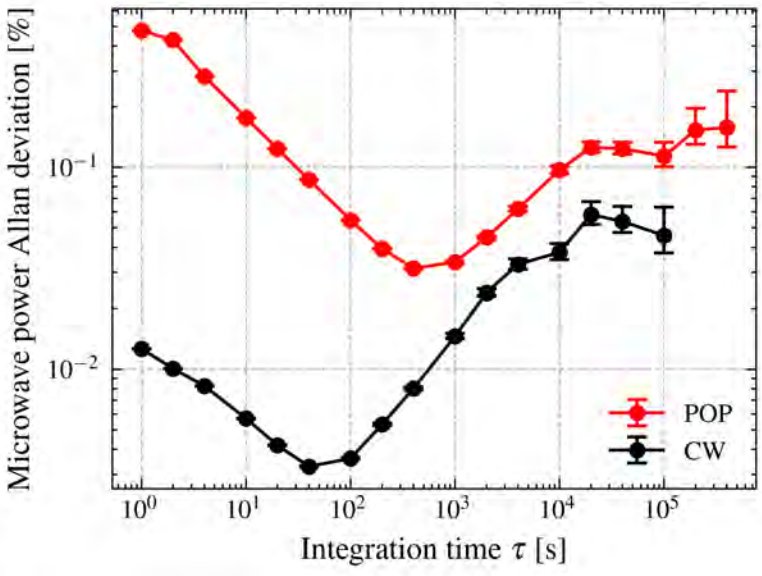

Figure 3.15: Typical microwave power relative stability in CW and POP modes acquired in μPOP nominal operation mode.

3.2.6 Position shift

During the μPOP studies, the sensitivity of the clock to the laser position was studied. The phenomena was discovered when trying to measure the frequency light-shift by varying the AOM frequency: the displacement of the laser position on the physics package window was responsible for a frequency shift much greater than that of the frequency light-shift detailed in section 3.2.3. This sensitivity is attributed to the low beam diameter (1 mm [1]) compared to the cell diameter (4 mm [129]). In principle this effect could be attenuated by expanding the beam cross-section or using a diffuser before the physics package.

3.2.6.1 Determination of sensitivity coefficient

Sensitivity coefficient is measured by placing a ruler above the physics package window. The position of the beam was changed using the AOM. Changing the beam position using the mirrors on the optics table was disregarded for lack of reproducibility. For each position, the clock frequency is measured by locking the quartz to the atomic transition. The measurement span ranges from the left side of the cell (-2 mm) to almost the right side ($+2$ mm) with a limitation to an AOM driving frequency of 84 MHz due to the laser head geometry. The measurement of the coefficient is presented on Figure 3.16. This study was performed for a cell temperature of 96°C.

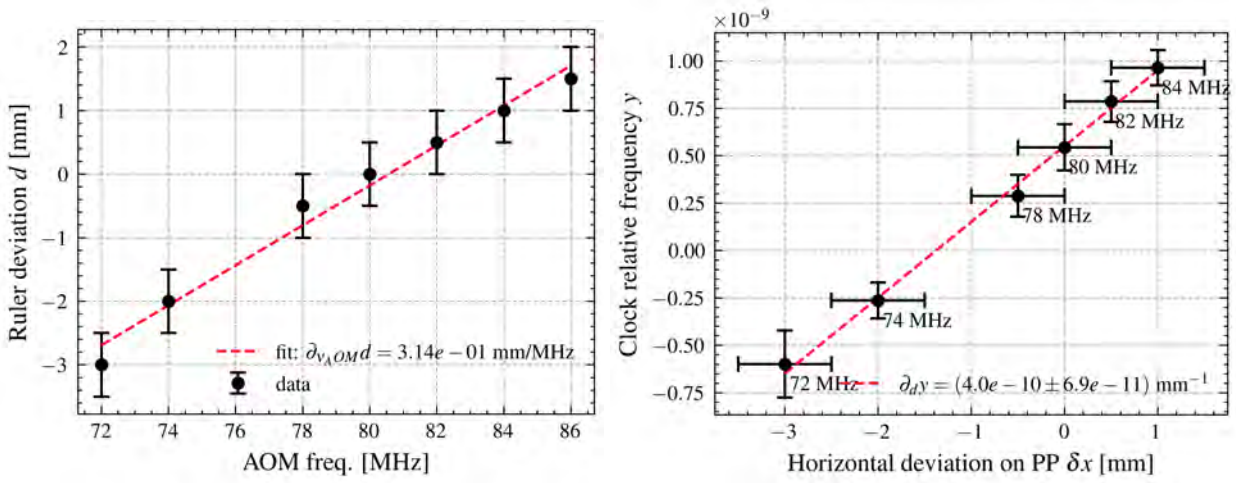

Figure 3.16: **Left:** Laser beam horizontal position on the physics package with respect to the AOM frequency. **Right:** Clock fractional frequency with respect to the lasers beam horizontal position on the physics package window for the 96°C measurement.

The sensitivity of the clock frequency with respect to the AOM frequency is:

$$\frac{\partial y}{\partial \nu_{AOM}} = \frac{\partial \delta h}{\partial \nu_{AOM}} \cdot \frac{\partial y}{\partial \delta h} = 1.3 \times 10^{-10}\,\text{MHz}^{-1} \gg \beta_{LS} \approx 7 \times 10^{-14}\,\text{MHz}^{-1} \tag{3.7}$$

with δh the horizontal beam position and δv the vertical beam position. The shift is almost two orders of magnitude bigger than the frequency light-shift coefficient β_{LS} shown in section 3.2.3. This shows that the new phenomenon is not the frequency light-shift but rather a form of position shift as described in section 2.1.1.2.

The shape of the sensitivity is clearly linear with respect to the cell center with $\nu_{AOM} = 80$ MHz. Interestingly, the symmetry is odd (i.e. anti-symmetric around the cell center) and not even (i.e. symmetric around the cell center) which would be expected from the general symmetry of the setup. Indeed, the physics package and the laser beam both exhibit even symmetry around the resonator principal axis. Hypothetically, this could be explained by the presence of an odd symmetric neighbouring mode near resonance. For instance, a TE_{111}-like mode as shown on Figure 4.1 exhibits an odd symmetry around the cavity principal axis. The S_{11} spectrum (see Figure 3.1) indeed shows the presence of a parasite mode from which the clock position shift could originate. Unfortunately, no details on the nature of the neighbouring mode is given in [129] but given the sensitivity of the clock to the spatial fluctuations of the laser beam it is reasonable to speculate that this mode is indeed of such nature. Development of future versions of the μLGR should hence try to mitigate the presence of neighbouring modes, if possible.

3.2.6.2 Fluctuation of the laser position

Fluctuation of the laser position was measured using the AOM first order beam. Its optical path is made as long as 5 m to magnify the beam position fluctuations by a factor of 10. A camera is placed at the end of the path. Every minute a 2d gaussian profile is fitted from the intensity image as shown on Figure 3.17. The effect is not assessed for lower integration times as taking one picture every second would rapidly overflow the computer memory. Furthermore, the effect is likely to affect the long-term stability only as it was shown that the short-term stability is dominated by the laser RIN contribution [1]. Note that during this measurement the vibrations of the optic table were not assessed. The measurement of the laser beam position on the camera however show the relative position of the beam with respect to the physics package.

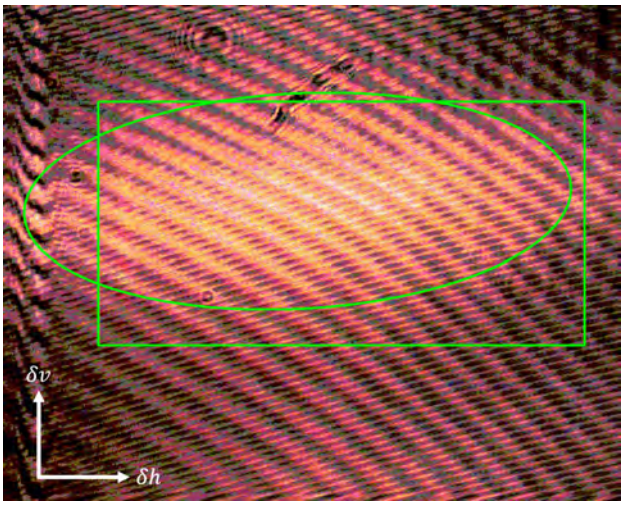

Figure 3.17: Gaussian profile of the laser beam 5 meters after the laser head. The green rectangle represents the fit region of interest. The ellipsis is the 95% confidence ellipsis from the fit.

Figure 3.18 shows the position of the beam on both axes as well as the correlation between the two.

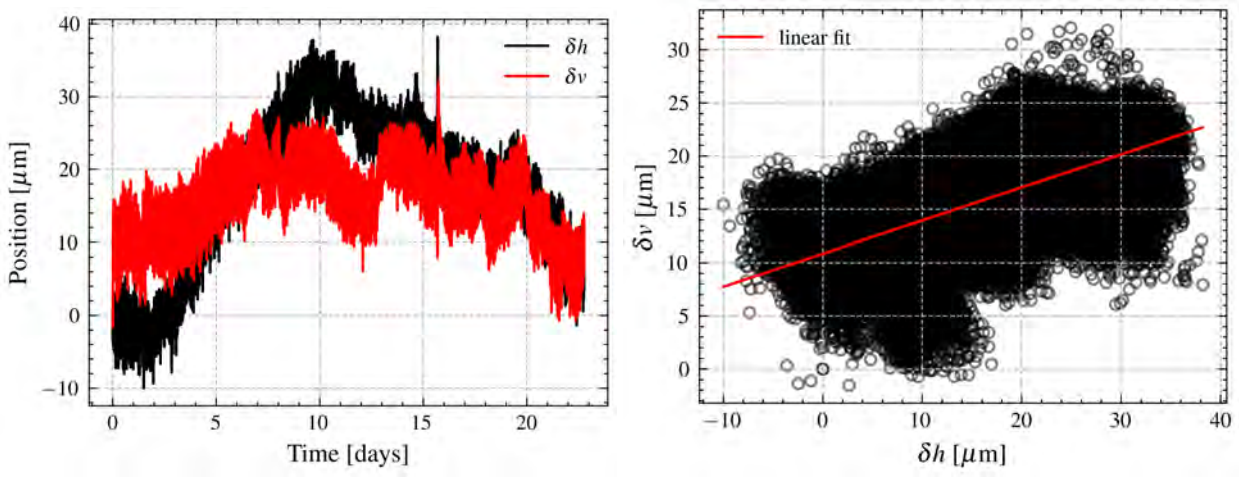

Figure 3.18: **Left:** Laser beam horizontal (δh) and vertical (δv) positions on the physics package with respect to time. **Right:** Correlation of the two components.

Given the non-zero correlation between the laser horizontal and vertical positions, the Allan deviation of the sum of the two must be corrected with the Groslambert covariance, as demonstrated in equation (2.37), namely:

$$\sigma^2_{\delta_h+\delta_v} = \sigma^2_{\delta h} + \sigma^2_{\delta v} + 2\,\mathrm{GCov}\,(\delta h, \delta v), \tag{3.8}$$

where we assumed that the sensitivity coefficient is the same on the vertical and horizontal axes, namely:

$$\frac{\partial}{\partial \delta h} y \approx \frac{\partial}{\partial \delta v} y, \tag{3.9}$$

with δh (δv) the horizontal (vertical) beam position on the physics package.

Figure 3.19-left shows the Groslambert codeviation (see eq. (2.39)) with respect to τ. Interestingly, the codeviation is negative for lower τ and positive for larger τ, showing anti-correlation and correlation, respectively. More importantly, without the Groslambert correction, the estimated contribution of the position shift effect would be overestimated in the mid-term ($\tau \approx 10^3$ s) and underestimated in the long-term.

In is worth insisting on this last point: the corrected deviation with proper handling of covariances corrects the total instability contribution negatively (black circles in Figure 3.19 right) and positively in the short and long-term respectively. This behaviour is illustrated with the A and B arrows on Figure 3.19, respectively.

Figure 3.19-right shows the total beam position deviation, compared to the quadratic sum $\sigma^2_{\delta h} + \sigma^2_{\delta v}$. At one day the fluctuation level is $\sigma_{\delta_h+\delta_v}(\tau = 10^5 s) = 4.3^{+0.5}_{-0.3}$ μm. Note that as mentioned in section 2.3.3, determination of Groslambert codeviation errorbars is very involved and was hence not conducted.

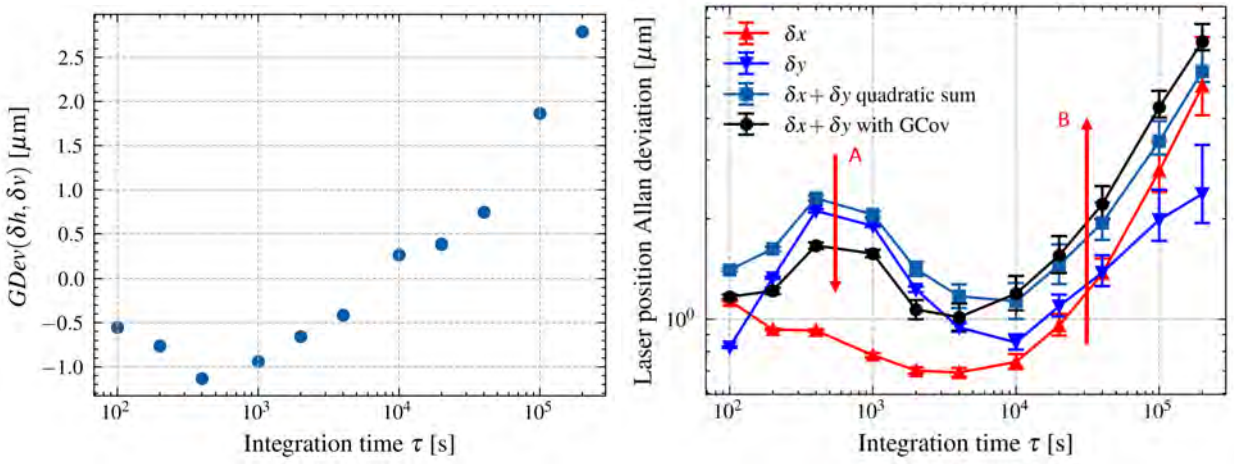

Figure 3.19: **Left:** Groslambert codeviation. **Right:** Laser position Allan deviation.

3.2.6.3 Correlation with external parameters

During the 96°C stability measurement, monitoring of the laboratory temperature and humidity was conducted. As suggested by Figure 3.20, the clock frequency and the vertical position is strongly correlated to the dew temperature point inside of the laboratory. Note that the dew point is calculated from the measured temperature, humidity and pressure inside of the laboratory [130]. This suggests that the laser position fluctuations are induced by a moisture sensitive component which is not clearly identified to this date. It is reasonable to think that the AOM crystal could be sensitive to the variation of moisture in the lab but there is no literature to support this statement.

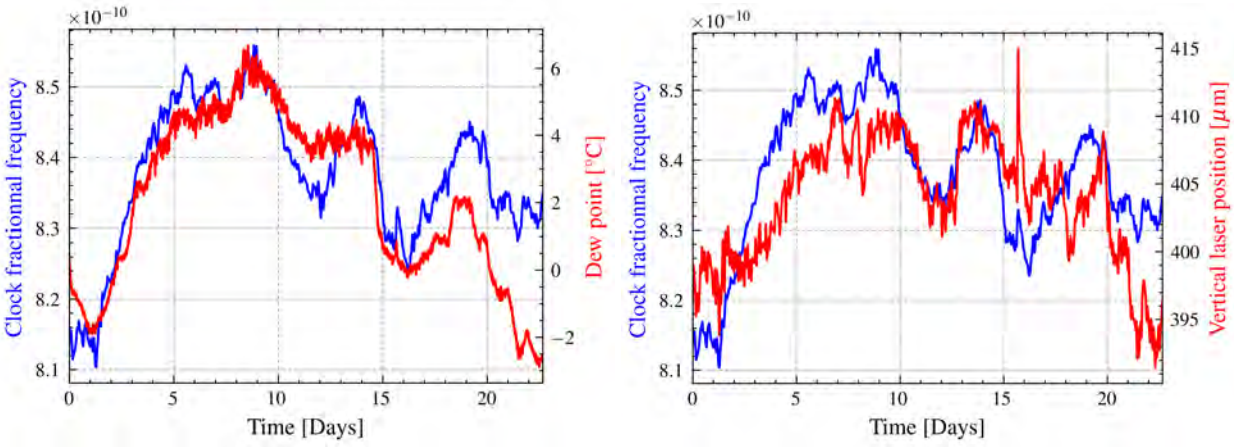

Figure 3.20: **Left: (right)** 96°C clock fractional frequency with respect to the dew temperature (vertical laser position).

During the measurement, parallel acquisition of light intensity, laboratory temperature, pressure

and humidity fluctuations were conducted. Only the dew point showed convincing correlation with the clock frequency. The imperfect, yet good, correlation of the clock frequency with respect to the dew temperature is attributed to microwave-shift-induced limitation in the mid-term stability, as discussed in section 3.2.7.

3.2.7 Full budget

Table 3.2 presents the full long-term instability budget for 99°C and 96°C at $\tau = 10^5$ s. The contribution of all the effects evaluated in the previous sections are shown on Figure 3.21.

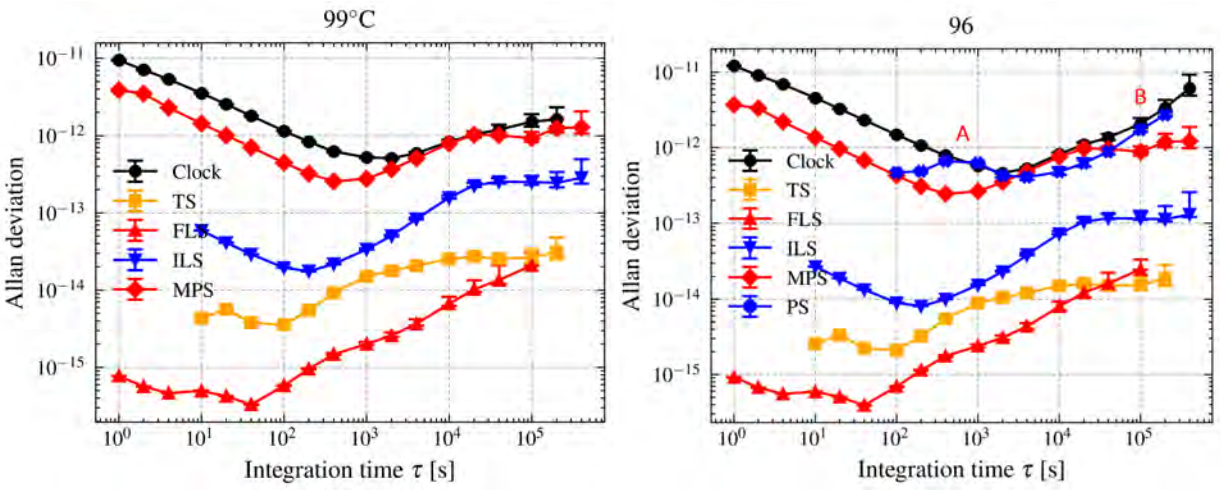

Figure 3.21: **Left:** (**Right**) 99°C (96°C) clock Allan deviation along with the contributions of all the considered shifts. TS: temperature shift, ILS: intensity lightshift, FLS: frequency lightshift, MPS: microwave powershift, PS: position shift.

			99° cell temp.		96° cell temp.	
Effect	**Parameter A**	$\sigma_A(10^5)$	$\lvert \partial y/\partial A \rvert$	$\sigma_y^A(10^5)$	$\lvert \partial y/\partial A \rvert$	$\sigma_y^A(10^5)$
Temperature shift	Cell temperature [mK]	$0.2^{+0.04}_{-0.02}$	$(0.9 \pm 1.3) \times 10^{-13}$	$2.6^{+0.8}_{-0.4} \times 10^{-14}$	$(0.0 \pm 1.3) \times 10^{-13}$	$1.5^{+0.5}_{-0.2} \times 10^{-14}$
Frequency lightshift	Laser frequency [MHz]	$0.312^{+0.106}_{-0.004}$	$(6.7 \pm 2.6) \times 10^{-14}$	$2.09^{+0.98}_{-0.02} \times 10^{-14}$	$(0.97 \pm 7.01) \times 10^{-14}$	$2.49^{+0.85}_{0.03} \times 10^{-14}$
Intensity lightshift	Laser intensity [%]	$0.3^{+0.05}_{-0.03}$	$(8.3 \pm 2.0) \times 10^{-13}$	$2.5^{+0.5}_{-0.2} \times 10^{-13}$	$(3.8 \pm 2.4) \times 10^{-13}$	$1.15^{+0.30}_{-0.05} \times 10^{-13}$
Microwave powershift	Microwave power [%]	$0.11^{+0.02}_{-0.01}$	$(8.16 \pm 1.3) \times 10^{-12}$	$9.3^{+1.9}_{-0.9} \times 10^{-13}$	$(7.78 \pm 0.11) \times 10^{-12}$	$8.8^{+1.5}_{-0.9} \times 10^{-13}$
Position shift	Laser deviation [μm]	$4.3^{+0.5}_{-0.3}$	-	-	$(4.0 \pm 0.7) \times 10^{-13}$	$1.7^{+0.2}_{-0.1} \times 10^{-12}$
Total				$1.3^{+0.8}_{-0.3} \times 10^{-12}$		$1.2^{+1.3}_{-0.5} \times 10^{12}$
Measured				$1.5^{+0.4}_{-0.2} \times 10^{-12}$		$2.1^{+04}_{-0.3} \times 10^{-12}$

Table 3.2: Comparison of the two long-term stability measurements for $\tau = 10^5$ s.

In the $99°$C case, the stability is limited by the microwave powershift up to $\tau = 4\times10^4$ s after which the limitation is not as convincing. It is reasonable to think that the position shift could be responsible for the very long-term limitation. Looking at the $96°$C budget, it appears that the clock is limited by the position shift in the interval $\tau \in [300, 2000] \cup [4 \times 10^4, 2 \times 10^5]$ whereas the limiting contribution comes form the microwave powershift in the $\tau \in [2000, 4 \times 10^4]$ interval. It worth insisting that on point A and B (see Figure 3.21), the contribution of the position smoothly fits the measured stability with the respective negative and positive Groslambert codeviation correction described in Figure 3.19. Without this correction, the estimated position shift stability would overshoot and undershoot at point A and B, respectively.

In $\tau \in [300, 2000]$ interval, the fluctuations of the laser beams are dominated by the vertical fluctuations as shown on Figure 3.19 for which the sensitivity coefficient was assumed to be the same as the horizontal one (see eq. (3.9)). It is reasonable to think that this coefficient could be slightly lower due to the asymmetry of the microwave field inside the physics package.

Comparing the two measurements, it seems that the 99°C position shift coefficient is lower than that compared to the $96°$C coefficient.

3.2.8 Conclusion

In this section, the long-term instability budget of the μPOP was presented. The evaluation of the temperature cell shift, the microwave-power shift, the frequency and intensity light shifts and the position shifts have been carried.

The contribution of the frequency and intensity light shifts to the instability at one day are two and one order of magnitude lower than the measured stability (see Table 3.2) thanks to the Ramsey operation. The remaining shift is attributed to the light leakage through the AOM during the microwave part of the the cycle (see Figure 2.3).

In the mid and long-term, the clock is limited by the microwave-power and position shifts, alternatively, with the latter being the ultimate long-term contributor the stability. Evaluation of correlations between the horizontal and vertical laser beam positions by means of Groslambert covariance calculation is necessary to properly explain the measured stability.

3.3 A stable method for measuring relaxation rates in Ramsey type clocks

3.3.1 Introduction

Relaxation rates are one of the main limitations of the short-term performances of Ramsey-type atomic clocks: indeed, as illustrated by eq. (2.28), the longer T_R, the better the short-term stability of the clock, but the lower the contrast due to the coherence relaxation rate (see eq. (3.11)). In practise, these two effects compete to an optimal Ramsey time T_R [1]. Lower relaxation hence allow greater optimal T_R which improve the short-term stability of the clock. In this section, a method for measuring the relaxation rates with high statistical confidence is presented.

3.3.2 Method

3.3.2.1 Problem statement

It is tempting to think that the relaxation rates could be measured from the Ramsey fringes whose shape is described by eq. (2.26). Unfortunately, in absorption measurement, one has to take account for the Beer-Lambert law (see eq. 2.31). In the thin layer approximation, the signal $I(\Omega_m)$ read on the photodiode is:

$$\begin{aligned} I(\Omega_m) &= \alpha\Delta(\Omega_m) + \beta \\ &= \alpha\Delta_0 e^{-\gamma_1 T_R}\left(m_{33}^2 - e^{-(\gamma_2-\gamma_1)T_R}(m_{13}^2+m_{23}^2)\cos\left(\Omega_m T_R - \varphi\right)\right) + \beta, \end{aligned} \tag{3.10}$$

with $\Delta(\Omega_m)$ the population difference at the end of the Ramsey cycle as described by eq. (2.26) and α and β two empirical constants who depend on the vapor density and light detuning. Looking at eq. 3.10 it is clear that fitting the experimental Ramsey fringes would only allow to estimate the quantities $\Delta\gamma = \gamma_2 - \gamma_1$ and β.

Measurements of the relaxation rates can be achieved by measuring successive Ramsey fringes for sweeping T_R and using the well-known relations [131]:

$$\text{contrast} \propto e^{-\gamma_2 T_R} \tag{3.11}$$

and [132]:

$$\text{background} \propto e^{-\gamma_1 T_{Dark}} \tag{3.12}$$

where T_{Dark} is the time separating pumping and interrogation in a Ramsey cycle without microwave pulses also known as a Franzen cycle [132]. The two cycles are compared on Figure 3.22.

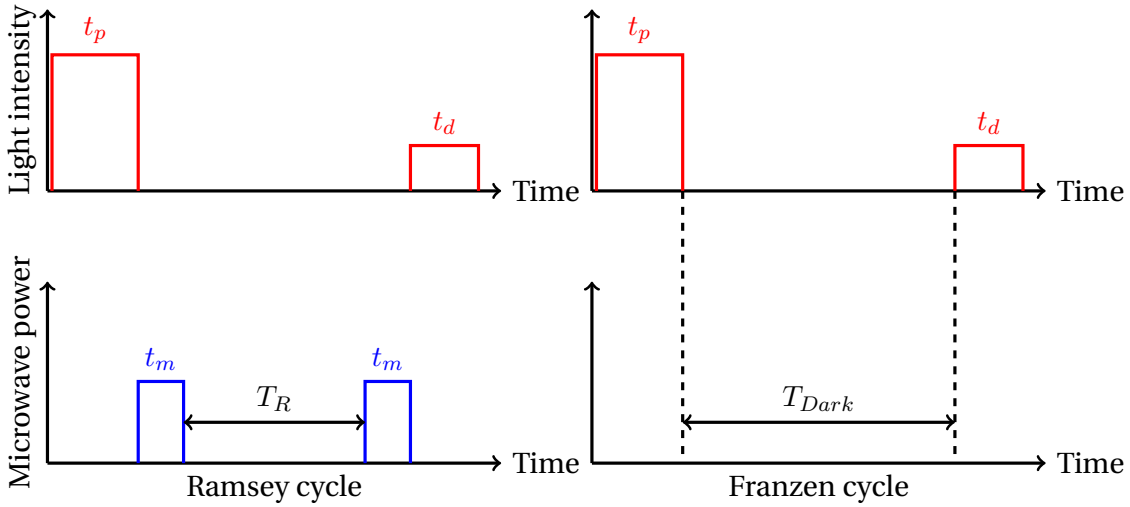

Figure 3.22: **Left:** Ramsey cycle. **Right:** Franzen cycle.

However, rapidly sweeping the Ramsey time changes the thermal cycle of the AOM, requiring to wait for thermal equilibrium between each Ramsey fringes acquisition. This is not suitable for measuring the relaxation rates efficiently for a wide range of cell temperatures. This is illustrated on Figure 3.23.

3.3.2.2 Solution

This section presents a solution to the problems raised in the previous section. The method is inspired by the work of [133] and [134] who spatially imaged the relaxation rates fields inside of a vapor-cell. It is straightforward to extend the formalism developed in section 2.2.2 for the Franzen cycle. In particular, eq. (2.22) becomes:

$$M_m^{Franzen}(T_R) = \text{diag}(1,1,1). \tag{3.13}$$

It is then also straightforward to show that the equivalent of eq. (2.26) for the Franzen cycle becomes, with $T_{Dark} = T_R + 2t_m$:

$$\Delta_{Franzen} = \Delta_0 e^{-\gamma_1 T_R}, \tag{3.14}$$

which does not depend on the microwave detuning.

In both Ramsey and Franzen cases, the signal on the photodiode reads:

$$I_{cyc}(\Omega_m, t) = I_0(t) e^{\alpha \Delta_{cyc}(\Omega_m)+\beta}, \quad cyc \in \{Ramsey, Franzen\}, \tag{3.15}$$

were $I_0(t)$ indicates that the input laser intensity can vary with time.

We can now compute the change in optical density, namely:

$$\begin{aligned}\Delta OD(\Omega_m, T_R) &= \ln\left(I_{Ramsey}/I_{Franzen}\right) \\ &= \alpha\Delta_0\left(\Delta_{Ramsey} - \Delta_{Franzen}\right) \\ &= \underbrace{\alpha\Delta_0\left(m_{33}^2 - 1\right)}_{A(\Omega_m)}\left(e^{-\gamma_1 T_R} + e^{-\gamma_2 T_R}\cos\left(\Omega_m T_R - \varphi\right)\right),\end{aligned} \tag{3.16}$$

were one used the identity $m_{33}^2 - 1 = m_{13}^2 + m_{23}^2$ (see eq. (2.27)). Eq. (3.16) shows that acquiring a set of Ramsey fringes and Franzen allows to extract (γ_1, γ_2) by looking at the evolution of the signal at one Ω_m and fitting eq. (3.16) as a function of T_R. Consequently, many estimations of the relaxation rates can be extracted from the same set of ΔOD fringes. Furthermore, eq. (3.16) does not depend on external time fluctuation of the light intensity. This is illustrated in Figure 3.23.

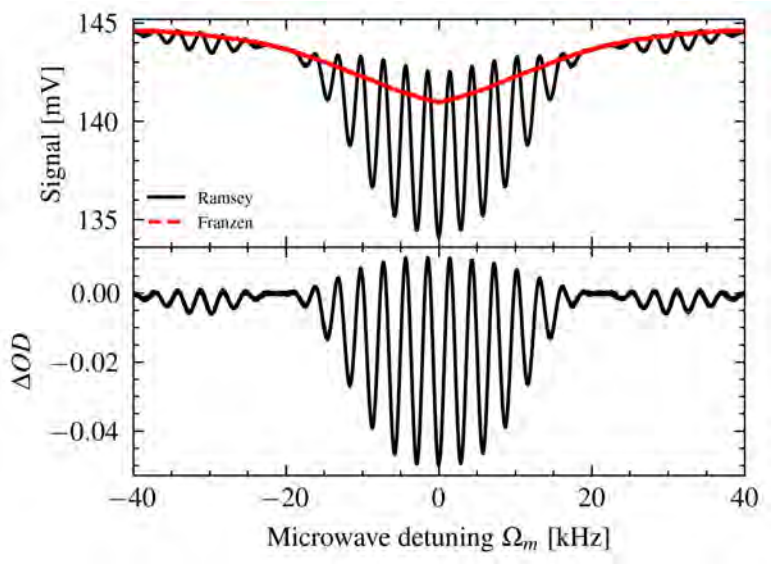

Figure 3.23: **Top:** Ramsey and Franzen signal with respect to microwave detuning. Ramsey and Franzen signals are taken sequentially for each detuning, starting at $\Omega_m = 0$. In the absence of microwave (i.e. Franzen), the signal should be flat. The variation is solely due to the fluctuation of the light intensity. **Bottom:** Variation of optical density, independent of the light intensity fluctuations.

3.3.2.3 Data usability restrictions

When fitting eq. (3.16) as a function of T_R, not all microwave detunings allow to have enough oscillations or points per oscillations to fit eq. (3.16) with good enough statistical confidence. Let us note δ_R the microwave step when scanning ΔOD fringes and T_R^{max} and T_R^{min} the maximum and minimum swept Ramsey times. The number of points N available for plotting eq. (3.16) is hence:

$$N = \frac{T_R^{max} - T_R^{min}}{\delta_R} + 1. \tag{3.17}$$

The number of oscillations n is given by:

$$\Omega_m \cdot (T_R^{max} - T_R^{min}) = n \cdot (2\pi) \quad \Rightarrow \quad \Omega_m/(2\pi) = \frac{n}{T_R^{max} - T_R^{min}}. \tag{3.18}$$

The number of points per oscillation, m, is related to these quantities with:

$$m = N/n \quad \Rightarrow \quad \Omega_m/(2\pi) = \frac{1}{\delta_R(m-1)}. \tag{3.19}$$

Setting constraints on the number of oscillations and number of points per oscillations, one has:

$$\frac{n}{T_R^{max} - T_R^{min}} \leq |\Omega_m/(2\pi)| \leq \frac{1}{\delta_R(m-1)}. \tag{3.20}$$

In practise, oscillations were acquired with $n = 3$, $m = 10$, $T_R^{max} = 450$ μs, $T_R^{min} = 0$ μs and $\delta_R = 10$ μs which means that the usable detunings are:

$$6.6 \text{ kHz} \leq |\Omega_m/(2\pi)| \leq 11.1 \text{ kHz}. \tag{3.21}$$

Example of oscillations are shown on Figure 3.24 along with the estimation of the relaxation rates for one selected cell temperature.

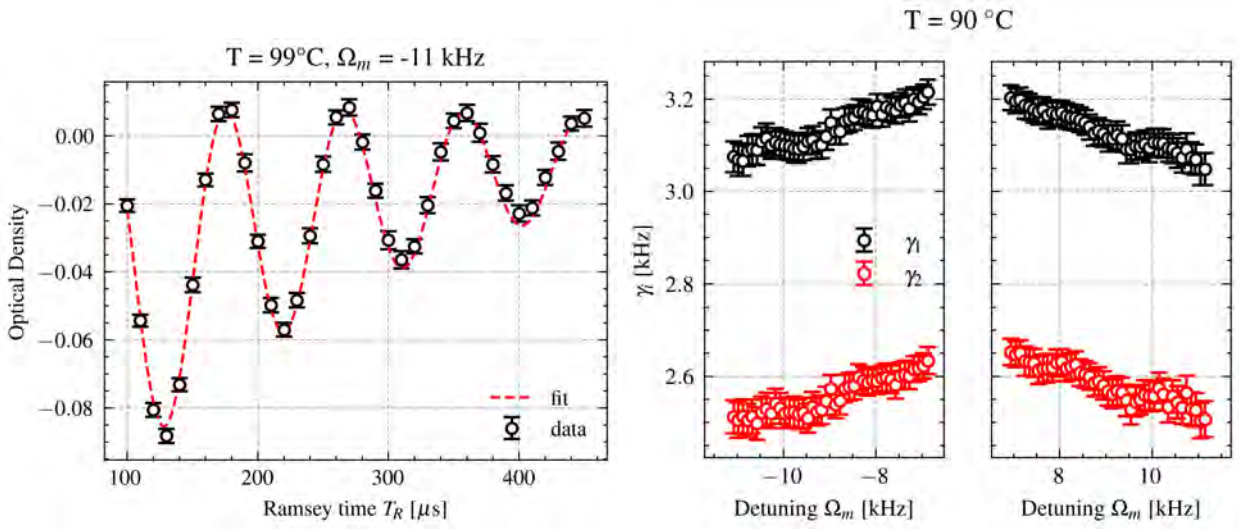

Figure 3.24: **Left:** Optical density oscillations obtained for the detuning $\Omega_m/(2\pi) = -11$ kHz at $T_{cell} = 99°$C. **Right:** All relaxation rates obtained for $T_{cell} = 90°$C.

3.3.3 Relaxation rates dependency with respect to the cell temperature

The relaxation rates in the cell are given by [135]:

$$\gamma_i = \gamma_i^{wall} + \gamma_i^{coll} + \gamma_i^{se} \tag{3.22}$$

with γ_i^{wall} the diffusion term depending on the cell radius R, the cell height L, the diffusion constant D_0 at a reference pressure P_0, P the buffer gas pressure and T [K] the cell temperature:

$$\gamma_i^{wall} = \left[\left(\frac{2.405}{R}\right)^2 + \left(\frac{\pi}{L}\right)^2\right] \tilde{D}\frac{P_0}{P}\left(\frac{T}{273}\right)^{3/2}, \tag{3.23}$$

with $\tilde{D}$ the effective diffusion constant of Rb atoms in the buffer gas mixture given by [136]:

$$\frac{1}{\tilde{D}} = \sum_j \frac{p_j}{D_j}, \quad \sum_j p_j = 1 \tag{3.24}$$

with $\{D_j\}$ the individual diffusion constants of the Rb atoms in the j species. Note that contrarily to [135], the dependence of the diffusion constant to temperature is explicitly written. Note that eq. (3.24) was proved incorrect for some exotic cases by the same authors [136].

γ_i^{coll} is the buffer-gas collision term:

$$\gamma_i^{coll} = \sum_j L_0 \frac{P}{P_0} \cdot \bar{v}_{Rb-j}(T) \cdot \sigma_{i,Rb-j}(P) \tag{3.25}$$

with $L_0 \approx 2.7 \times 10^{25}$ [m^{-3}] the Loschmidt constant, $\bar{v}_{Rb-bg}(T)$ [m/s] the average velocity between the Rb atoms and the buffer gas j and $\sigma_{i,Rb-j}(P)$ [m^{-2}] the collision cross-section between the Rb and the buffer gas j.

γ_i^{se} is the Rb-Rb spin-exchange term is independent on the buffer-gas pressure and depends on the Rb atom density $n_{Rb}(T)$ [m^{-3}] [137] only:

$$\gamma_1^{se} = n_{Rb}(T) \cdot \bar{v}_{Rb-Rb}(T) \cdot \sigma_{se} \quad \text{and} \quad \gamma_2^{se} = \frac{6I+1}{8I+1}\gamma_1^{se} \tag{3.26}$$

with $v_{Rb-Rb}(T)$ [m/s] the mean velocity between the Rb atoms, σ_{se} [m^{-2}] the Rb-Rb collision cross section and $I = 3/2$ the nuclear spin.

3.3.4 Results

Relaxations rates were measured for a wide range of cell temperatures, namely $T_{cell} \in [60, 99]$°C. For each temperature, 150 Ramsey and Franzen fringes are measured to build the change in optical density ΔOD oscillations of eq. (3.16) and dozen of (γ_1, γ_2) estimations are measured. The result is presented on Figure 3.25 along with the model of eq. (3.22). Note that the theoretical line is not fitted

on the data but calculated from eq. (3.22) which only uses atomic parameters published in literature.

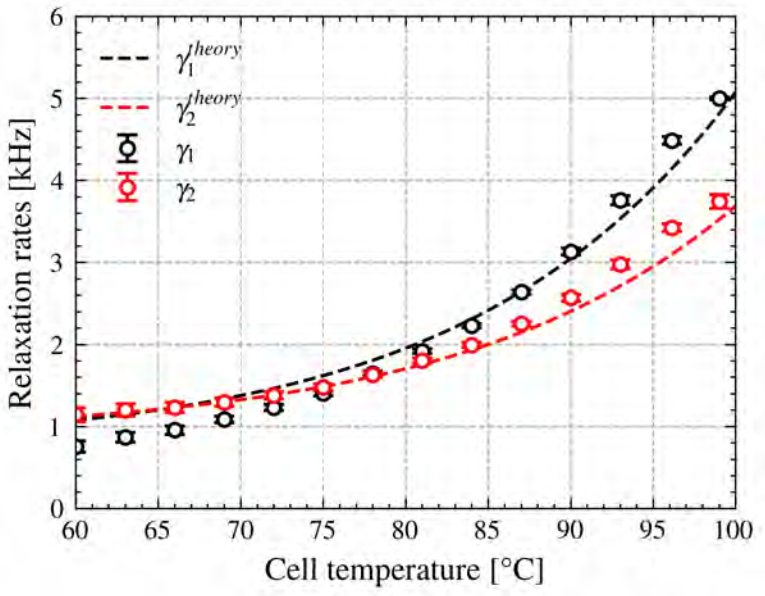

Figure 3.25: Measured and estimated relaxation rates with respect to the cell temperature.

Measurements of the relaxation rates fit the theory relatively well. The inversion point (i.e. where $\Delta\gamma$ changes sign) is experimentally reached at $T \approx 78°$C and was expected to be reached at $67°$C. Overall, the measured and expected values order of magnitude correspond. The γ_2 discrepancy increases with respect to temperature for a maximum of 10%. The γ_1 discrepancy is more important and changes sign with higher and lower prediction in the lower and higher cell temperatures, respectively. The highest discrepancy is found at $T = 60°$C and is around 20%.

Possible explanations for the discrepancies arise from the model. First, eq. (3.24) is known to be inexact is some exotic cases. Second, the individual diffusion constants dependence on temperature found in eq. (3.23) is known to be exact to 8% [138], which is of the same order of magnitude of the found discrepancy. In the same term, the geometrical term depending on the cell geometry is a first order approximation assuming that the interrogated atoms are far from the cell's wall [5] which is questionable for the miniature cell case. Finally, all terms of eq. (3.22) depend on many experimental parameters (e.g. cross sections, diffusion constants) whose uncertainties are amplified by the needed corrections for pressure, temperature and multi-buffer-gas mixture. in view of these considerations, the witnessed small discrepancy is reasonable.

3.4 Comparison with other miniature-cell clocks

Figure 3.26 shows the μPOP performances compared to the most recent and relevant miniature cell atomic clocks. Although figure 3.26 is quite busy, the μPOP distinguishes itself with the best overall performances. At one day, the μPOP performances with $\leq 2 \times 10^{-12}$ are matched by the most recent work form [96] with Cs CPT that features a rather complicated scheme with microwave power and light intensity servos and improved vapor-cell with low permeation windows. It is worth mentioning that implementing a microwave power servo loop would also greatly improve the μPOP performances as is was shown that this is the second limiting contributor to the long-term stability. Table 3.2 suggests that reducing the microwave-power and position shifts contributions would improve the performances of the clock to 2×10^{-13} at one day, with a limitation by the intensity light-shift.

Apart from the μPOP, only two Rb DR clocks are displayed among which is the mRO with the second best short and mid-term performances which advocates for the Rb DR approach compared to Cs and Rb CPT. The mRO features a VCSEL which could give and idea of the performances of a potential second version of the μPOP with lower SWaP featuring a VCSEL instead of a DFB. Indeed, VCSEL having higher RIN and the μPOP being limited by the laser RIN as shown in [1], it seems reasonable to expect that the short-term performances would be slightly degraded.

3.5 SWaP estimate

In order to give an estimate of the muPOP SWaP, it is assumed that electronics can be miniaturized and hence its SWaP can be neglected. The used laser head has a volume of 2.4 L and power consumption 1.5 W [105] for a weight of the order of 0.5 kg. For the physics package, we will assume similar SWaP as the LEMAC **Pellaton2012!** (**Pellaton2012!**) with a volume of 0.36 L with an estimated weight of 0.1 kg. Neglecting the heating current and microwave power generation, the estimated SWaP is ≈ 2.5 L·kg·W. It is hence clear that the clock's SWaP is dominated by the laser head's. As developed in this chapter's conclusion, efforts towards a lower SWaP μPOP clock should focus on the laser head.

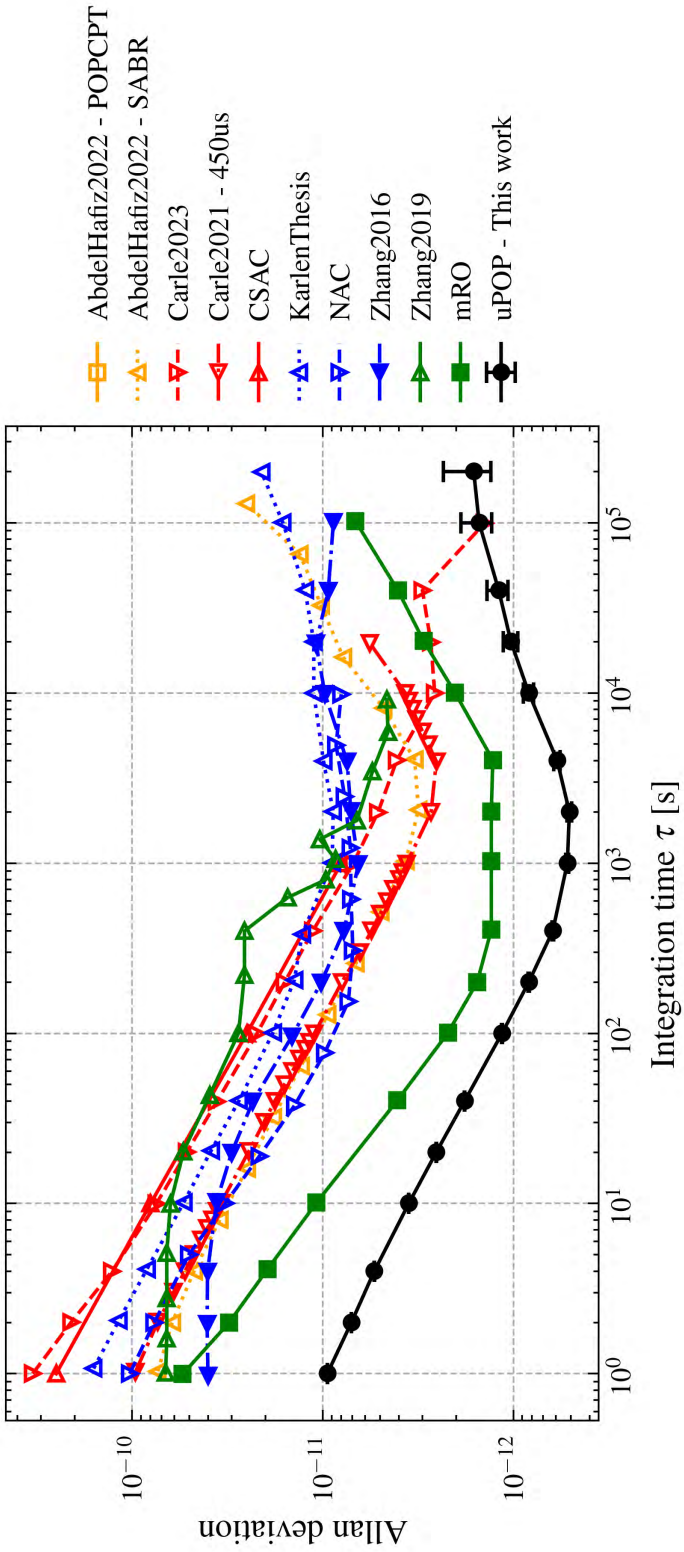

Figure 3.26: Performances of current state-of-the-art microcells, product or research, atomic clocks. Red (blue) colors represent Cs (Rb) atomic clocks. Filled (not filled) markers represent DR (CPT) atomic clocks. When different Allan deviations were available, the trace with the best long-term stability was chosen. When available, traces with drift have been preferred. Most recent results of the same clock have been preferred. AbdelHafiz2022 POPCPT and SABR: [139], Carle2023: [96], Carle2021: [140], CSAC: [141], mRO: [50], NAC: [142], Zhang2016: [143] and Zhang2019: [144].

3.6 Conclusion and next steps

This chapter has presented results on the μPOP studies. First, the feasibility of Ramsey-type operation in Rb miniature vapor-cell was demonstrated with state-of-the-art stability with accurate short-term stability optimization and estimation [1].

Supplementary studies on the μPOP experiment have been discussed. The full long-term stability budget was given. The first important result is the evident reduction of the frequency and intensity light-shift effects which normally limit high-performance Rb DR and CPT clocks. In the long-term, as shown in Table 3.2, both effects results in clock stability limitation two and one order of magnitude lower than the measured stability, respectively.

The re-evaluated long-term stability budget presented here matches well the clock stability measured at $96°$C cell temperature. Consolidation of the budget was performed thanks to two improvements: first, taking into account for correlations between the vertical and horizontal positions of the laser on the physics package could explain the stability in the early mid-term and long-term. Second, measurement of the microwave power stability of the Local Oscillator (LO) in POP mode showed deteriorated performances compared to the CW mode which explains the limitation of the clock in the mid-term.

The fluctuations of the laser position can be attenuated in different ways. First, the physics package could be placed in a atmospheric-controlled environment at the expense of higher SWaP or in a sealed package with no impact on SWaP which would mitigate the humidity fluctuations which are correlated to the clock frequency. Second, the optical path between the laser head and the physics package could be shortened. Unfortunately, in the current laboratory setup, the minimal distance is constrained by the length needed to separate the AOM first order from the others. One possible solution would be to use a fibre-coupled AOM or miniature optical switch.

The microwave sensitivity of the clock could be lowered by implementing a slightly different cycle as proposed by [145]. Such efforts would allow for improved mid-term stability as the microwave powershift is closely tailing the position shift contribution.

In the last section, a new method for measuring the relaxation rates was detailed. This new method is insensitive to fluctuations of the light intensity and allows to extract more data from the same type of measurements which strongly increases the statistical confidence levels. The measured relaxation reasonably fit theory.

There are two obvious next steps: first, implementing the μPOP approach in the newly developed LEMAC compact physics package [146] which features improved C-field homogeneity which could potentially lower the position shift effect. Furthermore, the package could possibly encapsulate a fibre-coupled AOM which goes towards the SWaP reduction needed for portable applications.

Second, developing an AOM-free pulsed laser head as proposed in [147] is a step needed for truly portable applications that could benefit all current Rb POP DR clocks.

Chapter 4

Design and realization of an additive-manufactured microwave cavity for a grating magneto-optical-trap cold-atom clock

This chapter presents the steps and studies towards the realization of an additively manufactured microwave cavity for a GMOT cold-atom clock. This work was published in the journal article [12] included on the following pages. The rest of the chapter aims at completing the work presented in the paper. In particular, deeper details on the simulation and fabrication process are discussed before concluding on the next steps.

Journal of Applied Physics ARTICLE scitation.org/journal/jap

An additive-manufactured microwave cavity for a compact cold-atom clock

Cite as: J. Appl. Phys. 133, 224401 (2023); doi: 10.1063/5.0151207
Submitted: 20 March 2023 · Accepted: 16 May 2023 ·
Published Online: 8 June 2023

Etienne Batori,[1] Alan Bregazzi,[2] Ben Lewis,[2] Paul F. Griffin,[2] Erling Riis,[2] Gaetano Mileti,[1,a)] and Christoph Affolderbach[1]

AFFILIATIONS

[1]Université de Neuchâtel, Institut de Physique, Laboratoire Temps-Fréquence, Avenue de Bellevaux 51, 2000 Neuchâtel, Switzerland
[2]SUPA and Department of Physics, University of Strathclyde, G4 0NG Glasgow, United Kingdom

[a)]**Author to whom correspondence should be addressed:** gaetano.mileti@unine.ch

ABSTRACT

We present an additive-manufactured microwave cavity for a Ramsey-type, double resonance, compact cold-atom clock. Atoms can be laser cooled inside the cavity using a grating magneto-optic trap with the cavity providing an excellent TE_{011}-like mode while maintaining sufficient optical access for atomic detection. The cavity features a low Q-factor of 360 which conveniently reduces the cavity pulling of the future clock. Despite the potential porosity of the additive-manufacturing process, we demonstrate that the cavity is well-suited for vacuum. A preliminary clock setup using cold atoms allows for measuring the Zeeman spectrum and Rabi oscillations in the cavity which enables us to infer excellent field uniformity and homogeneity, respectively, across the volume accessed by the cold atoms. Ramsey spectroscopy is demonstrated, indicating that the cavity is suitable for clock applications. Finally, we discuss the limitations of the future clock.

I. INTRODUCTION

In the field of atomic clocks and frequency standards, the application of laser cooling and trapping has brought significant breakthroughs, in particular, with cold atomic fountain clocks.[1] It is also widely used in more portable or compact industrial clocks[2,3] and gravimeters.[4,5] In the meantime, Ramsey-type optical-microwave double resonance (DR) clocks based on hot vapor-cells have been studied extensively for future portable,[6] compact and space-grade,[7,8] and miniature cell[9] clocks. Although they achieve state-of-the-art stabilities, they remain limited by a variety of effects such as strong coupling with fluctuating external parameters,[6,10] vapor-cell frequency ageing,[11] and high relaxation rates. Similar limitations apply to vapor-cell coherent population trapping (CPT) clocks. Cold-atom CPT and DR frequency standards are, hence, excellent candidates for the next generation of compact atomic clocks.

To reduce the cooling and trapping complexity for reduced size, weight, and power (SWaP) applications, grating magneto-optical traps (GMOTs) can be used to create a 3D MOT.[12] In this case, a silicon grating is etched to diffract one incoming beam into three opposing beams. The four beams allow the creation of a 3D MOT. This technology has already been applied to CPT Ramsey clocks[13–15] and a CPT mini-fountain.[16] However, CPT clocks' low contrast and strong light-shift sensitivities make them less stable in the short- and long-term, respectively. Unlike in miniature cell clocks, portable and high-performance CPT and DR Ramsey clocks based on vapor-cell or cold atoms share similar SWaPs, which eventually favors the latter at the price of developing a microwave cavity allowing for cooling and trapping the atoms.

To date, different microwave cavity geometries for compact cold-atom and vapor-cell clocks have been used: spherical,[2] cylindrical,[17,18] and loop-gap resonator (LGR).[19–22] lGR techniques allow the creation of sub-wavelength, and hence, more compact cavities as small as a few mm wide.[23] Additive manufacturing (AM) of such microwave cavities for compact vapor-cell clocks has already been demonstrated[24,25] with a typical quality factor of $Q_c \approx 70$. While a high cavity quality factor favors low phase shift and, hence, more accurate clocks,[19] a low-quality factor lowers the cavity-pulling effect[26] which is of great interest for realizing more stable clocks.

Here, we present the conception, simulation, and realization of a vacuum-grade aluminum AM microwave cavity for a compact ^{87}Rb cold-atom clock. The atom cooling and trapping are achieved using only one laser beam incident on a GMOT hosted inside the cavity.

II. CLOCK CONCEPT AND CAVITY

A. Concept

In DR Ramsey ^{87}Rb clocks, the clock transition with $\nu_0 = 6.835$ GHz [see Fig. 1(c)] is interrogated with light and microwaves in a pulsed manner. After a trapping and cooling stage for a time t_{load}, a short optical state selection stage is utilized to prepare the atoms in the relevant initial clock state for interrogation. This state preparation beam propagates perpendicular to the cavity axis. The atoms are then driven between the atomic levels $|F = 2, m_F = 0\rangle$ and $|F = 1, m_F = 0\rangle$ using two $\pi/2$ microwave pulses of length t_m separated by the Ramsey time T_R. The atomic populations are subsequently readout using an absorption method, with an additional beam, also aligned perpendicular to the cavity axis co-parallel to the state selection beam, during a time t_{det}. This concept is illustrated in Figs. 1(a) and 1(b).

In these conditions, the so-called light-shift effects on the clock transition are minimized compared to CW or CPT operation where the light is on during the clock part of the cycle. In principle, the short-term stability of the clock linearly improves with t_m and T_R as the atomic transition quality factor Q_a equals,[27]

$$Q_a = 2\nu_0\left(T_R + \frac{4}{\pi}t_m\right), \tag{1}$$

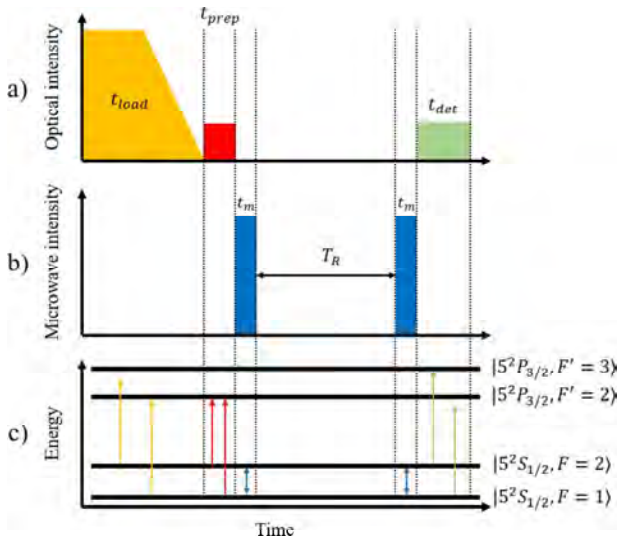

FIG. 1. (a) Optical intensity with respect to time. Pulses lengths are not to scale. The different pulses heights represent the differences in intensities. (b) $\pi/2$ microwave pulses separated by Ramsey time T_R. (c) Relevant ^{87}Rb D2 line energy levels with corresponding excitation frequencies with respect to time.

and the short-term stability of a signal-to-noise ratio (SNR)-limited clock is estimated as

$$\sigma(\tau) = \frac{1}{\pi C Q_a}\frac{1}{SNR}\sqrt{\frac{T_C}{\tau}}, \tag{2}$$

with $T_C = t_{load} + t_{prep} + 2t_m + T_R + t_{det}$ is the total cycle time and C is the fringe contrast.

Cold atoms allow for increased interrogation times T_R due to low atomic speed (low atom temperature) and, hence, extended interrogation time in a finite interaction region. High-performance vapor-cell Ramsey operations typically show Ramsey times of the order of 3 ms[6], whereas a GMOT CPT mini-fountain demonstrated T_R as long as 100 ms.[16]

Atom trapping and cooling is achieved using a diffraction grating, placed at the bottom of the cavity (see Fig. 2). In this geometry, a single input beam is sufficient. Two side holes in the cavity body are placed at the relevant height to prepare and probe the atom cloud. This simplifies the cavity design requirements as only three holes instead of the traditional six are necessary. Furthermore, the flat grating allows us to interrogate the atoms right after the MOT sequence which would not be possible in a pyramid structure.[20] In principle, the atoms can be interrogated either with an absorption or fluorescence measurement.

B. Cavity design

The LGR cavity geometry model is presented in Fig. 3. With this electrode structure, cavities much smaller than the wavelength of the mode can be realized which is of great interest for compact physics packages. The use of additive manufacturing allows for greater control and repeatability on such exotic electrode structures which cannot be easily attained with traditional manufacturing, especially when it comes to producing unique and small batches. A

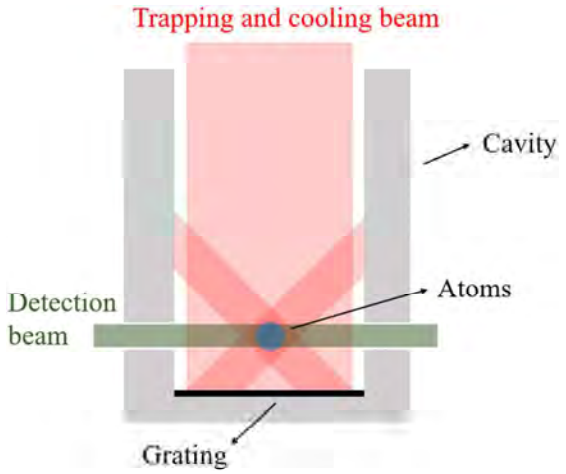

FIG. 2. Concept of a microwave cavity with integrated grating. The ensemble is placed in a vacuum chamber.

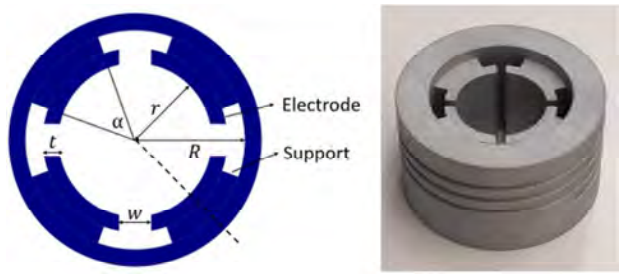

FIG. 3. Left: planar view of the LGR geometry. The dashed line indicates the zero-degree reference for the microwave coupling loop, see Fig. 8. Right: AM cavity body prior to holes being drilled.

coarse estimate of the cavity resonance frequency ν_c can be made using Eq. (3) with n being the number of electrodes, R and r the outer and inner diameters, and t and w the width and thickness of the gaps,[28]

$$\nu_c = \frac{1}{2\pi}\sqrt{\frac{nt}{\pi r^2 \epsilon \mu w}}\sqrt{1+\frac{r^2}{R^2-(r+w)^2}}\sqrt{\frac{1}{1+2.5\frac{t}{w}}}, \tag{3}$$

with ϵ(F/m) and μ(N/A^2) being the permittivity and permeability inside of the cavity, respectively. Due to the absence of a vapor cell, the design is slightly simpler and the values for vacuum permittivity and permeability are used. Although Eq. (3) yields the correct order of magnitude for the mode frequency, it is necessary to take the full geometry into account such as the height of the cavity h, the electrode support angle α (see Fig. 1), the cavity material and the placement and geometry of the microwave coupling loop.

The grating is excluded from the simulations for the sake of time saving and because it has shown little impact on the final mode frequency. The cavity geometry is slightly different from previous vapor-cell designs with the addition of newer constraints. First, the presence of two 4-mm diameter side holes for the purpose of MOT diagnostics, state preparation, and detection at the position of the atom cloud. Second, an inner cavity diameter that is sufficiently large to house the $2\times2\,\mathrm{cm}^2$ grating chip and an upper aperture wide enough to allow the alignment of the trapping and cooling beam onto the grating surface.

These last requirements mainly put lower limit constraints on R and r.

Eigenfrequency analysis sweeping n, h, α, R, r, w, and t is first performed to find a suitable set of parameters yielding a TE$_{011}$-like mode. The distance to the closest neighboring mode should be much larger than the full width at half maximum (FWHM) of the mode. An example of such a sweep is shown in Fig. 4, sweeping t and w which shows that a large set of (t, w) combinations is suitable for realizing the cavity indicated by the area between the two white contours. The figure shows the chosen combination which favors high t and w so that eventual manufacturing inaccuracies have a smaller impact. For all suitable configurations, the closest neighboring mode is at least 800 MHz away.

The expected magnetic field H$_z$ component and phase along the central axis of the cavity above the grating are presented in Fig. 5. In the current experimental design, the atoms are prepared above the grating and then fall toward it in the least uniform part of the cavity field. Future designs should make use of the most uniform part of the cavity by pushing the atoms away from the grating. In all cases, as the field spatially varies between the two points where the atoms are interrogated, the pulses might have to show different injected microwave power or duration to ensure $\pi/2$

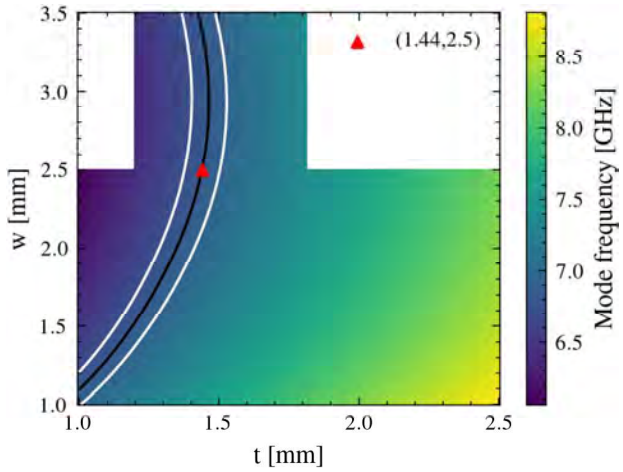

FIG. 4. Best TE$_{011}$-like mode frequency (GHz). The black line represents configurations with 6.8347 GHz mode frequency. The white lines are ±100 MHz boundaries that represent the range that can be recovered by adjusting the cavity height.

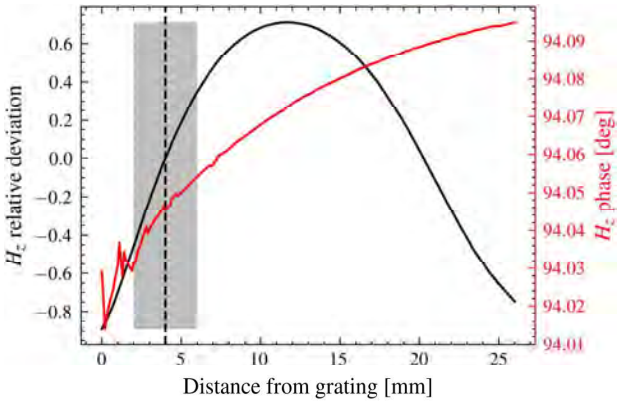

FIG. 5. H$_z$ amplitude deviation and phase above the grating. The dashed line represents the initial atom cloud position. The deviation is normalized by the value of the H$_z$ field at the initial position of the atoms. The gray area shows the region accessible to the first version of the clock setup.

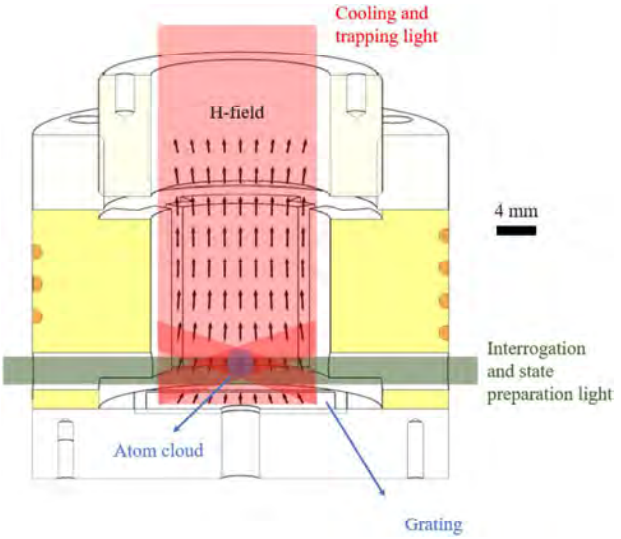

FIG. 6. Final cavity model, to scale.

pulses.[19] In a sphere of 1 mm diameter—which is of the order of the initial size of the atomic cloud—at its initial position, the H_z field and phase show deviations of 4% and 42 ppm, respectively.

The final cavity model is presented in Fig. 6, to scale. The cavity body shown in Fig. 3 was manufactured by a commercial additive-manufacturing service, using a standard CL31AL material according to DIN EN 1706 AlSi10Mg(b), while the other simpler and less critical parts were manufactured in our workshop in 6082 Al alloy.

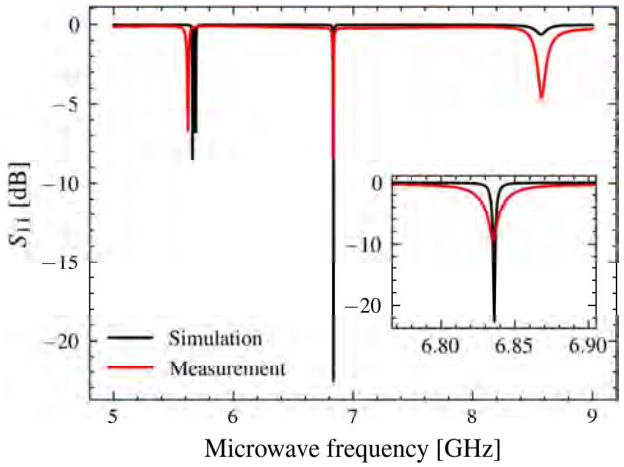

FIG. 7. Simulated and measured S_{11} spectrum of the cavity. The main figure and the inset share the same axis units.

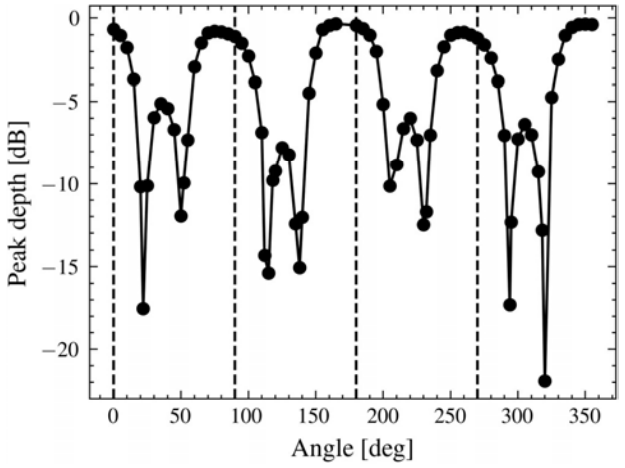

FIG. 8. Measured microwave mode peak depth with respect to the rotation angle between the microwave coupling loop and the cavity. See Fig. 3 for the 0° reference position. Given the angle, coupling to the mode of interest can be either enhanced or depleted.

C. Mode characterization

Figure 7 compares the simulated and measured cavity S_{11} microwave reflection spectrum over a wide frequency range. The simulation and measurement agree well on the mode positions with a small discrepancy of 60 MHz for the mode of interest, which can be easily compensated by adjusting the height of the cavity. As predicted by the simulation, the left and right neighboring modes are 1.2 and 1.8 GHz away, respectively. They do not overlap with the mode of interest so that the field geometry is not degraded. The 8.5 GHz resonance is associated with a mode whose field energy is concentrated around the microwave coupling loop and low sensitivity to the other cavity parameters. The loop is realized as a small, rectangular copper wire loop of approximately 9 mm^2 cross section with one end connected to the SMA core.[29] According to our simulations, the precise loop geometry does not strongly influence the mode of interest, but rather the 8.5 GHz mode, which is of no major concern for our application due to the large distance between the two modes. However, the loop position relative to the electrodes is quite critical for the efficient coupling of microwave radiation to the cavity, as illustrated by Fig. 8.

The simulated and measured S_{11} of the 6.835 GHz mode (see the inset of Fig. 7 and Table I) differ in depth and FWHM. This is explained first because the simulation did not include any wall

TABLE I. Cavity mode FWHM and Q-factor simulation vs measurement comparison.

	FWHM (MHz)	Q_c	Depth (dB)
Simulation	4	1709	−23
Measurement	19	360	−9

roughness which is not realistic, given the AM process. Second, for the sake of simulation time, the grating was not included in the simulation. With its etched nature, it exhibits increased impedance to surface currents which also participates in power losses and, hence, line broadening. Lastly, the loss of mode amplitude is attributed to the high sensitivity of the mode to the angle between the microwave coupling loop and the electrodes, see the measured data in Fig. 8. Although the angle was manually optimized to get a peak depth around −17 dB, corresponding to the loop placed approximately under one of the electrode wings, it was not perfectly preserved when securing the cavity, as evidenced by Fig. 7.

The rather low-quality factor minimizes the cavity-pulling effect, indeed, the cavity-pulling shift,[6,26]

$$\Delta\nu_{cp} = -\frac{4}{\pi}\frac{Q_c}{Q_a}c(\theta)\Delta\nu_c, \tag{4}$$

with Q_c and Q_a being the cavity and atomic transition quality factors, respectively, $c(\theta)$ a function of the microwave pulse area that can be made < 0.005,[26] and $\Delta\nu_c$ the cavity detuning which, under vacuum, only depends on the cavity temperature. The temperature coefficient is measured as $\Delta\nu_c/\Delta T_{cav} = (-156 \pm 9)$kHz/K which is similar to the other models of AM cavities.[6,25]

III. SETUP

A. Experimental clock apparatus

The cavity is mounted in a commercial vacuum chamber, with the grating placed at the bottom of the cavity. Resistively heated dispensers provide the necessary ^{87}Rb vapor. The outgassing properties of the aluminum-based additively manufactured material were studied in a dedicated test chamber using the gas accumulation method.[30] Its outgassing properties were compared to a sample of bulk aluminum. Both samples show similar outgassing rates estimated around 7×10^{-9} mbar m^3 s^{-1} m^{-2} which suggests little to no degradation caused by the additive-manufacturing material compared to the traditional aluminum alloy. Furthermore, measurement of the cold-atom cloud 1/e lifetime[31] gives an estimate of the pressure of the order of 1×10^{-8} mbar, which also indicates this material's suitability for in-vacuum cold-atom applications.

The magnetic field is controlled with three orthogonal sets of Helmholtz coils placed outside of the chamber to minimize the field in the grating plane and apply a C-field along the principal axis of the cavity to separate the Zeeman sublevels. A pair of anti-Helmholtz coils are placed inside the vacuum chamber to allow trapping and cooling. The cavity loop is connected to a commercial microwave generator (Keysight E8257D).

A single 780 nm extended cavity diode laser (ECDL), frequency stabilized with saturated absorption spectroscopy is used throughout. This light is passed through an electro-optical modulator (EOM) to allow the generation of optical sidebands on carrier frequency for hyperfine repumping of the atoms. A tapered amplifier is then used to amplify the light before dividing it into three beam paths for trapping, state selection, and state-detection. Each beam path contains a double-pass acousto-optic modulator (AOM) for intensity and frequency control. Trapping light is coupled into an optical fiber, the output of which is incident on the grating through an aperture in the top of the cavity after expansion and collimation. State selection and detection light are coupled into a common additional fiber. From the fiber, the light is linearly polarized with respect to the magnetic bias field and split with a non-polarizing beam splitter (NPBS). This allows a portion of the light to be monitored on a reference photodiode while the rest of the light is aligned through the side holes in the cavity body and retro-reflected by a mirror back onto a second signal photodiode. This allows normalization of the absorption signal for fluctuations in laser intensity during state-detection.

B. Experimental cycle

The experimental cycle is presented in Fig. 1. The traditional Ramsey cycle is preceded by a trapping and cooling phase by optical molasses of duration t_{load} where the intensity is linearly ramped down from $5I_{sat}$ to $0.1I_{sat}$,[32] while simultaneously scanning the detuning from −12to −30 MHz. After this step, $\approx 1 \times 10^6$ atoms are in the states $|F = 2,\ m_F = \pm 2,\ \pm 1, 0\rangle$ with temperature $\approx 10\,\mu$K. A state selection phase of duration t_{prep} utilizing light of intensity $0.02I_{sat}$ that is linearly polarized with respect to the C-field is then used to prepare the atoms in the clock state. This light is incident on the atoms through the cavity side-hole and is tuned to the $|F = 2 \rightarrow |F' = 2\rangle$state with repump light driving the $|F = 1 \rightarrow |F' = 2\rangle$ transition. Due to selection rules, this pumps more than 95% of the atoms into the $|F = 2,\ m_F = 0\rangle$ level,[33] increasing the signal contrast.

The atoms are then driven with two $\pi/2$ microwave pulses of duration $t_m = 167\,\mu$s separated by a free evolution (or Ramsey) time T_R. The population P_2 in level $|F = 2\rangle$ is estimated by measuring the absorption of a side beam tuned on $|F = 2 \rightarrow |F' = 3\rangle$. This value is normalized by the absorption of the same beam with $\approx$5% $|F = 1 \rightarrow |F' = 2\rangle$ sideband. This second pulse recycles atoms initially shelved in the $F = 1$ ground-state back to the cycling transition and allows normalization for variation of the number of atoms present at each shot. The C-field is optimized for atom cooling and is kept constant during the clock cycle to avoid eddy currents.

IV. RESULTS

A. Rabi oscillations

Rabi oscillations (see Fig. 9) are measured by setting $T_R = 0$ ms. To sweep the microwave pulse area, the microwave time is kept constant and the microwave power is swept. The opposite approach, constant power and sweeping microwave time is disregarded to avoid the influence of time-dependent relaxation processes and atom losses. The first minimum of the Rabi oscillations is used to calibrate the input microwave power to generate $\pi/2$ pulses.

The decay of the Rabi oscillation is due to the residual magnetic field inhomogeneities inside of the atomic volume.[34] The number of visible oscillations, 9, is a sign of excellent H_z homogeneity, which is comparable to other compact cold-atom clocks that show 14 or more oscillations,[35] whereas high-performance vapor-cell clocks such as a ^{87}Rb Ramsey maser show several oscillations

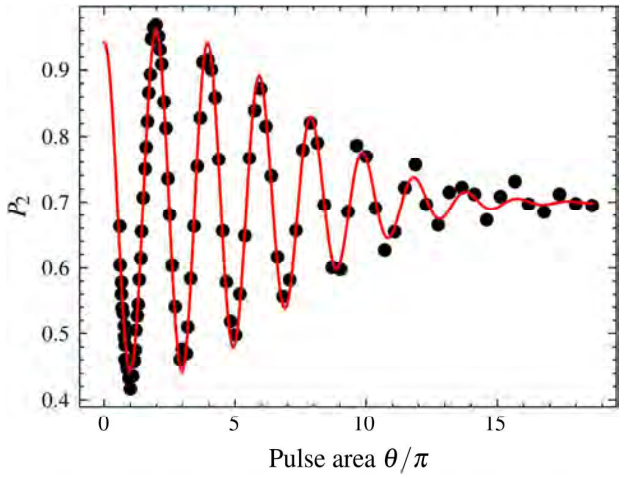

FIG. 9. Rabi oscillations. The pulse area axis is rescaled assuming the first minimum is π.

as low as 3.[36] In the case of vapor-cell clocks, the atoms cover a larger volume inside the cavity, and the field homogeneity is dominated by the TE_{011}-like distribution. In contrast, the oscillation decay presented in Fig. 9 is compatible with a pulse area θ with a gaussian distribution. Indeed, if one assumes a gaussian distribution with a standard deviation σ, relative to the pulse area mean θ, one can show that the form of the textbook $\cos^2(\theta/2)$ Rabi oscillations is modified as follows:

$$P_2(\theta) = \frac{A}{2}\left(1 + e^{-\sigma^2\theta^2/2}\cos(\theta)\right) + C, \tag{5}$$

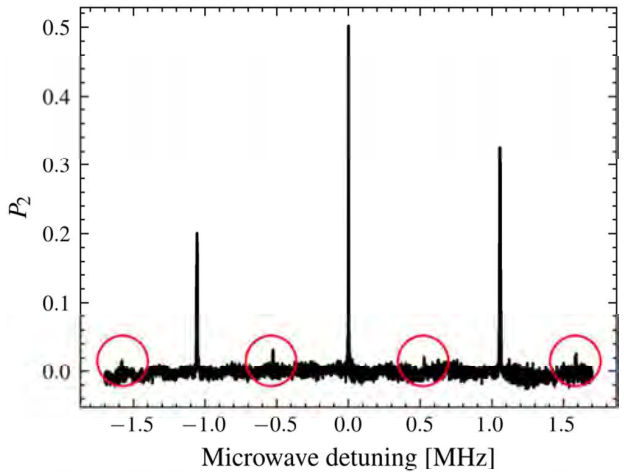

FIG. 10. Zeeman spectrum without state selection. The peaks circled in red are the $\sigma^{\pm}$ transitions.

with A and C as two fit parameters that account for the absorption measurement. With this model, from a fit to Fig. 9, we measure $\sigma = (6.3 \pm 0.1)\%$. The distribution of the field felt by the atoms is given by the convolution of the distribution of the atoms—which is assumed gaussian—and the distribution of the TE_{011}-like field. The smaller the volume spanned by the atoms, the more uniform, the field distribution.

B. Zeeman spectrum

The Zeeman spectrum is presented in Fig. 10. It is intentionally acquired with repump light in the state selection beam extinguished, shelving atoms in the $|F = 1\rangle$ ground-state. The Ramsey cycle is set with $T_R = 0$ ms and optimal microwave power deduced from the Rabi oscillations. Note that the amplitude of π transitions (i.e., transitions with $m_F = m'_F$) peaks at ± 1.1 MHz are slightly asymmetric which is attributed to a small imbalance in the $\sigma^{\pm}$-polarized beams used for trapping and cooling. The Zeeman spectrum shows peaks instead of dips because, in the absence of repump light, the majority of the atoms populate the sublevels $|F = 1, m_F = \pm 1, 0\rangle$ before the microwave cycle.

Note that the $\sigma^{\pm}$ transitions (i.e., transitions with $m'_F = m_F \pm 1$) peaks are only slightly above the noise level, which indicates excellent field homogeneity and alignment with the C-field. The Zeeman spectrum allows us to measure a field orientation factor ξ of 97%, which is a measure of field uniformity that was defined in Ref. 29, namely,

$$\xi = \frac{\int d\nu\, S_\pi}{\int d\nu (S_\pi + S_\sigma)} = \frac{\int_V d^3\vec{r} \cdot H_z^2}{\int_V d^3\vec{r} \cdot \vec{H}^2}, \tag{6}$$

with S_π and S_σ being the Zeeman spectrum π and σ components only, respectively. V is the volume spanned by the interrogated atoms.

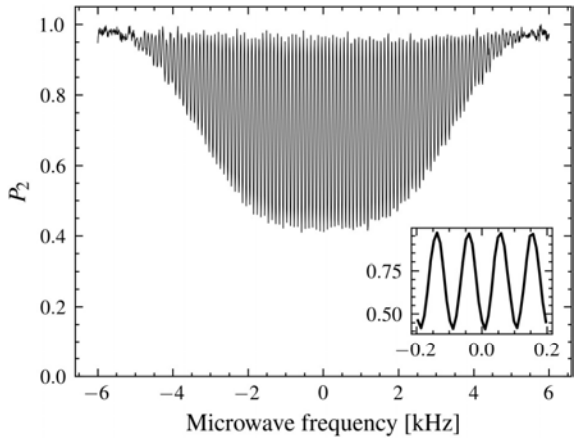

FIG. 11. Ramsey fringes for $T_R = 10$ ms and $t_m = 167\,\mu$s. The main figure and the inset share the same axes.

TABLE II. Nominal time sequence.

Pulse	Duration
T_{load}	516 ms
t_{prep}	1 ms
t_m	167 μs
T_R	10 ms
t_{det}	1.4 ms
T_C (total)	528.7 ms

C. Ramsey fringes and expected clock performances

Ramsey fringes were obtained for Ramsey times up to 20 ms, limited in the current setup by the atoms falling under gravity and leaving the transverse optical beam after this time.[37] Figure 11 shows the optimal[37] SNR Ramsey fringes with $T_R = 10$ ms. The FWHM of the central fringe is 49 Hz and is compatible with Eq. (1). The contrast is 58% due to the state selection. Without the state selection, the maximum contrast is 33%. The noise on the fringes is primarily attributed to magnetic field noise.

The nominal cycle time sequence is shown in Table II.

At one second, the Allan deviation of the future clock should be $\sigma(\tau = 1s) = 4.4 \times 10^{-11}$. The SNR of Eq. (2) is estimated from a sine fit to the central fringe of Fig. 11.[38] A preliminary estimation shows that the Dick effect contribution[39] should be at the level of $\sigma_{Dick}(\tau = 1s) = 1.2 \times 10^{-12}$. A more detailed short-term analysis of the increased performances clock is presented in a more advanced version of the setup.[37] Finally, we estimate the cavity pulling [see Eq. (4)] to be of the order of 2.1×10^{-15} for a reasonable relative cavity temperature fluctuation of 10^{-3}, which is typical at 10^5 s.

V. CONCLUSION

We demonstrated the successful design, simulation, and implementation of a microwave cavity for a novel compact cold-atom DR clock based on intra-cavity atom cooling using a diffractive optical element. An efficient simulation workflow allows us to design the cavity with a small mismatch of the resonance frequency which is easily compensated via a small adaptation of the cavity height. Rabi oscillations and Zeeman spectrum show proof of good field uniformity and homogeneity, respectively.

Short-term performances of the future proof-of-concept clock are estimated to be closer than that of miniature vapor-cell clocks,[9,40] with a Dick effect limitation, one order of magnitude lower. Accordant stability measurement has been demonstrated in an early-stage clock setup with an optimized signal.[37] In order to improve on the short-term stability of future setups, the Ramsey time could be increased by either putting the cavity upside down and interrogating the atoms further down or operating the clock in a mini-fountain fashion with Ramsey times up to 50 and 100 ms,[16] respectively. This will also allow us to interrogate the atoms in regions where the field is more uniform, as suggested by Fig. 5. To improve the Dick effect limit, T_C must be reduced, which can be achieved by implementing atom recapturing at the end of the cycle.[41,42]

ACKNOWLEDGMENTS

E. Batori, C. Affolderbach, and G. Mileti thank V. Dolgovskiy for his contributions in the early design phase, P. Scherler for technical assistance, and G. Bourban for his continued support. This work was financially supported by the Swiss Space Center (Swiss Confederation) and the European Space Agency (ESA, Contract No. 4000131046). The views expressed herein can in no way be taken to reflect the official opinion of the European Space Agency. A.B. was supported by a Ph.D. studentship from the Defence Science and Technology Laboratory (Dstl). We gratefully acknowledge support from the International Network for Microfabrication of Atomic Quantum Sensors (No. EPSRC EP/W026929/1).

AUTHOR DECLARATIONS

Conflict of Interest

The authors have no conflicts to disclose.

Author Contributions

Etienne Batori: Conceptualization (equal); Data curation (equal); Formal analysis (equal); Investigation (lead); Methodology (lead); Software (lead); Validation (lead); Visualization (lead); Writing – original draft (lead); Writing – review & editing (lead). **Alan Bregazzi:** Conceptualization (equal); Data curation (equal); Formal analysis (equal); Investigation (equal); Methodology (equal); Software (equal); Validation (equal); Visualization (supporting); Writing – original draft (supporting); Writing – review & editing (equal). **Ben Lewis:** Conceptualization (equal); Investigation (equal); Methodology (equal); Software (equal). **Paul Griffin:** Conceptualization (equal); Data curation (equal); Funding acquisition (equal); Investigation (supporting); Methodology (supporting); Project administration (equal); Resources (equal); Supervision (equal); Validation (supporting); Writing – original draft (supporting); Writing – review & editing (equal). **Erling Riis:** Conceptualization (equal); Funding acquisition (equal); Project administration (equal); Resources (equal); Supervision (equal); Writing – review & editing (supporting). **Gaetano Mileti:** Conceptualization (equal); Funding acquisition (equal); Project administration (equal); Resources (lead); Supervision (lead); Writing – review & editing (supporting). **Christoph Affolderbach:** Conceptualization (equal); Data curation (equal); Formal analysis (equal); Funding acquisition (equal); Investigation (supporting); Methodology (supporting); Project administration (lead); Resources (equal); Supervision (equal); Validation (supporting); Visualization (supporting); Writing – original draft (equal); Writing – review & editing (equal).

DATA AVAILABILITY

The data that support the findings of this study are openly available in figshare at doi.org/10.6084/m9.figshare.23276357, Ref. 23276357.

REFERENCES

[1]R. Wynands and S. Weyers, Metrologia **42**, S64 (2005).

[2]F. X. Esnault, N. Rossetto, D. Holleville, J. Delporte, and N. Dimarcq, Adv. Space Res. **47**, 854 (2011).
[3]SpectraDynamics, "CRb–clock" (2019), available at https://spectradynamics.com/products/crb–clock/.
[4]IX Blue, "Absolute quantum gravimeter" (2021), available at https://www.ixblue.com/quantum-gravimeter/.
[5]Q. Bodart, S. Merlet, N. Malossi, F. P. Dos Santos, P. Bouyer, and A. Landragin, Appl. Phys. Lett. **96**, 134101 (2010).
[6]N. Almat, M. Gharavipour, W. Moreno, C. Affolderbach, and G. Mileti, in *2019 Joint Conference of the IEEE International Frequency Control Symposium & European Frequency and Time Forum* (IEEE, 2019), pp. 1–2.
[7]E. Batori, N. Almat, C. Affolderbach, and G. Mileti, Adv. Space Res. **68**(12), 4723–4733 (2020).
[8]M. Huang, A. Little, and J. Camparo, in *2022 Joint Conference of the European Frequency and Time Forum & IEEE International Frequency Control Symposium* (IEEE, 2022), pp. 1–4.
[9]E. Batori, C. Affolderbach, M. Pellaton, F. Gruet, M. Violetti, Y. Su, A. K. Skrivervik, and G. Mileti, Phys. Rev. Appl. **18**, 054039 (2022).
[10]W. Moreno, M. Pellaton, C. Affolderbach, and G. Mileti, IEEE Trans. Ultrason. Ferroelectr. Freq. Control **65**, 1500 (2018).
[11]S. Abdullah, C. Affolderbach, F. Gruet, and G. Mileti, Appl. Phys. Lett. **106**, 163505 (2015).
[12]C. C. Nshii, M. Vangeleyn, J. P. Cotter, P. F. Griffin, E. A. Hinds, C. N. Ironside, P. See, A. G. Sinclair, E. Riis, and A. S. Arnold, Nat. Nanotechnol. **8**, 321 (2013).
[13]R. Elvin, M. W. Wright, B. Lewis, B. L. Keliehor, A. Bregazzi, J. P. McGilligan, A. S. Arnold, P. F. Griffin, and E. Riis, Adv. Opt. Technol. **9**, 297 (2020).
[14]R. Elvin, G. W. Hoth, M. Wright, B. Lewis, J. P. McGilligan, A. S. Arnold, P. F. Griffin, and E. Riis, Opt. Express **27**, 38359 (2019).
[15]G. W. Hoth, R. Elvin, M. Wright, B. Lewis, A. S. Arnold, P. F. Griffin, and E. Riis, Proc. SPIE **10934**, 109342E (2019).
[16]B. Lewis, R. Elvin, A. S. Arnold, E. Riis, and P. F. Griffin, Appl. Phys. Lett. **121**, 164001 (2022).
[17]F. G. Ascarrunz, Y. O. Dudin, M. C. Delgado Aramburo, L. I. Ascarrunz, J. Savory, A. Banducci, and S. R. Jefferts, in *2018 IEEE International Frequency Control Symposium* (IEEE, 2018), pp. 1–3.
[18]M. Gozzelino, S. Micalizio, C. E. Calosso, A. Godone, H. Lin, and F. Levi, IEEE Trans. Ultrason. Ferroelectr. Freq. Control **68**, 872 (2021).
[19]S. Lee, G. W. Choi, H.-G. Hong, T. Y. Kwon, S.-B. Lee, M.-S. Heo, and S. E. Park, Appl. Phys. Lett. **119**, 064002 (2021).
[20]M. Givon, L. Habib, A. Waxman, Y. Bar-Haim, O. Amit, Y. Cina, G. Boneh, D. Groswasser, T. David, B. Levy, A. Stern, and R. Folman, arXiv:2208.09038 (2022).
[21]Q. Hao, W. Xue, W. Li, F. Xu, X. Wang, W. Guo, P. Yun, and S. Zhang, IEEE Trans. Ultrason. Ferroelectr. Freq. Control **67**, 873 (2020).
[22]S. Kang, M. Gharavipour, F. Gruet, C. Affolderbach, and G. Mileti, in *2015 Joint Conference of the IEEE International Frequency Control Symposium & European Frequency and Time Forum* (IEEE, 2015), pp. 800–803.
[23]M. Violetti, M. Pellaton, C. Affolderbach, F. Merli, J.-F. Zurcher, G. Mileti, and A. K. Skrivervik, IEEE Sens. J. **14**, 3193 (2014).
[24]M. Pellaton, C. Affolderbach, A. K. Skrivervik, A. E. Ivanov, T. Debogovic, E. Rijk, and G. Mileti, Electron. Lett. **54**, 691 (2018).
[25]C. Affolderbach, W. Moreno, A. E. Ivanov, T. Debogovic, M. Pellaton, A. K. Skrivervik, E. de Rijk, and G. Mileti, Appl. Phys. Lett. **112**, 113502 (2018).
[26]S. Micalizio, A. Godone, F. Levi, and C. Calosso, IEEE Trans. Ultrason. Ferroelectr. Freq. Control **57**, 1524 (2010).
[27]S. Micalizio, C. E. Calosso, F. Levi, and A. Godone, Phys. Rev. A **88**, 33401 (2013).
[28]W. Froncisz and J. S. Hyde, J. Magn. Reson. **47**, 515 (1982).
[29]C. Stefanucci, T. Bandi, F. Merli, M. Pellaton, C. Affolderbach, G. Mileti, and A. K. Skrivervik, Rev. Sci. Instrum. **83**, 104706 (2012).
[30]P. A. Redhead, J. Vac. Sci. Technol. A **20**, 1667 (2002).
[31]C. Monroe, W. Swann, H. Robinson, and C. Wieman, Phys. Rev. Lett. **65**, 1571 (1990).
[32]D. A. Steck, "Rubidium 87 D Line Data," available online at http://steck.us/alkalidata (revision 2.2.2, 9 July 2021).
[33]Y.-X. Duan, B. Wang, J.-F. Xiang, Q. Liu, Q.-Z. Qu, D.-S. Lü, and L. Liu, Chin. Phys. Lett. **34**, 073201 (2017).
[34]W. Moreno, M. Pellaton, N. Almat, M. Gharavipour, C. Affolderbach, and G. Mileti, in *2019 Joint Conference of the IEEE International Frequency Control Symposium & European Frequency and Time Forum* (IEEE, 2019).
[35]P. Liu, Y. Meng, J. Wan, X. Wang, Y. Wang, L. Xiao, H. Cheng, and L. Liu, Phys. Rev. A **92**, 62101 (2015).
[36]A. Godone, S. Micalizio, F. Levi, and C. Calosso, Rev. Sci. Instrum. **82**, 074703 (2011).
[37]A. Bregazzi, E. Batori, B. Lewis, C. Affolderbach, G. Mileti, E. Riis, and P. F. Griffin, arXiv:2305.02944.
[38]S. Negusse and P. Zetterberg, IEEE Trans. Instrum. Measurement **63**, 1514 (2014).
[39]S. Micalizio, A. Godone, C. Calosso, F. Levi, C. Affolderbach, and F. Gruet, IEEE Trans. Ultrason. Ferroelectr. Freq. Control **59**, 457 (2012).
[40]C. Carlé, M. Petersen, N. Passilly, M. A. Hafiz, E. De Clercq, and R. Boudot, IEEE Trans. Ultrason. Ferroelectr. Freq. Control **68**, 3249 (2021).
[41]F.-X. Esnault, E. Blanshan, E. N. Ivanov, R. E. Scholten, J. Kitching, and E. A. Donley, Phys. Rev. A **88**, 42120 (2013).
[42]A. V. Rakholia, H. J. McGuinness, and G. W. Biedermann, Phys. Rev. Appl. **2**, 054012 (2014).

4.1 Supplementary material to "An additive-manufactured microwave cavity for a compact cold-atom clock" [12]

4.1.1 Cavity

4.1.1.1 Cylindrical cavities and TE_{lmn} modes

Let us recall the solutions of Maxwell equations for the magnetic field $\vec{H}$ in a cylindrical cavity of height L and radius r [148]:

$$\begin{aligned} H_r &= \frac{k_3}{k} J_l'(k_1 r)\cos(l\theta)\cos(k_3 z), \\ H_\theta &= -l\frac{k_3}{k}\frac{J_l(k_1 r)}{k_1 r}\sin(l\theta)\sin(k_3 z), \\ H_z &= \frac{k_1}{k} J_l(k_1 r)\cos(l\theta)\sin(k_3 z), \end{aligned} \tag{4.1}$$

where the solution is expressed in cylindrical coordinates with z the cylinder principal axis. $l \in \mathrm{N}$ and $n, m \in \mathrm{N}^*$ are three quantification numbers that represent the number of half-wavelength variations in the radial, axial and longitudinal directions, respectively [148]. J_l and J_l' are the first Bessel function and its derivative, respectively, $k_1 = x_{lm}/r$ with x_{lm} the m-th zero of J_l, $k_3 = n\pi/L$ and $k^2 = k_1^2 + k_3^2$. Note that only the solutions for TE-like modes, namely modes with transverse electric field and longitudinal magnetic field, are included. The frequency f of the mode is given by [148]:

$$f_{lmn} = \frac{c}{\lambda}, \quad \lambda = \frac{2\pi}{k}. \tag{4.2}$$

Figure 4.1 shows the fields distribution of the four lowest frequency modes TE_{111}, TE_{011}, TE_{021} and TE_{022} for a cylindrical cavity with dimension close to the LGR cavity developed in the next sections. Unlike the TE_{111}, the TE_{011} mode is particularly suitable for microwave clocks as the mode shows more homogeneous H_z field in the center of the cavity. Taking $L = 4$ cm and $r = 2$ cm, which is close to the dimensions of the cavity described in the following sections, one calculates $f_{011} \approx 9.8$ GHz. To get closer to the ^{87}Rb clock frequency, the cavity should indeed be bigger. This anticipates the main interest of LGR cavities described in the following section as more compact alternative for TE_{011}-like cavities.

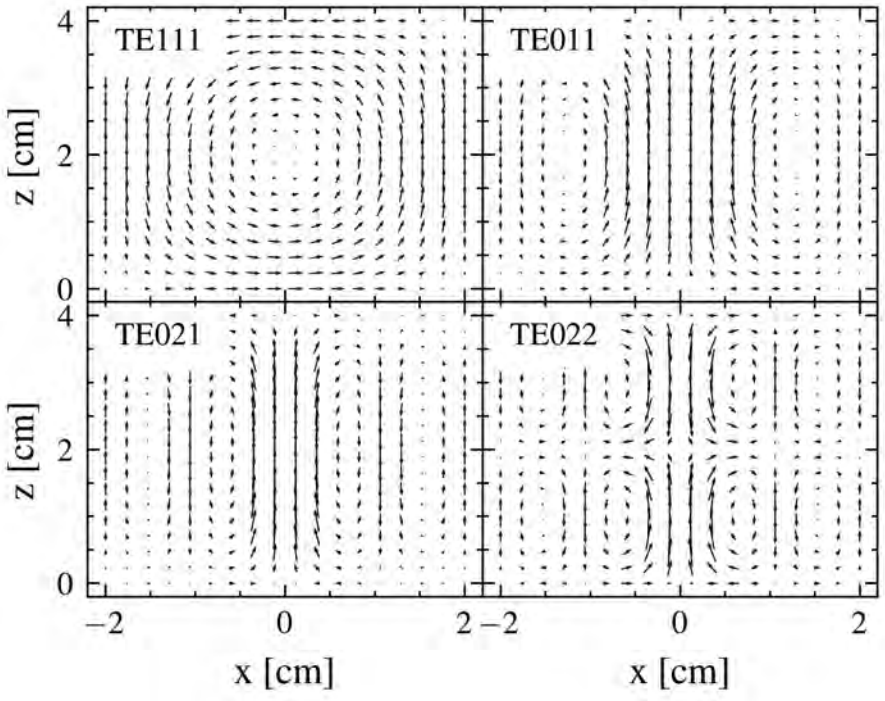

Figure 4.1: Field distribution of four TE_{lmn} modes in a cylindrical cavity with $L = 4$ cm and $r = 2$ cm.

4.1.1.2 The loop gap resonator model

The cavity model is presented on Figure 4.2. Aside from the parameters presented in [12], the cavity electrodes height H [mm], the space between the bottom and the electrodes and the space between the top and the electrodes ΔH [mm] must be taken into account. The latter is used to fine tune the cavity to the desired frequency. Thanks to its electrode structure, the LGR geometry allows for building microwave cavities with TE-like modes with lower volumes compared to the cylindrical approach [149], which is of great interest for building compact atomic clocks and has been widely used as discussed in section 1.3.

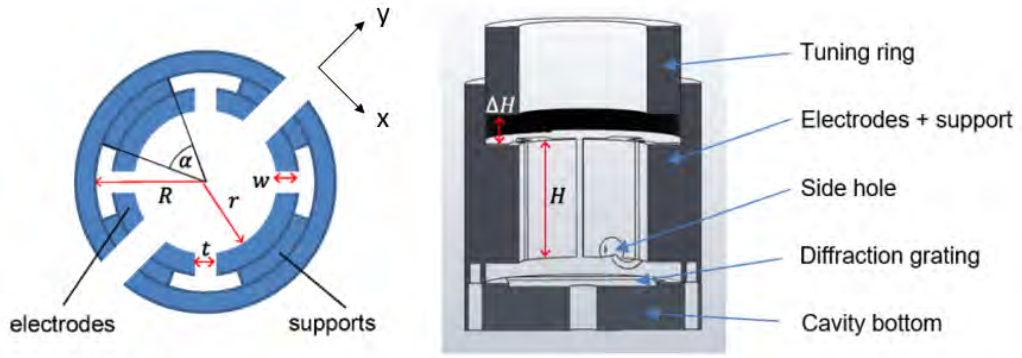

Figure 4.2: **Left:** LGR model. R and r are called the outer and inner radii, respectively. w and t are called the gaps width and thickness, respectively. α is the electrode's support width. Note that the side holes are parallel to the y axis. **Right:** Cavity section.

Note that a bottom aperture with diameter 1 mm was added to the model as it was initially planned to interrogate the atoms with a beam parallel to the cavity principal axis. This may still be useful in future clock designs.

4.1.1.3 Numerical model

The simulations of the cavity are executed in a multiphysics finite-element program named COMSOL. The cavity is made in aluminium. The boundary conditions at the end of the apertures is set to ideal conductor. Ideal conductor boundary conditions are sufficient for long enough cutoffs. However, this point could be improved in future studies using Perfectly Matched Layers (PML) [150]. Although implementing PML is likely to add computational time it might also result in a reduced cavity footprint as no artificially long cut-off would be needed to ensure correct boundary conditions. Indeed, as suggested by Figure 4.5, the field is already close to zero in the first 5 mm of the cut-off.

4.1.1.4 Figures of merit

Two figures of merit (FOM) are used to assess of the TE_{011} mode quality, namely:

$$\delta H := \frac{\sigma_{H_z}}{\mu_{H_z}} \tag{4.3}$$

and

$$\delta \widetilde{H} := \frac{\sigma_{\widetilde{H}_z}}{\mu_{\widetilde{H}_z}}, \quad \widetilde{H}_z := H_z/|\vec{H}| \tag{4.4}$$

which respectively measure field uniformity and homogeneity of H_z (see Figure 4.3). σ_A and μ_A denote the standard deviation and mean of the quantity A, respectively. In the ideal case, both FOM must be close to zero. In practise, they are calculated from the simulations in a cylinder volume of

diameter 1 mm and height 3 cm starting 3 mm above the grating which is the volume where the atoms would be interrogated in a mini-fountain [151] or free-fall situation (see Figure 6.1).

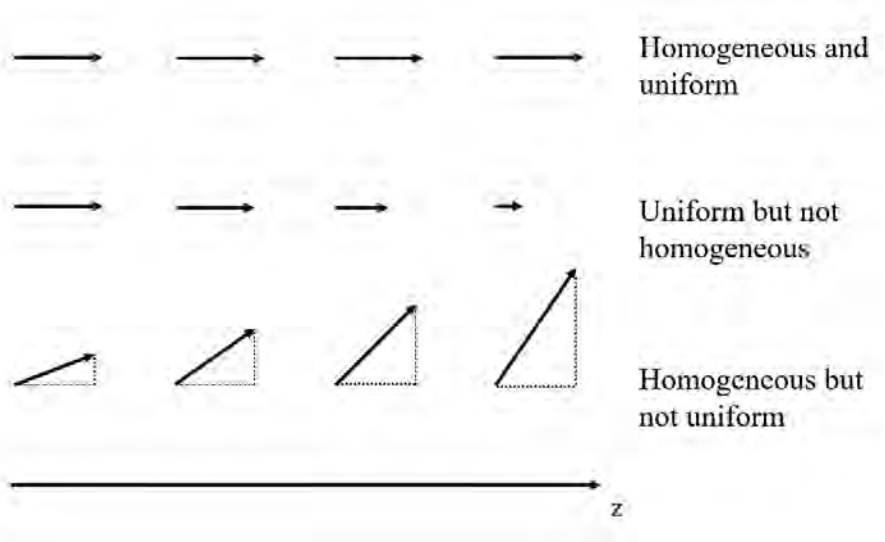

Figure 4.3: Field homogeneity versus uniformity.

4.1.1.5 Simulation of the nominal cavity

Figure 4.4 shows an example of (w,t) parameter scan around the nominal cavity. Many different configuration for $t \in [1.0, 1.5]$ mm and $w \in [1.0, 3.5]$ mm yield the correct frequency. In all configurations, the nearest mode is at least 500 MHz away from the main mode. The FOM of eq. (4.3) and eq. (4.4) range from 0% to 5% and -15% to -10%, respectively. In other words, the uniformity and the homogeneity are of the order of 1% and 10%, respectively.

Sweeps of other parameters, such as the number of electrodes or the outer radius, show similar results: many different geometries allow to realize the desired TE_{011}-like mode at the ^{87}Rb clock frequency. Nonetheless, particular care in the study of the influence of t and w have been taken as they are likely to be the most affected by the additive manufacturing process. In the end, practical arguments led to decide for the final cavity parameters. Some of the parameters are presented in Table 4.1.

Parameter	**Value**
Number of electrodes n	4
Inner radius R	15 mm
Outer radius r	9.5 mm
Electrode with w	2.5 mm
Electrode thickness t	1.38 mm

Table 4.1: Set of parameters for the nominal cavity.

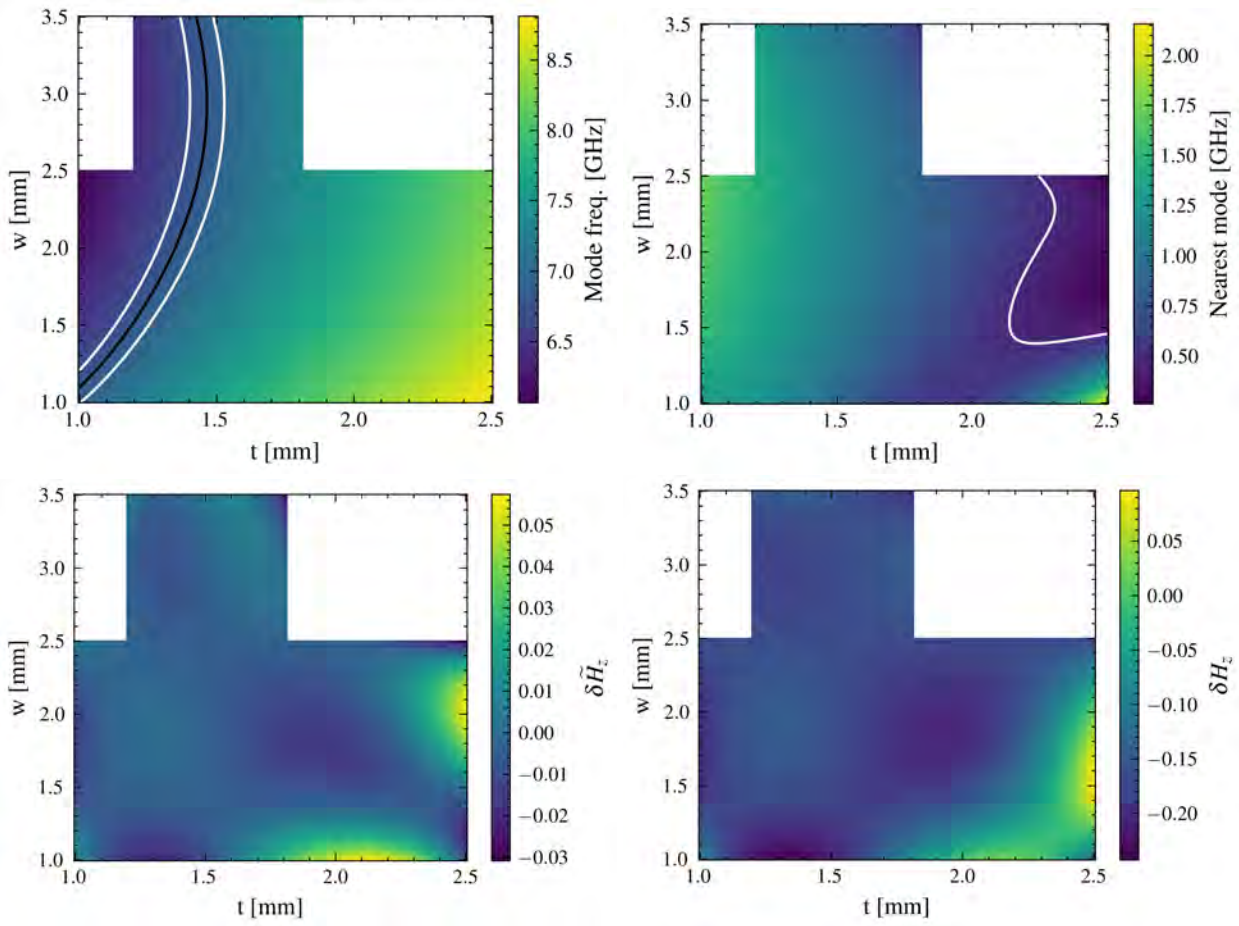

Figure 4.4: **Top left:** Mode frequency. The black contour corresponds to the rubidium frequency ν_{Rb}. The white contour indicates $\nu_{Rb} \pm 100$ [MHz]. **Top right:**: Distance of the nearest mode. The white contour is set to 500 MHz. **Bottom left:** FOM of eq. (4.4). **Bottom right:** FOM of eq. (4.3).

Using table 4.1, the equation (3) of [12] evaluates to 3.96 GHz, leading to a 42% error with respect to the simulated frequency which emphasizes the necessity simulate the mode numerically. In particular, the influence of the electrode supports and the apertures [149].

4.1.1.6 Mode properties

Figure 4.5 and 4.6 show the properties of the H_z field in the plane at the height of the initial atom cloud and in the (110) plane passing in-between two electrodes. Both figures show excellent field distribution close to the desired TE_{011} geometry. The highest field amplitude is found behind the electrodes which is compatible with Maxwell laws. Indeed, there is less space available behind the electrodes compared to the inside of the cavity.

As shown on Figure 4.5, the field amplitude is low ($< 1\%$) at the end of the side holes, showing that the side holes are small enough and do not perturb the mode.

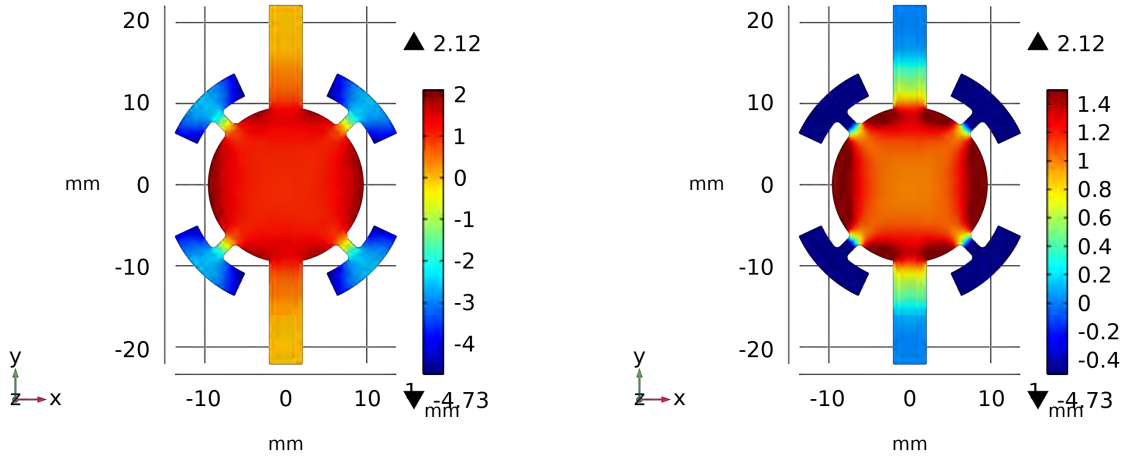

Figure 4.5: **Left:** H_z field component normalized by the value at the atom cloud position in the horizontal plane at the same height. **Right:** Same data but with finer color scale.

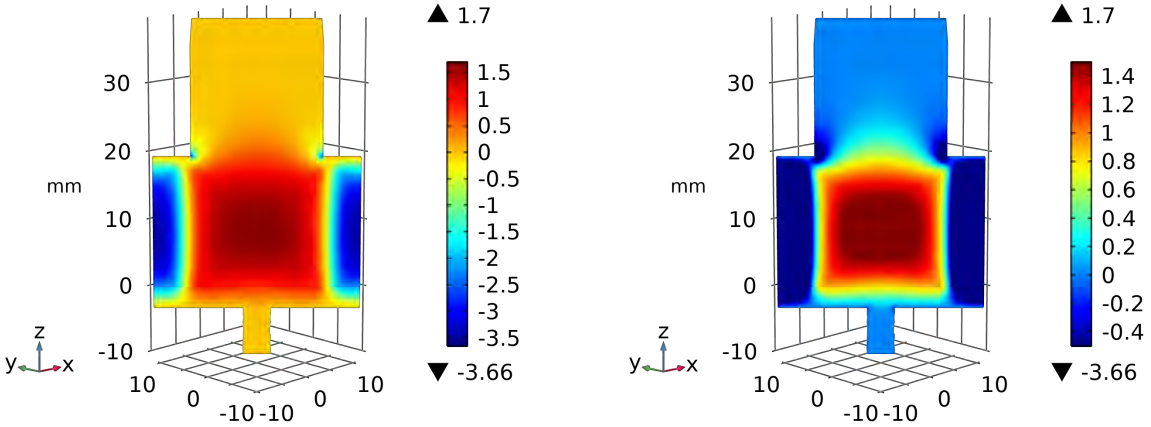

Figure 4.6: **Left:** H_z field component normalized by the value at the atom cloud position in the (110) plane. **Right:** Same data but with finer color scale.

Figure 4.7 shows the magnetic field components above the grating. The H_x and H_y components are at least one order of magnitude smaller than the H_z component even really close from the grating, showing once again excellent TE_{011}-likeliness.

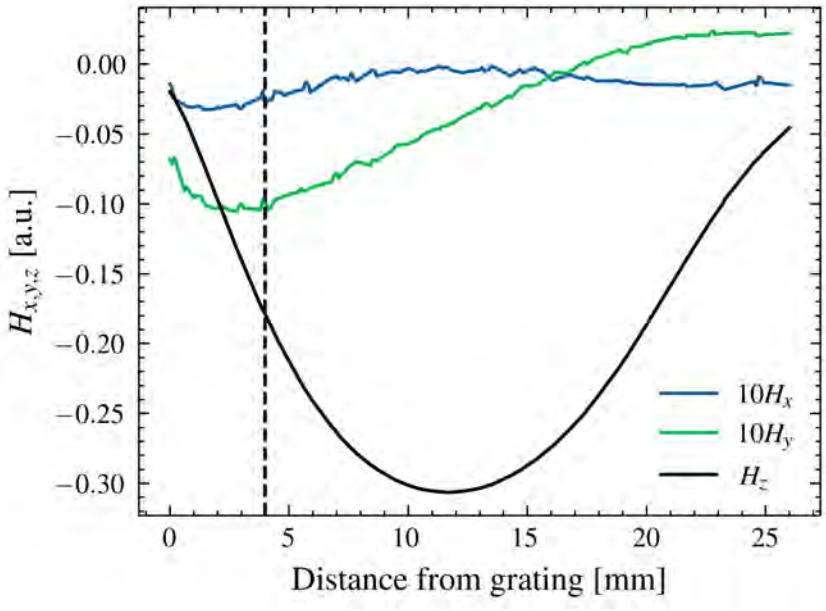

Figure 4.7: $\vec{H}$ field components above the grating. The H_x and H_y have been enhanced for clarity. The dashed black line represent the initial position of the atom cloud.

4.1.1.7 Phase distribution and phase shift

The phase profile above the grating is shown on Figure 4.8. From where the atoms are prepared and the end of the cavity, the phase variation is $0.04°$ or 0.7 mrad for a free-fall of 21 mm, allowing a free-fall-dominated Ramsey time of 65 ms. Using eq. 2.29, this corresponds to a phase shift of 2.5 Hz.

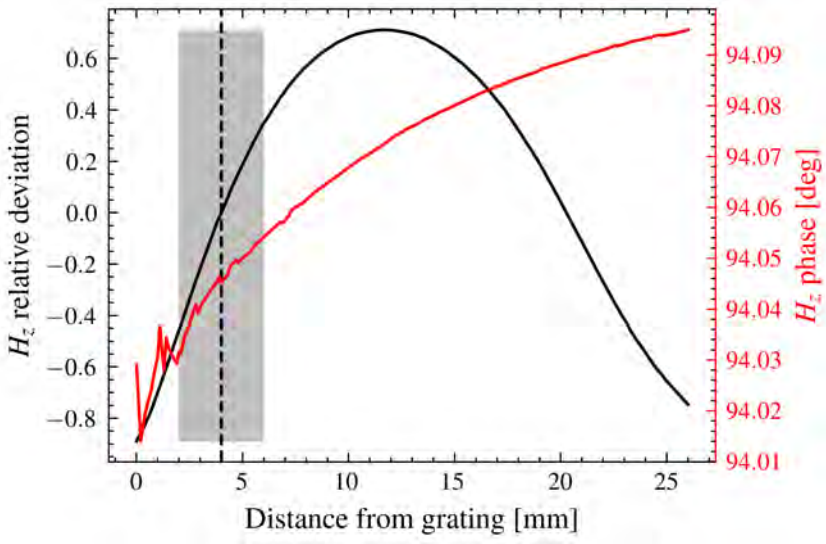

Figure 4.8: $\vec{H}$ field z component and phase above the grating.

4.1.1.8 Neighbouring modes

Special care must be taken to ensure that neighbouring modes do not overlap with the mode of interest. Figure 4.9 shows the H_z field distribution of the closest left and right modes with frequencies $\approx$ 5.7 GHz and $\approx$ 8.5 GHz, respectively. The former mode shows a TM structure with rotating magnetic field on the Oxy plane and electric field parallel to the $\hat{z}$ axis. The latter is called a *loop mode* as the field distribution is located near the coupling loop for the microwave radiation, on the right side of Figure 4.9-right. Furthermore, as seen on Figure 4.12, the frequency of this mode changes less than 50 MHz while the mode of interest and the left-neighbouring mode show variations around 400 MHz over the whole cavity tuning range.

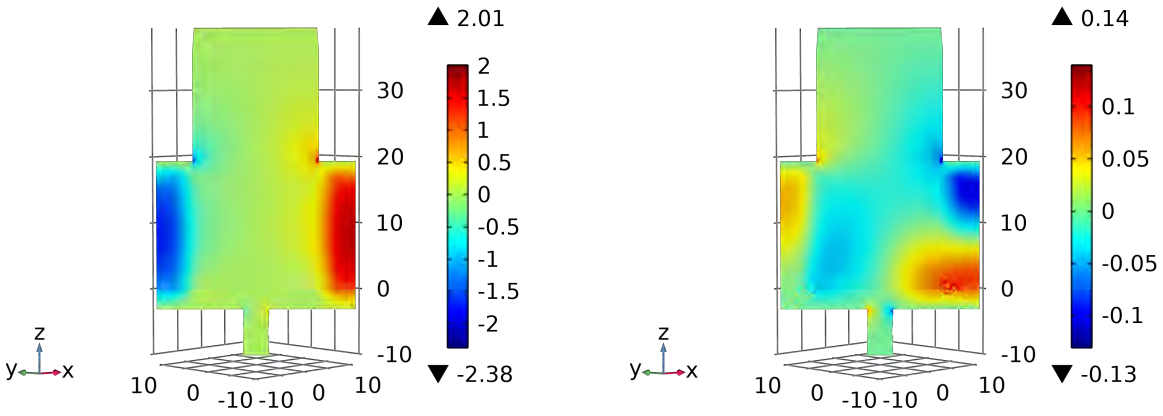

Figure 4.9: **Left:** H_z field component for the 5.7 GHz left-neighbouring mode. **Right:** Same data for the right-neighbouring 8.5 GHz mode.

4.1.2 Realization

4.1.2.1 Cavity elements

The cavity parts are shown on Figure 4.10. The electrodes part is additively manufactured. The rest is traditionally manufactured in our university mechanical workshop. The coarser nature of the additive manufactured aluminium is clearly visible. However, this does not impact the vacuum level as shown in [12]. Figure 4.11 shows the finished cavity, with grating inside.

Figure 4.10: Left to right: cavity bottom with grating insert, additive manufactured electrodes part and top part.

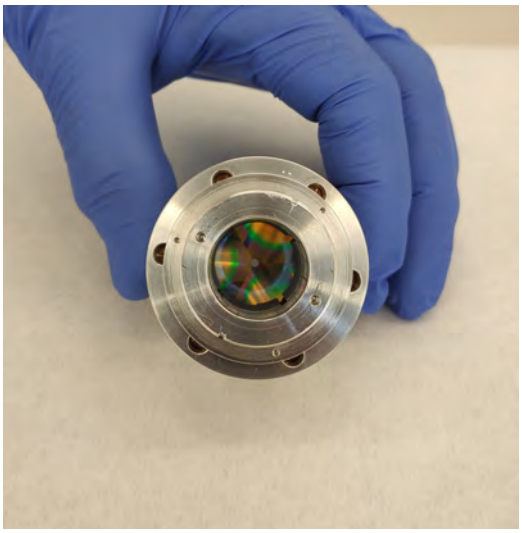

Figure 4.11: Final cavity with grating inside. The hole in the grating was primarily drilled to allow for interrogation along the principal axis of the cavity. It could be used in future designs.

4.1.2.2 Tuning range

Figure 4.12 shows the experimentally measured S_{11} spectrum of the cavity for minimal and maximal cavity heights. The frequency of the mode of interest can be tuned between 6.7 and 7.4 GHz for a total tuning range of 730 MHz. Note that each spectrum was optimized using the rotational degree of freedom described in [12].

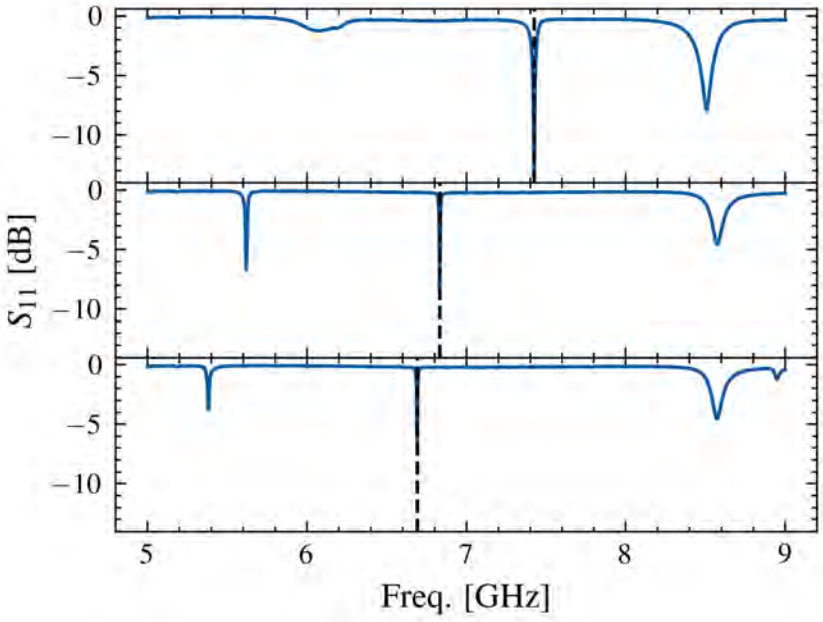

Figure 4.12: Cavity tuning range. The top and center S_{11} were taken by setting the cavity height in its two extremal positions. The center part shows a tuned cavity.

4.1.2.3 Grating influence

The influence of the grating on the mode frequency is illustrated on Figure 4.13. As discussed in [12], the FWHM is degraded because of the etched nature of the grating. The mode's center frequency is shifted by -19 MHz which is easily recoverable with our 730 MHz tuning range. The sign is compatible with the shortening of the cavity by 1 mm: indeed, when no grating is inserted in the cavity, the dedicated slot for hosting the grating artificially increases the cavity's height.

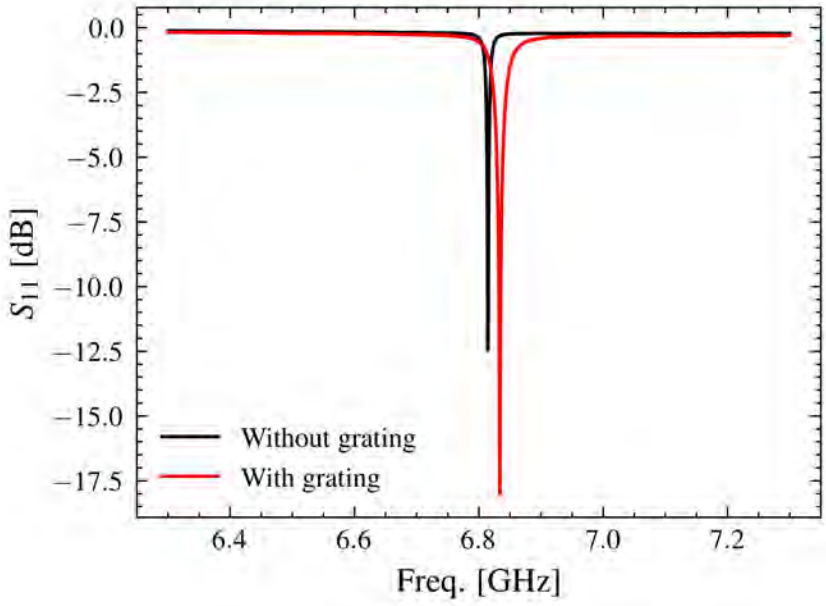

Figure 4.13: Influence of the grating on the mode shape. Note that the angle was optimized each time.

The ability to compensate for small discrepancies between the actual cavity and the simulation allows to neglect the grating from the simulation model, which greatly reduces the simulation time.

4.1.2.4 Temperature coefficient

Measurement of the temperature coefficient is shown on Figure 4.14. It is measured by placing the cavity in an oven. Each point if measured by changing the oven temperature and measuring the mode frequency by fitting the S_{11} spectrum after waiting for thermal equilibrium. The linear fit gives:

$$\frac{\partial}{\partial T}\nu = (-156 \pm 9)\ \text{kHz/K}, \tag{4.5}$$

with T [°C] the cavity temperature and ν [GHz] the mode's frequency. This coefficient is compatible with the relative dilatation coefficient of aluminium if $\approx 22\ \text{K}^{-1}$ [152]. This coefficient is relevant for estimating the cavity-pulling contribution to the instabilities.

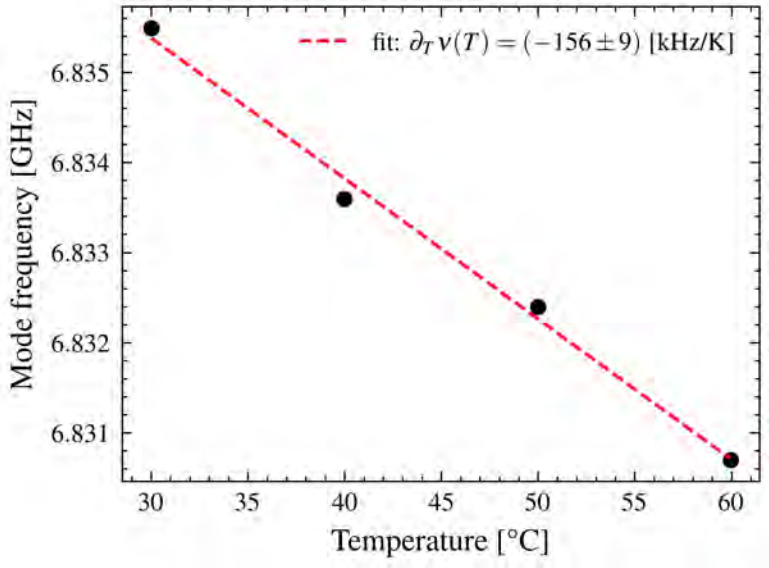

Figure 4.14: Cavity temperature coefficient.

4.1.3 Rabi oscillations

This section shows how equation (5) of [12] was derived. In the absence of relaxation processes, Rabi oscillations have the form:

$$P_2(\theta) = \cos^2(\theta/2), \tag{4.6}$$

where P_2 is fraction of atoms in $|5S_{1/2}, F = 2, m_F = 0\rangle$ after the Ramsey cycle (see chapter 5).

It has been shown that these oscillations are damped in presence of magnetic field inhomogeneities [101]. In other words, if one assumes that the pulse area θ has distribution $\mathrm{P}(\theta)\mathrm{d}\theta$ in the volume of interrogated atoms, the oscillations are transformed in the following manner:

$$P_2(\theta) = \cos^2(\theta/2) \quad \rightarrow \quad \langle \cos^2(\theta/2) \rangle = \int_{-\infty}^{\infty} \cos^2(\theta/2)\mathrm{P}(\theta)\mathrm{d}\theta, \quad \int_{-\infty}^{\infty} \mathrm{P}(\theta)\mathrm{d}\theta = 1. \tag{4.7}$$

In the case of vapor-cell clocks, since the interrogated atoms span a volume close to that of the total microwave cavity volume compared to cold atom clocks, the distribution $P(\theta)$ in eq. (4.7) is - at best - close to the TE_{011}-like distribution. The distribution is however very likely to be more complex which will exhibit non-trivially shaped oscillations. In those case, the matching of the oscillations with the simulation results is necessary.

In the case of the cold atom clock cavity, the atoms span a much smaller volume which makes possible to approximate the distribution of pulse area by a gaussian profile and derive an analytical

expression. Indeed, with a gausian distribution of mean θ_0 and standard deviation σ:

$$\begin{aligned} \mathrm{P}(\theta) &= \frac{1}{\sqrt{2\pi}\sigma} e^{-\frac{1}{2\sigma^2}(\theta-\theta_0)^2} = \frac{1}{\sqrt{2\pi}\sigma} e^{-\frac{\theta_0^2}{2\sigma^2}(\theta/\theta_0-1)^2} \\ &= \frac{1}{\sqrt{2\pi}\sigma} e^{-\frac{\theta_0^2}{2\sigma^2}(\lambda-1)^2}, \end{aligned} \tag{4.8}$$

with $\lambda := \theta/\theta_0$ and $\tilde{\sigma} := \sigma/\theta_0$ relative standard deviation. Inserting eq. (4.8) in eq. (4.7) allows to recover the result presented in the paper, namely:

$$\begin{aligned} &\int_{-\infty}^{\infty} \cos^2(\theta/2)\mathrm{P}(\theta)\mathrm{d}\theta \\ &\qquad = \int_{-\infty}^{\infty} \cos^2(\lambda\theta_0/2) \frac{1}{\sqrt{2\pi}\tilde{\sigma}} e^{-\frac{1}{2\tilde{\sigma}^2}(\lambda-1)^2} \mathrm{d}\lambda \\ &\qquad = \frac{1}{2} + \frac{1}{4}\int_{-\infty}^{\infty} \left(e^{i\lambda\theta_0} + e^{-i\lambda\theta_0}\right) \frac{1}{\sqrt{2\pi}\tilde{\sigma}} e^{-\frac{1}{2\tilde{\sigma}^2}(\lambda-1)^2} \mathrm{d}\lambda \\ &\qquad = \frac{1}{2} + \frac{1}{4}\int_{-\infty}^{\infty} \left(\frac{1}{\sqrt{2\pi}\tilde{\sigma}} e^{-\frac{1}{2\tilde{\sigma}^2}(\lambda-(1+2i\theta_0\tilde{\sigma}^2))^2 + i\theta_0 - \theta_0^2\tilde{\sigma}^2/2} + c.c.\right) \mathrm{d}\lambda \\ &\qquad = \frac{1}{2}\left(1 + e^{-\tilde{\sigma}^2\theta_0^2/2}\cos\theta_0\right). \end{aligned} \tag{4.9}$$

Equation (4.9) shows that the bigger the inhomogeneity, which is described by $\tilde{\sigma}$, the faster the oscillation damping. In practise, because not all atoms participate to the signal and because P_2 is measured in absorption mode, the effective fitted function $f(\theta)$ is:

$$f(\theta) = A\left(1 + e^{-\tilde{\sigma}^2\theta_0^2/2}\cos\theta_0\right) + C. \tag{4.10}$$

4.2 Conclusion and next steps

In this chapter, complementary material on the cavity design and realization were given. A well-defined workflow allows to derive different sets of parameters each yielding a relevant cavity with TE_{011}-like mode distant enough from neighbour modes and with excellent field homogeneity and uniformity. Next possible steps could improve the cavity footprint, versatility and performances.

To reduce the footprint, simulating the cavity using PML could allow to reduce the cavity total radius by up to 5 mm, as it is illustrated on Figure 4.5. The future clock footprint could also be reduced by realizing a cavity out of Titanium. This way, in principle, there would be no need to place the cavity in a vacuum chamber and the cavity could act as vacuum chamber itself.

Improved clock performances could be reached by putting the cavity upside down and driving the atoms with the second $\pi/2$ pulse further down its principal axis. To achieve this, a second pair of holes must be drilled at the appropriate distance. Further studies have shown that a supplementary pair of holes would not impact the mode quality. This is also true for slightly elongated holes which would allow more versatility. These improvements would have two benefits: first, increasing the

Ramsey time T_R. Second, allowing to interrogate the atoms in more homogeneous parts of the cavity. Indeed, the clock presented in chapter 5 works with the lower part of the field presented on Figure 4.7 whereas best regions with better field homogeneity exist above 4 mm.

4.3 Acknowledgements

I would like to thank Vladimir Dolgovskiy who started working for the Ultra-compact physics package for miniature cold-atom clock (UppMac) project. He designed the first cavities and started building the simulation workflow. I then finished the first batch of cavities and produced the second batch within the UppMac 2$^{\text{nd}}$ Generation (UppMac-2G) project based on his preliminary investigations. In parallel, we collaborated with the university of Strathclyde, in particular with Ben Lewis who designed an built the setup that will host the cavity and that will be described in chapter 5.

Chapter 5

A cold-atom clock using an additive-manufactured microwave cavity

This chapter presents the joint work between the University of Neuchâtel and the Universiy of Strathclyde towards a cold-atom clock. The microwave cavity developed in chapter 4 was sent to Strathclyde and put in a vacuum setup designed by Ben Lewis. The clock results study results are published in the article preprint [13] reproduced on the following pages. These studies are then complemented in the following pages. In particular, it is shown that the short-term performances of the clock are strongly limited by gravity as a consequence of the current design. The Allan deviation of the clock is consistent with the fringes SNR. Note that all the measurements presented in this chapter were jointly acquired with Alan Bregazzi.

A cold-atom Ramsey clock with a low volume physics package

A. Bregazzi,[1] E. Batori,[2] B. Lewis,[1] C. Affolderbach,[2] G. Mileti,[2] E. Riis,[1] and P. F. Griffin[1, a)]
[1)]*SUPA and Department of Physics, University of Strathclyde, G4 0NG, Glasgow, United Kingdom*
[2)]*University of Neuchâtel, Institute of Physics, Laboratoire Temps-Fréquence, Avenue de Bellevaux 51, 2000 Neuchâtel, Switzerland*

(Dated: 5 May 2023)

We demonstrate a Ramsey-type microwave clock interrogating the 6.835 GHz ground-state transition in cold ^{87}Rb atoms loaded from a grating magneto-optical trap (GMOT) enclosed in an additively manufactured loop-gap resonator microwave cavity. A short-term stability of $1.5 \times 10^{-11}\ \tau^{-1/2}$ is demonstrated, in reasonable agreement with predictions from the signal-to-noise ratio of the measured Ramsey fringes. The cavity-grating package has a volume of ≈67 cm^3, ensuring an inherently compact system while the use of a GMOT drastically simplifies the optical requirements for laser cooled atoms. This work is another step towards the realisation of highly compact portable cold-atom frequency standards.

Compact frequency standards based on the interrogation of both ions and neutral atoms continue to receive much interest, with many different schemes now reported in the literature[1–9]. While compact clocks based on thermal atomic vapours and coherent population trapping (CPT) remain unrivalled in terms of size, weight and power (SWaP) they typically exhibit stabilities that are limited in the medium to long-term due to light-shift effects[10] and the buffer gasses required to reduce atomic collisions[1]. In addition to this, CPT clocks struggle to reach atomic shot noise due to the limited signal-to-noise ratio (SNR), a consequence of the low detected signal photon count per atom. This limitation often requires complex interrogation schemes to optimise the clock stability[11–13].

The development in the last decade of pulsed optically pumped (POP) clocks in thermal vapours has driven new research, with state-of-the-art stabilities[2,14,15]. However, these clocks still suffer from buffer gas shifts, providing the ultimate limitation to their long-term stabilities. Achievable Ramsey times within these systems are also limited to a few ms by spin relaxation of the thermal atoms[2,16], restricting the short-term stability performance.

In an effort to combat these limitations several groups have now developed compact cold atom microwave clocks based on spherical optical-integrating sphere cavities[17,18], cylindrical cavities[19,20] and more recently loop-gap-resonator cavities[21]. Three examples of cold atom microwave clocks are now even commercially available[22–24]. Different laser cooling schemes with varying optical geometries have been used within these systems, with isotropic cooling of an optical molasses[17,18,20,22], pyramid MOTs[25] and larger traditional 6-beam MOTs[19,21] all being utilised.

In this letter we demonstrate operation and first stability measurement of a cold-atom atomic clock based on an additively manufactured loop-gap resonator (LGR) cavity with a volume of ≈ 67 cm^3 incorporating an integrated GMOT[26]. Although vapour-cell atomic clocks based on LGR structures with external diameters of order 1 cm have been demonstrated[16], such small devices will have limited benefit when using cold atoms. Previous investigations with both GMOTs[27] and 6-beam MOTs[28] have shown that by constraining the trap beam diameter the maximum trapped atom number is limited, therefore constricting the potential stability of the final clock.

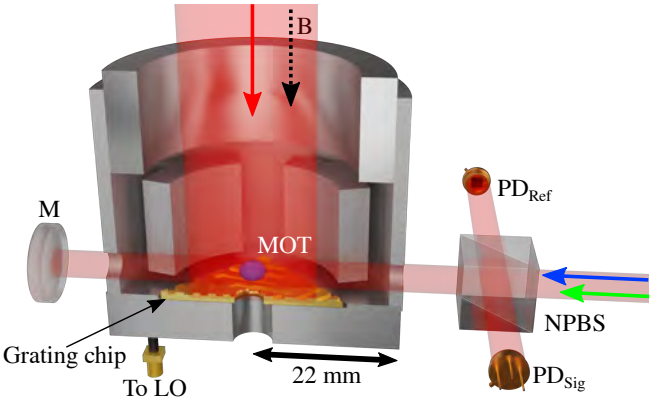

FIG. 1. Simplified schematic of the physics package. Trap light (red arrow) propagates parallel to the magnetic bias field (black dashed arrow), 90:10 non-polarising beam splitter (NPBS) splits the optical pumping (blue arrow) and readout (green arrow) light onto a reference photodiode (PD$_{Ref}$) and signal photodiode (PD$_{Sig}$) after being retro-reflected by a mirror (M). Local oscillator (LO) is connected via a SMA vacuum feedthrough.

In the present study a sample of cold atoms is optically pumped into the clock state, probed in a double resonance Ramsey-type scheme and the resulting state populations read out through an absorptive method. The use of additive manufacturing allows for complex electrode geometries, while maintaining a highly scalable manufacturing process due to the lack of precision machining and assembly required[29,30]. While the main aim of this work has been to demonstrate the feasibility of integrating this cavity design and its fabrication technique with the GMOT architecture, we envisage that further substantial reduction in size is possible by adapting the cavity to form the bulk of the vacuum system. The minimal optical access required of this scheme also allows for a reduction in the number of apertures present in the cavity body which must be carefully considered during the design process so as not to degrade the cavity mode and field

[a)]Electronic mail: paul.griffin@strath.ac.uk

homogeneity[21,30].

A commercial laser system (Muquans ILS) at 780 nm with an integrated electro-optic modulator (EOM) for the creation of optical sidebands on the carrier frequency is used throughout. The laser light is split into three distinct optical paths, each with a double passed acousto-optic modulator (AOM) for power and frequency control to enable trapping, optical pumping and state readout. The trapping light is coupled into a fibre to be passed to the physics package. The optical pumping and state readout beams are coupled into a single additional fibre and likewise passed to the physics package.

The microwave cavity itself, described in detail in Ref[30] consists of a loop-gap structure with a four electrode geometry and has an outer radius of 44 mm and a height of roughly 44 mm. The cavity operates in a TE_{011}-like mode, tuned to the ground-state-splitting of ^{87}Rb with a quality factor of Q≈360 and is mounted within a stainless steel vacuum chamber, maintained at ultra-high-vacuum (UHV) by an ion pump. Optical access is enabled via viewports in the vacuum chamber along two orthogonal axes. The first axis is parallel to the cylindrical symmetry axis of the cavity (in the following this is referred to as the cavity axis) and allows the trap light to be directed onto the grating chip after expansion and collimation from the fibre. Optical pumping and state readout light, expanded from the fibre to a $1/e^2$ diameter of 7 mm, is directed onto the atoms through two 4 mm holes drilled in the side of the cavity body. A retro-reflecting mirror for this light is placed outside the vacuum chamber to decrease the acceleration experienced by the atoms when interacting with the optical pumping and probe beams and increase signal amplitudes. A simplified schematic of this is shown in Fig.1. No significant degradation of the cavity field is observed by the introduction of the holes in the cavity body[30].

A pair of anti-Helmholtz coils are mounted within the vacuum chamber, along the cavity axis in order to create the quadrupole magnetic field required for the trapping process. Three orthogonal pairs of Helmholtz shim coils, mounted externally to the vacuum chamber are used for the cancellation of external stray DC magnetic fields and to apply a magnetic bias along the cavity axis of ≈ 100 mG in order to lift the atomic degeneracy during optical molasses and clock interrogation. We note that the current demonstration is a proof of concept with no magnetic shielding of the experiment present, limiting the potential stability of the system.

The experimental cycle is initiated by turning the trapping coils on with the trap light tuned to be approximately Δ=-2Γ red detuned ($\Gamma/2\pi$=6.07 MHz) from the ^{87}Rb D_2 F=2→F'=3 cycling transition, with re-pump light generated by the EOM operating at 6.57 GHz to produce 5% optical sidebands. A Rb vapour, maintained at the 1×10^{-9} Torr level, is produced by resistively heating a pair of alkali metal dispensers. We then perform a 6 ms optical molasses by turning the trap coils off and linearly ramping the light detuning to Δ=-5Γ while simultaneously decreasing the trap light intensity. After molasses we measure atomic temperatures of $\approx 10\ \mu K$. In order to decrease the clock cycle time and mitigate experimental dead time, we employ atom recapture between experimental cycles[3,31]. In steady state this allows the trapping of $> 3\times10^6$ atoms with a load time of 100 ms for a clock cycle operating at ≈7 Hz. Once the atoms have been trapped and cooled, the trap light is extinguished by an AOM and blocked by a mechanical shutter[32] to ensure no light leakage during microwave interrogation. After molasses, the atoms are assumed to be roughly evenly distributed between the five m_F levels of the $F=2$ hyperfine ground-state manifold. We therefore employ a 1 ms optical pumping stage with 10 μW total power of linearly polarised light, polarisation axis parallel to the quantization axis, tuned to the F=2→F'=2 and re-pump light tuned to the F=1→F'=2 transition. Due to selection rules this pumps $> 95\%$ of the atoms into the $5^2S_{1/2}$, $|F=2,m_F=0\rangle$ state[33] as seen by the almost complete elimination of the $m_F=1\rightarrow m_F'=1$ transitions, when scanning the microwave detuning, increasing the contrast of the resulting clock signal.

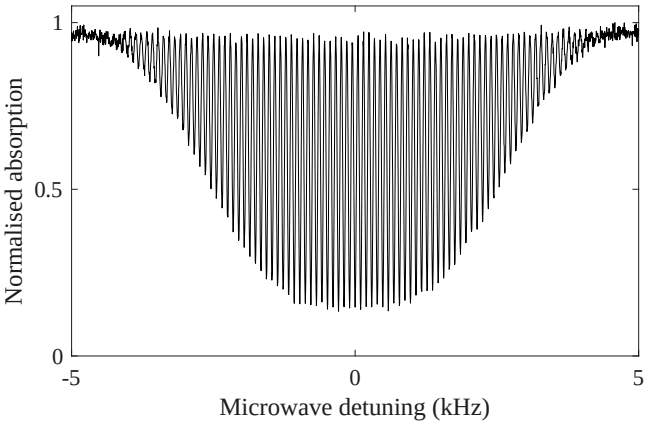

FIG. 2. Typical Ramsey fringe taken with a 10 ms free evolution time.

A Keysight E8257D microwave synthesizer is used as a local oscillator and microwave source throughout. Square microwave $\pi/2$ pulses with a duration of 200 μs and typical power levels of 0.04 mW are applied to the atoms. The specified phase noise performance of the local oscillator allows the Dick effect[34] to be reduced to the 6.12×10^{-13} level at 1 s for the experimental cycle time. After the desired microwave pulses have been applied, the atomic states are read out by an absorption method using 30 μW of optical power, measured by recording the transmission on a photodiode of two subsequent probe pulses. First a short pulse of readout light tuned to the F=2→F'=3 transition is applied, giving an measure of the number of atoms in the $F=2$ ground-state. We then apply a second readout pulse with re-pump light present. This measures the total number of atoms, providing a normalisation of the signal and reduced sensitivity to atom number fluctuations. Intensity noise in the readout pulses is reduced by the use of a reference photodiode.

An example Ramsey fringe taken with a Ramsey time, T_R=10 ms, corresponding to a fringe linewidth of 50 Hz is shown in Fig.2. This fringe exhibits an SNR of around 110, measured at the half-width points of the central fringe, where SNR is defined as the ratio of the peak amplitude divided by

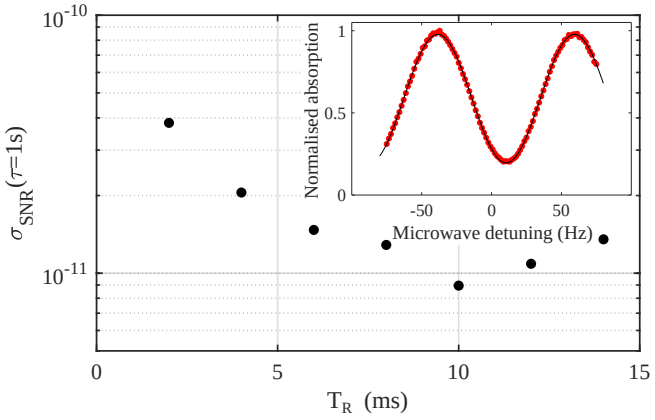

FIG. 3. Predicted short-term stability as a function of Ramsey time. Inset: Typical central Ramsey fringe obtained at 10 ms free evolution time. Red points indicate measured normalised probe absorption while the black line shows a sinusoidal fit to the data. The fringe offset from 0 Hz detuning corresponds to the frequency shift expected from the second-order Zeeman shift at a 100 mG bias field.

the amplitude noise. The predicted SNR limited short-term relative frequency instability of a local oscillator stabilised to an atomic transition in terms of Allan deviation is given by[35]:

$$\sigma_{SNR}(\tau) = \frac{1}{\pi C}\frac{\Delta f}{f_0}\frac{1}{SNR}\sqrt{\frac{T_C}{\tau}} \qquad (1)$$

where C is the fringe contrast, Δf is the signal linewidth ($\approx 1/2T_R$), f_0 is the central frequency (6.8346... GHz), T_C is the full experimental cycle time ($T_C = 140$ms) and τ is the averaging time. We use this relationship as a basis to optimise our experimental cycle to maximise the potential stability of our clock. A plot of the predicted stability, using the measured SNR, as a function of the Ramsey time is shown in Fig.3. From this we find that as the Ramsey time is increased the predicted stability also improves up to the level of 8.95×10^{-12} for a 10 ms Ramsey time. After this time however the stability begins to decrease as the SNR is degraded. This degradation in SNR is attributed to atomic losses due to both the thermal expansion of the cloud and the atoms falling out of the probe region under gravity. The extension of this Ramsey time should be possible by moving the holes in the cavity body lower down, introducing elliptical holes to maintain good probe-atom overlap along the path of gravity or by implementing a grating-chip atomic fountain[36]. This last option is particularly attractive because as with traditional atomic fountains it would be possible apply both $\pi/2$ pulses when the atoms are at the same vertical point of the cavity. This will allow the phase difference observed by the atoms between the two microwave pulses to be minimised, essential for high contrast Ramsey fringes in a relatively low-Q cavity such as used here. A grating-chip atomic fountain (using CPT interrogation) such as this has already demonstrated Ramsey times out to 100 ms, with a corresponding fringe linewidth of 5 Hz[36].

To assess the stability of our system we stabilise the local oscillator to the atomic signal. The signal is modulated and demodulated at the fringe's half maximum to construct the error signal which is used to feedback onto the local oscillator by voltage tuning its 10 MHz internal reference. Fig.4 shows an overlapping Allan deviation of the resulting frequency stability when compared to an oven controlled quartz crystal oscillator (Wenzel Associates 501-29647) disciplined to GPS (GPSDO). From Fig.4 we see that the clock stability averages down with a $1.5 \times 10^{-11}\ \tau^{-1/2}$ dependence out to 10 s, at which point it deviates slightly from the ideal $\tau^{-1/2}$ dependence. This is in reasonable agreement with the theoretical stability obtained from Fig.3 at a 10 ms Ramsey time and is well above the ultimate stability limit set by the quantum projection noise (QPN) of $4.9 \times 10^{-13}\ \tau^{-1/2}$, calculated by replacing the SNR term in (1) by $\sqrt{N}$, where N is the atom number.

As the experiment is currently operated in a magnetically unshielded environment the instability contribution due to the second-order Zeeman shift was expected to limit the clock stability in the medium-term. This was confirmed by measuring the magnetic field stability via the $|F=1,m_F=1\rangle \rightarrow |F'=2,m'_F=1\rangle$ microwave transition, exhibiting a magnetic field sensitivity of β_1=1.4 MHz/G[37]. The expected stability of the $m_F = 0$ clock transition (β_0=575 Hz/G^2 [37]) could then be calculated, shown as black points in Fig.4. This plot shows that the second-order Zeeman shift is indeed an important limitation to the clock stability at $\tau >$10 s, due to a pronounced hump in the magnetic field stability around this time, after which the stability averages down slightly to the level of $< 2 \times 10^{-12}$. For future iterations of this set-up it will be imperative to introduce magnetic shielding for long-term stability performance.

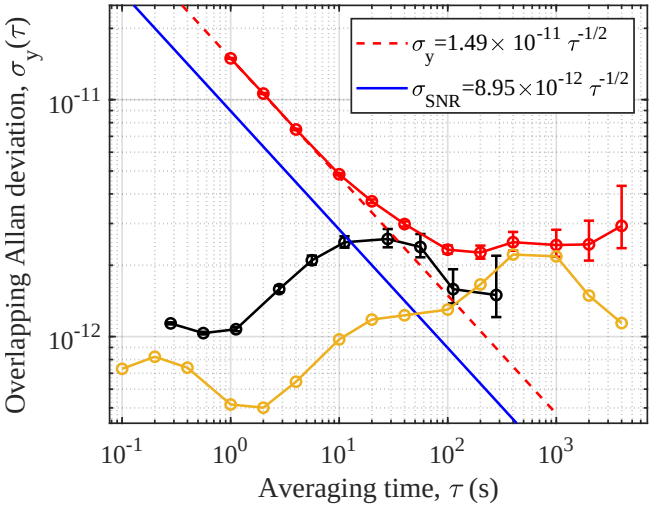

FIG. 4. Red points: Overlapping Allan deviation of local oscillator's stability when locked to atomic signal. Blue solid line: stability predicted by (1) and measured fringe SNR. Red dashed line: $\tau^{-1/2}$ dependence of the measured 1 s stability. Black points: stability limit due to the second-order Zeeman shift. Yellow points: measured GPSDO reference oscillator stability. Error bars represent 1σ confidence bound.

Noise source	σ contribution ($\tau = 1s$)
SNR	8.95×10^{-12}
Electronic noise	1.14×10^{-12}
Dick	6.12×10^{-13}
Zeeman	1.07×10^{-12}
QPN	4.90×10^{-13}
Total $\left(\sqrt{\sigma_{SNR}^2 + \sigma_{LO-tune}^2 + \sigma_{Dick}^2}\right)$	9.04×10^{-12}
Measured	1.49×10^{-11}

TABLE I. Table of noise sources and their contributions to the 1 s Allan deviations stability.

Another limiting factor to the clock stability in the medium term is the GPSDO reference. Three-corner-hat stability measurements of this reference against two commercial Cs beam clocks (OSA 3235B and Microchip 5071A) indicates excellent short-term performance of the GPSDO $< 1 \times 10^{-12}$. At 700 s however, a peak in the instability is observed at $\approx 2 \times 10^{-12}$. This peak is associated with the time constant of the tuning loop used to reference the oscillator to the GPS signal. When taken in conjunction with the stability limit due to the Zeeman effect, these two effects help explain the flattening of the clock stability for averaging times >100 s.

To more fully characterise the short-term stability (τ=1 s) of the system a stability budget of the main instability contributions to the clock was constructed, shown in Table I. The short-term clock performance is found to be primarily limited by the Ramsey fringe SNR, discussed above. In future we expect to be able to improve the SNR contribution to short-term stability towards the projection noise limit. This will be achieved by increasing the Ramsey time, optimisation of the optical detection process and suppression of intensity and frequency fluctuations in the probe beam.

The next largest contributor to the 1 s clock stability after the fringe SNR is electronic noise on the voltage line used to tune the 10 MHz local oscillator. While this is not a limiting factor to the clock stability at present, careful minimisation of this noise source will be required when moving towards a magnetically shielded experiment where the expected clock stability should improve below the 1×10^{-12} level. The total predicted short term stability from Table I is found to be 1.6 times better than the measured stability. Efforts are ongoing to identify the remaining instability contributions in order to minimise them in future iterations of the set-up.

In conclusion, we have demonstrated a compact cold-atom microwave clock based on an additively manufactured loop-gap-resonator cavity interacting with laser cooled atoms loaded from a GMOT chip. In the present system the experimentally optimised short-term clock stability is measured as $\sigma_y(\tau) = 1.5 \times 10^{-11}\ \tau^{-1/2}$, primarily limited by the Ramsey fringe SNR. In the medium-term the clock stability is primarily limited by the second-order Zeeman shift due to operating in an unshilded environment. A secondary limit is placed on the medium-term stability performance by the reference oscillator itself exhibiting a stability bump at around 700 s. By addressing these issues, we expect to improve the short-term stability to be more in-line with other cold-atom cavity clock demonstrations[17,21–23].

The current physics package is inherently compact and remains highly amenable to further miniaturisation. The use of additive manufacturing also maintains a highly scalable manufacturing process. Additively manufactured vacuum chambers have also recently demonstrated compatibility with UHV[38] pressure levels. This raises the enticing possibility of the cavity body itself simultaneously acting as a UHV chamber, allowing the entire physics package to be manufactured as a single bulk component, drastically reducing the size of the system. In addition to this, passively pumped vacuum chambers have now been shown to maintain the UHV levels required for atom trapping for extended periods[39,40], allowing for a reduction in power consumption by negating the continuous use of an ion pump. While the stability of our clock is currently several orders of magnitude below the state-of-the-art, the scope for improved performance and further miniaturisation is very good. We therefore believe this work represents a step towards highly compact and portable cold-atom frequency standards.

ACKNOWLEDGMENTS

The authors would like to thank R. Elvin and J. P. McGilligan for useful conversations and J. P. McGilligan for careful reading of the manuscript. A.B. was supported by a Ph.D. studentship from the Defence Science and Technology Laboratory (Dstl). E. B., C.A. and G. M. acknowledge funding from the European space Agency (ESA) and the Swiss Space Office (Swiss Confederation). We gratefully acknowledge funding from the International Network for Microfabrication of Atomic Quantum Sensors (EPSRC EP/W026929/1).

DATA AVAILABILITY STATEMENT

The data that support the findings of this study are available from https://doi.org/10.15129/bb0d3614-6394-4d0e-8649-b1bf66c71722

[1] S. Knappe, V. Shah, P. D. D. Schwindt, L. Hollberg, J. Kitching, L.-A. Liew, and J. Moreland, "A microfabricated atomic clock," Applied Physics Letters **85**, 1460–1462 (2004).

[2] S. Micalizio, C. E. Calosso, A. Godone, and F. Levi, "Metrological characterization of the pulsed Rb clock with optical detection," Metrologia **49**, 425–436 (2012).

[3] F.-X. Esnault, E. Blanshan, E. N. Ivanov, R. E. Scholten, J. Kitching, and E. A. Donley, "Cold-atom double-Λ coherent population trapping clock," Physical Review A **88** (2013), 10.1103/physreva.88.042120.

[4] S. Kang, M. Gharavipour, C. Affolderbach, F. Gruet, and G. Mileti, "Demonstration of a high-performance pulsed optically pumped Rb clock based on a compact magnetron-type microwave cavity," Journal of Applied Physics **117**, 104510 (2015).

[5] R. L. Tjoelker, J. D. Prestage, E. A. Burt, P. Chen, Y. J. Chong, S. K. Chung, W. Diener, T. Ely, D. G. Enzer, H. Mojaradi, C. Okino, M. Pauken, D. Robison, B. L. Swenson, B. Tucker, and R. Wang, "Mercury ion clock for a NASA technology demonstration mission," IEEE Transactions on Ultrasonics, Ferroelectrics, and Frequency Control **63**, 1034–1043 (2016).

[6] J. Cao, P. Zhang, J. Shang, K. Cui, J. Yuan, S. Chao, S. Wang, H. Shu, and X. Huang, "A compact, transportable single-ion optical clock with 7.8 × 10-

17 systematic uncertainty," Applied Physics B **123** (2017), 10.1007/s00340-017-6671-5.

[7] R. Elvin, G. W. Hoth, M. Wright, B. Lewis, J. P. McGilligan, A. S. Arnold, P. F. Griffin, and E. Riis, "Cold-atom clock based on a diffractive optic," Optics Express **27**, 38359 (2019).

[8] V. Maurice, Z. L. Newman, S. Dickerson, M. Rivers, J. Hsiao, P. Greene, M. Mescher, J. Kitching, M. T. Hummon, and C. Johnson, "Miniaturized optical frequency reference for next-generation portable optical clocks," Optics Express **28**, 24708 (2020).

[9] C. Carle, M. Petersen, N. Passilly, M. A. Hafiz, E. de Clercq, and R. Boudot, "Exploring the use of Ramsey-CPT spectroscopy for a microcell-based atomic clock," IEEE Transactions on Ultrasonics, Ferroelectrics, and Frequency Control **68**, 3249–3256 (2021).

[10] M. A. Hafiz, G. Coget, M. Petersen, C. E. Calosso, S. Guérandel, E. de Clercq, and R. Boudot, "Symmetric autobalanced Ramsey interrogation for high-performance coherent-population-trapping vapor-cell atomic clock," Applied Physics Letters **112**, 244102 (2018).

[11] X. Liu, J.-M. Mérolla, S. Guérandel, C. Gorecki, E. de Clercq, and R. Boudot, "Coherent-population-trapping resonances in buffer-gas-filled Cs-vapor cells with push-pull optical pumping," Physical Review A **87** (2013), 10.1103/physreva.87.013416.

[12] P. Yun, S. Guérandel, and E. de Clercq, "Coherent population trapping with polarization modulation," Journal of Applied Physics **119**, 244502 (2016).

[13] V. Yudin, A. Taichenachev, M. Y. Basalaev, T. Zanon-Willette, J. Pollock, M. Shuker, E. Donley, and J. Kitching, "Generalized autobalanced Ramsey spectroscopy of clock transitions," Physical Review Applied **9** (2018), 10.1103/physrevapplied.9.054034.

[14] C. Stefanucci, T. Bandi, F. Merli, M. Pellaton, C. Affolderbach, G. Mileti, and A. K. Skrivervik, "Compact microwave cavity for high performance rubidium frequency standards," Review of Scientific Instruments **83**, 104706 (2012).

[15] Q. Hao, W. Li, S. He, J. Lv, P. Wang, and G. Mei, "A physics package for rubidium atomic frequency standard with a short-term stability of $2.4 \times 10^{-13}\ \tau^{-1/2}$," Review of Scientific Instruments **87**, 123111 (2016).

[16] E. Batori, C. Affolderbach, M. Pellaton, F. Gruet, M. Violetti, Y. Su, A. K. Skrivervik, and G. Mileti, "μPOP clock: A microcell atomic clock based on a double-resonance Ramsey scheme," Physical Review Applied **18** (2022), 10.1103/physrevapplied.18.054039.

[17] F.-X. Esnault, D. Holleville, N. Rossetto, S. Guerandel, and N. Dimarcq, "High-stability compact atomic clock based on isotropic laser cooling," Physical Review A **82** (2010), 10.1103/physreva.82.033436.

[18] F. Esnault, N. Rossetto, D. Holleville, J. Delporte, and N. Dimarcq, "HORACE: A compact cold atom clock for Galileo," Advances in Space Research **47**, 854–858 (2011).

[19] S. T. Müller, D. V. Magalhães, R. F. Alves, and V. S. Bagnato, "Compact frequency standard based on an intracavity sample of cold cesium atoms," Journal of the Optical Society of America B **28**, 2592 (2011).

[20] P. Liu, Y. Meng, J. Wan, X. Wang, Y. Wang, L. Xiao, H. Cheng, and L. Liu, "Scheme for a compact cold-atom clock based on diffuse laser cooling in a cylindrical cavity," Physical Review A **92** (2015), 10.1103/physreva.92.062101.

[21] S. Lee, G. W. Choi, H.-G. Hong, T. Y. Kwon, S.-B. Lee, M.-S. Heo, and S. E. Park, "A compact cold-atom clock based on a loop-gap cavity," Applied Physics Letters **119**, 064002 (2021).

[22] Muquans, "Muclock data sheet," Available Online at https://www.muquans.com/product/muclock/ (Accessed Jan 2023).

[23] Spectra Dynamics, "cRb clock data sheet," Available Online at https://spectradynamics.com/products/crb-clock/ (Accessed Jan 2023).

[24] AOSense, "Cold-atom frequency standard data sheet," Available Online at https://aosense.com/product/cold-atom-frequency-standard/ (Accessed Jan 2023).

[25] M. Givon, L. Habib, A. Waxman, Y. Bar-Haim, O. Amit, Y. Cina, G. Boneh, D. Groswasser, T. David, B. Levy, A. Stern, and R. Folman, "In-vacuum microwave resonator for a compact cold atom frequency standard," (2022), arXiv:2208.09038.

[26] C. C. Nshii, M. Vangeleyn, J. P. Cotter, P. F. Griffin, E. A. Hinds, C. N. Ironside, P. See, A. G. Sinclair, E. Riis, and A. S. Arnold, "A surface-patterned chip as a strong source of ultracold atoms for quantum technologies," Nature Nanotechnology **8**, 321–324 (2013).

[27] A. Bregazzi, P. F. Griffin, A. S. Arnold, D. P. Burt, G. Martinez, R. Boudot, J. Kitching, E. Riis, and J. P. McGilligan, "A simple imaging solution for chip-scale laser cooling," Applied Physics Letters **119**, 184002 (2021).

[28] G. W. Hoth, E. A. Donley, and J. Kitching, "Atom number in magneto-optic traps with millimeter scale laser beams," Optics Letters **38**, 661 (2013).

[29] C. Affolderbach, W. Moreno, A. E. Ivanov, T. Debogovic, M. Pellaton, A. K. Skrivervik, E. de Rijk, and G. Mileti, "Study of additive manufactured microwave cavities for pulsed optically pumped atomic clock applications," Applied Physics Letters **112**, 113502 (2018).

[30] E. Batori, A. Bregazzi, B. Lewis, P. F. Griffin, E. Riis, G. Mileti, and C. Affolderbach, "An additive-manufactured microwave cavity for a compact cold-atom clock," In preparation (2023).

[31] A. V. Rakholia, H. J. McGuinness, and G. W. Biedermann, "Dual-axis high-data-rate atom interferometer via cold ensemble exchange," Physical Review Applied **2** (2014), 10.1103/physrevapplied.2.054012.

[32] G. H. Zhang, B. Braverman, A. Kawasaki, and V. Vuletić, "Note: Fast compact laser shutter using a direct current motor and three-dimensional printing," Review of Scientific Instruments **86**, 126105 (2015).

[33] Y.-X. Duan, B. Wang, J.-F. Xiang, Q. Liu, Q.-Z. Qu, D.-S. Lü, and L. Liu, "State preparation in a cold atom clock by optical pumping," Chinese Physics Letters **34**, 073201 (2017).

[34] G. Santarelli, C. Audoin, A. Makdissi, P. Laurent, G. Dick, and A. Clairon, "Frequency stability degradation of an oscillator slaved to a periodically interrogated atomic resonator," IEEE Transactions on Ultrasonics, Ferroelectrics and Frequency Control **45**, 887–894 (1998).

[35] F. Riehle, *Frequency standards: basics and applications* (John Wiley & Sons, 2006).

[36] B. Lewis, R. Elvin, A. S. Arnold, E. Riis, and P. F. Griffin, "A grating-chip atomic fountain," Applied Physics Letters **121**, 164001 (2022).

[37] D. A. Steck, "Rubidium 87 D line data," Available Online at http://steck.us/alkalidata, Version 2.1.5.

[38] N. Cooper, L. Coles, S. Everton, I. Maskery, R. Campion, S. Madkhaly, C. Morley, J. O'Shea, W. Evans, R. Saint, P. Krüger, F. Oručević, C. Tuck, R. Wildman, T. Fromhold, and L. Hackermüller, "Additively manufactured ultra-high vacuum chamber for portable quantum technologies," Additive Manufacturing **40**, 101898 (2021).

[39] B. J. Little, G. W. Hoth, J. Christensen, C. Walker, D. J. D. Smet, G. W. Biedermann, J. Lee, and P. D. D. Schwindt, "A passively pumped vacuum package sustaining cold atoms for more than 200 days," AVS Quantum Science **3**, 035001 (2021).

[40] O. S. Burrow, P. F. Osborn, E. Boughton, F. Mirando, D. P. Burt, P. F. Griffin, A. S. Arnold, and E. Riis, "Stand-alone vacuum cell for compact ultracold quantum technologies," Applied Physics Letters **119**, 124002 (2021).

5.1 Supplementary material to "A cold-atom Ramsey clock with a low volume physics package" [84]

5.1.1 Setup description

5.1.1.1 History

During our studies towards a cold-atom clock, the setup evolved from the first version to a second version. In particular two improvements were made: first the Extended Cavity Diode Laser (ECDL) was replaced with the single-frequency-fiber-laser-based MuQuans ILS and second atom recapturing was implemented which improved the atom number and reduces the cycle duration which both improve the clock short-term stability. The first version of the setup was used during my visit in Strathclyde while the second improved version was implemented after I had left. The results of chapters 4 and 5 were all obtained with the first setup while the results from [84] were obtained with the second version. All the main differences between the two setups are summed up in Table 5.1.

Feature	**First setup (this chapter)**	**Second setup [84]**
State selection	Yes	Yes
Atom recapturing	No	Yes
Laser	ECDL	MuQuans ILS
Microwave time t_m [μs]	167 and 200	200
Optimal Ramsey time T_R [ms]	10	10
Cycle duration T_C [ms]	528.7	140
Dick effect at $\tau = 1$ s	1.2×10^{-12}	6.12×10^{-13}
Short-term stability at $\tau = 1$ s	4.4×10^{-11}	1.5×10^{-11}

Table 5.1: Differences between the two setups mentionned in this chapter.

5.1.1.2 Optics part

The setup is described in more details on Figure 5.1. As described in [84], the power from the 780-nm ECDL is split in three after passing trough an EOM and a tappered amplifier (TA). Each arm passes through an AOM that allows to tune the light to different frequencies depending on the cycle phase. The first arm (AOM1) serves as trapping and cooling light and shines the cavity along its principal axis from the top. The light is coupled to the physics package with an optical fibre. The two other arms are rejoined in a single optical fiber. The second AOM is tuned to allow for state selection whilst the third one is used for the readout phase. In each cycle phase, the EOM is driven with the desired frequency if necessary to generate side bands. Each arm is shut using mechanical shutters [100] and telescopes. For the sake of simplicity, they are not shown on Figure 5.1. A CCD camera allows to image the cloud using the fluorescence emitted by the atoms when flipping the mirror next to it.

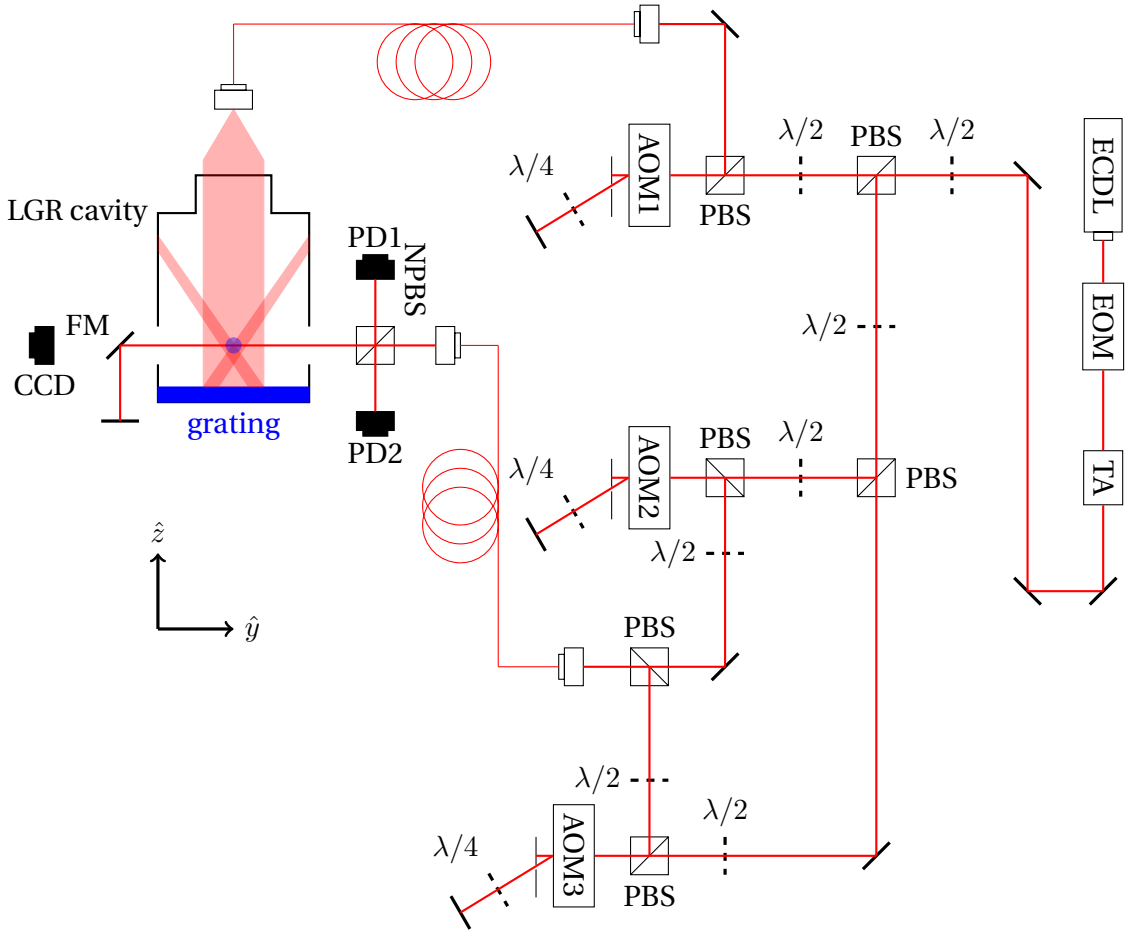

Figure 5.1: Optical setup: TA: Tappered amplifier, AOM: acusto-optical mudulator, EOM: electro-optical modulator, ECDL: extended cavity diode laser. PBS: Polarizing beam splitter. NPBS: Non-polarizing beam splitter. CCD: Camera used to image the atoms. FP: Flip mirror.

It is worth mentioning that unlike in most vapor-cell designs, the preparation and interrogation beams are linearly polarized in the $\hat{z}$ direction, which is parallel to the C-field magnetic quantification axis. This geometry leads to more complicated pumping scheme, but it was analytically shown [57], [153] that the atoms accumulate in the sublevels near $m_F = 0$.

5.1.1.3 Microwave generator and Dick effect

The microwave pulses are generated with a commercial Keysight E8257D microwave synthesizer with UNX option whose phase noise is presented on Figure 5.2. The phase noise is presented with the LO2 phase noise used in the μPOP experiment (see chapter 3) as mean of comparison. It is important to emphasize that the E8257D phase noise spectrum taken from the datasheet does not feature the expected noise spurs like the one shown on the LO2 spectrum. In other words, the Dick effect estimation of [12], [84] are lower bounds.

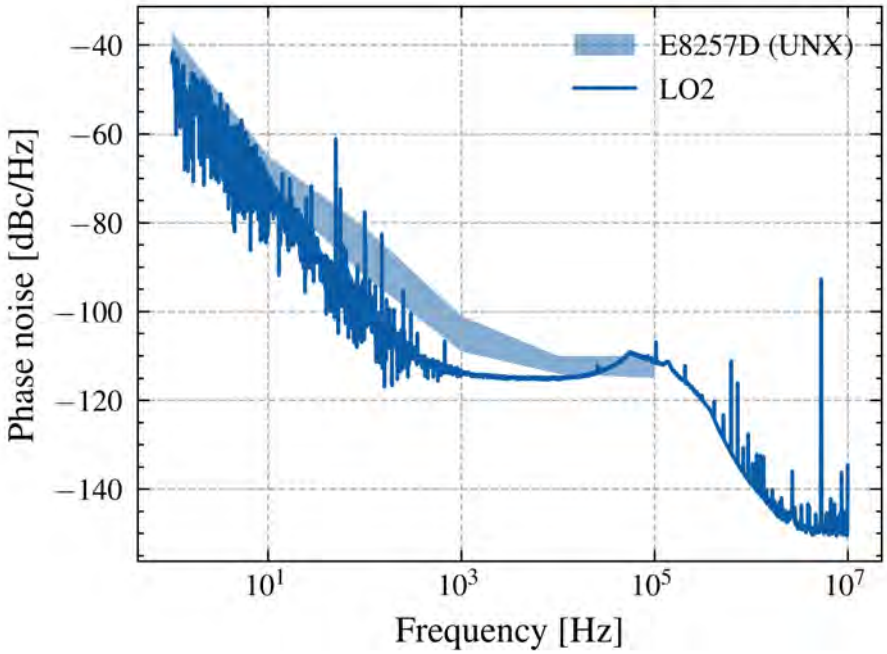

Figure 5.2: E8257D (UNX-option) and LO2 phase noises at carrier frequency 6.835 GHz inferred from the datasheet. The former is taken from the datasheet and the latter is measured with a phase noise analyzer.

In Ramsey-type atomic clocks, the Dick effect [154] is estimated with [62]:

$$\sigma_y^{Dick}(\tau) = \left(\sum_{k=1}^{\infty} \mathrm{sinc} \left(\frac{k\pi T_R}{T_C} \right)^2 S_y^{LO} \left(\frac{k}{T_C} \right) \right)^{1/2} \tau^{-1/2} \tag{5.1}$$

with T_R the Ramsey time and T_C the total cycle time and S_y^{LO} [Hz^{-1}] the relative frequency noise of the oscillator computed from the frequency noise S_ϕ [116]:

$$S_y(f) = \frac{f^2}{f_0^2} S_\phi(f) \tag{5.2}$$

with f_0 the nominal frequency, in our case the ^{87}Rb clock frequency.

Figure 5.3 shows the estimated Dick effect with respect to cycle time T_C. The contribution is calculated from the phase noise of Figure 5.2. In the setup second version with shorter total cycle time T_C, the Dick effect is improved from 1.5×10^{-12} to 0.3×10^{-12} compared to the first setup version. In both cases the Dick effect is not the limiting effect of the clock short-term stability, although it will be a serious limitation in future versions of the clock when competing with existing cold-atom frequency standards (see Table 1.1).

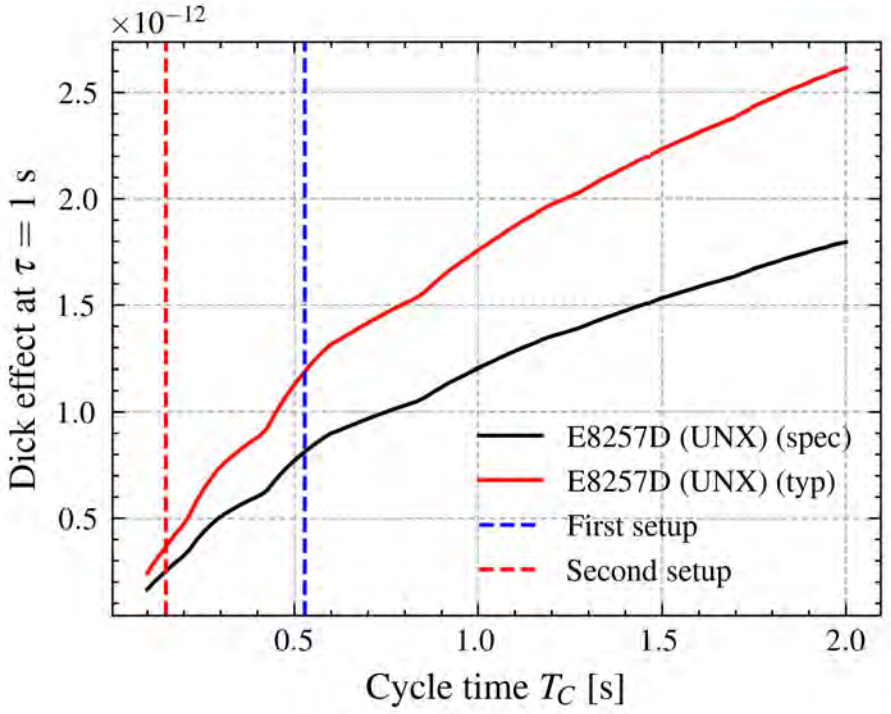

Figure 5.3: Dick effect for $\tau = 1$ s. The spec (typ) is the specification (typical) phase noise of the E8257D with UNX option according the the datasheet. Calculated with $T_R = 10$ ms.

5.1.2 Setup characterization

5.1.2.1 Atom cloud description

The number of atoms with respect to the loading time, in the absence of atom recapturing, is shown on Figure 5.4. The method for estimating the atoms is well-described in [155]. These values are representative of the order of magnitude as different values of the shims-generated magnetic field or the ^{87}Rb dispenser current would lead to slightly higher or lower number of atoms. For 1 s, one traps $N_A = (849 \pm 7) \cdot 10^3$ atoms. The 0.8% deviation is the reason why the state selection must feature a normalizing photodiode (see Figure 5.1).

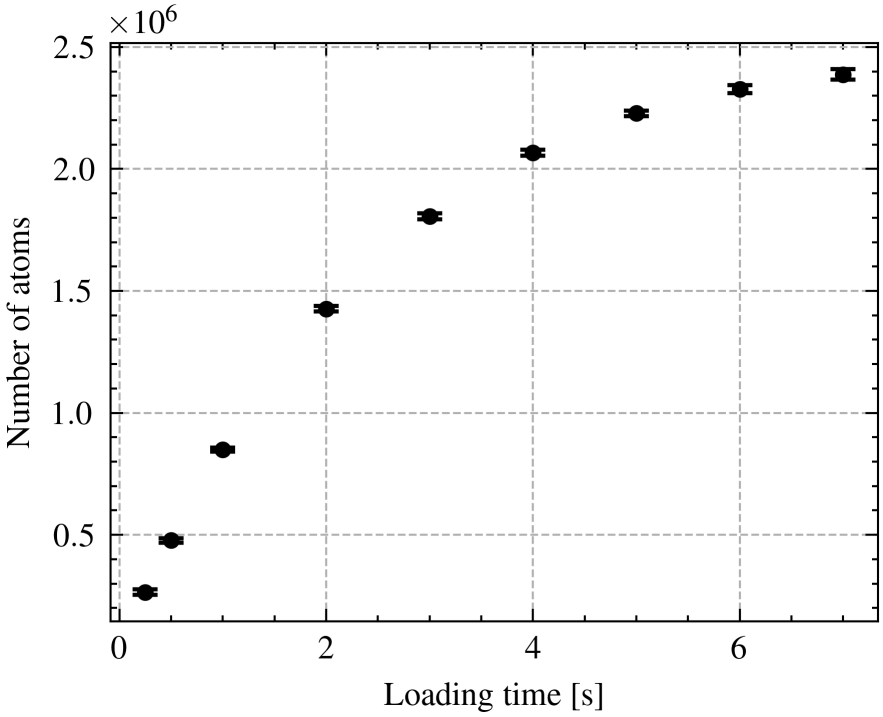

Figure 5.4: Number of atoms with respect to loading time. The data was taken in the first setup version in absence of atom recapturing.

Figure 5.5 shows the atom cloud using the CCD (see Figure 5.1) with respect to the falling time τ_{free} after the cooling and trapping phases. The 4 mm side hole is clearly visible on the images. Even though the image taken at 20 ms suggests that the atoms have all disappeared, Ramsey fringes could be measured, as shown on Figure 5.10.

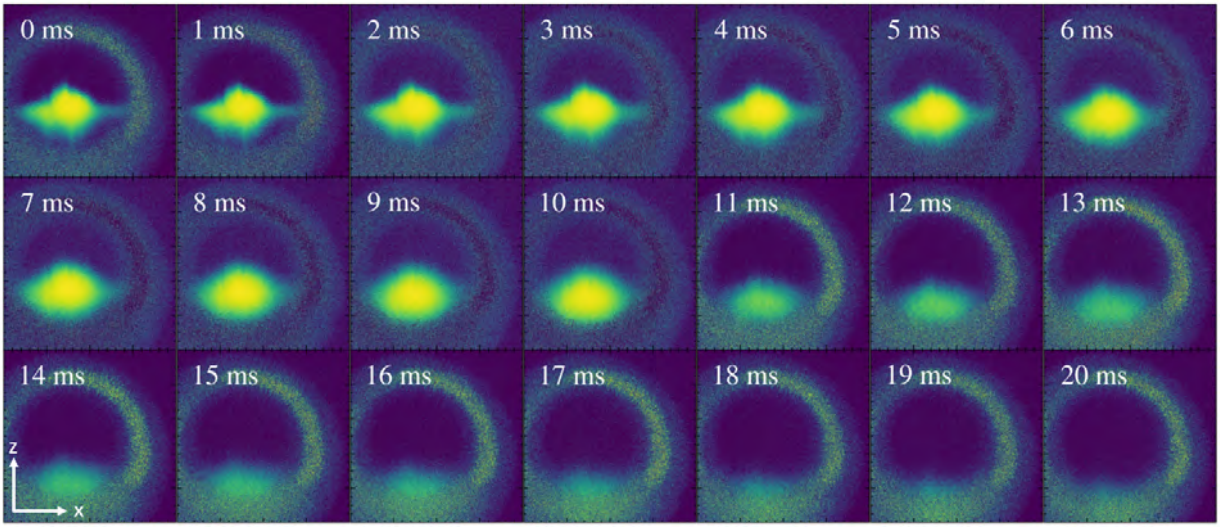

Figure 5.5: Atom cloud with respect to falling time τ_{free} time after cooling and trapping.

Figure 5.6 shows the position of the cloud and its Oxz section with respect to time. The cloud vertical and horizontal position and width are fitted with a 2d gaussian function from Figure 5.5. We fit the vertical vertical z position with respect to time of the cloud with:

$$z(t) = \frac{1}{2}at^2 + z_0. \tag{5.3}$$

The acceleration is $a = (-7.5 \pm 0.3)$ m/s^2, which is not compatible with the gravitation constant g, shows that the atoms are imaged with an angle of $\approx 40°$.

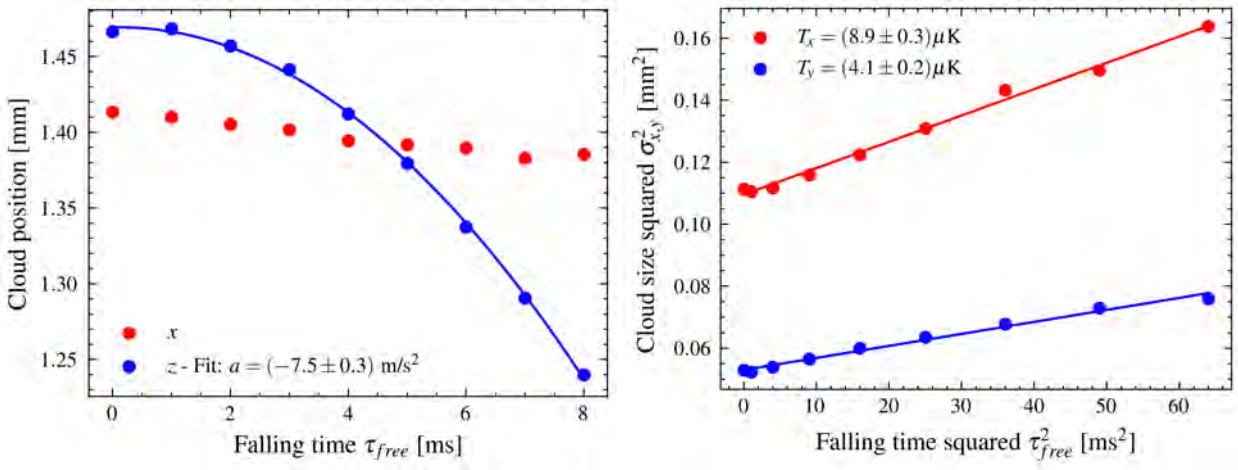

Figure 5.6: **Left:** Atom cloud position with respect to time. **Right:** Atom cloud size with respect to the free fall time squared. Note that the data was acquired with the EQOP in-house program which did not provide uncertainty on the fit parameters.

The temperature of the cloud can — in principle — be estimated by monitoring the cloud's size expansion with time. However, the region of interest is clipped by the side hole, which could lead to false results. For this reason, only the data up to 10 ms is used. The cloud temperature can be measured using [155]:

$$\sigma_{x,z}^2(t) = \left(\sigma_{x,z}^{(0)}\right)^2 + \frac{k_B T}{M_{Rb87}} t^2, \tag{5.4}$$

with k_B the Boltzmann constant and M_{Rb87} the mass of the ^{87}Rb atom and $\sigma_{x,z}$ the cloud spatial standard deviation assuming a gaussian distribution. $\sigma_{x,y}^2$ is hence interpreted as the atom size. The values extracted from the horizontal and vertical fit differ which is typical given the highly asymmetric clamping in the picture. It is however not always the case [155]. Since the atom moves less in the horizontal axis the fitted value is less likely to be affected by the atom loss due to gravity. It is reasonable to say that the temperature is:

$$T_{atoms} = (8.9 \pm 0.3)\mu\text{K} \approx 10\mu\text{K}. \tag{5.5}$$

5.1.3 Readout

As described in [84], the measurement photodiode PD1 signal (see Figure 5.1) is normalized using a second photodiode PD2. The two photodiodes' levels are balanced, namely the DC voltage is the same in the absence of atoms. P_2, the proportion of atoms in the states $|F=2,m_F=0\rangle$ before the readout is measured by acquiring two different signals, the first one with pump light tuned on the $|F=2\rangle \rightarrow |F'=3\rangle$ transition and the second one with $\approx 5\%$ sidebands repump light tuned on $|F=1\rangle \rightarrow |F'=3\rangle$ for pumping all the atoms in the $|F=2\rangle$ levels.

The signal is then constructed my mixing $\Phi_{out}^{(i=1,2)}$, the photon flux on PD1 during the first ($i=1$) and the second ($i=2$) pulse and Φ_{in} the photon flux on the reference photodiode. According to Beer-Lambert law in the thin layer approximation (see eq. (2.31)), one has:

$$\Phi_{out}^{(i)} = \Phi_{in} e^{-\alpha N_2^{(i)}} \tag{5.6}$$

with $N_2^{(i)}$ the number of atoms in $|F=2,m_F=0\rangle$ during pulse i and α a constant that depends on the atom size and light detuning. If one combines the two signals in the following manner:

$$\begin{aligned} \frac{\Phi_{out}^{(1)} - \Phi_{in}}{\Phi_{out}^{(2)} - \Phi_{in}} &\approx \frac{\Phi_{in}(1-\alpha N_2^{(1)}) - \Phi_{in}}{\Phi_{in}(1-\alpha N_2^{(2)}) - \Phi_{in}} \\ &= \frac{N_2^{(1)}}{N_2^{(2)}} = P_2, \end{aligned} \tag{5.7}$$

were we used that $N_2^{(1)}$ is the number of atoms in $|F=2,m_F=0\rangle$ before the readout and $N_2^{(2)}$ the total number of atoms pumped in this state because of the sideband.

Note that when the EOM is driven during the second pulse, the light intensity is partially spread in the sideband, namely $\Phi_{in}^{(2)} < \Phi_{in}^{(1)}$. Eq. (5.7) is transformed such that:

$$P_2 \rightarrow P_2' = \frac{\Phi_{in}^{(1)}}{\Phi_{in}^{(2)}} P_2 > P_2, \tag{5.8}$$

which explains why $P_2 > 1$ in some cases of Figure 5.9. Furthermore, the two photodiodes levels balance was not always guaranteed because of day-to-day drift which explains the fluctuating baseline level when acquiring Ramsey fringes. Note that this issue can be partially solved by measuring the two photodiodes levels in the absence of atoms which allows numerical correction of $\Phi_{in}^{(2)}$. This technique is however not implementable in a cycle with atom-repumping as in [84] as the atoms are always present. It is worth recalling that a slow unbalance drift between the two photodiodes is not critical when it comes to clocks performances.

5.1.4 State selection

After molasses, all the atoms are in the energy levels $|F = 2, m_F = 0, \pm 1, \pm 2\rangle$. By interaction of the atoms with pumping light tuned on $|F = 2\rangle \rightarrow |F' = 2\rangle$ and repumping light tuned on $|F = 1\rangle \rightarrow |F' = 2\rangle$, all the atoms are sent into the $|F = 2, m_F = 0\rangle$ sublevel [156]. To generate these two lights, the laser is stabilized to the $|F = 2\rangle \rightarrow |F' = 2\rangle$ transition and the EOM is modulated at 6.835 GHz to generate the repump sidebands.

Figure 5.7 shows the Zeeman spectrum with respect to different microwave input power injected in the EOM. The optimal power is $P_{EOM} = 17$ dBm as the π transitions at ± 150 kHz vanish. The σ transitions are not visible thanks to the low field inhomogeneity, as shown in [12]. It is interesting to note that, at lower P_{EOM}, the central and side π peaks have opposite signs. This is explained by weak repump light pumping the atoms in a statistical mixture of states $|F = 2, m_F = 0\rangle$ and $|F = 1, \pm m_F = 1\rangle$.

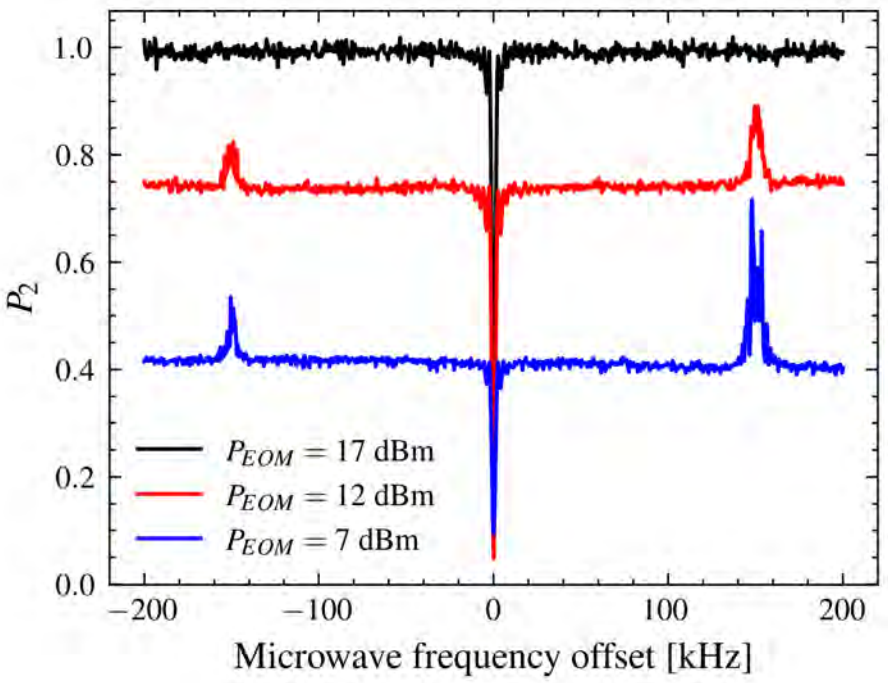

Figure 5.7: Zeeman spectrum after the state selection during preparation time t_{prep} (see Figure 1 of [12]) with respect to the power injected in the EOM.

The π peaks amplitude imbalance is attributed to a potential imbalance of $\sigma^{\pm}$-polarized light during trapping and cooling phase.

5.1.5 Zeeman central fringe

The Zeeman spectrum of Figure 5.8 was acquired in Rabi mode (i.e. with $T_R = 0$). Many pieces of informations can be extracted by analysing the central Zeeman peak. Indeed, fitting the peak with the model of eq. (2.26) with $T_R = 0$ allows for recovering the pulse area θ — which defines the fringes envelope shape — and the central frequency which allows to measure the C-field. An example of such Zeeman central fringe is shown on Figure 5.8. The shape is compatible to a sinc^2 shape which is expected from the square shape of the microwave pulse.

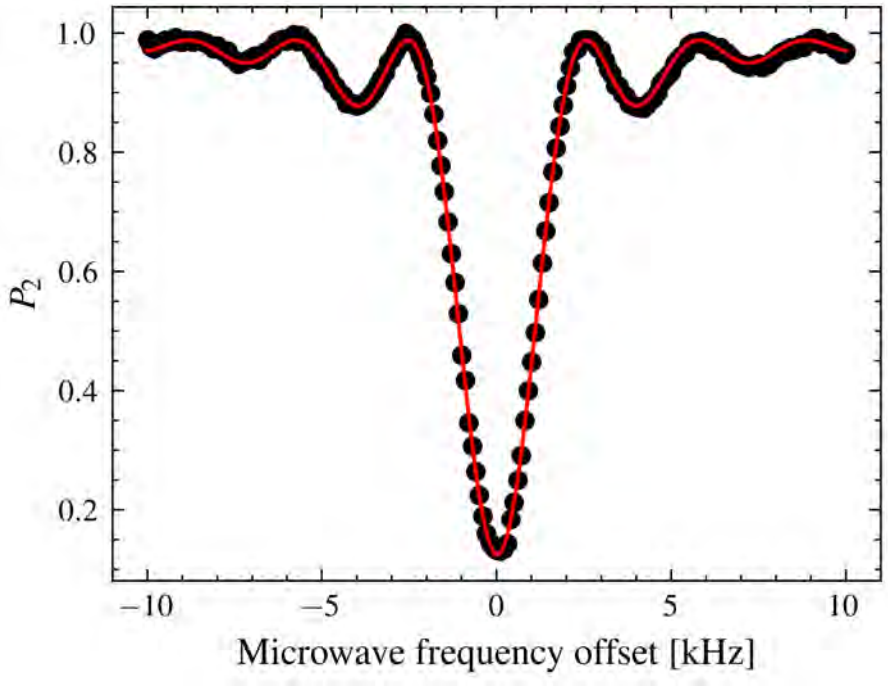

Figure 5.8: Zeeman central fringe acquired with $t_m = 167\mu$s in Rabi mode (i.e. $T_R = 0$). The single pulse area is $\Theta/\pi = (0.522 \pm 0.03)$. The 2$^{\text{nd}}$ order Zeeman shift allows to compute a C-field $B_3 = (61 \pm 2)$ mG.

5.1.6 Clock signal

5.1.6.1 Ramsey fringes

Ramsey fringes for different Ramsey times are shown on Figure 5.9. The outliers present on the Fringes for 8 and 10 ms are typically related to the lab door opening and closing, which shows the setup is sensitive to vibrations.

In practice Ramsey fringes with Ramsey times up to 20 ms could be acquired. Due to the high probability of the ECDL delocking for measurements featuring a high number of points, only few clean fringes with full frequency span are available, which explains why the next studies were

restricted to the central fringe only.

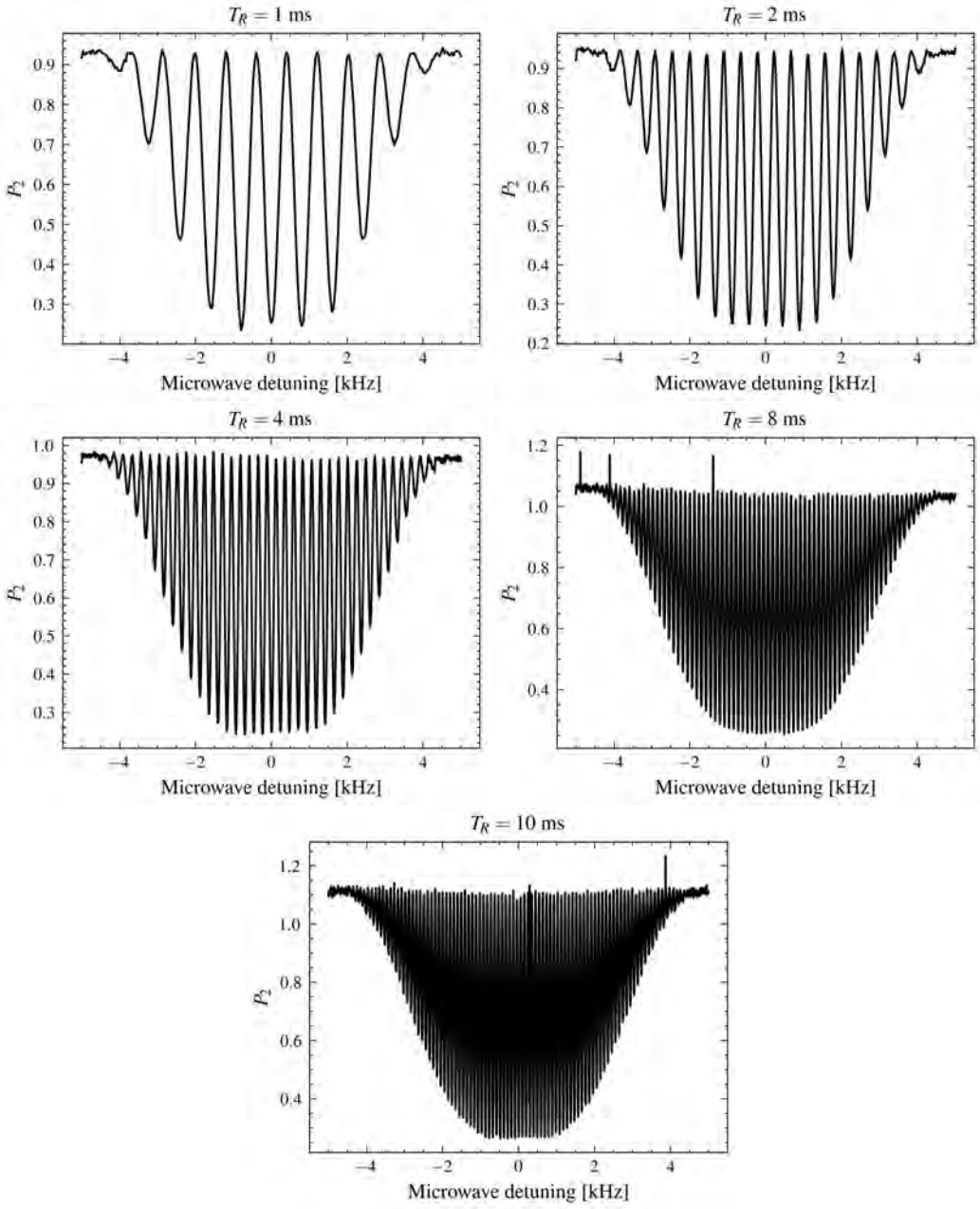

Figure 5.9: Ramsey fringes for $T_R = 1, 2, 4, 8, 10$ ms and $t_m = 200$ μs. See eq. (5.8) and the following discussion for $P_2 > 1$.

5.1.6.2 SNR optmization

Figure 5.10 shows Ramsey central fringes for a set of Ramsey time T_R. For 20 ms, the SNR is visually quite low which is consistent with the almost total absence of atoms as shown on Figure 5.5. Note that outliers are remove using the Median Absolute Deviation (MAD) method [112].

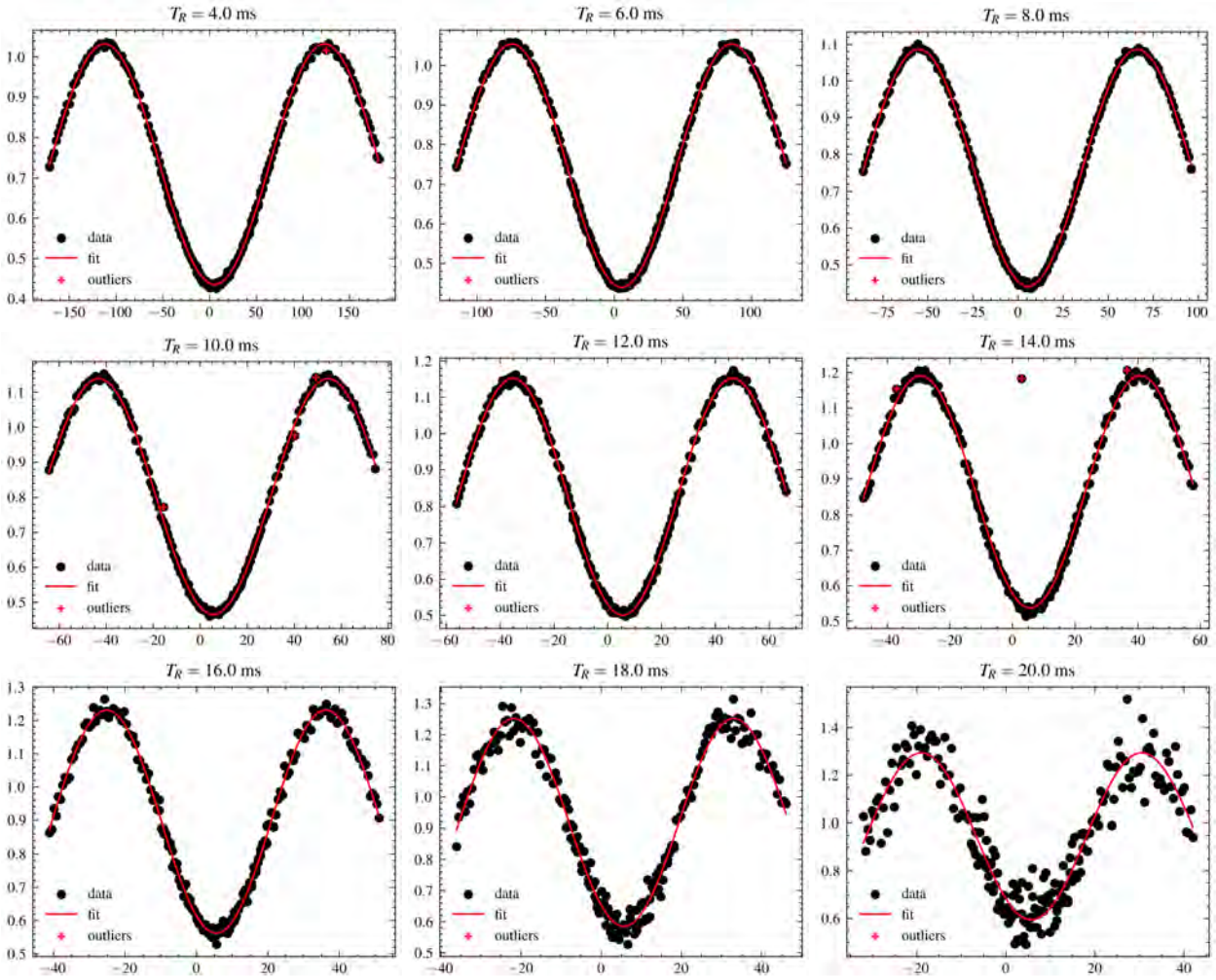

Figure 5.10: Different error signals.

The short-term stability of the clock is estimated using [3], namely:

$$\sigma_y(\tau) = \frac{1}{\pi \cdot C \cdot Q \cdot \mathrm{SNR}} \sqrt{\frac{T_C}{\tau}}, \tag{5.9}$$

with $T_C = 528.7$ ms [12]. The SNR is estimated using the residuals of the fits to Figure 5.10 — outliers excluded — namely [157]:

$$\mathrm{SNR} = \frac{\hat{A}^2}{\sigma_e^2}, \tag{5.10}$$

with $\hat{A}$ the amplitude of the fitted sinus and σ_e the deviation of the fit residuals. The errorbars on the SNR are given by the Cramer-Rao lower band [157] which gives the SNR lower-bound. Consequently, the error bars are smaller for low SNR.

Figure 5.11 shows the SNR and estimated 1s Alan deviation of the clock based on the SNR analysis of the fringes. The optimum is found for $T_R = 10$ ms were the SNR drop and the Q-factor balance to reach an optimum. The estimated short-term stability is $\sigma_y = 4.4(2) \times 10^{-11} \tau^{-1/2}$.

Similar optimization has been carried for [84]. Thanks to atom recapturing and the use of a better laser, the short-term stability could be improved to $\sigma_y(\tau) = 1.49 \times 10^{-11}\tau^{-1/2}$.

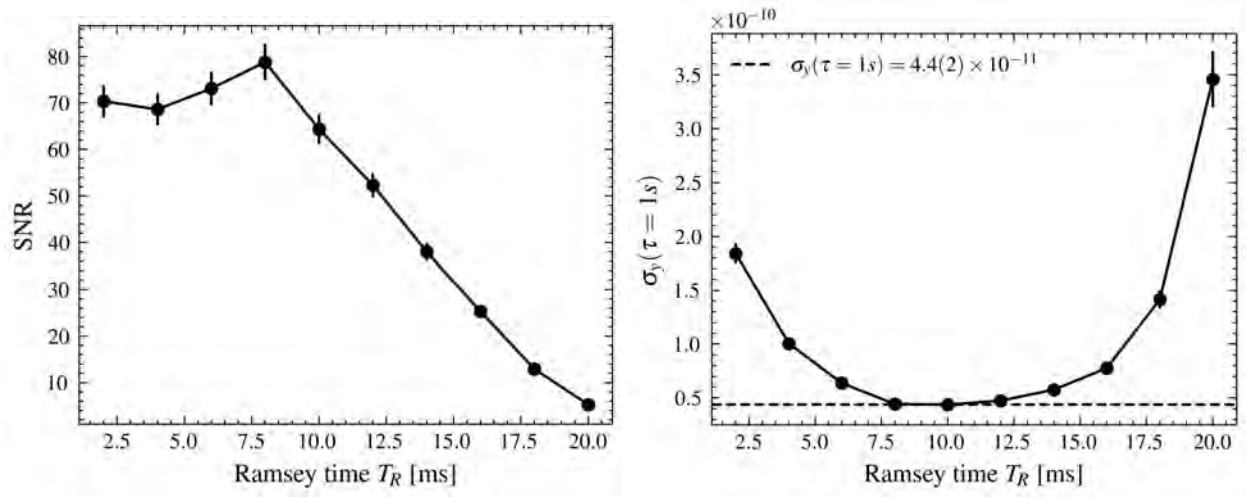

Figure 5.11: **Left:** Fringes SNR. **Right:** Estimated short-term stability.

5.2 Clock performances

5.2.1 Measurement

Figure 5.12 shows the relative frequency and stability measured in the first setup conditions (see Table 5.1). The data was acquired by A. Bregazzi shortly after I left Strathclyde. The measured short-term stability is $4.8 \times 10^{-11}\tau^{-1/2}$, which is compatible with the SNR estimation presented in section 5.1.6.2. The estimation being smaller than the measurement suggests that some extra phenomenon — like the Dick effect — is needed to explain the discrepancy. According to Figure 5.3, the Dick effect alone is however insufficient to explain the difference.

In the second setup version (see Table 5.1), the short-term stability is improved to $1.5 \times 10^{-12}\tau^{-1/2}$. The three-fold improved short-term stability coincidently corresponds to the three-fold improvement of atom number going from $\approx 10^6$ to $\approx 3 \times 10^6$ atoms.

In the mid-term as developed in [84], the clock is limited by the 2$^{\text{nd}}$ order Zeeman shift as it was always expected. This points to an obvious next-step improvement of shielding the setup with μ-metal magnetic shields.

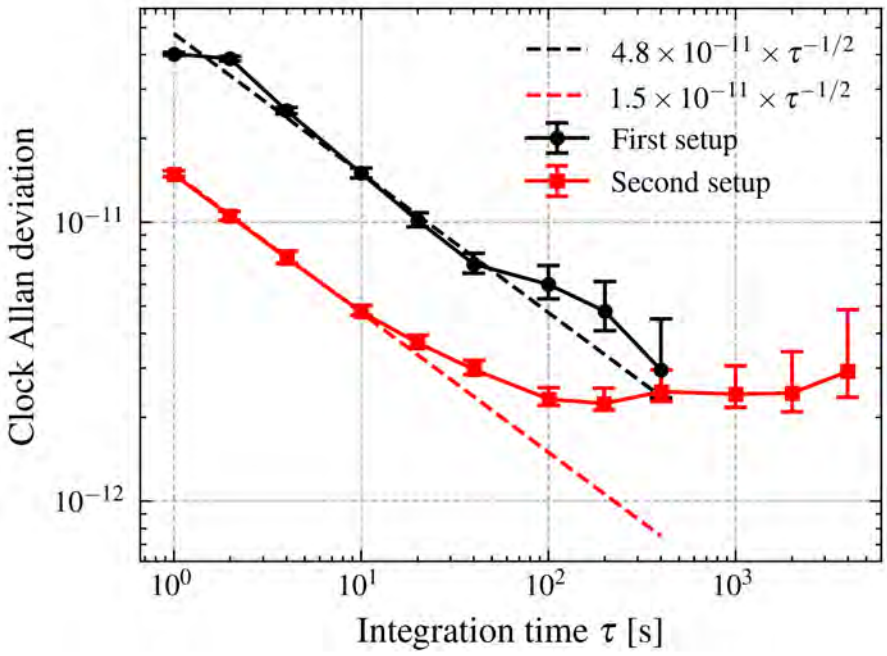

Figure 5.12: Clock short-term stability comparison between the two versions of the setup. Second version data: courtesy of Alan Bregazzi.

5.2.2 Discussion

Figure 5.13 shows the performances of our compact cold-atom clock [84] compared to the performances of the clocks of Table 1.1.

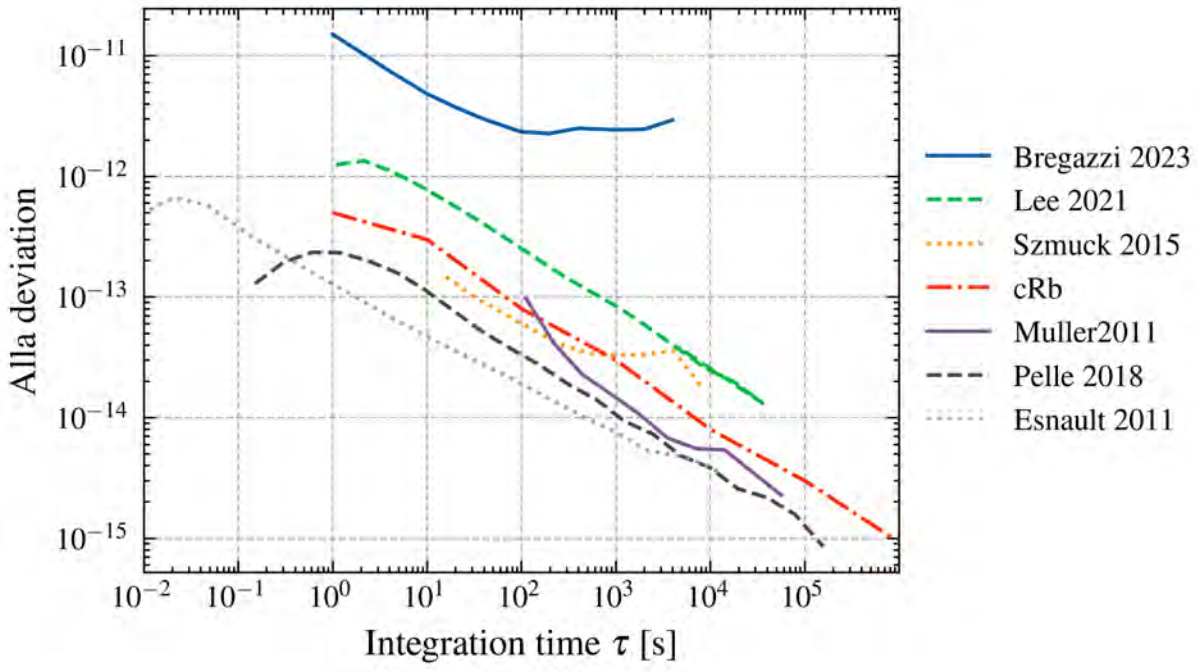

Figure 5.13: Performances of compact cold-atom DR standards listed in Table 1.1. Bregazzi 2023 [84], Lee 2021 [82], Szmuck 2015 [74], cRb [21], Muller 2011 [158], Pelle 2018 [72] and Esnault 2011 [22].

Evidently, the performances of this work are not comparable to other setups. Indeed, winning one order of magnitude and breaking the $10^{-12}\tau^{-1/2}$ limit would be desirable in future designs. As demonstrated in [84], the current limit is given by the laser RIN.

As mean of comparison, the setup of Lee2021 [82] (see Figure 1.1) use 10 times more atoms at a temperature of 2.5 μK, which is 4 times better than for the current setup discussed here. The SNR limit could be improved in two ways: by increasing the dispensers current to increase the number of atoms or increasing the Ramsey time. This latter point clearly is the main weakness of our proof of concept. Indeed, by placing the grating below the atoms with no mini-fountain mechanism, the optimal Ramsey time is not the best achievable given the low temperatures of the atoms. Indeed, in mini-fountain [151] or free-fall (see Figure 6.1) operation, for a reasonable $T_R = 50$ ms, the RIN contribution to the short-term stability should be improved by a factor of 5 (see eq. 2.28 and eq. (5.9)), reaching the Dick effect levels calculated in Figure 5.3.

Another way to emphasize this point is by comparing our performances with Szmuck2015 [74] of Figure 1.1 whose setup features the same number of atoms and a temperature of 20 μK but with a Ramsey time of 5 seconds. In the current conditions, increasing Ramsey time up to 50 ms — which was already demonstrated possible in [151] in a very similar setup — would push the SNR limit down to $3 \times 10^{-12}\tau^{-1/2}$, putting the performances comparable to [82] for a lower SWaP thanks to our GMOT approach.

5.3 Conclusion

In this chapter, advanced details on the building of the first version of the atomic clock presented in [84] were given. This first proof of concept is successful as it is the first demonstration of a cold-atom DR Ramsey clock using a grating for cooling an trapping the atoms.

The best achieved short-term stability so far, $1.49 \times 10^{-11}\tau^{-1/2}$, is limited in the short-term by the laser RIN [84]. The low stability compared to competitors is explained by the clock geometry that impose an optimal Ramsey time of 10 ms. This — as developed in chapter 4 conclusion — could be solved by using the setup in a mini-fountain fashion or by putting the cavity upside down. Second, our design features a smaller SWaP compared to other setups, which — according to [14] — is generally correlated to a decrease in performances with the benefit of more portability.

Chapter 6

Conclusion

In this thesis, results on two different clocks have been presented. This conclusion recalls all the important results and discusses potential next steps.

6.1 μPOP studies

Chapter 3 and paper [1] present results on a state-of-the-art miniature cell Ramsey DR clock with $\sigma_y(\tau) \leq 2 \times 10^{-11}\tau^{-1/2}$ short-term stability and 1.5×10^{-12} one day stability. Both short-term and long-term stability limitations were determined. As demonstrated in [1], the short-term stability is limited by the laser RIN. Thorough short-term optimization was carried out to minimize the contribution of the RIN and Dick effect with important constraints due to the high relaxation rates inside of the cell imposed by its small volume. Overall, the theory and measurement mismatch is only a mere 5% showing excellent control. As shown on chapter 3, the long-term stability budget is limited by the position and microwave-power shifts, alternatively. Special statistical care had to be taken to complete the analysis. In particular, the use of Groslambert covariance is necessary to account for cross-correlations between different contributors. The position shift ultimately limits the long-term stability. Fluctuations of the laser beam position are strongly correlated to the laboratory dew point temperature. Finally, a fast and reliable method for measuring relaxation rates in Ramsey-type DR clocks was described.

In order to improve on the compactness of the μPOP experiment, the laser head footprint must be reduced, pointing to the use of a Vertical-Cavity Surface-Emitting Laser (VCSEL) instead of a Distributed-Feedback Laser (DFB) with frequency stabilization on the physics package vapor-cell. Although the light could be switched on and off using a fibre-coupled AOM, this technique would not drastically reduce the SWaP of the setup. Although it is clear that building an AOM-free pulsed laser head, as demonstrated in [147] for CPT miniature atomic clocks, represents significant engineering efforts, it would also represent a significant SWaP improvement.

It is obvious that implementing the points discussed above would degrade the short-term stability of the clock as VCSEL show worse RIN than DFB. However, atomic clocks are not devices aiming for

optimal short-term stability. Moreover, a worse short-term stability could be compensated by the use a stable-enough quartz with an optimized steering time constant. The approach of degrading the short-term stability with the perk of improving SWaP and long-term performances is hence a perfectly sound approach, as it was recently illustrated in [96].

Improvement of long-term stability must focus on reducing microwave-power and position shifts influences. It is worth reminding that these two effects are intrinsically linked to the spatial distribution of resonance frequencies inside of the cell, as discussed in chapter 2. Therefore, improvement of the C-field homogeneity as proposed in the already built second version of the resonator [146] could be an elegant passive solution for reducing those two effects. The more compact solution of VCSEL, with or without fibre-coupled AOM, discussed in the previous paragraph is also likely to passively reduce the sensitivity to the position shift as the fluctuation of the laser position would be strongly reduced using optical fibres of more compact free-space geometry. Finally, reduction of microwave-power shift contribution can be achieved with microwave power stabilization via improved Ramsey cycle, as shown in [159]. With those implementations, measurements presented in Table 3.1 suggest that the ultimate μPOP approach could be as good as $\approx 2 \times 10^{-13}$ at one day, limited by the intensity light shift.

6.2 Microwave cavity for high-performance atomic clocks

In this chapter, the design and realization of a microwave cavity for a compact cold-atom clock with gMOT is presented. A thorough workflow allows to build a cavity with an error as low as 60 MHz, which is easily compensated with the tuning mechanism with a range of ≈ 200 MHz. Special care was taken to push neighboring modes as far as possible, which is not the case of the μPOP resonator. Implementation of the cavity in the clock setup in Strathclyde allowed us to measure Zeeman spectra, Rabi oscillations and Ramsey fringes with Ramsey time up to 20 ms. Zeeman spectra and Rabi oscillations allow to measure the excellent field homogeneity and uniformity, respectively.

Since the cold-atom clock featuring the cavity presented in chapter 5 is still under development, it is too early to give an exhaustive list of further improvements. However, it is already possible to anticipate a few points. First, the longest available Ramsey time is, in the current clock setup, limited by gravity and atom leaving the transverse probe beam. No update on the cavity is needed to operate the setup in a mini-fountain fashion, as proposed in [12] and [84]. However, we can propose a simpler approach to extend the Ramsey time by reversing the cavity vertically. In this geometry, shown on Figure 6.1, the atom would be prepared below the grating and probed further down the cavity which requires a second pair of holes. Note that the first pair is still mandatory to execute state selection as it is already done in [84]. Given that the atom fall freely, the vertical position h [m] of the side holes restrict the Ramsey time to $T_R = \sqrt{2h/g}$ which is not convenient if one wants to optimize T_R. A simple solution would be to drill elongated side holes, which does not impact the mode quality as shown by our simulations. In this geometry, it has been shown (see section 4.1.1.7) that the phase shift would be of the order of 2 Hz. This shift is likely to be much smaller in the mini-fountain approach.

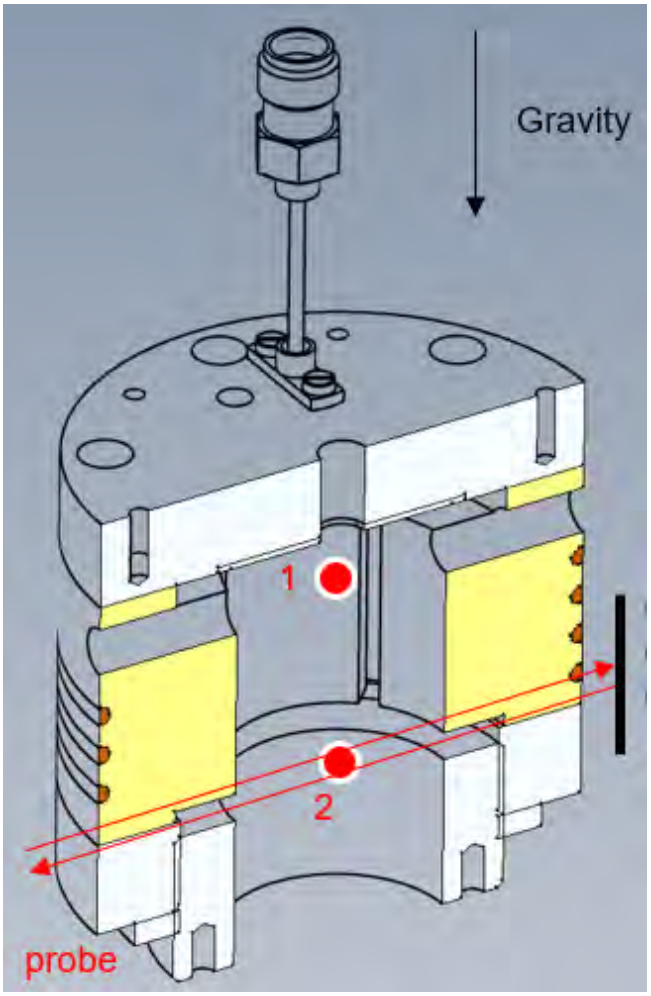

Figure 6.1: Another proposal for increasing the Ramsey time and improving the short-term performances of the clock. Atoms are prepared below the grating and driven with the first $\pi/2$ microwave pulse at point 1. The atoms then fall to point 2 where they are driven with the second microwave pulse and the population difference is probed.

Another relevant step towards a more compact setup would be to produce a Titanium cavity acting as a vacuum chamber. It has indeed been shown that a standalone ceramic vacuum chamber was able to retain vacuum conditions for building MOT for at least 500 days [160]. it is very likely that this lifetime could be significantly improved thanks to Titanium. In principle, building an additive-manufacturing Titanium microwave cavity should not be a major challenge as the cavity material is barely a relevant parameter as long as it is a good, non-magnetic conductor with low enough degassing for vacuum applications.

6.3 Cold-atom clock studies

First demonstration of a DR cold-atom clock using a gMOT was presented in chapter 5 and in [84]. The best short-term stability so far of 1.5×10^{-11} is limited by the laser RIN contribution shortly followed by the 2$^{\text{nd}}$-order Zeeman effect. Interestingly, it was last shown that the stability measurement was limited in the mid-term by the GPS disciplined oscillator as reference for $\tau \in [20, 1000]$ s. The optimal Ramsey time was, in the current setup, 10 ms, which is constrained by the geometry. Proof of effective state selection was demonstrated.

In the previous section, solutions for augmenting the Ramsey time were already discussed. Another critical improvement point is putting the setup in a doubly-shielded μ-metal for lowering the contribution of the 2$^{\text{nd}}$-order Zeeman effect.

The most delicate point is addressing the low short-term stability compared to state-of-the-art cold-atom clocks presented in Table 1.1. Indeed, among our competitors, the TACC [74], [80] shows similar Ramsey time and atom number with roughly 1.5 order of magnitude better short-term performance with $\sigma_y(\tau) = 5.8 \times 10^{-13}\tau^{-1/2}$ which should be achievable in a suppressed 2$^{\text{nd}}$-order Zeeman setup. It is important to note that two versions of the setup with two different lasers were used. The second laser, the MuQuans ILS, showed better performances than the previously used ECDL. Although the short-term stability was improved only from 4.4×10^{-11} to 1.5×10^{-11}, which corresponds to the increase of atom number thanks to state selection, this points out that the detection scheme was not fully optimized. Possible explanations range from unoptimized readout light intensity levels to photodiode noise.

6.4 Final thoughts

The performances of the μPOP and the cold-atom clocks are presented on Figure 6.2. Interestingly, they share similar short-term stability with $\sigma_y(\tau) < 2 \times 10^{-11}\tau^{-1/2}$. Although the cold-atom clock stability was not measured up to $\tau = 10^5$s, both clocks would qualify as *telecomgrade*. In the long-term, the μPOP would certainly show one order of magnitude better performances than the cold-atom clock.

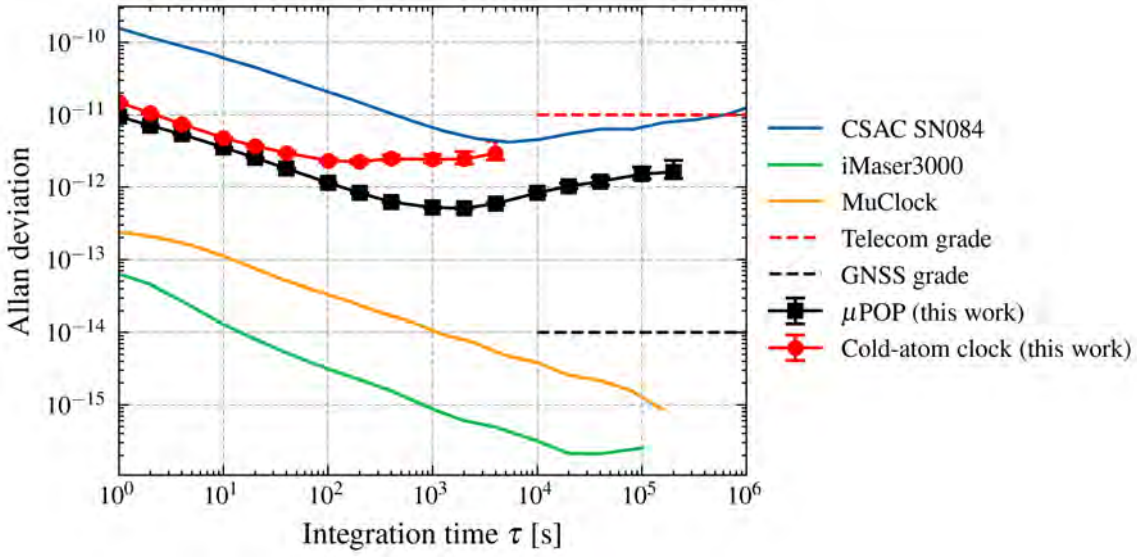

Figure 6.2: Performances of the two clocks presented in this manuscript along with other clocks for reference: CSAC SN04 [161], iMaser3000 [120] and Horace [22].

In principle, the cold-atom clock should exhibit better performances compared to the μPOP which is obviously not the case. This conclusion however illustrates the fundamental difference between the two projects maturity-wise: on the one side, the μPOP is the result of extensive studies on miniature-cell DR clocks with thorough short-term optimization. Although the success of the Ramsey approach was not guaranteed beforehand, these studies benefited from the strong knowledge accumulated in previous studies. For instance the LGR and the vapor-cell both featured in a previous CW clock [162] with previous state-of-the-art frequency stability. This is for all these reasons that the μPOP stands at the best end of the microwave miniature-cell clocks spectrum.

On the other hand, the cold-atom clock presented here stands at the far end of the cold-atom DR microwave standards spectrum. Unlike the μPOP, efforts were focused on the novelty of the concept and obtaining a clock signal. In this regard this demonstration can be regarded as an important step towards more compact cold-atom frequency standards. Indeed, the performances of the cold-atom clock are deliberately limited by its design: the orientation of the physics package limits the short-term performances as gravity quickly drags the atoms out of scope. Plus, the long-term stability is constrained by the absence of magnetic shielding which should be an obvious improvement in the next clock version. However, the cold-atom clock presented in this work features atom number and temperature close to the Horace clock [22] (see Figure 6.2 and Table 1.1) clock. It is hence reasonable to think that an optimized version of this clock should feature similar performances with the perk of compactness allowed by our new design featuring a GMOT integrated inside of the microwave cavity.

Bibliography

[1] E. Batori, C. Affolderbach, M. Pellaton, *et al.*, "μPOP Clock: A Microcell Atomic Clock Based on a Double-Resonance Ramsey Scheme", *Physical Review Applied*, vol. 18, no. 5, p. 054 039, 2022, ISSN: 2331-7019. DOI: 10.1103/PhysRevApplied.18.054039.

[2] J. G. Muga, R. S. Mayato, and I. L. Egusquiza, "Introduction", in *Time in Quantum Mechanics*, ser. Lecture Notes in Physics, J. Muga, R. S. Mayato, and Í. Egusquiza, Eds., vol. 734, Berlin, Heidelberg: Springer Berlin Heidelberg, 2008, pp. 1–30, ISBN: 978-3-540-73472-7. DOI: 10.1007/978-3-540-73473-4_1.

[3] F. Riehle, *Frequency Standards: Basics and Applications*. Wiley-VCH Verlag GmbH & Co. KGaA, Weinheim, 2004.

[4] B. M. Roberts, P Delva, A Al-Masoudi, *et al.*, "Search for transient variations of the fine structure constant and dark matter using fiber-linked optical atomic clocks", *New Journal of Physics*, vol. 22, no. 9, p. 093 010, 2020, ISSN: 1367-2630. DOI: 10.1088/1367-2630/abaace.

[5] J. Vanier and C. Audoin, *The Quantum Physics of Atomic Frequency Standards*. IOP Publishing Ltd, 1989, vol. 2, ISBN: 085274434X. DOI: 10.1887/085274434X.

[6] E. Batori, N. Almat, C. Affolderbach, and G. Mileti, "GNSS-grade space atomic frequency standards: Current status and ongoing developments", *Advances in Space Research*, vol. 68, no. 12, pp. 4723–4733, 2021, ISSN: 02731177. DOI: 10.1016/j.asr.2020.09.012.

[7] J. P. Gordon, H. J. Zeiger, and C. H. Townes, "The Maser—New Type of Microwave Amplifier, Frequency Standard, and Spectrometer", *Physical Review*, vol. 99, no. 4, pp. 1264–1274, 1955, ISSN: 0031-899X. DOI: 10.1103/PhysRev.99.1264.

[8] E. Batori, N. Almat, C. Affolderbach, F. Gruet, and G. Mileti, "High-performance pulsed laser-pumped Rb clock for GNSS", *© 2020 IEEE. Reprinted, with permission, from 2020 European Navigation Conference, ENC 2020,*, 2020. DOI: 10.23919/ENC48637.2020.9317388.

[9] L. A. Mallette, P. Rochat, and J. White, "Historical Review of Atomic Frequency Standards Used in Space Systems - 10 Year Update", in *Proceedings of the 38th Annual Precise Time and Time Interval Systems and Applications Meeting*, Reston, Virginia, 2006, pp. 69–80.

[10] L. Essen and J. V. Parry, "An atomic standard of frequency and time interval: A cæsium resonator", *Nature*, vol. 176, no. 4476, pp. 280–282, 1955, ISSN: 00280836. DOI: 10.1038/176280a0.

[11] CGPM. "Resolutions 1 of the 26th CGPM". (2018), [Online]. Available: https://www.bipm.org/en/CGPM/db/26/1/.

[12] E. Batori, A. Bregazzi, B. Lewis, *et al.*, "An additive-manufactured microwave cavity for a compact cold-atom clock", *Journal of Applied Physics*, vol. 133, no. 22, 2023, ISSN: 0021-8979. DOI: 10.1063/5.0151207.

[13] A. Bregazzi, E. Batori, B. Lewis, *et al.*, "A compact cold-atom double-resonance clock", in *Quantum Sensing, Imaging, and Precision Metrology*, S. M. Shahriar and J. Scheuer, Eds., SPIE, 2023, p. 18, ISBN: 9781510659995. DOI: 10.1117/12.2657390.

[14] B. L. S. Marlow and D. R. Scherer, "A Review of Commercial and Emerging Atomic Frequency Standards", *IEEE Transactions on Ultrasonics, Ferroelectrics, and Frequency Control*, vol. 68, no. 6, pp. 2007–2022, 2021, ISSN: 0885-3010. DOI: 10.1109/TUFFC.2021.3049713.

[15] ISO. "ISO 3159:2009". (2021), [Online]. Available: https://www.iso.org/standard/54804.html (visited on 04/12/2023).

[16] Microsemi, "Timing and Synchronization for LTE-TDD and LTE-Advanced Mobile Networks - White paper".

[17] W. J. Riley, "A History of the Rubidium Frequency Standard", 2019.

[18] A. Kotyukov, Y. Ivanov, and A. Nikonov, "Precise Frequency Sources Meeting the 5G Holdover Time Interval Error Requirement", *Microwave Journal*, vol. 61, no. 5, pp. 128–138, 2018.

[19] K Kebkal, O Kebkal, E Glushko, *et al.*, "Underwater acoustic modems with integrated atomic clocks for one-way travel-time underwater vehicle positioning", in *Proceefings of the Underwater Acoustics Conference and Exhibition (UACE)*, 2017.

[20] P. Tavella and G. Petit, "Precise time scales and navigation systems: mutual benefits of timekeeping and positioning", *Satellite Navigation*, vol. 1, no. 1, p. 10, 2020, ISSN: 2662-1363. DOI: 10.1186/s43020-020-00012-0.

[21] SpectraDynamics, "cRb-Clock", Tech. Rep., 2019.

[22] F. Esnault, N Rossetto, D Holleville, J Delporte, and N Dimarcq, "HORACE: A compact cold atom clock for Galileo", *Advances in Space Research*, vol. 47, no. 5, pp. 854–858, 2011, ISSN: 02731177. DOI: 10.1016/j.asr.2010.12.012.

[23] Muquans. "MuClock". (), [Online]. Available: https://www.muquans.com/wp-content/uploads/2019/03/muquans_muclock.pdf.

[24] K. Akiyama, A. Alberdi, W. Alef, *et al.*, "First M87 Event Horizon Telescope Results. IV. Imaging the Central Supermassive Black Hole", *The Astrophysical Journal*, vol. 875, no. 1, p. L4, 2019, ISSN: 2041-8213. DOI: 10.3847/2041-8213/ab0e85.

[25] R. F. Vessot, M. W. Levine, E. M. Mattison, *et al.*, "Test of relativistic gravitation with a spaceborne hydrogen maser", *Physical Review Letters*, vol. 45, no. 26, pp. 2081–2084, 1980, ISSN: 00319007. DOI: 10.1103/PhysRevLett.45.2081.

[26] J. C. Hafele and R. E. Keating, "Around-the-world atomic clocks: Predicted relativistic time gains", *Science*, vol. 177, no. 4044, pp. 166–168, 1972, ISSN: 00368075. DOI: 10.1126/science.177.4044.166.

[27] A Utkin, A Belyaev, and Y Pavlenko, "On-board active hydrogen maser for radioastron mission (design and experimental results)", in *6th International Symposium "METROLOGY OF TIME AND SPACE"*, Vremya-CH, Ed., "Vremya-CH", Nizhny Novgorod, Russia.

[28] L. C. Hernández Forero and N. B. Cortés, "Legal Time of the Republic of Colombia and its international traceability using the Cesium Atomic Clock – Time and Frequency National Standard", *Journal of Physics: Conference Series*, vol. 850, p. 012 016, 2017, ISSN: 1742-6588. DOI: 10.1088/1742-6596/850/1/012016.

[29] R. Bondarescu, A. Schärer, A. Lundgren, *et al.*, "Ground-based optical atomic clocks as a tool to monitor vertical surface motion", *Geophysical Journal International*, vol. 202, no. 3, pp. 1770–1774, 2015, ISSN: 1365-246X. DOI: 10.1093/gji/ggv246.

[30] M. Abgrall, B. Chupin, L. De Sarlo, *et al.*, "Atomic fountains and optical clocks at SYRTE: Status and perspectives", *Comptes Rendus Physique*, vol. 16, no. 5, pp. 461–470, 2015, ISSN: 16310705. DOI: 10.1016/j.crhy.2015.03.010.

[31] S Peil, S Crane, T Swanson, and C. R. Ekstrom, "The {USNO} Rubidium Fountain", in *2006 IEEE IFCS*, 2006, pp. 304–306.

[32] P. Dubé, "Ion Clock Busts into New Precision Regime", *Physics*, vol. 12, p. 79, 2019, ISSN: 1943-2879. DOI: 10.1103/Physics.12.79.

[33] C. Chou, D. Hume, J. Koelemeij, D. Wineland, and T. Rosenband, "Frequency Comparison of Two High-Accuracy Al+ Optical Clocks", *Physical Review Letters*, vol. 104, no. 7, p. 070 802, 2010, ISSN: 0031-9007. DOI: 10.1103/PhysRevLett.104.070802.

[34] M. Chwalla, J. Benhelm, K. Kim, *et al.*, "Absolute Frequency Measurement of the 40Ca+ 4s2 S1/2 - 3d2 D5/2 Clock Transistion", *Physical Review Letters*, vol. 102, no. 2, p. 023 002, 2009, ISSN: 0031-9007. DOI: 10.1103/PhysRevLett.102.023002.

[35] P. Zhang, J. Cao, H.-l. Shu, *et al.*, "Evaluation of blackbody radiation shift with temperature-associated fractional uncertainty at 10 –18 level for 40 Ca + ion optical clock", *Journal of Physics B: Atomic, Molecular and Optical Physics*, vol. 50, no. 1, p. 015 002, 2017, ISSN: 0953-4075. DOI: 10.1088/1361-6455/50/1/015002.

[36] P Dubé, A. A. Madej, and B Jian, "Sr + single-ion clock", *Journal of Physics: Conference Series*, vol. 723, p. 012 018, 2016, ISSN: 1742-6588. DOI: 10.1088/1742-6596/723/1/012018.

[37] H. S. Margolis, G. P. Barwood, G. Huang, *et al.*, "Hertz-Level Measurement of the Optical Clock Frequency in a Single 88 Sr + Ion", *Science*, vol. 306, no. 5700, pp. 1355–1358, 2004, ISSN: 0036-8075. DOI: 10.1126/science.1105497.

[38] N. Huntemann, C. Sanner, B. Lipphardt, C. Tamm, and E. Peik, "Single-Ion Atomic Clock with 3 x 10-18 Systematic Uncertainty", *Physical Review Letters*, vol. 116, no. 6, p. 063 001, 2016, ISSN: 0031-9007. DOI: 10.1103/PhysRevLett.116.063001.

[39] R. M. Godun, P. B. R. Nisbet-Jones, J. M. Jones, *et al.*, "Frequency Ratio of Two Optical Clock Transitions in Yb+171 and Constraints on the Time Variation of Fundamental Constants", *Physical Review Letters*, vol. 113, no. 21, p. 210 801, 2014, ISSN: 0031-9007. DOI: 10.1103/PhysRevLett.113.210801.

[40] S. Falke, N. Lemke, C. Grebing, *et al.*, "A strontium lattice clock with 3 × 10 –17 inaccuracy and its frequency", *New Journal of Physics*, vol. 16, no. 7, p. 073 023, 2014, ISSN: 1367-2630. DOI: 10.1088/1367-2630/16/7/073023.

[41] P. G. Westergaard, J Lodewyck, L Lorini, *et al.*, "Lattice-Induced Frequency Shifts in Sr Optical Lattice Clocks at the 10ˆ-17 Level", *Phys. Rev. Lett.*, vol. 106, no. 21, p. 210 801, 2011. DOI: 10.1103/PhysRevLett.106.210801.

[42] N. Hinkley, J. A. Sherman, N. B. Phillips, *et al.*, "An Atomic Clock with 10 –18 Instability", *Science*, vol. 341, no. 6151, pp. 1215–1218, 2013, ISSN: 0036-8075. DOI: 10.1126/science.1240420.

[43] Z. Barber, C. Hoyt, C. Oates, L. Hollberg, A. Taichenachev, and V. Yudin, "Direct Excitation of the Forbidden Clock Transition in Neutral 174Yb Atoms Confined to an Optical Lattice", *Physical Review Letters*, vol. 96, no. 8, p. 083 002, 2006, ISSN: 0031-9007. DOI: 10.1103/PhysRevLett.96.083002.

[44] J. Lodewyck, "On a definition of the {SI} second with a set of optical clock transitions", *Metrologia*, vol. 56, no. 5, p. 55 009, 2019. DOI: 10.1088/1681-7575/ab3a82.

[45] S. Hannig, L. Pelzer, N. Scharnhorst, *et al.*, "Towards a transportable aluminium ion quantum logic optical clock", *Review of Scientific Instruments*, vol. 90, no. 5, p. 053 204, 2019, ISSN: 0034-6748. DOI: 10.1063/1.5090583.

[46] M. Gellesch, J. Jones, R. Barron, *et al.*, "Transportable optical atomic clocks for use in out-of-the-lab environments", *Advanced Optical Technologies*, vol. 9, no. 5, pp. 313–325, 2020, ISSN: 2192-8584. DOI: 10.1515/aot-2020-0023.

[47] S. B. Koller, J. Grotti, S. Vogt, *et al.*, "Transportable Optical Lattice Clock with 7x10ˆ-17 Uncertainty", *Physical Review Letters*, vol. 118, no. 7, p. 073 601, 2017, ISSN: 0031-9007. DOI: 10.1103/PhysRevLett.118.073601.

[48] F. G. Ascarrunz, Y. O. Dudin, M. C. Delgado Aramburo, *et al.*, "A Portable Cold 87Rb Atomic Clock with Frequency Instability at One Day in the 10 -15 Range", in *2018 IEEE International Frequency Control Symposium (IFCS)*, IEEE, 2018, pp. 1–3, ISBN: 978-1-5386-3214-7. DOI: 10.1109/FCS.2018.8597585.

[49] S. Mulholland, S. Donnellan, G. Barwood, *et al.*, "A Portable Microwave Clock Using Laser-Cooled Trapped 171 Yb+Ions", in *2018 IEEE International Frequency Control Symposium (IFCS)*, IEEE, 2018, pp. 1–2, ISBN: 978-1-5386-3214-7. DOI: 10.1109/FCS.2018.8597512.

[50] J. Gouloumet, B. Leuenberger, C. Schori, S. Grop, and P. Rochat, "Progress towards a compact and low-power miniaturized Rubidium Oscillator (mRO™)", in *2020 IEEE/MTT-S International Microwave Symposium (IMS)*, IEEE, 2020, pp. 876–879, ISBN: 978-1-7281-6815-9. DOI: 10.1109/IMS30576.2020.9224008.

[51] J Kitching, S Knappe, P Schwindt, *et al.*, "Chip-Scale Atomic Devices", Solid-State Sensors, Actuators, and Microsystems Workshop, 2006.

[52] R Lutwak, A Rashed, M Varghesea, *et al.*, "The chip-scale atomic clock – prototype evaluation", in *39th Annual Precise Time and Time Interval (PTTI) Meeting*, 2007.

[53] A. M. Braun, T. J. Davis, M. H. Kwakernaak, *et al.*, "RF-interrogated end-state chip-scale atomic clock", in *39th Annual Precise Time and Time Interval (PTTI) Meeting*, 2007.

[54] R. Bondarescu, M. Bondarescu, G. Hetényi, L. Boschi, P. Jetzer, and J. Balakrishna, "Geophysical applicability of atomic clocks: direct continental geoid mapping", *Geophysical Journal International*, vol. 191, no. 1, pp. 78–82, 2012, ISSN: 0956540X. DOI: 10.1111/j.1365-246X.2012.05636.x.

[55] M. Arditi and T. R. Carver, "Atomic Clock Using Microwave Pulse-Coherent Techniques", *IEEE Transactions on Instrumentation and Measurement*, vol. IM-13, no. 2 & 3, pp. 146–152, 1964, ISSN: 15579662. DOI: 10.1109/TIM.1964.4313389.

[56] J. Hecht, "Short history of laser development", *Optical Engineering*, vol. 49, no. 9, p. 091 002, 2010, ISSN: 0091-3286. DOI: 10.1117/1.3483597.

[57] D. A. Steck. "Rubidium 87 D Line Data, rev. 2.2.2". (2021), [Online]. Available: http://steck.us/alkalidata.

[58] G. Mileti, Jinquan Deng, F. Walls, D. Jennings, and R. Drullinger, "Laser-pumped rubidium frequency standards: new analysis and progress", *IEEE Journal of Quantum Electronics*, vol. 34, no. 2, pp. 233–237, 1998, ISSN: 00189197. DOI: 10.1109/3.658700.

[59] T. Bandi, C. Affolderbach, C. Stefanucci, F. Merli, A. K. Skrivervik, and G. Mileti, "Compact high-performance continuous-wave double-resonance rubidium standard with 1.4 × 10–13 τ–1/2 stability", *IEEE Transactions on Ultrasonics, Ferroelectrics, and Frequency Control*, vol. 61, no. 11, pp. 1769–1778, 2014, ISSN: 0885-3010. DOI: 10.1109/TUFFC.2013.005955.

[60] A. Godone, S. Micalizio, and F. Levi, "Pulsed optically pumped frequency standard", *Physical Review A*, vol. 70, no. 2, p. 023 409, 2004, ISSN: 1050-2947. DOI: 10.1103/PhysRevA.70.023409.

[61] A Godone, S Micalizio, C. E. Calosso, and F Levi, "The pulsed rubidium clock", *IEEE Transactions on Ultrasonics, Ferroelectrics, and Frequency Control*, vol. 53, no. 3, pp. 525–529, 2006, ISSN: 0885-3010. DOI: 10.1109/TUFFC.2006.1610560.

[62] S Micalizio, A Godone, C Calosso, F Levi, C Affolderbach, and F Gruet, "Pulsed optically pumped rubidium clock with high frequency-stability performance", *IEEE Trans. Ultrason., Ferroelect., Freq. Control*, vol. 59, no. 3, pp. 457–462, 2012, ISSN: 0885-3010. DOI: 10.1109/TUFFC.2012.2215.

[63] W. Moreno, M. Pellaton, C. Affolderbach, and G. Mileti, "Barometric effect in vapor-cell atomic clocks", *IEEE Transactions on Ultrasonics, Ferroelectrics, and Frequency Control*, vol. 65, no. 8, pp. 1500–1503, 2018, ISSN: 08853010. DOI: 10.1109/TUFFC.2018.2844020.

[64] N. Almat, M. Gharavipour, W. Moreno, C. Affolderbach, and G. Mileti, "Long-Term Stability Analysis Towards < 10 -14 Level for a Highly Compact POP Rb Cell Atomic Clock", in *2019 Joint Conference of the IEEE International Frequency Control Symposium and European Frequency and Time Forum (EFTF/IFC)*, vol. 67, IEEE, 2019, pp. 1–2, ISBN: 978-1-5386-8305-7. DOI: 10.1109/FCS.2019.8856061.

[65] S. Kang, M. Gharavipour, C. Affolderbach, F. Gruet, and G. Mileti, "Demonstration of a high-performance pulsed optically pumped Rb clock based on a compact magnetron-type microwave cavity", *Journal of Applied Physics*, 47th ser., vol. 117, no. 10, E. Armandillo, J. Costeraste, and N. Karafolas, Eds., p. 104 510, 2015, ISSN: 0021-8979. DOI: 10.1063/1.4914493. arXiv: 1111.3450.

[66] G. D. Gongxun Dong, J. D. Jianliao Deng, J. L. Jinda Lin, *et al.*, "Recent improvements on the pulsed optically pumped rubidium clock at SIOM", *Chinese Optics Letters*, vol. 15, no. 4, pp. 040 201–40 204, 2017, ISSN: 1671-7694. DOI: 10.3788/COL201715.040201.

[67] G. Dong, J. Deng, J. Lin, Song Zhang, and Y. Wang, "The progress of pulsed optically pumped rubidium clock at SIOM", in *2016 Progress in Electromagnetic Research Symposium (PIERS)*, IEEE, 2016, pp. 3716–3719, ISBN: 978-1-5090-6093-1. DOI: 10.1109/PIERS.2016.7735410.

[68] M. Gozzelino, S. Micalizio, C. E. Calosso, A. Godone, H. Lin, and F. Levi, "Loaded Microwave Cavity for Compact Vapor-Cell Clocks", *IEEE Transactions on Ultrasonics, Ferroelectrics, and Frequency Control*, vol. 68, no. 3, pp. 872–879, 2021, ISSN: 0885-3010. DOI: 10.1109/TUFFC.2020.3011604.

[69] S Micalizio, ·. F. Levi, ·. C. E. Calosso, ·. M. Gozzelino, and ·. A. Godone, "A pulsed-Laser Rb atomic frequency standard for GNSS applications", *GPS Solutions*, vol. 25, p. 94, 2021. DOI: 10.1007/s10291-021-01136-9.

[70] S. T. Müller, D. V. Magalhães, R. F. Alves, and V. S. Bagnato, "Compact frequency standard based on an intracavity sample of cold cesium atoms", *Journal of the Optical Society of America B*, vol. 28, no. 11, p. 2592, 2011, ISSN: 0740-3224. DOI: 10.1364/JOSAB.28.002592.

[71] C. Fertig and K. Gibble, "Measurement and Cancellation of the Cold Collision Frequency Shift in an 87Rb Fountain Clock", *Physical Review Letters*, vol. 85, no. 8, pp. 1622–1625, 2000, ISSN: 0031-9007. DOI: 10.1103/PhysRevLett.85.1622.

[72] B. Pelle, R. Szmuk, B. Desruelle, D. Holleville, and A. Landragin, "Cold-Atom-Based Commercial Microwave Clock at the 10-15 Level", *IFCS 2018 - IEEE International Frequency Control Symposium*, pp. 1–5, 2018. DOI: 10.1109/FCS.2018.8597468.

[73] M. Givon, L. Habib, A. Waxman, *et al.*, "In-vacuum microwave resonator for a compact cold atom frequency standard", 2022. arXiv: 2208.09038.

[74] R Szmuk, V Dugrain, W Maineult, J Reichel, and P Rosenbusch, "Stability of a trapped-atom clock on a chip", *Physical Review A*, vol. 92, no. 1, p. 012 106, 2015, ISSN: 1050-2947. DOI: 10.1103/PhysRevA.92.012106.

[75] A Jallageas, L Devenoges, M Petersen, *et al.*, "First uncertainty evaluation of the FoCS-2 primary frequency standard", *Metrologia*, vol. 55, no. 3, p. 366, 2018. DOI: https://doi.org/10.1088/1681-7575/aab3fa.

[76] Muquans. "No Title". (2019), [Online]. Available: https://www.muquans.com/wp-content/uploads/2019/03/muquans_muclock.pdf (visited on 01/17/2023).

[77] P. Liu, Y. Meng, J. Wan, *et al.*, "Scheme for a compact cold-atom clock based on diffuse laser cooling in a cylindrical cavity", *Physical Review A*, vol. 92, no. 6, p. 062 101, 2015, ISSN: 1050-2947. DOI: 10.1103/PhysRevA.92.062101.

[78] AOSENSE. "Cold-atom clock datasheet". (), [Online]. Available: https://aosense.com/wp-content/uploads/2018/02/Cold-Atom-Frequency-Stadard.pdf (visited on 01/25/2023).

[79] M. Y. Yu, Y. L. Meng, M. F. Ye, *et al.*, "Development of the integrated integrating sphere cold atom clock", *Chinese Physics B*, vol. 28, no. 7, pp. 70 602–070 602, 2019, ISSN: 20583834. DOI: 10.1088/1674-1056/28/7/070602.

[80] C. Lacroute, F. Reinhard, F. Ramirez-Martinez, *et al.*, "Preliminary results of the trapped atom clock on a chip", *IEEE Transactions on Ultrasonics, Ferroelectrics and Frequency Control*, vol. 57, no. 1, pp. 106–110–106–110, 2010.

[81] J. Reichel, W. Hänsel, and T. W. Hänsch, "Atomic micromanipulation with magnetic surface traps", *Physical Review Letters*, vol. 83, no. 17, pp. 3398–3401, 1999, ISSN: 10797114. DOI: 10.1103/PhysRevLett.83.3398.

[82] S. Lee, G. W. Choi, H.-G. Hong, *et al.*, "A compact cold-atom clock based on a loop-gap cavity", *Applied Physics Letters*, vol. 119, no. 6, p. 064 002, 2021, ISSN: 0003-6951. DOI: 10.1063/5.0057150.

[83] E. Batori, A. Bregazzi, B. Lewis, *et al.*, "An additive-manufactured microwave cavity for a compact cold-atom clock", *To be published.*, 2023. arXiv: 2305.02898.

[84] A. Bregazzi, "A cold-atom Ramsey clock with a low volume physics package", *To be published.*, 2023. arXiv: 2305.02944.

[85] E. A. Burt, J. D. Prestage, R. L. Tjoelker, *et al.*, "Demonstration of a trapped-ion atomic clock in space", *Nature*, vol. 595, no. 7865, pp. 43–47, 2021, ISSN: 0028-0836. DOI: 10.1038/s41586-021-03571-7.

[86] M. Huang, A. Little, and J. Camparo, "LaLI-POP: Lamp and Laser Integrated Pulsed-Optically Pumped Atomic Clock", in *2022 Joint Conference of the European Frequency and Time Forum and IEEE International Frequency Control Symposium (EFTF/IFCS)*, IEEE, 2022, pp. 1–4, ISBN: 978-1-6654-9718-3. DOI: 10.1109/EFTF/IFCS54560.2022.9850793.

[87] T. Mccaskill, J. White, S. Stebbins, and J. Buisson, "NTS-2 Cesium Frequency Stability Results", in *32nd Annual Symposium on Frequency Control*, IEEE, 1978, pp. 560–566. DOI: 10.1109/FREQ.1978.200290.

[88] F Droz, P Mosset, G Barmaverain, *et al.*, "The on-board Galileo clocks: Rubidium standard and Passive Hydrogen Maser - current status and performance", in *Proceedings of the 20th European Frequency and Time Forum*, 2006, pp. 420–426.

[89] M. Guo, Y. Fan, X. Fan, G. Sun, J. Zhen, and W. Zhai, "Performance Analysis of BDGIM", in 2020, pp. 101–113. DOI: 10.1007/978-981-15-3715-8_10.

[90] QZSS. "Interview". (2021), [Online]. Available: https://qzss.info/interview01.html (visited on 04/17/2023).

[91] T. N. Bandi, N. M. Desai, J. Kaintura, *et al.*, "Advanced space rubidium atomic frequency standard for satellite navigation", *GPS Solutions*, vol. 26, no. 2, p. 54, 2022, ISSN: 1080-5370. DOI: 10.1007/s10291-022-01239-x.

[92] E. Batori, N. Almat, C. Affolderbach, F. Gruet, and G. Mileti, "High-Performance Pulsed Laser-Pumped Rb Clock for GNSS", in *2020 European Navigation Conference (ENC)*, IEEE, 2020, pp. 1–10, ISBN: 978-3-944976-27-3. DOI: 10.23919/ENC48637.2020.9317388.

[93] R. H. Dicke, "The Effect of Collisions upon the Doppler Width of Spectral Lines", *Physical Review*, vol. 89, no. 2, pp. 472–473, 1953, ISSN: 0031-899X. DOI: 10.1103/PhysRev.89.472.

[94] H. G. Dehmelt, "Slow Spin Relaxation of Optically Polarized Sodium Atoms", *Physical Review*, vol. 105, no. 5, pp. 1487–1489, 1957, ISSN: 0031-899X. DOI: 10.1103/PhysRev.105.1487.

[95] J Vanier, R Kunski, N Cyr, J. Y. Savard, and M.Têtu, "On hyperfine frequency shifts caused by buffer gases: Application to the optically pumped passive rubidium frequency standard", *J. Appl. Phys.*, vol. 53, no. 8, pp. 5387–5391, 1982. DOI: 10.1063/1.331467.

[96] C. Carlé, S. Keshavarzi, A. Mursa, *et al.*, "Reduction of helium permeation in microfabricated cells using aluminosilicate glass substrates and Al$_2$O$_3$ coatings", 2023. arXiv: 2303.13927.

[97] B. S. Mathur, H. Tang, and W. Happer, "Light Shifts in the Alkali Atoms", *Physical Review*, vol. 171, no. 1, pp. 11–19, 1968, ISSN: 0031-899X. DOI: 10.1103/PhysRev.171.11.

[98] J. Vanier and C. Mandache, "The passive optically pumped Rb frequency standard: the laser approach", *Appl. Phys. B*, vol. 87, no. 4, pp. 565–593, 2007, ISSN: 09462171. DOI: 10.1007/s00340-007-2643-5.

[99] W. Moreno, "Rubidium Vapour-cell Frequency Standards : Metrology of Optical and Microwave Frequency References", Ph.D. dissertation, Université de Neuchâtel., Neuchâtel, Switzerland., 2019. DOI: 10.35662/unine-thesis-2761.

[100] G. H. Zhang, B. Braverman, A. Kawasaki, and V. Vuletić, "Fast compact laser shutter using a direct current motor and three-dimensional printing", *Review of Scientific Instruments*, vol. 86, no. 12, p. 126 105, 2015, ISSN: 0034-6748. DOI: 10.1063/1.4937614.

[101] W Moreno, M Pellaton, N Almat, M Gharavipour, C Affolderbach, and G. Mileti, "Investigations on microwave power shift in compact vapor-cell atomic clock", in *2019 Joint Conference of the IEEE International Frequency Control Symposium and European Frequency and Time Forum*, 2019.

[102] J. D. Jackson, "Electrodynamics, Classical", in *digital Encyclopedia of Applied Physics*, Weinheim, Germany: Wiley-VCH Verlag GmbH & Co. KGaA, 2003. DOI: 10.1002/3527600434.eap109.

[103] A Risley, S Jarvis, and J Vanier, "The Dependence of Frequency Upon Microwave Power of Wall-coated and Buffer-gas-filled Gas Cell Rb^{87} Frequency Standards", *J. Appl. Phys.*, vol. 51, no. 9, pp. 4571–4576–4571–4576, 1980.

[104] W. Riley, "The physics of the environmental sensitivity of rubidium gas cell atomic frequency standards", *IEEE Transactions on Ultrasonics, Ferroelectrics and Frequency Control*, vol. 39, no. 2, pp. 232–240, 1992, ISSN: 0885-3010. DOI: 10.1109/58.139119.

[105] F. Gruet, M. Pellaton, C. Affolderbach, T. Bandi, R. Matthey, and G. Mileti, "Compact and frequency stabilised laser heads for rubidium atomic clocks", in *Proc. ICSO*, 2012. DOI: 10.1117/12.2309135.

[106] S. Micalizio, C. E. Calosso, F. Levi, and A. Godone, "Ramsey-fringe shape in an alkali-metal vapor cell with buffer gas", *Phys. Rev. A*, vol. 88, no. 3, p. 33 401, 2013. DOI: 10.1103/PhysRevA.88.033401.

[107] A Godone, F Levi, and S Micalizio, *Coherent Population Trapping Maser*. CLUT Editrice, 2002, p. 191, ISBN: 88-7992-166-5.

[108] L. A. N. Laboratory. "Rubidium". (2021), [Online]. Available: https://periodic.lanl.gov/37.shtml (visited on 05/12/2023).

[109] C. Cohen-Tannoudji, B. Diu, and F. Laloë, *Mecanique Quantique vol. I and II*. Hermann, 2000.

[110] A. Godone, F. Levi, S. Micalizio, and J. Vanier, "Theory of the coherent population trapping maser: A strong-field self-consistent approach", *Physical Review A*, vol. 62, no. 5, p. 053 402, 2000, ISSN: 1050-2947. DOI: 10.1103/PhysRevA.62.053402.

[111] W. Demtröder, *Laser Spectroscopy 1: Basic Principles*. Springer-Verlag Berlin Heidelberg, 2014. DOI: 10.1007/978-3-642-53859-9.

[112] W. J. Riley and D. A. Howe, *Handbook of Frequency Stability Analysis*. NIST Spec. Pubs., 2008.

[113] R. Baugh, "Frequency Modulation Analysis with the Hadamard Variance", in *25th Annual Symposium on Frequency Control*, IEEE, 1971, pp. 222–225. DOI: 10.1109/FREQ.1971.199860.

[114] D. Allan and J. Barnes, "A Modified "Allan Variance" with Increased Oscillator Characterization Ability", in *Thirty Fifth Annual Frequency Control Symposium*, IEEE, 1981, pp. 470–475. DOI: 10.1109/FREQ.1981.200514.

[115] D. Howe and T. Tasset, "Theo1: characterization of very long-term frequency stability", in *18th European Frequency and Time Forum (EFTF 2004)*, IEE, 2004, pp. 581–587, ISBN: 0-86341-384-6. DOI: 10.1049/cp:20040933.

[116] E. Rubiola and F. Vernotte, "The Companion of Enrico's Chart for Phase Noise and Two-Sample Variances", *IEEE Transactions on Microwave Theory and Techniques*, pp. 1–30, 2023, ISSN: 0018-9480. DOI: 10.1109/TMTT.2023.3238267.

[117] D. A. Howe, "ThêoH: A hybrid, high-confidence statistic that improves on the Allan deviation", *Metrologia*, vol. 43, no. 4, S322–S331–S322–S331, 2006, ISSN: 00261394. DOI: 10.1088/0026-1394/43/4/S20.

[118] F Vernotte and É Lantz, "Three-Cornered Hat and Groslambert Covariance: A First Attempt to Assess the Uncertainty Domains", *IEEE Transactions on Ultrasonics, Ferroelectrics, and Frequency Control*, vol. 66, no. 3, pp. 643–653, 2019, ISSN: 0885-3010. DOI: 10.1109/TUFFC.2018.2889703.

[119] E. Lantz, C. E. Calosso, E. Rubiola, *et al.*, "KLTS: A Rigorous Method to Compute the Confidence Intervals for the Three-Cornered Hat and for Groslambert Covariance", *IEEE Transactions on Ultrasonics, Ferroelectrics, and Frequency Control*, vol. 66, no. 12, pp. 1942–1949, 2019, ISSN: 0885-3010. DOI: 10.1109/TUFFC.2019.2931911.

[120] T4Science. "iMaser 3000 Smart Active Hydrogen Maser Clock". (), [Online]. Available: https://www.t4science.ch/products/imaser3000/ (visited on 03/21/2022).

[121] M. Weiss, G. Petit, and Z. Jiang, "A comparison of GPS common-view time transfer to all-in-view", in *Proceedings of the 2005 IEEE International Frequency Control Symposium and Exposition, 2005.*, IEEE, pp. 324–328, ISBN: 0-7803-9053-9. DOI: 10.1109/FREQ.2005.1573953.

[122] IGS. "IGS Products". (2023), [Online]. Available: https://igs.org/products/ (visited on 05/12/2023).

[123] A. Rovira-Garcia, J. M. Juan, J. Sanz, *et al.*, "Removing day-boundary discontinuities on GNSS clock estimates: methodology and results", *GPS Solutions*, vol. 25, no. 2, p. 35, 2021, ISSN: 1080-5370. DOI: 10.1007/s10291-021-01085-3.

[124] N. Almat, "Metrological and stability studies in high-performance rubidium vapor-cell atomic clocks", Ph.D. dissertation, Université de Neuchâtel., Neuchâtel, Switzerland., 2020. DOI: 10.35662/unine-thesis-2836.

[125] M Violetti, F Merli, J.-F. Zürcher, *et al.*, "New Miniaturized Microwave Cavity for Rubidium Atomic Clocks", in *proc. IEEE Sensors 2012*, proc. IEEE Sensors 2012, 2012.

[126] J. C. Camparo, "Conversion of laser phase noise to amplitude noise in an optically thick vapor", *J. Opt. Soc. Am. B*, vol. 15, no. 3, pp. 1177–1186, 1998. DOI: 10.1364/JOSAB.15.001177.

[127] C. E. Calosso, M. Gozzelino, A. Godone, H. Lin, F. Levi, and S. Micalizio, "Intensity Detection Noise in Pulsed Vapor-Cell Frequency Standards", *IEEE Transactions on Ultrasonics, Ferroelectrics, and Frequency Control*, vol. 67, no. 5, pp. 1074–1079, 2020, ISSN: 15258955. DOI: 10.1109/TUFFC.2019.2957418.

[128] S. Kang, M. Gharavipour, C. Affolderbach, and G. Mileti, "Stability limitations from optical detection in Ramsey-type vapour-cell atomic clocks", *Electronics Letters*, vol. 51, no. 22, pp. 1767–1769, 2015, ISSN: 0013-5194. DOI: 10.1049/el.2015.1902.

[129] Y Pétremand, C Affolderbach, R Straessle, *et al.*, "Microfabricated rubidium vapour cell with a thick glass core for small-scale atomic clock applications", *J. Micromech. Microeng.*, vol. 22, no. 2, p. 25 013, 2012.

[130] O. A. Alduchov and R. E. Eskridge, "Improved Magnus Form Approximation of Saturation Vapor Pressure", *Journal of Applied Meteorology*, vol. 35, no. 4, pp. 601–609, 1996, ISSN: 0894-8763. DOI: 10.1175/1520-0450(1996)035<0601:IMFAOS>2.0.CO;2.

[131] M. Gozzelino, S. Micalizio, C. E. Calosso, A. Godone, and F. Levi, "Kr-Based Buffer Gas for Rb Vapor-Cell Clocks", *IEEE Transactions on Ultrasonics, Ferroelectrics, and Frequency Control*, vol. 68, no. 4, pp. 1442–1447, 2021, ISSN: 15258955. DOI: 10.1109/TUFFC.2020.3026220.

[132] W. Franzen, "Spin Relaxation of Optically Aligned Rubidium Vapor", *Physical Review*, vol. 115, no. 4, p. 850, 1959, ISSN: 0031899X. DOI: 10.1103/PhysRev.115.850.

[133] A. Horsley, G.-X. Du, M. Pellaton, C. Affolderbach, G. Mileti, and P. Treutlein, "Imaging of relaxation times and microwave field strength in a microfabricated vapor cell", *Phys. Rev. A*, vol. 88, p. 63 407, 2013.

[134] C Affolderbach, G Du, T Bandi, A Horsley, P Treutlein, and G Mileti, "Imaging Microwave and DC Magnetic Fields in a Vapor-Cell Rb Atomic Clock", *IEEE Transactions on Instrumentation and Measurement*, vol. 64, no. 12, pp. 3629–3637, 2015, ISSN: 0018-9456. DOI: 10.1109/TIM.2015.2444261.

[135] M Gharavipour, C Affolderbach, S Kang, and G Mileti, "Double-resonance spectroscopy in Rubidium vapour-cells for high performance and miniature atomic clocks", *Journal of Physics: IOP Conf. Series*, vol. 793, no. 1, p. 12 007, 2017. DOI: 10.1088/1742-6596/793/1/012007.

[136] H. Watts, "Diffusion of krypton-85 in multicomponent mixtures of krypton with helium, neon, argon and xenon", *Transactions of the Faraday Society*, vol. 60, p. 1745, 1964, ISSN: 0014-7672. DOI: 10.1039/tf9646001745.

[137] C. B. Alcock, V. P. Itkin, and M. K. Horrigan, "Vapour Pressure Equations for the Metallic Elements: 298–2500K", *Canadian Metallurgical Quarterly*, vol. 23, no. 3, pp. 309–313, 1984, ISSN: 0008-4433. DOI: 10.1179/cmq.1984.23.3.309.

[138] E. L. Cussler, *Diffusion*. Cambridge University Press, 2009, p. 647, ISBN: 9780521871211. DOI: 10.1017/CBO9780511805134.

[139] M. Abdel Hafiz, C. Carlé, N. Passilly, J. M. Danet, C. E. Calosso, and R. Boudot, "Light-shift mitigation in a microcell-based atomic clock with symmetric auto-balanced Ramsey spectroscopy", *Applied Physics Letters*, vol. 120, no. 6, p. 064 101, 2022, ISSN: 0003-6951. DOI: 10.1063/5.0082156.

[140] C. Carlé, M. Petersen, N. Passilly, M. A. Hafiz, E. De Clercq, and R. Boudot, "Exploring the use of Ramsey-CPT spectroscopy for a microcell-based atomic clock", *IEEE Transactions on Ultrasonics, Ferroelectrics, and Frequency Control*, vol. 68, no. 10, pp. 3249–3256, 2021, ISSN: 0885-3010.

[141] Microsemi. "Chip Scale Atomic Clock, SA.45s CSAC". (), [Online]. Available: https://www.microsemi.com/document-portal/doc_download/133305-sa-45s-csac-datasheet.

[142] A. Stern, B. Levy, C. Levy, *et al.*, "The NAC - a miniature CPT Rubidium clock", in *2016 European Frequency and Time Forum (EFTF)*, IEEE, 2016, pp. 1–4, ISBN: 978-1-5090-0720-2. DOI: 10.1109/EFTF.2016.7477765.

[143] Y. Zhang, W. Yang, S. Zhang, and J. Zhao, "Rubidium chip-scale atomic clock with improved long-term stability through light intensity optimization and compensation for laser frequency detuning", *Journal of the Optical Society of America B*, vol. 33, no. 8, p. 1756, 2016, ISSN: 0740-3224. DOI: 10.1364/josab.33.001756.

[144] H. Zhang, H. Herdian, A. T. Narayanan, *et al.*, "ULPAC: A Miniaturized Ultralow-Power Atomic Clock", *IEEE Journal of Solid-State Circuits*, vol. 54, no. 11, pp. 3135–3148, 2019, ISSN: 1558173X. DOI: 10.1109/JSSC.2019.2941004.

[145] M Gozzelino, S Micalizio, F Levi, A Godone, and C. E. Calosso, "Reducing cavity-pulling shift in Ramsey-operated compact clocks", *IEEE Transactions on Ultrasonics, Ferroelectrics, and Frequency Control*, p. 1, 2018, ISSN: 0885-3010. DOI: 10.1109/TUFFC.2018.2828987.

[146] M. Pellaton, C. Affolderbach, E. Batori, *et al.*, "LEMAC: LTF-EPFL Miniature Atomic Clock : current status", in *2022 Joint Conference of the European Frequency and Time Forum and IEEE International Frequency Control Symposium (EFTF/IFCS)*, IEEE, 2022, pp. 1–2, ISBN: 978-1-6654-9718-3. DOI: 10.1109/EFTF/IFCS54560.2022.9850715.

[147] T. Ide, S. Goka, and Y. Yano, "CPT pulse excitation method based on VCSEL current modulation for miniature atomic clocks", *2015 Joint Conference of the IEEE International Frequency Control Symposium and the European Frequency and Time Forum, FCS 2015 - Proceedings*, vol. 978, pp. 167–170, 2015. DOI: 10.1109/FCS.2015.7138815.

[148] C. G. Montgomery, *Technique of Microwave Measurements. Edited by C.G. Montgomery, Etc* ([Massachusetts Institute of Technology. Radiation Laboratory Series. no. 11.]). McGraw-Hill Book Company, 1947.

[149] C. Stefanucci, T. Bandi, F. Merli, *et al.*, "Compact microwave cavity for high performance rubidium frequency standards", *Review of Scientific Instruments*, vol. 83, no. 10, p. 104 706, 2012, ISSN: 0034-6748. DOI: 10.1063/1.4759023.

[150] A. Bermúdez, L. Hervella–Nieto, A. Prieto, and R. Rodríguez, "Perfectly Matched Layers", in *Computational Acoustics of Noise Propagation in Fluids - Finite and Boundary Element Methods*, Berlin, Heidelberg: Springer Berlin Heidelberg, pp. 167–196. DOI: 10.1007/978-3-540-77448-8_7.

[151] B. Lewis, R. Elvin, A. S. Arnold, E. Riis, and P. F. Griffin, "A grating-chip atomic fountain", *Applied Physics Letters*, vol. 121, no. 16, p. 164 001, 2022, ISSN: 0003-6951. DOI: 10.1063/5.0115382.

[152] R. L. David, *CRC Handbook of Chemistryand Physics, Internet Version 2005*. CRC Press, BocaRaton, FL, 2005.

[153] B. Gao, "Effects of Zeeman degeneracy on the steady-state properties of an atom interacting with a near- resonant laser field: Analytic results", *Physical Review A*, vol. 48, no. 2443, 1993.

[154] G. Santarelli, C. Audoin, A. Makdissi, P. Laurent, G. Dick, and A. Clairon, "Frequency stability degradation of an oscillator slaved to a periodically interrogated atomic resonator", *IEEE Transactions on Ultrasonics, Ferroelectrics and Frequency Control*, vol. 45, no. 4, pp. 887–894, 1998, ISSN: 0885-3010. DOI: 10.1109/58.710548.

[155] R. Elvin, "Phase-sensitive optical spectroscopy of a laser-cooled, microwave atomic clock", Ph.D. dissertation, Strathclyde, 2020. DOI: 10.48730/q3zy-ad71.

[156] Y. X. Duan, B. Wang, J. F. Xiang, *et al.*, "State Preparation in a Cold Atom Clock by Optical Pumping", *Chinese Physics Letters*, vol. 34, no. 7, p. 073 201, 2017, ISSN: 17413540. DOI: 10.1088/0256-307X/34/7/073201.

[157] S. Negusse, P. Handel, and P. Zetterberg, "IEEE-STD-1057 Three Parameter Sine Wave Fit for SNR Estimation: Performance Analysis and Alternative Estimators", *IEEE Transactions on Instrumentation and Measurement*, vol. 63, no. 6, pp. 1514–1523, 2014, ISSN: 0018-9456. DOI: 10.1109/TIM.2013.2293226.

[158] S. T. Müller, D. V. Magalhães, R. F. Alves, and V. S. Bagnato, "Compact frequency standard based on an intracavity sample of cold cesium atoms", *Journal of the Optical Society of America B*, vol. 28, no. 11, p. 2592, 2011, ISSN: 0740-3224. DOI: 10.1364/JOSAB.28.002592.

[159] M. Gozzelino, A. Godone, S. Micalizio, F. Levi, and C. Calosso, "Microwave field amplitude stabilization using Ramsey spectroscopy signal", in *2018 European Frequency and Time Forum (EFTF)*, IEEE, 2018, pp. 80–82, ISBN: 978-1-5386-5620-4. DOI: 10.1109/EFTF.2018.8409002.

[160] O. S. Burrow, P. F. Osborn, E. Boughton, *et al.*, "Stand-alone vacuum cell for compact ultracold quantum technologies", *Applied Physics Letters*, vol. 119, no. 12, p. 124 002, 2021, ISSN: 0003-6951. DOI: 10.1063/5.0061010.

[161] R. Lutwak, A. Rashed, M. Varghese, *et al.*, "The chip-scale atomic clock - prototype evaluation", *39th Annual Precise Time and Time Interval (PTTI) Systems and Applications Meeting 2007*, vol. 85, no. 9, pp. 269–290, 2007, ISSN: 00036951. DOI: 10.1063/1.1787942.

[162] P. Matthieu, "High-resolution spectroscopic studies in glass-blown and micro-fabricated cells for miniature rubidium atomic clocks", Ph.D. dissertation, Université de Neuchâtel., Neuchâtel, Switzerland., 2014. DOI: 10.35662/unine-thesis-2406.

Profile
Etienne Batori
14.07.1993
etienne.batori@gmail.com
+41 76 341 04 21
Rue Etraz 10
1003 Lausanne
Suisse

Etienne Batori

PhD in Physics

Motivation I am always looking for the next challenge to apply and develop my skills. I am driven by curiosity and the perspective of a steep learning curve.

Experience

August 2019 to July 2023

PhD in Physics - Université de Neuchâtel

- **Thesis**: *Studies on Miniature and Compact Ramsey Double-Resonance Rubidium Atomic Clocks using Hot Vapor and Cold Atoms*
- 2021 to 2022: UFFC student representative for frequency control
- Summer 2022: Visiting researcher at University of Strathclyde
- Spring 2020: Winner of University of Neuchâtel *Ma thèse en 180 secondes* selection - `bit.ly/3K4PFQv`

2018 to 2019

Administrative assistant at Hôpital-Riviera-Chablais

2016 to 2018

Student assistant in various EPFL physics courses

Summer 2017

Summer job as SQL programmer at TaxaForm Sàrl

2016 to 2017

40+ hours as substitute teacher

Education

August 2018

Master of Science in Physics - EPFL
Master thesis: *Multiexciton states symmetries in C_{3v} quantum dots*

August 2016

Bachelor of Science in Physics - EPFL
Third year spent in Zürich (ETHZ) as exchange student

2012

Highschool degree

- Received the informatics award

Until 2012

Compulsory education in Echallens

Language skills

French

Native speaker

English

Highly proficient in spoken and written English

Other skills and interests

Programming languages

Intermediate level in C++, Python, MATLAB, SQL, Rust

Hobbys

- **Outdoors** Climbing, Hiking, Beekeeping
- **Indoors** Programming, Board games